APPLICATION OF ODT TO TURBULENT FLOW PROBLEMS

Anwendung von ODT auf turbulente Strömungsprobleme

Von der Fakultät für Maschinenbau, Elektrotechnik und Wirtschaftsingenieurwesen der Brandenburgischen Technischen Universität Cottbus zur Erlangung des akademischen Grades eines

Doktors der Ingenieurwissenschaften
(Doktor-Ingenieurs)

genehmigte Dissertation vorgelegt von

Diplom-Ingenieur
Falko T. Meiselbach, geb. Schulz

geboren am 11.12.1982 in Berlin, Deutschland

Vorsitzender:	Prof. Dr.-Ing. Ennes Sarradj	(BTU Cottbus)
Gutachter:	Prof. Dr.-Ing. Heiko Schmidt	(BTU Cottbus)
Gutachter:	Prof. Dr.-Ing. Christian O. Paschereit	(TU Berlin)

Tag der mündlichen Prüfung: 24. März 2015

APPLICATION OF ODT TO TURBULENT FLOW PROBLEMS

DIPL.-ING. FALKO T. MEISELBACH

University:
Brandenburg University of Technology Cottbus-Senftenberg

Faculty:
Mechanical, Electrical and Industrial Engineering

Department:
Assistent Professor flow modeling

March 2015

Dipl.-Ing. Falko T. Meiselbach:
Application of ODT to turbulent flow problems,
© March 2015

SUPERVISORS:
Prof. Dr.-Ing. Heiko Schmidt
Dr. Alan R. Kerstein

REVIEWER:
Prof. Dr.-Ing. Heiko Schmidt
Prof. Dr.-Ing. Christian O. Paschereit

LOCATION:
Cottbus

TIME FRAME:
March 2015

ABSTRACT

The continual optimization process for more efficiency of industrial flows has raised the need for providing deeper understanding of turbulence. These details can be provided by direct numerical simulation (DNS), which is impossible for most flows with current computers. Therefore, progress in optimizing Reynolds averaged Navier-Stokes (RANS) and large eddy simulation (LES) modeling strategies will need to continue. Another ansatz is the reduction to 2D or 1D models to reduce the numerical cost.

One dimensional turbulence (ODT) as presented by A. R. Kerstein[1] is a new modeling strategy that reduces the 3D simulation to a 1D line of sight through the flow region. Due to the higher resolution afforded by the 1D model, it is possible to simulate even the smallest scales and to provide insight into turbulence statistics.

To assess the advantages and disadvantages of the model, ODT has to be validated against several flows. Within this thesis, ODT is validated against the channel flow, the passive scalar transport and the channel flow with a fluctuating pressure gradient. These flows are simplified test cases for the phenomena present in single-phase industrial flows. ODT produces meaningful results for friction Reynolds numbers up to $\mathrm{Re}_\tau = 6 \cdot 10^5$ and for Prandtl numbers from $\mathrm{Pr} = 0.025$ to 50. Statistics of the wall shear stress are presented and the influence of pressure fluctuations is discussed.

Based on these channel results, the non-breaking and breaking jet are simulated. While the former is a simplified case of a free-surface flow, the latter is of primary interest for spray formation and fuel injection. Detailed statistics of the TKE budgets and the breakup are presented.

As the last case, the cloud top of a stratocumulus-topped boundary layer (STBL) was simulated. The case combines the interaction of an active and a passive scalar. It further combines the simulation of a stable and an unstable stratified region that suppresses and enhances turbulence respectively. The simulations reproduce the entrainment velocity and generate comparable mean and flux profiles compared to DNSs.

---

[1] A. R. Kerstein: One-dimensional turbulence: Model formulation and application to homogeneous turbulence, shear flows, and buoyant stratified flows, *Journal of Fluid Mechanics* **392**, 1999 (reference [46])

KURZFASSUNG

Der stetige Optimierungsprozess industrieller Strömungen erfordert ein immer detaillierteres Verständnis der Turbulenzen innerhalb dieser Strömungen. Die benötigten Details können durch direkte numerische Simulationen (DNS) generiert werden, welche für die meisten industriellen Strömungen mit der heutigen Rechentechnik zu aufwändig sind. Daher ist es notwendig die Modellierungsmethoden basierend auf den Reynolds gemittelten Navier-Stokes Gleichungen (RANS) oder der Großskalensimulation (LES) zu verbessern. Alternativ können auch neue Modelle entwickelt werden, die die Dimensionen auf 2D oder 1D reduzieren.

One dimensional turbulence (ODT), welches von A. R. Kerstein[2] entwickelt und veröffentlicht wurde, ist ein Modell, welches 3D Simulationen auf eine 1D Linie durch das Strömungsgebiet reduziert. Durch die Reduktion der Dimensionen ist es möglich die Gitterauflösung zu erhöhen und selbst die kleinsten physikalischen Skalen zu simulieren. Um die Vor- und Nachteile des Modells bewerten zu können, ist es erforderlich ODT an verschiedensten Strömungen zu verifizieren. Innerhalb dieser Dissertation wurden Vergleiche zur einfachen Kanalströmung, zur Kanalströmung mit passivem Skalar und zur Kanalströmung mit einem fluktuierenden Druckgradienten durchgeführt. Diese Testfälle wurden aufgrund ihrer Einfachheit und Allgemeingültigkeit für industrielle Strömungen ausgewählt. Mit Hilfe von ODT konnten Kanalströmungen mit Reynoldszahlen bis $Re_\tau = 6 \cdot 10^5$ und Prandtlzahlen im Bereich von $Pr = 0.025$ bis 50 simuliert werden. Statistiken zum Wandschubgradienten werden päsentiert und der Einfluss von Druckfluktuationen diskutiert.

Basierend auf diesen Ergebnissen wurden weitere Untersuchungen zum Flüssigkeitsstrahl mit und ohne Tropfenbildung durchgeführt. Ohne Tropfenbildung kann der Flüssigkeitsstrahl als exemplarische Strömung für freie Oberflächen dienen. Hingegen bildet die Strömung mit Tropfenbildung die Basis für Simulationen von Aerosolen oder Einspitzvorgängen. Detaillierte Statistiken zu den Anteilen der TKE und der Tropfenbildung werden diskutiert.

Als letzter Testfall wurde ein Ersatzsystem für eine atmosphärische Grenzschicht mit Stratokumulus-Wolken simuliert. Diese Strömung kombiniert einerseits die Simulation von zwei gekoppelten Skalaren, andererseits die Effekte von stabilen und instabilen Schichtungen, wobei erstere die Turbulenz unterbinden und letztere die Turbulenz anfachen. Bei den Skalaren ist einer aktiv und beeinflusst somit die Stabilität der Schichtung, während der andere passiv ist. Im Vergleich zur DNS konnte die Einmischungsgeschwindigkeit sowie die mittleren Profile und Flüsse reproduziert werden.

---

[2] A. R. Kerstein: One-dimensional turbulence: Model formulation and application to homogeneous turbulence, shear flows, and buoyant stratified flows, *Journal of Fluid Mechanics* **392**, 1999 (reference [46])

ACKNOWLEDGMENTS

This thesis is the summary of my journey to my Ph.D. First I want to thank Prof. Dr.-Ing Heiko Schmidt who offered me this opportunity during a christmas party of a different chair within the Mechanical, Electrical and Industrial Engineering faculty I was working. He advised me throughout the entire research process and taught me to be always critical. I learned from him to base all ideas on the combination of basic physical principles and precise assumptions.

Secondly, I want to thank Alan Kerstein for all discussions. He was always available to explain different facts of ODT or to discuss the sometimes strange results of my numerical experiments.

Further thanks go to my colleagues Eckhard Dietze, Christoph Glawe and Zoltan Jozefic as well as our student Mark Simon Schöps for all discussions about numerics, physics, politics, finances, and other important and unimportant things. I also would like to thank them for their advices in Linux administration, which showed me that it is much easer than I alway thought.

My special thanks go to my best friend and best man Lando Schebsdat for his continuous motivations. Without these motivations this thesis would have never been finished.

Finally I would like to especially thank my wife Ariane Meiselbach. She has helped my in so many ways that here is not enough room here to list them all.

CONTENTS

LIST OF FIGURES

LIST OF TABLES

ACRONYMS

aODT	adaptive one-dimensional turbulence
CFD	computational fluid dynamics
CFL	Courant Friedrichs Lewy
CIP	cubic interpolation pseudo-particle
DNS	direct numerical simulation
ELSA	Eulerian-Lagrangian spray atomization
GF	ghost fluid
LEM	linear eddy model
LES	large eddy simulation
LESM	large eddy suppression method
LESODT	large eddy simulation with ODT as a sub-grid-scale model
LHS	left hand side
LS	level-set
MARS	multi-interface advection and reconstruction solver
ODT	one-dimensional turbulence
ODTLES	one-dimensional turbulence with a 3D coupling
PDF	probability density function
RANS	Reynolds averaged Navier-Stokes
RHS	right hand side
RMS	root-mean-square
STBL	stratocumulus-topped boundary layer
TBL	turbulent boundary layer
TKE	turbulent kinetic energy
TWBF	turbulent wall-bounded flows
VOF	volume of fluid

NOMENCLATURE

Dimensionless parameters

Pr	Prandtl number $Pr = \frac{\nu}{a}$
Pr_t	turbulent Prandtl number $Pr_t = \frac{\nu_t}{a_t}$
Re	Reynolds number $Re = \frac{u_c l_c}{\nu} = \frac{\rho u_c l_c}{\mu}$
Re_B	bulk Reynolds number $Re_B = \frac{u_B l_c}{\nu}$
Re_t	turbulent Reynolds number $Re_t = \frac{u_t L}{\nu}$
Re_τ	friction Reynolds number $Re_\tau = \frac{u_\tau l_c}{\nu}$
Ri	Richardson number $Ri = \left(\frac{g}{T_0} \frac{\partial T}{\partial z}\right) \left(\frac{\partial u}{\partial z}\right)^{-2}$
We	Weber number $We = \frac{\rho_l u^2 D}{\sigma}$

Latin characters

A	amplitude of a fluctuation, $[-]$
A	surface, $[\mathrm{m}^2]$
a	thermal diffusivity $a = \frac{\lambda}{\rho c_p}$, $\left[\frac{\mathrm{m}^2}{\mathrm{s}}\right]$
b	buoyancy $b = g\frac{T-T_0}{T_0}$, $\left[\frac{\mathrm{m}}{\mathrm{s}^2}\right]$
B_0	reference buoyancy flux, $\left[\frac{\mathrm{m}^2}{\mathrm{s}^3}\right]$
bal	balance of all turbulent kinetic energy budgets, $\left[\frac{\mathrm{m}^2}{\mathrm{s}^3}\right]$
b_i	constant for kernel addition J, $[-]$
b_{LESM}	constant for time LESM, $[-]$
C	ODT parameter influencing the overall eddy rate, $[-]$
c	a constant value, $[-]$
C_f	skin-friction coefficient, $[-]$
c_i	constant for kernel addition K, $[\mathrm{s}^{-1}]$
c_p	specific heat capacity for constant pressure $c_p = c_v + \frac{R}{M_R}$, $\left[\frac{\mathrm{m}^2}{\mathrm{s}^2\mathrm{K}}\right]$
c_v	specific heat capacity for constant volume $c_v = z\frac{R}{M_R}$, $\left[\frac{\mathrm{m}^2}{\mathrm{s}^2\mathrm{K}}\right]$
D	diameter, $[\mathrm{m}]$
d	dissipation, $\left[\frac{\mathrm{m}^2}{\mathrm{s}^3}\right]$
E	energy, $\left[\frac{\mathrm{kg\,m}^2}{\mathrm{s}^2}\right]$
E	the eddy function within ODT representing the advection, $\left[\frac{\mathrm{m}^2}{\mathrm{s}}\right]$
e	specific internal energy $e = c_v T + \alpha$, $\left[\frac{\mathrm{m}^2}{\mathrm{s}^2}\right]$
E_{es}	extra shear kinetic energy, $\left[\frac{\mathrm{kg\,m}^2}{\mathrm{s}^2}\right]$
E_{kin}	kinetic energy, $\left[\frac{\mathrm{kg\,m}^2}{\mathrm{s}^2}\right]$
E_{mod}	model energy, e. g. viscous damping term, $\left[\frac{\mathrm{kg\,m}^2}{\mathrm{s}^2}\right]$
E_{pot}	potential energy, e. g. buoyant potential energy, $\left[\frac{\mathrm{kg\,m}^2}{\mathrm{s}^2}\right]$

E_{surf}	surface potential energy, $\left[\frac{\mathrm{kg\,m^2}}{\mathrm{s^2}}\right]$
F	specific external force, $\left[\frac{\mathrm{m}}{\mathrm{s^2}}\right]$
f	inverse mapping function, [m]
G	location of maximum in diagnostic plot, $G = \left(\frac{\overline{u}}{u_\infty}\right)$
g	gravitational acceleration $g = 9.81\,\frac{\mathrm{m}}{\mathrm{s^2}}$
h	channel half height, [m]
$\underline{\underline{I}}$	identity matrix $\underline{\underline{I}} = \delta_{ij}$, [–]
$\mathcal{I}$	arbitrary interpolation function
K	the kernel addition within ODT, $\left[\frac{\mathrm{m^2}}{\mathrm{s}}\right]$
K	the kernel function, [m]
L	characteristic macro length scale, [m]
L	line (1D volume), [m]
l	length scale, [m]
l	size of an eddy, [m]
l_τ	friction length $l_\tau = {}^{\nu}/_{u_\tau}$, [m]
M	the mapping process within ODT, $\left[\frac{\mathrm{m^2}}{\mathrm{s}}\right]$
M_R	molar mass $\left[\frac{\mathrm{kg}}{\mathrm{mol}}\right]$
N	number of grid points or control volumes, [–]
$\mathcal{N}$	number of realizations of a ODT simulation, [–]
$\vec{n}$	normal vector on surface $\partial\mathcal{V}$, [–]
P	overall eddy rate, $\left[\frac{1}{\mathrm{s}}\right]$
p	pressure, $\left[\frac{\mathrm{kg}}{\mathrm{m\,s^2}}\right]$
p	probability, [–]
p	production, $\left[\frac{\mathrm{m^2}}{\mathrm{s^3}}\right]$
ps	pressure scrambling, $\left[\frac{\mathrm{m^2}}{\mathrm{s^3}}\right]$
Q	maximal extractable energy due to an eddy process, $\left[\mathrm{J} = \frac{\mathrm{kg\,m^2}}{\mathrm{s^2}}\right]$
q	turbulent kinetic energy $q = \frac{1}{2}\overline{u_i'^2}$, $\left[\frac{\mathrm{m^2}}{\mathrm{s^2}}\right]$
Q_{cbl}	cooling of the cloud bulk, $\left[\frac{\mathrm{m^2}}{\mathrm{s^3}}\right]$
Q_{inv}	cooling of the inversion layer, $\left[\frac{\mathrm{m^2}}{\mathrm{s^3}}\right]$
$\vec{q}$	heat flux vector, usually $\vec{q} = -\lambda\nabla T$, $\left[\frac{\mathrm{kg}}{\mathrm{s^3}}\right]$
R	universal gas constant $R = 8.314462\,\frac{\mathrm{J}}{\mathrm{mol\,K}}$
S	the scrambling part of the kernel addition K, $\left[\frac{\mathrm{m^2}}{\mathrm{s}}\right]$
S_Φ	source term of the Φ balance equation, Φ $\left[\frac{\mathrm{kg}}{\mathrm{m^3\,s}}\right]$
$S_{u_i}, S_{\vec{u}}$	source term of the u_i balance equations, $\left[\frac{\mathrm{kg}}{\mathrm{m^2\,s^2}}\right]$
T	cycle duration of a fluctuation, [s]
T	temperature, [K]
T	the transport part of the kernel addition K, $\left[\frac{\mathrm{m^2}}{\mathrm{s}}\right]$
t	time [s]
ta	turbulent advection, $\left[\frac{\mathrm{m^2}}{\mathrm{s^3}}\right]$
T_{ij}	energy redistribution matrix, [–]
tv	viscous transport, $\left[\frac{\mathrm{m^2}}{\mathrm{s^3}}\right]$
$\vec{u}, \vec{v}$	velocity vectors $\vec{u} = u_i = (u_1; u_2; u_3) = (u; v; w)$, $\left[\frac{\mathrm{m}}{\mathrm{s}}\right]$

u	streamwise velocity, $\left[\frac{m}{s}\right]$
u_B	streamwise bulk velocity, [m]
u_t	turbulent streamwise fluctuation velocity, $\left[\frac{m}{s}\right]$
u_∞	free stream streamwise velocity, $\left[\frac{m}{s}\right]$
u_τ	friction velocity $u_\tau = \sqrt{\tau_W/\rho}$, $\left[\frac{m}{s}\right]$
ut	unsteady term, $\left[\frac{m^2}{s^3}\right]$
$V, \mathcal{V}$	volume, [m^3]
w_e	entrainment velocity $w_e = \overline{\frac{dh}{dt}}$, $\left[\frac{m}{s}\right]$
x	arbitrary coordinate direction
x, y, z	cartesian coordinates $x_i = (x; y; z)$; z is vertically oriented or the coordinate aligned with the ODT line, [m]
Z	ODT parameter scaling the viscous damping of eddies, [−]
z	degrees of freedom $\frac{2}{\gamma-1}$, [−]
zf	location of cell face, [m]
zi	inversion point $b(zi) = 0$, [m]
z_0, y_0	starting position of an eddy, within the jet simulation y_0 is used, [m]

Greek characters

α	ODT parameter defining the energy redistribution, [−]
α	potential chemical energy of a gas, $\left[\frac{m^2}{s^2}\right]$
β	test function for inner scaling $\beta = \frac{y^+}{\overline{u}^+}\frac{\partial \overline{u}^+}{\partial y^+}$
γ	adiabatic exponent, [−]
γ	estimated rate distribution for eddy sampling, $\left[\frac{1}{m^2 s}\right]$
γ	test function for inner scaling $\gamma = y^+ \frac{\partial \overline{u}^+}{\partial y^+}$
δ	outer scaling length, [m]
δ_{99}	boundary layer thickness, [m]
δt	mean time step for sampling next eddy trial time, [s]
ζ	external influences on volume $\mathcal{V}$
η	Kolmogorow length scale, [m]
η	bulk viscosity, $\left[\frac{kg}{s\,m}\right]$
Θ	thickness of the hyperbolic tangent profile initially used for smoke cloud simulations, [m]
θ	upward shift of the initial buoyancy profile within a smoke cloud simulation, [m]
κ	von Kármán constant, [−]
κ_Φ, κ	diffusion coefficient of variable Φ, $\left[\frac{kg}{s\,m}\right]$
Λ	optical depth of smoke cloud for radiation, [m]
λ	physical accurate rate distribution for eddy sampling, $\left[\frac{1}{m^2 s}\right]$
λ	thermal conductivity, $\left[\frac{kg\,m}{s^3\,K}\right]$
μ	dynamic viscosity $\mu = \nu\rho$, $\left[\frac{kg}{s\,m}\right]$
ν	kinematic viscosity, $\left[\frac{m^2}{s}\right]$
ξ	absorption of radiation within volume $\mathcal{V}$
π	production within volume $\mathcal{V}$

ρ	density, $\left[\frac{kg}{m^3}\right]$
σ	surface tension, $\left[\frac{N}{m}\right] = \left[\frac{kg}{s^2}\right]$
$\underline{\underline{\sigma}}$	stress tensor $\underline{\underline{\sigma}} = -p\underline{\underline{I}} + \underline{\underline{\tau}}$, $\left[\frac{kg}{s^2\,m}\right]$
τ	turnover time of an eddy, [s]
τ_W	wall shear stress $\tau_W = \left.\mu\frac{\partial u}{\partial z}\right\vert_{z=0}$, $\left[\frac{kg}{s^2\,m}\right]$
$\tau_{t,ij}$	turbulent stress tensor $\underline{\underline{\tau_t}} = \tau_{t,ij} = \overline{u_i' u_j'}$, $\left[\frac{m^2}{s^2}\right]$
$\underline{\underline{\tau}}$	fluid stress tensor, usually Newton stress tensor, $\left[\frac{kg}{s^2\,m}\right]$ $\underline{\underline{\tau}} = \mu\left(\nabla\circ\vec{u} + (\nabla\circ\vec{u})^T\right) + (\nabla\cdot\vec{u})\left(\eta - \frac{2}{3}\mu\right)\underline{\underline{I}}$
Φ	arbitrary variable
Ψ	non-convective flux in volume $\mathcal{V}$

Mathematical symbols

$\circ$	outer product
$\Delta\Phi$	part of value Φ, e. g. ΔE energy part, Δx grid spacing
ΔV	control volume of volume $\mathcal{V}$
δx	grid spacing between two control volume centers
δ_{ij}	Kronecker delta $\delta_{ij} = \begin{cases} 1 & \text{if } i=j \\ 0 & \text{if } i\neq j \end{cases}$
$\frac{d}{dt}$	material derivative $\frac{d\Phi}{dt} = \frac{\partial\Phi}{\partial t} + \vec{u}\cdot\nabla\Phi$
∇	nabla operator $\nabla = \frac{\partial}{\partial x_i} = \left(\frac{\partial}{\partial x}; \frac{\partial}{\partial y}; \frac{\partial}{\partial z}\right)^T$
$\partial\mathcal{V}$	boundary of volume $\mathcal{V}$
sgn	the sign function
O	one symbol of the Landau notation

Diacritics

$\overline{\Phi}$	Reynolds averaged mean value of Φ, $\Phi = \overline{\Phi} + \Phi'$
Φ'	fluctuations of Φ, $\Phi = \overline{\Phi} + \Phi'$
$\vec{\Phi}$	vector $\vec{\Phi} = \Phi_i = (\Phi_1; \Phi_2; \Phi_3)$
$\widehat{\Phi}$	PDF of rate distribution
$\widetilde{\Phi}$	values for candidate eddy
$\widetilde{u}_i$	velocity after mapping and kernel addition

Subscrips and superscripts

Φ_{Jet}	value of a jet simulation
Φ_0	starting or reference value
Φ_τ	value depending on the wall shear stress τ_W
Φ_{min}	minimum value of function Φ
Φ_{RMS}	root mean square value of Φ
Φ_B	bulk value
Φ_c	characteristic value or center position
Φ_g	value belonging to the gas phase

Φ_g	value depending of gravitation
Φ_i	grid index, $i \in \{0; N\}$
Φ_i	vector index, $i \in \{1; 2; 3\}$
Φ_j	further grid indexes similar to Φ_i
Φ_l	value belonging to the liquid phase
Φ_t	turbulent value
Φ^+	normalization with inner scaling
Φ^*	critical value
Φ^n	time index $t^n = t_0 + n\,\Delta t$ with $n \in \mathbb{N}$

Part I

THEORY

1

INTRODUCTION

One of the greatest research areas in modern fluid mechanics is computational fluid dynamics (CFD). The reason for this is that direct numerical simulation (DNS), the simulation of the exact balance equations without any assumptions, as one possibility of CFD is infeasible for industrial purposes. Most industrial problems are at high values of dimensionless parameters, e. g. the Reynolds number Re, the Prandtl number Pr, or the Richardson number Ri, where the required grid resolution, which is discussed in section 2.1, is too high to be simulated on currently available computers. This trend will continue for the next years.

Therefore, the need for modeling the smallest scales, which are the reason for the needed high resolution, or the reduction of the dimensions from 3D to 2D or even 1D arises. Classical approaches in CFD are the Reynolds averaged Navier-Stokes equations or the large eddy simulation. Both methods reduce the computational cost due to modeling the smallest scales and simulating the larger scales. The wide use of these methods in industrial development has led to optimized formulations.

Nevertheless, the steady optimization process for more efficiency is bounded by the amount of information generated by the simulations. More information can only be generated by (i) a higher resolution leading to a DNS or the same problem as known from DNS, (ii) an improvement of the models, or (iii) by the development of new models, where the last two are difficult due to the limited representation of the flow.

One of these new models is called one-dimensional turbulence. Within one-dimensional turbulence (ODT), the flow simulation is limited to a 1D line of sight through the flow. This restriction provides the opportunity for high grid resolution so that each scale can be resolved. Due to the simulation of every scale, ODT has a similar characteristic as a DNS and can therefore be used for fundamental simulations of turbulence, providing the information needed to improve the models used by LES and RANS. Nevertheless, ODT is also a model, which needs to be verified against DNS. At this point it has to be mentioned that ODT without coupling to 3D flow simulations is restricted to canonical flows without dominant 3D flow structures.

The fundamental simulations for turbulence research are termed canonical flows. One class of these flows is the group of turbulent wall-bounded flows (TWBF), including the turbulent boundary layer (TBL), the pipe and the channel flow. Even if current DNSs are done for friction Reynolds numbers $\mathrm{Re}_\tau = \frac{u_\tau l_c}{\nu} \approx 5000$, where u_τ is the friction velocity, l_c a characteristic length scale and ν the kinematic viscosity, industrial applications are at $\mathrm{Re}_\tau \approx 10^5$ or higher. Some of these applications are the flow around cars, trains, airplanes, buildings or even the wind profile within the atmosphere or the gas or fluid flow in pipelines or channels. Therefore, one major focus of this thesis lies on the simulation of the single-phase channel flow part of the mentioned category of flows.

Besides the pure simulation of the fluid flow many applications also need the inclusion of additional properties of the flow as the temperature and the transport of species or impurities. Most of these flow properties can be treated in first order as passive scalars within the flow not influencing other properties. Major applications are the heat transport at the wall, the separation or mixing of different fluids or the tracking of reaction species.

Especially in case of high temperature ratios within the flow or flows of a supercritical fluid with conditions slightly above the critical point, the temperature could influence the density, resulting in a buoyant flow. This also influences the behavior of turbulence due to preventing or assisting eddies. Other major research fields besides the heat transport and the tracking of species including the mentioned complexity are oceanic flows, clouds, climate research, astrophysics, supercritical flows and non-newtonian flows.

Up to here all flows could be treated as single-phase flows. Another major part of turbulence research is the behavior of turbulence at the interface between two immiscible fluids and the influence of turbulence on the generation of droplets or species transport across the interface. Corresponding industrial applications are fuel injection, droplet generation due to wave propagation, the oxidation process during wine production, and supercritical flows with conditions around the critical point, where gas, liquid, and supercritical fluid coexist.

Within this thesis, ODT is validated against DNS results of several flows belonging to these groups. The capabilities of ODT are presented and further parameter studies or additional statistics are presented.

First, the turbulent channel flow is extended to $\mathrm{Re}_\tau \approx 6 \cdot 10^5$, statistics of the wall shear stress τ_W are presented, and the influence of the fluctuation of the forcing pressure gradient is discussed. Simulations for the passive scalar are performed and the behaviors at high and low Prandtl numbers are discussed.

Secondly, the simulations of a non-breaking and a breaking liquid jet are introduced and compared to measurements. Statistics of the breakup location and the droplet size distribution are shown.

Finally, the simulation of a smoke cloud, a specialization of real clouds, is done to analyze the interaction of a buoyant flow with turbulence.

2

BASICS FOR NUMERICAL SIMULATION

The bases for the development of numerical simulations are the conservation laws, namely mass, momentum, and energy conservation. All of them can be derived from an universal balance equation, by interpreting the corresponding summands as it is described among others by Müller and Müller [69]. For the derivation of the balance equation, an arbitrary volume $\mathcal{V}$ with surface normal vector $\vec{n}$ is taken and all possible changes of a measure Φ are described. The measure within the volume can be changed in time by (i) an advective flow over the moving surface $\partial\mathcal{V}$, (ii) a diffusive flow across the surface, (iii) production within the volume, and (iv) additions within the volume. The resulting general equation is given by:

$$\frac{d}{dt}\int\limits_{\mathcal{V}(t)} \rho\Phi\,dV = -\int\limits_{\partial\mathcal{V}(t)} \rho\Phi(\vec{u}-\vec{v})\cdot\vec{n}\,dA - \int\limits_{\partial\mathcal{V}(t)} \vec{\Psi}\cdot\vec{n}\,dA + \int\limits_{\mathcal{V}(t)} \rho\pi\,dV + \int\limits_{\mathcal{V}(t)} \rho\zeta\,dV. \tag{2.1}$$

The velocity of the volume surface is given by $\vec{v}$, and the velocity of the fluid by $\vec{u}$, so that $\vec{u}-\vec{v}$ gives the relative velocity of the fluid crossing the surface. ρ is the density within the flow. The difference between the last two terms in equation 2.1, the generation and the external influences, is that the latter one can in principle be modified while the generation within the volume cannot be affected. Examples of external influences are the gravity and radiation, which can be eliminated by using an orbital experiment or an uniform heated, opaque box, respectively.

For a closed system 2.2, where the volume surface has the same velocity as the flow, $\vec{v} = \vec{u}$, the advective term is zero giving the Lagrange formulation of the conservation laws. If the volume is fixed as in equation 2.3, $\vec{v} = \vec{0}$ and $\mathcal{V}(t) = \mathcal{V}$, the time derivative on the left hand side can be put into the integral as a partial derivative using the Reynolds transport theorem applied to a non-moving surface.

$$\frac{d}{dt}\int\limits_{\mathcal{V}(t)} \rho\Phi\,dV = -\int\limits_{\partial\mathcal{V}(t)} \vec{\Psi}\cdot\vec{n}\,dA + \int\limits_{\mathcal{V}(t)} \rho\pi\,dV + \int\limits_{\mathcal{V}(t)} \rho\zeta\,dV \tag{2.2}$$

$$\int\limits_{\mathcal{V}} \frac{\partial\rho\Phi}{\partial t}\,dV = -\int\limits_{\partial\mathcal{V}} \rho\Phi\vec{u}\cdot\vec{n}\,dA - \int\limits_{\partial\mathcal{V}} \vec{\Psi}\cdot\vec{n}\,dA + \int\limits_{\mathcal{V}} \rho\pi\,dV + \int\limits_{\mathcal{V}} \rho\zeta\,dV \tag{2.3}$$

Using the divergence theorem and the requirement, that the conservation laws have to be valid for each volume, the conservation law for a material point can be derived.

$$\frac{\partial\rho\Phi}{\partial t} = -\nabla\cdot(\rho\Phi\vec{u}) - \nabla\cdot\vec{\Psi} + \rho\pi + \rho\zeta \tag{2.4}$$

With the replacements given in table 2.1, one can get mass, momentum, and energy conservation. Important to note is that for all conservation laws the production has to be zero. $\underline{\underline{\sigma}}$ is the stress tensor and combines the effect of pressure p and fluid stresses $\underline{\underline{\tau}}$ with $\underline{\underline{\sigma}} = -p\underline{\underline{I}} + \underline{\underline{\tau}}$, where $\underline{\underline{I}}$ is the identity matrix. $\vec{F}$ is the vector of external forces, e. g. gravity. e is the internal energy and is given by the caloric equation of state, e. g. $e = c_v T + \alpha$ for ideal gases, where T is the temperature, $c_v = z\frac{R}{M_R}$ the specific heat capacity and α represents the potential chemical energy within the fluid. z can be expressed as $z = \frac{1}{\gamma - 1}$, where γ is the adiabatic exponent. ξ is the absorption of radiation and $\vec{q}$ the heat flux vector with $\vec{q} = -\lambda \nabla T$, where λ is the thermal conductivity. Within this thesis, all fluids follow the Newtonian expression of the rheological equation of state, which gives the following form of the stress tensor, where $\circ$ describes the dyadic product.

Table 2.1: Replacements to derive the conservation laws from the general balancing equation

Conservation law	Φ	$\vec{\Psi}$	π	ζ
Mass	1	0	0	0
Momentum	$\vec{u}$	$-\underline{\underline{\sigma}}$	0	$\vec{F}$
Energy	$e + \frac{1}{2}\vec{u}^2$	$-\underline{\underline{\sigma}} \cdot \vec{u} + \vec{q}$	0	$\vec{F} \cdot \vec{u} + \xi$

$$\underline{\underline{\tau}} = \mu \left(\nabla \circ \vec{u} + (\nabla \circ \vec{u})^T - \frac{2}{3}(\nabla \cdot \vec{u})\underline{\underline{I}} \right) + \eta (\nabla \cdot \vec{u})\underline{\underline{I}} \qquad (2.5)$$

Herein, μ is the dynamic viscosity and η the bulk viscosity. For most applications - also within this thesis - the bulk viscosity is negligible. Using this definition of the stress tensor, the above set of conservation laws becomes the compressible Navier-Stokes equations. The pressure is given by the thermal equation of state, e. g. for ideal gases.

Incompressible Navier-Stokes equations

Within this thesis, the incompressible Navier-Stokes equations are used, wherefore it is essential to mention the assumption made to derive them. To derive the incompressible Navier-Stokes equations, it is often mentioned that the density is constant or that the velocity field is solenoidal. Both statements are partly correct but are not the assumptions to be made to derive the incompressible Navier-Stokes equations. A more accurate assumption is given by the material derivative $\frac{d\rho}{dt} = \frac{\partial \rho}{\partial t} + u_i \frac{\partial \rho}{\partial x_i}$ of the density, which has to vanish. Therefore, the mass conservation reduces to a solenoidality condition for the velocity field instead of assuming $\nabla \cdot \vec{u} = 0$. Furthermore, this assumption also gives that the density of a fluid parcel has to be constant instead of the density within the whole field.

But even this assumption is overly restrictive. As the asymptotic analysis from R. Klein [49] for low Mach numbers shows, the correct assumption is that the terms of the energy equation influencing the divergence of the velocity field have to balance each other. The following equation can be derived from the energy equation using the caloric equation of state.

$$(z-1)p\nabla\cdot\vec{u}=-\frac{dzp}{dt}-\left(\frac{\partial\rho\alpha}{\partial t}+\nabla\cdot(\rho\alpha\vec{u})\right)-\nabla\cdot\vec{q}+\rho\zeta+\underline{\underline{\tau}}:(\nabla\cdot\vec{u}) \tag{2.6}$$

$$\text{with}\quad \underline{\underline{\tau}}:(\nabla\cdot\vec{u})=\tau_{ij}\frac{\partial u_i}{\partial x_j}$$

Especially, this is also valid if the terms are identically to zero, resulting in

(i) a constant pressure within a fluid parcel $\frac{dp}{dt}=0$,

(ii) no reaction changing the potential chemical energy $\alpha=$ const.,

(iii) no heat flux $\vec{q}=\vec{0}$,

(iv) and no radiative absorption $\zeta=0$.

For the last term containing the stress tensor no assumption is needed due to the fact that it scales with the squared Mach number and therefore vanishes due to the asymptotic. These assumptions also result in a constant temperature of a fluid parcel.
Using this condition, the general balance equation can be written as follows using the replacements from table 2.1:

$$\frac{\partial\Phi}{\partial t}+\nabla\cdot\Phi\vec{u}=-\frac{1}{\rho}\nabla\cdot\Psi+\pi+\zeta. \tag{2.7}$$

Within this thesis the incompressible equations are used, even if a heat flux or radiation is present. In these cases, (i) the temperature is treated as a passive scalar or (ii) the Boussinesq approximation is used.

2.1 DNS, LES, RANS

Within the development of numerical simulations, the first simulations were DNS. A DNS discretizes the conservation laws as they are without any assumptions. Only a discretization error not influencing the physical result has to be accepted, which will be explained in section 2.3. A DNS needs to resolve every scale within the flow field, even the smallest one termed the Kolmogorov scale η. A detailed description of DNS is among others given by Ferziger and Perić [27].
The needed resolution for a DNS can be estimated from the turbulent Reynolds number $Re_t = u_t L \nu^{-1} \sim (L\eta^{-1})^{\frac{4}{3}}$, where u_t is the turbulent fluctuation velocity, L a characteristic large length scale, and ν the kinematic viscosity. For industrial flows, this resolution requirement could reach as much as 10^{15} or more grid cells. Depending on the time discretization method the time step could be coupled to the grid resolution resulting in a further increase of computational cost. To date, the most expansive state of the art simulations are done with less than 10^{11} grid points, e. g. Lee et. al [54]. Therefore, DNS is currently restricted to fundamental research and problems at small to

moderate Reynolds numbers.
In the beginning of numerical research, this restriction limited its applicability and raised the need for modeling. The first idea is based on the separation of the flow field into a mean value and overlaying fluctuations $\Phi = \overline{\Phi} + \Phi'$, the so called Reynolds decomposition. The application of this decomposition to the conservation laws results in the Reynolds averaged Navier-Stokes (RANS) equations.
While the mass conservation is reproduced by the Reynolds averaging, within the momentum and the energy conservation new terms representing the interaction of the fluctuations with each other arise. Due to these new terms, the set of equations is no longer closed and new unknown quantities have to be solved. The most famous term is the turbulent stress $\frac{\partial \tau_{t,ij}}{\partial x_i}$ with $\tau_{t,ij} = \overline{u_i' u_j'}$, where the overbar symbolizes the Reynolds-averaging. Much of the research field of turbulence modeling is the description of this and/or other equivalent terms from the energy conservation by properties already known in the flow field, which then close the system of equations. A detailed overview of the derivation of $\tau_{t,ij}$, the major turbulence models and their applicability is given by Wilcox [94].
Another ansatz similar to the Reynolds-averaging is to filter the equations with a spatial low-pass filter. The so called large eddy simulation (LES) provides the same benefits as RANS, with the additional advantage of resolving some fluctuations in the flow. While the results of a RANS are always time averaged mean information, LES provides also time dependent flow field information. This advantage comes at the cost of needing to model or neglect additional unknown parameters. LES is therefore a compromise between DNS and RANS, such that it is capable of providing more information than RANS, at less cost than DNS. A detailed description of LES is given by Sagaut [76].
The use of the RANS model for industrial applications in the last decades has been very beneficial. However, due to these improvements and the currently unrealizable wish of using DNS for industrial problems, there is a steady need for improving simulation methods. One new development in this field not based on the RANS or LES ansatz is the ODT model, which was first published in 1999 by A. R. Kerstein [46] and will be described next.

2.2 ODT

This section gives an overview of the ODT model which is an outgrowth of the linear eddy model (LEM). The descriptions are based on several publications, (i) Kerstein [46] which gives the basic formulation, (ii) Wunsch and Kerstein [104] which introduces the buoyancy term to ODT, (iii) Kerstein et al. [48] which expands the formulation to three velocity components, and (iv) Ashurst and Kerstein [9] which focuses on the variable density formulation of ODT. Another publication which has to be mentioned here, was published by Lignell et al. [56]. It doesn't expand the physical modeling but introduces a non-equidistant spatial discretization.

In contrast to common approaches based on the Navier-Stokes equations, ODT uses a set of mechanisms modeling the physical effects phenomenologically on a 1D line of sight through the domain.
For RANS and LES the advective term is crucial due to the generation of additional unknown properties as described in the previous section. For DNS also this term is the source of problems due to the generation of smaller and smaller scales. ODT overcomes this problem by representing the advective term phenomenologically by a so called eddy process. Excluding the advective term, the Navier-Stokes equations become diffusion equations with source terms where applicable. As in the Navier-Stokes equations, the diffusion and the eddy process are applied to all property fields, e. g. the velocity, the temperature and other scalar fields, using the operator splitting idea. Therefore, the Navier-Stokes equations can be written in a ODT representation as follows:

$$\frac{\partial \rho u_i}{\partial t} + E(u_i) = \frac{\partial}{\partial z}\left(\mu \frac{\partial u_i}{\partial z}\right) + S_{u_i} \tag{2.8}$$

$$\frac{\partial \rho \Phi}{\partial t} + E(\Phi) = \frac{\partial}{\partial z}\left(\kappa_\Phi \frac{\partial \Phi}{\partial z}\right) + S_\Phi. \tag{2.9}$$

Here E is an eddy function representing the eddy process and therefore the advective term on the 1D line. Φ is an arbitrary scalar representing the temperature or other scalar fields with a diffusion coefficient κ_Φ and the source term S_Φ. S_{u_i} is the source term for the velocity, e. g. the pressure gradient.
The following section describes the realization of an eddy representing the advective term.

2.2.1 *Realization of an eddy*

One major idea of ODT is the representation of the advective term and therefore the eddy motion in turbulent flows. Within ODT a map representing an eddy of size l acts instantaneously on each property field in the range $[z_0; z_0 + l]$, where z_0 is the starting position of the eddy spatial interval.
The mathematical formulation of the instantaneous map has to satisfy two fundamental requirements: (i) the measure preservation which is required by the solenoidal condition, and (ii) the continuity of the property field after the mapping process. The common choice of this function within all ODT formulations is the triplet map where the original profile within the eddy range is spatially compressed by a third. The eddy range is filled by three copies of the compressed profile while the second one is reversed to avoid discontinuities. Outside the eddy range the profiles are unaffected by the eddy process. Therefore the mapping process can be written as:

$$\hat{u}_i(z, t) = u_i(f(z, t), t) \tag{2.10}$$

$$\hat{\Phi}_i(z, t) = \Phi(f(z, t), t), \tag{2.11}$$

where the inverse map

$$f(z,t) = z_0(t) + \begin{cases} 3(z - z_0(t)) & \text{if } z_0 \leqslant z < z_0 + \frac{1}{3}l \\ -3(z - z_0(t)) + 2l(t) & \text{if } z_0 + \frac{1}{3}l \leqslant z < z_0 + \frac{2}{3}l \\ 3(z - z_0(t)) - 2l(t) & \text{if } z_0 + \frac{2}{3}l \leqslant z \leqslant z_0 + l \\ z - z_0(t) & \text{otherwise} \end{cases} \tag{2.12}$$

is the pre-map location that is mapped to location z.

This formulation is not unique, as discussed by Kerstein [45], who has also tested a quintiplet map, where instead of three five compressed copies are used, while the second and the fourth one are reversed. Due to the simplicity of the triplet map and only slight differences by choosing the quintiplet instead of the triplet map on the relevant outputs, the triplet map is commonly used in ODT implementations.

2.2.2 *Energy conservation by an eddy*

Due to energy conservation, the instantaneous mapping process has to be conservative which means that the energy change ΔE

$$\Delta E = \Delta E_{\text{kin}} + \sum \Delta E_{\text{pot}} + \sum \Delta E_{\text{mod}} \tag{2.13}$$

has to be zero. Here $\sum \Delta E_{\text{pot}}$ is the sum of all potential energy changes and $\sum \Delta E_{\text{mod}}$ the sum of all additional energies from modeling approaches. For example, a buoyant stratified flow satisfying the Boussinesq approximation would be simulated using the constant property formulation and a potential energy term in the formulation of the energy conservation representing the buoyancy term of the Navier-Stokes equations. The difference between potential and model energies is that model energies are mostly only used for calculating the eddy acceptance, as described in section 2.2.3, while potential energies are always taken into account.

To ensure energy conservation, needed potential energy has to be provided by the velocity components or freed potential energy has to be stored in the velocity components. Therefore, another process, the kernel addition, is introduced as shown in equation (2.14) below. At this point, it has to be mentioned that, even if ODT uses three velocity components, they are treated primarily as energy holding containers. The effect of the kernel addition is twofold; (i) it ensures energy conservation within the mapping process and (ii) it models pressure scrambling by redistributing the kinetic energy among velocity components, which represents the tendency toward isotropy. The final flow state is then

$$\tilde{u}_i(z,t) = u_i(f(z,t),t) + c_i(t)K(z,t). \tag{2.14}$$

The kernel $K(z,t) = z - f(z,t)$ is defined as the displacement of fluid parcels due to the mapping process. It is non-zero within the eddy range and integrates to zero, so that it doesn't influence momentum conservation. Within the formulation for variable density, another kernel $J = |K|$ has to be introduced to allow enforcement of energy and momentum conservation resulting in

$$\widetilde{u}_i(z,t) = u_i(f(z,t),t) + c_i(t)K(z,t) + b_i(t)J(z,t)\,. \tag{2.15}$$

The constants c_i and b_i are calculated by setting the energy change ΔE to zero, where the energy changes are calculated using:

$$\begin{aligned}\Delta E_{\mathrm{kin},i} &= \frac{1}{2}\int \rho(f(z))[u_i(f(z)) + c_i K(z) + b_i J(z)]^2\,dz \\ &\quad - \frac{1}{2}\int \rho(z)[u_i(z)]^2\,dz, \qquad (2.16)\\ \Delta E_{\mathrm{pot},g} &= g\int[\rho(f(z)) - \rho(z)]z\,dz. \qquad (2.17)\end{aligned}$$

Here $\Delta E_{\mathrm{pot},g}$ denotes the potential energy change induced by buoyancy. Other potential energy terms, e. g. due to surface tension, have to be calculated in a similar way.

As derived by Ashurst and Kerstein [9] the coefficients can be calculated as follows. A detailed and commented derivation is given in appendix A. Specializing here to constant density ρ_0 gives:

$$c_i = \frac{27}{4l}\left(-u_{K,i} + \mathrm{sgn}(u_{K,i})\sqrt{u_{k,i}^2 + \alpha\sum_j T_{ij}u_{k,j}^2 - \frac{8}{27}\frac{1}{\rho_0 l}\frac{\sum \Delta E_{\mathrm{pot}}}{3}}\right)$$

$$T_{ij} = \begin{cases}-1 & \text{if } i = j\\ \frac{1}{2} & \text{if } i \neq j\end{cases} \qquad u_{K,i} = \frac{1}{l^2}\int u_i(f(z))K(z)\,dz. \tag{2.18}$$

Here, $\mathrm{sgn}(\Phi)$ is the sign function, which ensures that c_i approaches zero for ΔE approaching zero, and α is historically the third model parameter of ODT. It is a factor determining the amount of kinetic energy that is redistributed to the other velocity components, where $\alpha = 0$ gives no and $\alpha = 2/3$ uniform redistribution. The formulation (2.18) has to be changed for the variable density formulation and is given by equations (A.21) and (A.24).

As given by equation (2.14), the energy is distributed among the velocity components. If the argument of the square root is negative, e. g. due to stable stratification, the eddy is energetically prohibited.

As can be noticed, equation (2.18) omits the modeling energy terms ΔE_{mod}. Typically, the added energy due to modeling is used to modify the acceptance probability as shown in the next part, but is excluded from the energy redistribution. As long as the modeling energy is negative, as it is for the viscous damping term ΔE_{visc} described in the next section, the energy conservation is fulfilled and the term only influences the acceptance probability. If it is positive, special handling is needed, if the argument of the square root becomes negative without the modeling energy, but the eddy would be accepted due to the modeling energy.

The maximum kinetic energy Q that can be removed for conversion into potential energy is given by the minimum of $\sum \Delta E_{\mathrm{kin},i}$ and is $Q = -\Delta E_{\mathrm{min}} = \frac{27}{8}\rho_0 l u_{K,i}^2$ for the constant property formulation. The equivalent for the variable density formulation is given by equation (A.26) in appendix A.2.

2.2.3 *Eddy selection*

One important physical modeling within ODT is the selection of the eddy size l and eddy location z_0. They are randomly sampled from a rate distribution λ, which determines the occurrence probability $p_\lambda(l, z_0, t) = \lambda(l, z_0, t)\,dl\,dz_0\,dt$ of an eddy of size $[l; l + dl]$ at the location $[z_0; z_0 + dz_0]$ within the time interval $[t; t + dt]$. Therefore, λ is proportional to the squared inverse eddy length times an inverse time scale, where the time scale is the ODT representation of the eddy turnover time $\tau(l, z_0, t)$. The overall eddy rate P_λ and the probability density function (PDF) $\hat{\lambda}$ of the eddy parameters are expressed in terms of λ as follows:

$$\lambda(l, z_0, t) = \frac{C}{l^2 \tau(l, z_0, t)} \tag{2.19}$$

$$P_\lambda(t) = \iint \lambda(l, z_0, t)\,dl\,dz_0 \tag{2.20}$$

$$\hat{\lambda}(l, z_0, t) = \frac{\lambda(l, z_0, t)}{P_\lambda(t)} \tag{2.21}$$

Here C is the first model parameter of ODT controlling the overall eddy rate P_λ.

Using the eddy turnover time τ, an eddy velocity ${}^{l}\!/_{\tau}$ and an eddy kinetic energy per unit mass $\left({}^{l}\!/_{\tau}\right)^2$ can be defined. Due to the fact that the eddy kinetic energy has to be provided by the energy within the flow, the following proportionality can be established:

$$\left(\frac{l}{\tau}\right)^2 \sim u_{K,i}^2 + \alpha \sum_j T_{ij} u_{k,j}^2 - \frac{8}{27} \sum \frac{\Delta E_{\mathrm{pot}} + \Delta E_{\mathrm{mod}}}{\rho_0 l} - Z \frac{\nu^2}{l^2}. \tag{2.22}$$

The last summand

$$-Z\frac{\nu^2}{l^2} = -\frac{8}{27\rho_0 l}\left(\frac{27}{8} Z \frac{\nu^2 \rho_0}{l}\right) = -\frac{8}{27\rho_0 l}\Delta E_{\mathrm{visc}}$$

is a special threshold model energy called viscous penalty to prohibit unphysically low-energy eddies; mostly eddies smaller than the Kolmogorov length scale. The parameter Z for the threshold energy is the second model parameter of ODT. Although this term is a model energy and ΔE_{visc} should be included into ΔE_{mod}, due to its special relevance for ODT, it is mostly handled separately throughout this thesis.

Using equation (2.20) and (2.22) it is in principle possible to calculate

λ. Due to the time dependency of λ, which results from the influence of the mapping process and other advancement processes on the velocity profiles and profiles of energetically active scalars, it is infeasible to evaluate the distribution economically.
Therefore, an arbitrary test distribution $\gamma(l, z_0, (t))$, with equivalently defined $P_\gamma >> P_\lambda$ and $\hat{\gamma}$, is introduced, where P_γ and $\hat{\gamma}$ are also time dependent when efficient estimation of the time dependency is possible. The candidate eddies $[\tilde{l}, \tilde{z}_0]$ at time $\tilde{t}$ are sampled from $\hat{\gamma}$ and the corresponding eddy rates $\lambda(\tilde{l}, \tilde{z}_0, \tilde{t})$ are calculated. Each eddy is accepted with a probability

$$p_{\lambda\gamma} = \frac{\lambda(\tilde{l}, \tilde{z}_0, \tilde{t})}{\gamma(\tilde{l}, \tilde{z}_0)} = \frac{\lambda(\tilde{l}, \tilde{z}_0, \tilde{t})}{\hat{\gamma}(\tilde{l}, \tilde{z}_0)\, P_\gamma}. \tag{2.23}$$

To ensure that the accepted eddies follow the eddy rate distribution λ the overall rate P_γ has to be greater than the overall rate P_λ. This is enforced within ODT by oversampling that is adjusted using a target mean acceptance probability $\overline{p}_{\lambda\gamma}$.
As mentioned in the last section, not all model energies used in the calculation of the acceptance probability are also used within the redistribution of the energy due to the kernel addition. The threshold energy, one of the key elements of ODT, is also one example for an energy only used within the calculation of the acceptance probability. Two other examples for model energies only present within the probability calculation are the Rayleigh wave energy and the extra shear energy as mentioned in section 6.3.3 and 7.3, respectively.
Again, it has to be mentioned that if a model energy is only used within the probability calculation and the energy is positive, there is the possibility that an eddy, which is energetically accepted due to the calculation of the acceptance probability, could be also energetically rejected by the calculation of the energy redistribution. One example for this could be an eddy within a region of positive buoyant stratification, where the stratification suppresses all eddies. If a positive model energy within the calculation of the acceptance probability is used to allow this eddy it would be inconsistent with the energy redistribution, which would energetically reject this eddy.

2.3 NUMERICAL BASICS

This section gives a short overview of the numerical basics used within the adaptive one-dimensional turbulence (aODT) code. The code is based on the finite volumes method, which is shortly described in the following section. A more detailed introduction to finite volume methods is given by e. g. Ferziger and Perić [27] or R. J. Le Veque [55]. The next section specifies the finite volume method for the ODT equations (2.10) and (2.11). Section 2.3.3 gives an overview of the calculation of the budgets of the turbulent kinetic energy. Finally, the numerical basics section is closed with an introduction to interpolation methods used within aODT.

2.3.1 *Finite volume methods*

The finite volume method uses the integral form of the conservation laws as given by equation (2.3). For the calculation of the solution, the simulation domain $\mathcal{V}$ is divided into arbitrary control volumes ΔV. In contrast to the finite differences method, which approximates the unknown continuous solution of the variables given by the conservation laws at specific grid points the finite volume method integrates the solution within these control volumes. Due to the fact that the conservation law is valid for each control volume, the summation of all volumes result in the conservation within the whole simulation domain.

Nevertheless, this concept reduces the problem of the solution calculation to the control volumes. From the definition of the mean value it is known that the integral of the solution is equal to the product of the mean value and the volume. This reduces the conservation law to an algebraic equation for the mean values. These mean values have to be approximated by approximating the function within the control volume. The simplest approximation at the geometric center x_c is given by the midpoint rule, also termed rectangle method, where the mean value is approximated by the value at x_c.

$$\int\limits_{\Delta V} \Phi \, dV = \overline{\Phi} \Delta V \approx \Phi(x_c) \Delta V \tag{2.24}$$

Generally, this approximation is of second order, $O(\Delta V^2)$, where O denotes the upper boundary of the error. If the function within the control volume is a constant or a linear function, the midpoint rule is exact. Higher order integrations are possible but need more information at other points, e. g. the midpoints of the surfaces, the corners of the volume, or the midpoints of neighboring control volumes[1]. It is also possible to use the information about derivatives at these points, which is equivalent to using more points. Detailed information about numerical integration is given by e. g. Bronstein et al. [12]. A similar derivation could be done for surface and line segments.

Using these approximations, the unknown integrals can be replaced by discrete values and the set of conservation laws for each control volume can be reduced to a set of algebraic equations. In the following, this is illustrated for the universal balance for fixed volumes equation (2.3) using the midpoint rule and time-independent control volumes with flat surfaces. Here, it should be recalled that the surface integrals describe the fluxes across the surfaces as explained in the beginning of this chapter (see page 5). Figure 2.1 shows an exemplary

---

[1] Within 2D the additional points could be the midpoints of the borders, the corners of the volume, or the midpoints of surrounding control volumes. In 1D the only possibilities for additional points are the border points of the line segments (the 1D control volumes) or also the midpoints of adjacent volumes.

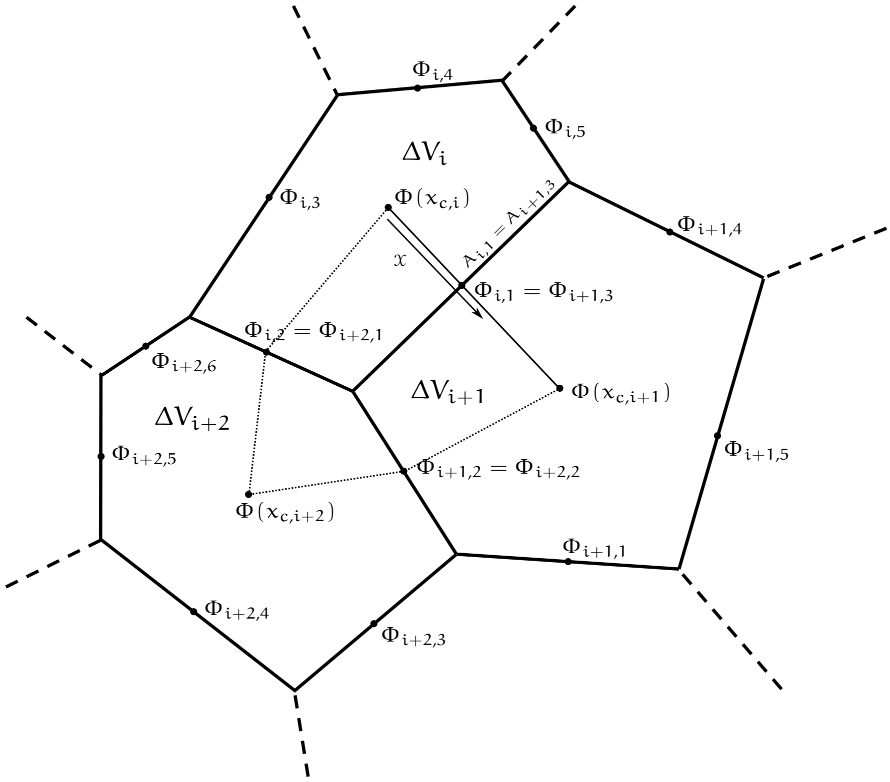

Figure 2.1: Sketch for the finite volume method. $\Phi_i = \Phi(x_{c,i})$ is the value at the volume center $x_{c,i}$ of the control volume ΔV_i. Φ_{ij} terms the values at the volume surfaces used for the flux calculation on surface A_{ij}. Here, $\mathcal{x}$ terms the direction of a local coordinate system.

control volume in 2D.

$$\int_{\mathcal{V}} \frac{\partial \rho\Phi}{\partial t}\, dV = -\int_{\partial\mathcal{V}} \rho\Phi\vec{u}\cdot\vec{n}\, dA - \int_{\partial\mathcal{V}} \vec{\Psi}\cdot\vec{n}\, dA + \int_{\mathcal{V}} \rho\pi\, dV + \int_{\mathcal{V}} \rho\zeta\, dV$$

$$\frac{\partial}{\partial t}\int_{\Delta V_i} \rho\Phi\, dV = -\int_{\partial\Delta V_i} \rho\Phi\vec{u}\cdot\vec{n}\, dA - \int_{\partial\Delta V_i} \vec{\Psi}\cdot\vec{n}\, dA + \int_{\Delta V_i} \rho\pi\, dV + \int_{\Delta V_i} \rho\zeta\, dV \tag{2.25}$$

$$\begin{aligned} \frac{\partial}{\partial t}\Big(\rho\Phi\Big)_i \Delta V_i = &-\sum_j \Big(\rho\Phi\vec{u}\Big)_{ij}\cdot\vec{n}_{ij}\Delta A_{ij} - \sum_j \vec{\Psi}_{ij}\cdot\vec{n}_{ij}\Delta A_{ij} \\ &+ \Big(\rho\pi\Big)_i \Delta V_i + \Big(\rho\zeta\Big)_i \Delta V_i \end{aligned} \tag{2.26}$$

Here the subscript i denotes the value at the geometric center of the control volume i, e. g. $\rho_i = \rho(x_c(\Delta V_i))$. The subscripts ij denotes the midpoint on surface j of the volume i, e. g. $\rho_{ij} = \rho(x_c(A_j(\Delta V_i)))$. This approximation generates one set of equations per control volume for the values at the volume midpoints. While these sets of equations are used to calculate the values at the volume centers, the values at the surface midpoints are still unknown. They have to be approximated by interpolation from the surrounding volume points. This can be done using the Taylor series, here written in 1D for surface part $A_{i,1} = A_1(\Delta V_i)$:

$$\begin{aligned}\Phi_{i,1} &= \Phi_i + \Delta x_i \left.\frac{\partial \Phi}{\partial x}\right|_i + \frac{\Delta x_i^2}{2!} \left.\frac{\partial^2 \Phi}{\partial x^2}\right|_i + O(\Delta x_i^3) \\ \Phi_{i+1,3} &= \Phi_{i+1} - \Delta x_{i+1} \left.\frac{\partial \Phi}{\partial x}\right|_i + \frac{\Delta x_{i+1}^2}{2!} \left.\frac{\partial^2 \Phi}{\partial x^2}\right|_i \mp O(\Delta x_{i+1}^3).\end{aligned} \tag{2.27}$$

Here it is assumed that the surface midpoint is on the line between the midpoints of volumes i and $i+1$, as it is valid for the shown case. Δx_i is the distance between the surface midpoint and the volume midpoint i and x is the direction from midpoint i to midpoint $i+1$. In the same meaning Δx_{i+1} is the distance between the surface midpoint and the volume midpoint $i+1$. Generally the surface midpoint is not aligned with the volume centers as it is shown for volume ΔV_{i+2}. Therefore, multidimensional interpolations are often needed. In case of a structured grid, the volume centers are always aligned with the surface center points.

At this point, it has to be mentioned that the accuracy of the finite volume method depends on two distinct accuracies. The first one is given by the used numerical integration scheme, which is e. g. second order for the midpoint rule on structured grids. The second accuracy is given by the interpolation of the unknown values to the surfaces, which should be second order if the midpoint rule is used as mentioned. Therefore, to generate a higher order finite volume approximation both accuracies have to be increased separately.

Furthermore, it is not specified how combined values like $\rho\Phi\vec{u}$ are calculated. In principle there are two possibilities; (i) to calculate the product at the volume midpoints and then interpolate the calculated products or (ii) to interpolate each property separately and afterwards calculate the product of the interpolated values. Especially for diffusive fluxes the first method could lead to uncertainties if there are great variations in the diffusion coefficient. Therefore, at least the diffusion coefficient is interpolated separately, e. g. using the harmonic interpolation as described by R. J. Le Veque [55].

Using these interpolations the unknown values at the surfaces can be expressed by values at the midpoints of the control volumes resulting in a closed system of equations.

$$\begin{aligned}\frac{\partial}{\partial t}\left(\rho_i \Phi_i\right)\Delta V_i = &-\sum_j \mathcal{J}_\rho \mathcal{J}_\Phi \mathcal{J}_{\vec{u}} \cdot \vec{n}_{ij} \Delta A_{ij} - \sum_j \mathcal{J}_{\vec{\Psi}} \cdot \vec{n}_{ij} \Delta A_{ij} \\ &+ \rho_i \pi_i \Delta V_i + \rho_i \zeta_i \Delta V_i\end{aligned} \tag{2.28}$$

$$\begin{aligned}\text{with } \mathcal{J}_\rho &= \mathcal{J}_\rho(\rho_i, \rho_{i+1}, \dots) \\ \mathcal{J}_\Phi &= \mathcal{J}_\Phi(\Phi_i, \Phi_{i+1}, \dots) \\ \mathcal{J}_{\vec{u}} &= \mathcal{J}_{\vec{u}}(\vec{u}_i, \vec{u}_{i+1}, \dots) \\ \mathcal{J}_{\vec{\Psi}} &= \mathcal{J}_{\vec{\Psi}}(\vec{\Psi}_i, \vec{\Psi}_{i+1}, \dots),\end{aligned}$$

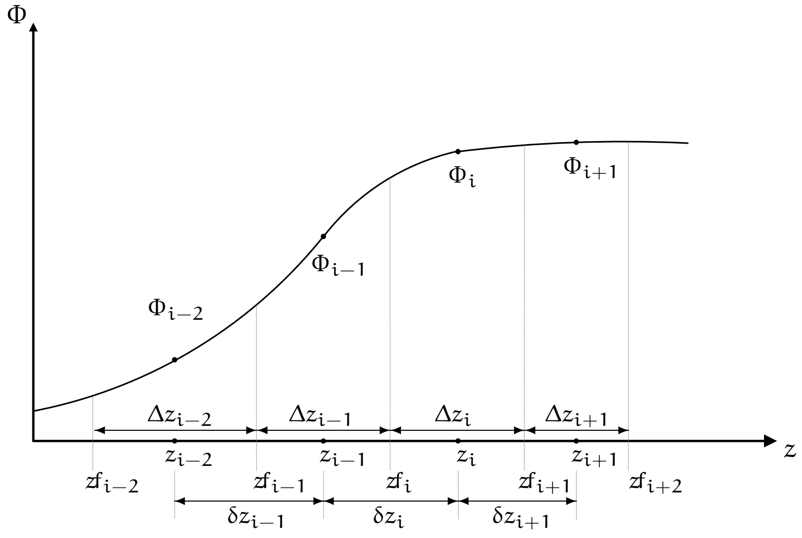

Figure 2.2: Sketch for the finite volume method used in ODT. The notation is the same as within the implementation of aODT.

where $\mathcal{J}$ denotes an arbitrary interpolation function for the subscribed value.

Finally, the time derivative has to be expressed. To solve the time derivative, the algebraic equations are integrated from time t to $t+\Delta t$, where $t+\Delta t$ is indicated by the superscript $n+1$. While the left hand side (LHS) can be integrated exactly, the right hand side (RHS) has to be approximated using a numerical integration method as done for the spatial integrals before. Depending on the approximation method the resulting equations are explicit or implicit. Three examples are (i) the forward time integration, where the RHS is evaluated at time t, (ii) the backward time integration, where the RHS is evaluated at time $t+\Delta t$, and (iii) the trapezoidal rule, where the RHS is evaluated as the average of the two time steps. These methods correspond to the explicit Euler, the implicit Euler, and the Crank-Nicolson method, respectively. For simplicity the RHS is abbreviated by RHS.

$$\left(\rho_i^{n+1}\Phi_i^{n+1} - \rho_i^n\Phi_i^n\right)\Delta V_i = \mathrm{RHS}_i^n \Delta t \tag{2.29}$$

$$\left(\rho_i^{n+1}\Phi_i^{n+1} - \rho_i^n\Phi_i^n\right)\Delta V_i = \mathrm{RHS}_i^{n+1} \Delta t \tag{2.30}$$

$$\left(\rho_i^{n+1}\Phi_i^{n+1} - \rho_i^n\Phi_i^n\right)\Delta V_i = \frac{1}{2}\left(\mathrm{RHS}_i^n + \mathrm{RHS}_i^{n+1}\right) \Delta t \tag{2.31}$$

2.3.2 *Finite volume method for ODT*

This section uses the presented finite volume concept to specify it for ODT as it is implemented within the structured non-equidistant aODT code. Figure 2.2 illustrates the naming within this section.

The derivation starts with the differential equations of ODT (equation (2.8) and (2.9)). These equations are integrated over the control volume ΔV_i represented by line control volumes ΔL of size Δz resulting in:

$$\begin{aligned}
\int\limits_{\Delta L_i} \frac{\partial \rho \vec{u}}{\partial t}\, dz &= \int\limits_{\Delta L_i} \frac{\partial}{\partial z}\left(\mu \frac{\partial \vec{u}}{\partial z}\right) dz + \int\limits_{\Delta L_i} S_{\vec{u}}\, dz \\
\int\limits_{\Delta L_i} \frac{\partial \rho \Phi}{\partial t}\, dz &= \int\limits_{\Delta L_i} \frac{\partial}{\partial z}\left(\kappa_{\Phi} \frac{\partial \Phi}{\partial z}\right) dz + \int\limits_{\Delta L_i} S_{\Phi}\, dz. \qquad (2.32)
\end{aligned}$$

The eddy process is excluded from this equation due to the fact that eddy events are instantaneous effects and the diffusion process is applied between two eddy events.
In ODT, the positions z_i are located at the cell centers between the cell faces zf_i and zf_{i+1}. Using the midpoint rule, this results in a second order approximation of the integrals as mentioned by Ferziger and Perić [27]. Similar to the mentioned time integration, the diffusion terms (first term on the RHS) can be integrated exactly resulting in the following algebraic equations:

$$\begin{aligned}
\frac{\partial \rho_i \vec{u}_i}{\partial t} \Delta z_i &= \mu_{zf_{i+1}} \left.\frac{\partial \vec{u}}{\partial z}\right|_{zf_{i+1}} - \mu_{zf_i} \left.\frac{\partial \vec{u}}{\partial z}\right|_{zf_i} + S_{\vec{u},i} \Delta z_i \\
\frac{\partial \rho_i \Phi_i}{\partial t} \Delta z_i &= \kappa_{zf_{i+1}} \left.\frac{\partial \Phi}{\partial z}\right|_{zf_{i+1}} - \kappa_{zf_i} \left.\frac{\partial \Phi}{\partial z}\right|_{zf_i} + S_{\Phi,i} \Delta z_i. \qquad (2.33)
\end{aligned}$$

For the derivatives at the cell boundaries, the Taylor series around zf_i and zf_{i+1} are used giving the following discretization:

$$\begin{aligned}
\Phi_i &= \Phi_{f_{i+1}} - \frac{\Delta z_i}{2} \left.\frac{\partial \Phi}{\partial z}\right|_{f_{i+1}} + O(\Delta z^2) \\
\Phi_{i+1} &= \Phi_{f_{i+1}} + \frac{\Delta z_{i+1}}{2} \left.\frac{\partial \Phi}{\partial z}\right|_{f_{i+1}} + O(\Delta z^2) \\
\left.\frac{\partial \Phi}{\partial z}\right|_{f_{i+1}} &\approx \frac{\Phi_{i+1} - \Phi_i}{\delta z_{i+1}}. \qquad (2.34)
\end{aligned}$$

The diffusion coefficients are calculated using the harmonic average.

$$\mu_{zf_{i+1}} = \frac{2}{\frac{1}{\mu_{zi+1}} + \frac{1}{\mu_{zi}}} \qquad \kappa_{zf_{i+1}} = \frac{2}{\frac{1}{\kappa_{zi+1}} + \frac{1}{\kappa_{zi}}} \qquad (2.35)$$

This results in the following discretizations:

$$\frac{\partial \rho_i \vec{u}_i}{\partial t} = \frac{\frac{\mu_{zf_{i+1}}}{\delta z_{i+1}} \vec{u}_{i+1} - \left(\frac{\mu_{zf_{i+1}}}{\delta z_{i+1}} + \frac{\mu_{zf_i}}{\delta z_i}\right) \vec{u}_i + \frac{\mu_{zf_i}}{\delta z_i} \vec{u}_{i-1}}{\Delta z_i} + S_{\vec{u},i} \qquad (2.36)$$

$$\frac{\partial \rho_i \Phi_i}{\partial t} = \frac{\frac{\kappa_{zf_{i+1}}}{\delta z_{i+1}} \Phi_{i+1} - \left(\frac{\kappa_{zf_{i+1}}}{\delta z_{i+1}} + \frac{\kappa_{zf_i}}{\delta z_i}\right) \Phi_i + \frac{\kappa_{zf_i}}{\delta z_i} \Phi_{i-1}}{\Delta z_i} + S_{\Phi,i} \qquad (2.37)$$

Using the mentioned time discretizations give the implemented explicit and implicit solver within aODT. Also the Crank-Nicolson discretization is implemented.

2.3.3 *Budgets of the turbulent kinetic energy*

One of the key usage of DNS is to improve the turbulence models used by RANS and LES. In this regard, ODT is on the one hand a model but on the other hand it can also provide detailed information to improve the turbulence models.

An important property of a turbulent flow is the turbulent kinetic energy. It is essential for accurate RANS simulations and LESs of highly turbulent flows.

Therefore, it is essential to know how the turbulent kinetic energy and its budgets are calculated and how they are represented within ODT. The derivation of the equation for the turbulent kinetic energy can be found within several books, e. g. Schlichting and Herrmann [82] or Wilcox [94], while the ODT representation is published by Kerstein et al. [48]. Within this section a short overview of these derivations is given.

The derivation starts using the incompressible Navier-Stokes equations (2.7) and its representation within ODT (2.8) for constant viscosity.

$$\frac{\partial u_i}{\partial t} + \frac{\partial u_i u_j}{\partial x_j} = -\frac{1}{\rho}\frac{\partial p}{\partial x_i} + \frac{1}{\rho}\frac{\partial \tau_{ij}}{\partial x_j} + F_i \qquad \text{physical}$$

$$\frac{1}{\rho}\frac{\partial \tau_{ij}}{\partial x_j} = \frac{\mu}{\rho}\frac{\partial^2 u_i}{\partial x_j^2}$$

$$\frac{\partial u_i}{\partial t} + E_i(z) = -\frac{1}{\rho}\frac{\partial p}{\partial x_i} + \frac{\mu}{\rho}\frac{\partial^2 u_i}{\partial z^2} + F_i \qquad \text{ODT}$$

Within ODT, there is no direct representation of the pressure, wherefore the first term on the right hand side could be treated as an external force. The eddy process $E_i(z)$ is given by two processes, the mapping $M_i(z)$ and the kernel addition $K_i(z)$, as described previously. As Kerstein [48] describes, the kernel addition could be viewed as a representation of a local pressure effect and be separated into a transport $T_i(z)$ and a scrambling $S_i(z)$ contribution.

These equations are averaged using the Reynolds decomposition giving (i) the Reynolds equations and (ii) the corresponding ODT representation.

$$\frac{\partial \overline{u}_i}{\partial t} + \frac{\partial \overline{u_i}\,\overline{u_j}}{\partial x_j} = -\frac{1}{\rho}\frac{\partial \overline{p}}{\partial x_i} + \frac{\mu}{\rho}\frac{\partial^2 \overline{u}_i}{\partial x_j^2} + \overline{F}_i - \frac{\partial \overline{u_i' u_j'}}{\partial x_j} \tag{2.38}$$

$$\frac{\partial \overline{u}_i}{\partial t} + \overline{E}_i(z) = -\frac{1}{\rho}\frac{\partial \overline{p}}{\partial x_i} + \frac{\mu}{\rho}\frac{\partial^2 \overline{u}_i}{\partial z^2} + \overline{F}_i \tag{2.39}$$

$$\overline{E}_i(z) = \overline{M}_i(z) + \overline{T}_i(z) + \overline{S}_i(z) \tag{2.40}$$

Afterwards, the incompressible Navier-Stokes equations (2.7) are multiplied by $2u_i$ giving the equation for the total kinetic energy. The difference between the mean of the total kinetic energy equation and the equation of the kinetic energy of the mean flow, given by the multiplication of the Reynolds equations by twice the mean velocity $2\overline{u}_i$, gives the equation of the turbulent kinetic energy $q = \frac{1}{2}\overline{u_i'^2}$.

$$\frac{\partial \overline{u_i'^2}}{\partial t} + \frac{\partial \overline{u_i'^2}\,\overline{u}_j}{\partial x_j} = \frac{\partial \overline{u_j' u_i'^2}}{\partial x_j} - \frac{\partial \frac{2}{\rho}\overline{u_i' p'}}{\partial x_i} - 2\overline{u_i' u_j'}\frac{\partial \overline{u}_i}{\partial x_j} + \frac{\mu}{\rho}\frac{\partial^2 \overline{u_i'^2}}{\partial x_j^2} - 2\frac{\mu}{\rho}\overline{\left(\frac{\partial u_i'}{\partial x_j}\right)^2} \qquad (2.41)$$

Application of this procedure to equation (2.39) gives

$$\frac{\partial \overline{u_i'^2}}{\partial t} + 2\left(\overline{u_i}\,\overline{E}_i - \overline{u_i E_i}\right) = \nu\frac{\partial^2 \overline{u_i'^2}}{\partial z^2} - 2\nu\overline{\left(\frac{\partial u_i'}{\partial z}\right)^2}. \qquad (2.42)$$

As can be seen, the unsteady term $ut = \frac{\partial \overline{u_i'^2}}{\partial t}$, the viscous transport $tv = \nu\frac{\partial^2 \overline{u_i'^2}}{\partial x_j^2}$, and the dissipation $d = -2\nu\overline{\left(\frac{\partial u_i'}{\partial x_j}\right)^2}$ are directly represented by ODT. For incompressible statistically stationary 1D flows the advective term $a = \frac{\partial \overline{u_i'^2}\,\overline{u}_j}{\partial x_j}$ within equation (2.41) is zero. The turbulent advection $ta = \frac{\partial \overline{u_j' u_i'^2}}{\partial x_j}$, the pressure scrambling $ps = -\frac{\partial \frac{2}{\rho}\overline{u_i' p'}}{\partial x_i}$, and the production $p = -2\overline{u_i' u_j'}\frac{\partial \overline{u}_i}{\partial x_j}$ are represented by the eddy process $2\left(\overline{u_i}\,\overline{E}_i - \overline{u_i E_i(z)}\right)$. A detailed derivation for these budgets is given by A. R. Kerstein [48] and is briefly presented next.

As described at the beginning of this section, the eddy process E_i can be divided into the mapping process M_i and the kernel addition K_i. The kernel itself can further be divided into a transport term T_i and a pressure scrambling term S_i resulting in $E_i = M_i + T_i + S_i$. Comparisons between the Reynolds equation (2.38) and the ODT equivalent (2.39) shows that no pressure fluctuation term is present, wherefore $\overline{S}_i$ is chosen to be zero. Furthermore, as A. R. Kerstein [48] shows, the Reynolds stresses can be expressed by:

$$-\frac{\partial \overline{u_i' u_z'}}{\partial z} = \overline{M}_i + \overline{T}_i := -\frac{\partial \overline{J}_i}{\partial z} \qquad (2.43)$$

$$\overline{u_i' u_z'} = \int_{z^*}^{\infty} \left(\overline{M}_i + \overline{T}_i\right) dz := \overline{J}_i \qquad (2.44)$$

Within ODT, due to the limited physical meaning of u_i, the term $2\overline{u_i E_i}$ cannot be calculated. Instead $\overline{E}_{ii} = \overline{M}_{ii} + \overline{T}_{ii} + \overline{S}_{ii}$ is defined representing $2\overline{u_i E_i}$, where $\overline{M}_{ii}$, $\overline{T}_{ii}$, and $\overline{S}_{ii}$ are the means of the mapping, transportation and pressure scrambling effects on u_i^2. In contrast to the Reynolds equation, within the equation of the total kinetic energy the pressure scrambling term doesn't vanish, wherefore $\overline{S}_{ii} \neq 0$. For more details about the definition of S_i and S_{ii} it is referred to A. R. Kerstein [48].

Using these definitions, equation (2.39) can be written as follows.

$$
\begin{aligned}
\frac{\partial \overline{u_i'^2}}{\partial t} &= -2\overline{u}_i\left(\overline{M}_i + \overline{T}_i\right) + \left(\overline{M}_{ii} + \overline{T}_{ii}\right) + \overline{S}_{ii} + \nu\frac{\partial^2 \overline{u_i'^2}}{\partial z^2} - 2\nu\overline{\left(\frac{\partial u_i'}{\partial z}\right)^2} \\
&= 2\overline{u}_i\frac{\partial \overline{J}_i}{\partial z} - \frac{\partial \overline{J}_{ii}}{\partial z} + \overline{S}_{ii} + \nu\frac{\partial^2 \overline{u_i'^2}}{\partial z^2} - 2\nu\overline{\left(\frac{\partial u_i'}{\partial z}\right)^2} \\
&= \frac{\partial\left(2\overline{u}_i\overline{J}_i - \overline{J}_{ii}\right)}{\partial z} - 2\overline{J}_i\frac{\partial \overline{u}_i}{\partial z} + \overline{S}_{ii} + \nu\frac{\partial^2 \overline{u_i'^2}}{\partial z^2} - 2\nu\overline{\left(\frac{\partial u_i'}{\partial z}\right)^2}
\end{aligned}
\tag{2.45}
$$

Here $\overline{J}_{ii}$ is defined in a similar way as $\overline{J}_i$.

$$
-\frac{\partial \overline{J}_{ii}}{\partial z} := \overline{M}_{ii} + \overline{T}_{ii} \qquad J_{ii} := \int_{z^*}^{\infty} \left(\overline{M}_{ii} + \overline{T}_{ii}\right) dz \tag{2.46}
$$

As already shown, the unsteady term, the viscous transport, and the dissipation are directly represented. The first term on the RHS of equation (2.45) represents the turbulent advection. Within this thesis, due to the current implementation of the budget calculation within the aODT code, the third term representing the pressure scrambling is added to the turbulent advection. The second term on the RHS is the ODT representation of the production.

Although this derivation is done for statistically stationary flows, the method is also used for time developing flows. It is shown by Schulz et al. [5] that if the data averaging periods are short enough, the difference between the budget calculation based on a short time period and the calculation based on snapshots at specific times is small. At this point it has to be mentioned, that within the snapshot based calculation it is impossible to calculate the unsteady term, wherefore it has to be small. Otherwise, it is possible to calculate the unsteady term using a approximation of the time derivative based on the mean profiles at different time steps.

Within this thesis, the derived budgets based on data averaging periods are used also for time developing flows.

2.3.4 *Approximation and interpolation methods*

Within numerical simulations, it is often necessary to interpolate information from one grid to another one. One example for this is the surface between two moving grids, where the information at the boundary of one grid has to be interpolated onto the boundary of the other grid. Due to the finite number of grid points or grid cells, the correct profile is unknown and has to be approximated before the information can be interpolated. Within a finite element simulation the correct profile is also unknown, but the approximation is directly given through the test functions.

This raises two different issues. First the unknown profile has to be approximated, where continuity of the profile and the derivatives are

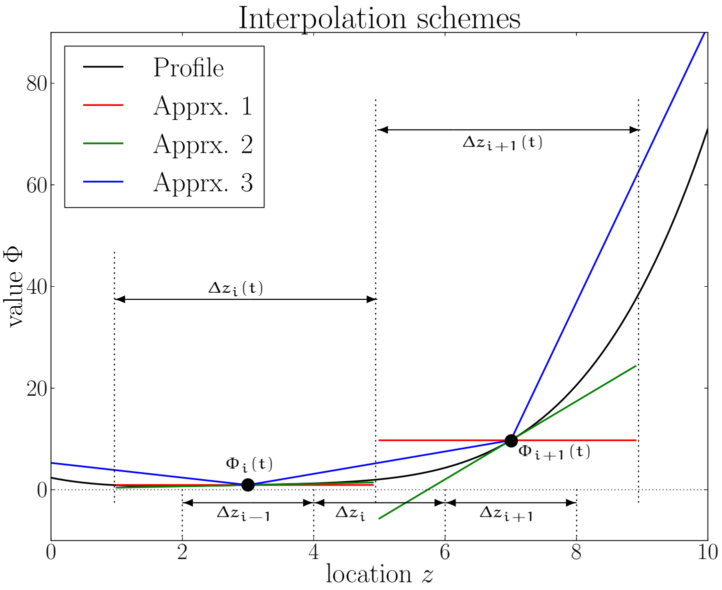

Figure 2.3: Different interpolation schemes. "Profile" shows the unknown profile of Φ represented by the midpoint values $\Phi_i(t)$ calculated by the finite volume method. $\Delta z_i(t)$ and Δz_i indicate (i) the time-varying adaptive and (ii) the stationary statistics grid, respectively.

important, and second the interpolation, which could have the need to be fast, conservative or accurate at specific points.

Figure 2.3 shows three different possible approximations of the unknown profile representative for most approximation methods. The first and the second approximation are based on cell center information with assumed cell centers at $z = 3$ and $z = 5$. The first one uses the value at the cell center, while the second one also uses the first derivative. Higher order approximation methods have to use more derivatives at the cell centers, while the corresponding interpolation methods could also replace one derivative value by the conservation condition. Nevertheless, all strictly cell centered methods are discontinuous and show the greatest errors at the cell boundaries, e. g. at $z = 5$ or $z = 9$. While both shown cell centered methods are conservative, higher order methods are not always conservative. The conservation assumption is only valid as long as one assumes that the value at the cell center is the mean value of the cell, which is valid for a finite volume method.

In contrast to the cell center logic used within aODT, the point logic is used by finite differences, where the information is given at specific points. Within finite volume schemes these points could be the cell centers or the boundary points. The third approximation is a paradigm for all approximations based on information at points, here shown with a linear approximation between the values at the cell centers. These methods, and specifically the next higher cubic spline method, are often used for the approximation of surfaces. All approximation methods based on the point logic are continuous. The corresponding interpolation methods are - in case of use for finite volumes

- generally not conservative due to the lag of the mean value information of the cell. Due to the lag of integrated information within finite differences, it is only possible to ensure conservation in a global sense by integrating the profile before and after interpolation.

Combined methods, using the cell centered as well as point logic, can combine the advantages of both groups but are more complex.

Depending on the need of the application, different approximation and interpolation methods should be used. Within aODT, where the interpolation is used multiple times during an eddy trial cycle, the calculation time is essential. A further decision to be made is, if the interpolation has to be conservative or not.

Detailed information about approximations and interpolations could be found within several books about numerics, digital signal or image processing, mesh moving, or finite volume schemes (e. g. Ferziger and Perić [27] or R. J. Le Veque [55] for finite volume methods, J. Stoer and R. Bulirsch [92] for numerics, P. O'Shea et al. [72] or B. Jähne [37] for image processing, or R. E. Crochiere and L. R. Rabiner [16] for signal processing).

3

PHYSICAL PROBLEMS

As described in the introduction, one of the most complex flow problems is e. g. the pipe flow of two or more immiscible fluids. This flow is getting more complex if at least one of the fluids has a large variation in density for small temperature fluctuations, as is the case for supercritical fluids when the conditions are near the critical point.
Due to this complexity, it is currently impossible to capture all effects with a DNS in a full 3D flow field of a straight pipe or even more complex geometries. Therefore, it is essential to model specific aspects of the flow.
The idea of this thesis is to simulate specific flow problems, part of the complex flow field, targeting one physical effect and described in the following sections, (i) to check the capabilities of ODT (ii) to expand the validated simulations to industrial relevant parameter regimes and (iii) to provide the opportunity to combine the models in one simulation. The simplest problem on the way to the multi-phase buoyant pipe flow is the single phase, incompressible pipe flow. From a modeling point of view, the channel flow is much easier than the pipe flow, wherefore the channel flow is the first test case. As described in the introduction, the channel flow and the pipe flow both belong to the group of TWBF, which are described in detail in the following section. The extension of the work of this thesis to a pipe flow is avoided due to the current cartesian formulation of ODT. It is possible to extend ODT to cylindrical geometries, but for studying the problems of this thesis and testing the capabilities of ODT it is unnecessary to expand the method to cylindrical coordinates due to the existence of the same effects in channel flows and planar jets. A first study of cylindrical ODT is given by N. Krishnamoorthy [50] and is still under development.
The first extension to ODT allows the behavior of a passive scalar within a single phase flow to be studied. This could be tracing different species, which are part of reactions, or just impurities in the fluid. It is simulated by a passive scalar channel flow which is described in detail in section 3.1.2.
Each multi-phase flow of at least two immiscible fluids has interfaces between the two fluids. These faces are free surfaces in terms of surface velocity and position. Hence, the next physical problem should capture this behavior. The examined flow is a free liquid jet exiting into still gases. This is described in detail in section 3.2.1.
Due to the constantly generated turbulence through a constant forcing within a multi-phase channel, it is self-evident that, if the surface tension is low enough, droplets will be generated. But not only the constant forcing could lead to droplets. Also the existing turbulence within a liquid jet could result in droplet generation. This generation through turbulence can be best studied by extending the previous liq-

uid jet with an initial breakup model. The current state of research of the initial breakup of a liquid jet is summarized in section 3.2.2.

The last studied phenomenon, which is part of the multi-phase channel or other flows mentioned in the introduction, is the buoyancy driven flow. For the study, the simulation of the smoke cloud, which is a simplification of a real cloud, was chosen. The advantage of the smoke cloud case over Rayleigh-Bénard convection, which is also a standard test case for buoyant driven flows, is that the smoke cloud has, on the one hand, a stably stratified flow region at the top of the cloud and, on the other hand, an unstably stratified one within the cloud. Therefore, it is possible to analyze the stabilizing and the destabilizing effect of buoyancy within one case. The smoke cloud case is detailed in section 3.3.

Besides the examined phenomena, there are additional effects in the multi-phase channel or pipe flow that are not handled in this thesis. Some examples are phase transitions, evaporation and condensation, surface waves, secondary breakup, droplet movement, and the recombination of fluid parts of the same phase.

3.1 TURBULENT WALL-BOUNDED FLOWS

Since the first publication reporting the existence of a boundary layer at the surface of a body within a flow by Prandtl [75], the study of turbulent wall-bounded flows has received continuous attention due to their importance for all flows with boundaries. This attention has led to formulations of the scaling and structure of wall turbulence. Since the first publications of Prandtl and von Kármán Clauser [15] has published a comprehensive review of the scaling laws, which has been repeated and extended by Gad-el-Hak and Bandyopadhyay [28] among other authors. A fully detailed description of the boundary layer and its importance is given by Schlichting and Gersten [82].

The boundary layer is measured and simulated mostly for three different cases. The first case is the TBL, in which a free stream interacts with a boundary and generates a boundary layer caused by the no-slip condition at the surface. This case is mostly used to study the development of a boundary layer. The second case is the channel flow, which is the combination of two boundary layers from opposite sides of the flow region resulting in a flow bounded in one direction. These measurements are mostly done to study the turbulence in a fully developed restricted boundary layer at specific dimensionless parameter values. Due to the limited aspect ratio (channel height to channel width), effects caused by the sidewalls have to be taken into account. To avoid the problem of the side walls the third case, the pipe flow, has a circular cross-section. Within all three cases the boundary layer looks the same except with little changes at the centerline of the pipe or the midplane of the channel, where the boundary layers interact with each other, and the surface of the TBL, where the influence of the free stream on the surface cannot be neglected.

The scalings of the boundary layer are based on the mean flow profile of the boundary layer and composed of two separate regions. One of these regions is at the wall and is mostly affected by viscosity, the other region is detached from the wall, where turbulence has major effects. The scaling of the inner one is based on the friction velocity $u_\tau = \sqrt{\frac{\tau_W}{\rho}}$ and the friction length $l_\tau = \frac{\nu}{u_\tau}$, where τ_W is the wall shear stress, ν the viscosity and ρ the density. The other region is based on the same velocity, due to the fact that the outer region is influenced by the inner one, and a macro length defining the boundary layer, which is the boundary layer thickness δ_{99} for TBLs, half the pipe diameter D, or the channel half height h. For TBLs the free stream velocity u_∞ is also often used for scalings of the outer part. Due to the absence of a free stream in pipe and channel flows, the mean bulk velocity $\overline{u}_B$ is often used.

As described among others by Marusic et al. [62] the mean flow scalings can be expressed by the form of a law of the wall:

$$u^+ = \mathfrak{f}(y^+) + \mathfrak{g}\left(\frac{y}{\delta}\right). \tag{3.1}$$

Here u is the mean flow velocity, y the distance from the wall, the superscript $^+$ indicates nondimensionalization using the friction velocity and the friction length and δ is the outer scaling length (δ_{99}, D, or h). For each region, two different subregion scalings can be derived from the boundary layer equations. The derivation is given by Schlichting and Gersten [82]. Here only the inner region is considered, whose subregion scalings are:

$$u^+ \sim y^+ \qquad \text{viscous region} \tag{3.2}$$

$$u^+ = \frac{1}{\kappa}\ln(y^+) + c \qquad \text{logarithmic region.} \tag{3.3}$$

For the "classical" scaling, κ is regarded as a constant and c is a geometry dependent additive constant. These scalings are illustrated in figure 3.1. The viscous layer is limited to about $y^+ < 5$, while in the classical theory the logarithmic region starts at about $y^+ \approx 40$ [1]. The upper bound of the logarithmic region depends on the boundary thickness (TBL) or the bulk flow parameters (pipe and channel flow) and is followed by a outer buffer layer (also called defect layer). Depending on the flow, the defect layer is the transition region from one boundary layer to the one from the opposite wall (channel and pipe flow) or to the free stream (TBL). The viscous and the logarithmic layer are linked by a buffer layer.

One of the current major research areas is the Reynolds numbers (Re) dependency of these scalings and its applicability to high Re. Therefore, a race for simulations and measurements at higher Reynolds numbers has started. Due to the strong increase of numerical cost of DNSs for high friction Reynolds number $Re_\tau = \frac{u_\tau \delta}{\nu}$, Re_τ is currently limited to about $Re_\tau \sim 5000$ ($Re_\tau = 2003$ was done by Hoyas and Jiménez [33] and $Re_\tau = 4200$ by Lozano-Duran and Jiménez [59]. Lee et al. [54] are running a DNS for about $Re_\tau \sim 5000$.). The increase of

---

[1] Depending on the publication different values ranging from 30 to 70 are said to be the start of the logarithmic region.

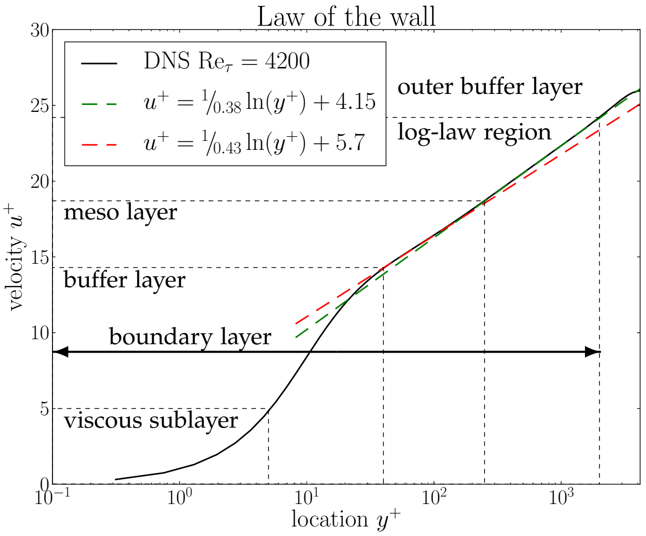

Figure 3.1: Schematic plot of the law of the wall. The DNS data is provided by Lozano-Duran et al. [59]. The red and the green dashed lines indicate the possible identifications of a logarithmic law. While the green one indicates the "correct" log-law, the red line shows the possibility of a wrong interpretation of the *meso* layer as the log-law caused by early low to moderate friction Reynolds number DNSs.

the Reynolds number in DNS is needed to enlarge the logarithmic region for comparison, where the region itself can be bounded by $40 \leqslant y^+ \lesssim \frac{1}{10}\mathrm{Re}_\tau$ ($40 \leqslant y^+ \lesssim \frac{1}{20}\mathrm{Re}_\tau$ for TBLs) in the "classical" view of the boundary layer. Recent discussions by Jimenez and Moser [39], Zagarola and Smits [107] and McKean [63] range over a start of the log region $200 \leqslant y^+_{\text{start}} \leqslant 600$ resulting in a much higher required friction Reynolds number for measuring a logarithmic region.

This is consistent with an early publication by Long and Chen [58], who have concluded that the buffer layer ranging from $y^+ \approx 5$ to $y^+ \approx 40$ is followed by a *meso* layer ranging from $y^+ \approx 40$ to $y^+ \approx 200$. This publication was reviewed by Wosnik et al. [97] and is also discussed by Marusic et al. [62], where the latter one doesn't call the region *meso layer* but concludes that the logarithmic layer starts at $y^+ > 200$.

The *meso* layer itself gives reasonable explanations for different questions concerning the law of the wall. First, there are discrepancies in the von Kármán number determined by measurements (Zanoun et al. [108] found $\kappa \approx 0.37$) and DNSs (Kawamura et al. [42] $\kappa \approx 0.43$, Lozano-Duran et al. [59] $\kappa \approx 0.38$). Due to the limitation of early DNSs and the Re_τ-dependent upper bound of the logarithmic layer, DNS could first provide a logarithmic layer for friction Reynolds numbers greater than about 2000. Figure 3.1 shows the DNS results from Lozano-Duran et al. [59] for $\mathrm{Re}_\tau = 4200$ and the approximated logarithmic layer (green dashed line). Simulations with a lower friction Reynolds number cannot create a logarithmic layer due to the fact that the outer buffer layer ranges into the *meso* or even into the inner buffer layer. Nevertheless, the early simulations provide the assump-

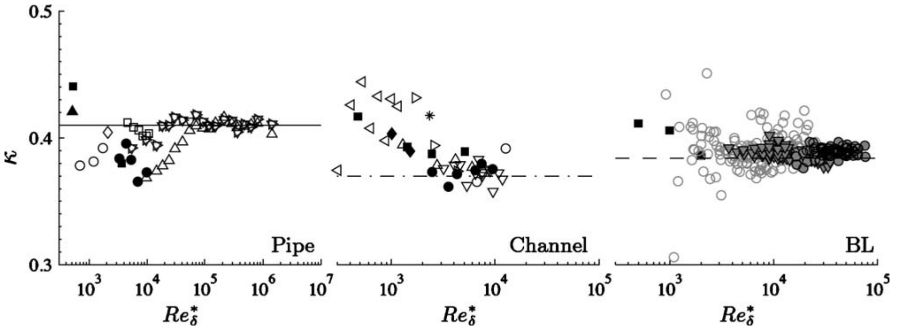

Figure 3.2: Reynolds dependency of κ. The figure is taken from Marusic et al. [62] .
"——" $\kappa_P = 0.41$, "-·-·-·-" $\kappa_C = 0.37$, "- - - -" $\kappa_{BL} = 0.384$
[Reproduced with permission from I. Marusic, B. J. McKean, P. A. Monkewitz, H. M. Nagib, A. J. Smith, and K. R. Sreenivasan: Wall-bounded turbulent flows at high Reynolds numbers: Recent advances and key issues. *Physics of Fluids* (065103), **22**(6), 2012. DOI: 10.1063/1.3453711. Copyright 2012, API Publisching LLC.]

tion of a log-law illustrated by the red dashed line in figure 3.1 with a higher von Kármán constant.

Besides the discussion of the value of the constant it is unclear if the law of the wall is really "logarithmic". A different ansatz involving a power law was given by George et al. [29] and Barenblatt [10]. As described by Moser et al. [68] both formulations can be tested by analyzing the following formulations.

$$\gamma = y^+ \frac{\partial \overline{u}^+}{\partial y^+} \tag{3.4}$$

$$\beta = \frac{y^+}{\overline{u}^+} \frac{\partial \overline{u}^+}{\partial y^+} \tag{3.5}$$

The first one shows a constant value at $^1/_\kappa$ if the mean flow follows a logarithmic law while the second one gives a constant value of n for a power law with an exponent of n. Analysis of the DNS results shows that the *meso* layer could be approximated by a $^1/_7$-power law in the range $50 \leqslant y^+ \leqslant 250$. This approximation is improved by the outer buffer layer for low Re_τ, where only a short or no logarithmic layer is present.

In contrast to DNS, measurements of the boundary layer can be done for high Reynolds numbers (a summary of current projects for high Reynolds number measurements is given by Marusic [62]). The highest Re_τ studies for pipe flow are done at about $Re_\tau = 3 * 10^5$, for channel flow at $Re_\tau = 5000$ and for TBLs at $Re_\tau \sim 2 * 10^4$. An exception to this is given by the measurements from the Surface Layer Turbulence and Environmental Science Test (SLTEST) site on the salt flats of Utah's Western desert by Metzger and Klewicki [65], which reaches friction Reynolds numbers of order 10^6.

The same problem, the size of the smallest scales causing the strong increase of numerical cost of DNS, is also causing trouble for measurements. On the one hand, with increasing Reynolds number the size of the viscous layer decreases as $y = y^+ h Re_\tau^{-1}$, which can be derived using the definition of Re_τ and $y^+ = \frac{y u_\tau}{\nu}$, resulting in the problem of minimizing the size of the measuring instruments, which is the limiting factor. The decrease of the size of the viscous layer can be compensated by enlarging the measurement facility, which results in an increase of cost for measurements. On the other hand, the decrease of the smallest scales also causes higher measuring errors as shown for the hot-wire sensor technique by Hutchins et al. [36]. Nevertheless, the conclusions from McKean et al. [63] for pipe flow and from Zanoun et al. [108] for channel flow show clearly the existence of the logarithmic layer ranging over $200 \leqslant y^+ \leqslant 0.1\mathrm{Re}_\tau$.

Nagib and Chauhan [70] have compared the results for the constant κ of equation (3.3) for the three TWBFs for different Reynolds numbers. Their results are shown in figure 3.2 where Re_{δ^*} is the TBL equivalent to the friction Reynolds number. For the pipe flow and the TBL a constant can be directly seen. For the channel flow a constant at $\kappa = 0.37$ can be estimated, while the value $\kappa \approx {}^1/_e$ was originally published by Zanoun et al. [108] and is supported by the DNS from Lozano-Duran et al. [59].

3.1.1 *Additional research topics for TWBF*

As described in the previous section, the scaling of the mean flow is still a major research topic for TWBFs. A second major topic is the fluctuation velocity in the streamwise direction which seems not to follow an inner/outer scaling. A detailed discussion for TBLs was published by Alfredsson et al. [8]. They have compared several DNS and measurement data sets up to $\mathrm{Re}_\tau = 18000$ with regard to the existence of an *outer peak* in the profile of the fluctuation velocity u^+_{RMS}, where the subscribe *RMS* denotes the root-mean-square (RMS) value.

For their comparisons, they have introduced a new so called diagnostic plot where the fluctuation velocity is plotted against the mean velocity $\overline{u}$ and both are normalized by the free stream velocity u_∞. The result is a plot where the inner as well as the outer scaling converges for all Reynolds numbers. Furthermore, they have also introduced another plot where u_{RMS} is instead normalized by the mean velocity profile, here denoted as U. This different normalization converges the data sets for the outer scaling to a decreasing line up to $\frac{\overline{u}}{u_\infty} = 0.9$. Both plots are shown in figure 3.3. With the assumption of a logarithmic law of the wall and a logarithmic skin friction law they have calculated the location of the outer peak at $y^+_{\max(u_{\mathrm{RMS}})} = 0.81(\mathrm{Re}_\tau)^{0.56}$, which is close to the observed exponent for pipe flows of 0.52 from Morrisson et al. [67]. Therefore, the outer peak can only be seen if the location has an appropriate distance to the inner maximum. Additionally, it has to be noted that for measurements the accuracy of the measurement technique has a major influence on the existence of an outer peak, as shown by Hutchins et al. [36]. They have recognized a strong dependence of the accuracy and existence of the inner peak to the length of a hot-wire sensor and they concluded that the normalized sensor length should be $L^+_{\mathrm{sensor}} < 22$.

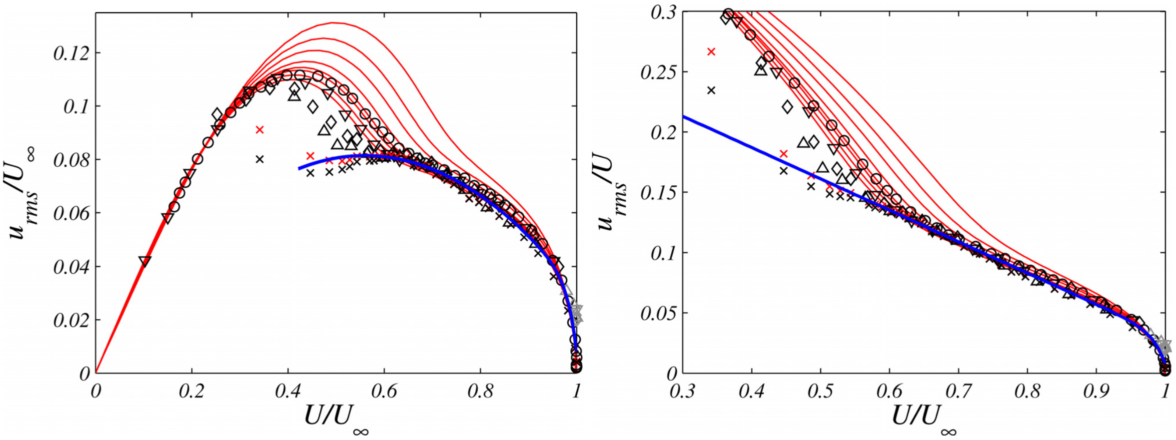

Figure 3.3: Diagnostic plots of u_{RMS} for TBLs at different Reynolds numbers. The red lines are DNS results and the symbols represent TBL measurements. The figures are published by Alfredsson et al. [8]. The left figure shows the converged inner and outer scaling. The right one shows the outer scaling with convergence to the blue line up to $\frac{\overline{u}}{u_\infty} = 0.9$ and a least square fit of the measurement data up to $\frac{\overline{u}}{u_\infty} = 1$. Within this figure $U = \overline{u}$.
[Reproduced with permission from P. H. Alfredsson, A. Segalini, and R. Örlü: A new scaling for the streamwise turbulence intensity in wall-bounded turbulent flows and what it tells us about the "outer" peak. *Physics of Fluids* (041702), **23**, 2011. DOI: 10.1063/1.3581074. Copyright 2012, API Publisching LLC.]

Another topic of current research of TWBF is the distribution of wall shear stress τ_W. This topic was raised by Wu and Moin [103] and is discussed by Örlü and Schlatter [71]. Following the expansion from Afredsson et al. [7], the fluctuation can be calculated as follows.

$$\tau^+_{W,\mathrm{RMS}} = \frac{\tau_{W,\mathrm{RMS}}}{\overline{\tau}_W} = \lim_{y\to 0} \frac{u_{\mathrm{RMS}}}{\overline{u}} \tag{3.6}$$

Here $\overline{\tau}_W = \tau_W$ is the mean wall shear stress and the overbar is used to illustrate the mean character of the value.

The classical value of $\tau^+_{W,\mathrm{RMS}}$ is estimated to be constant at 0.4. Alfredsson et al. [7] have noted a slight increase of the TBL wall shear stress fluctuation with the Reynolds number following $\tau^+_{W,\mathrm{RMS}} = 0.298 + 0.018\ln(\mathrm{Re}_\tau)$ while Keirsbulck et al. [43] give a different scaling of $\tau^+_{W,\mathrm{RMS}} = 0.432 - \frac{11}{\mathrm{Re}_\tau} + \frac{500}{\mathrm{Re}_\tau^2}$ (for channel flow $\tau^+_{W,\mathrm{RMS}} = 0.432 - \frac{11}{\mathrm{Re}_\tau}$ is used). The comparisons to multiple DNS data sets and to measurement results for the TBL and the channel flow, given by Keirsbulck et al. [43], show that the bounded approximation by Keirsbulck is more reasonable. Therefore, the current approximation gives an upper bound for the fluctuation of $\tau^+_{W,\mathrm{RMS}}(\mathrm{Re}_\tau \to \infty) = 0.432$. The corresponding figure from Keirsbulck et al. is given in figure 3.4.

Besides the value of $\tau^+_{W,\mathrm{RMS}}$, which is a basic signature of near wall fluctuation effects, the shape of the full PDF of τ^+_W is important for understanding the near wall flow field. As Örlü and Schlatter [71] describe, the outer-layer large-scale motions have a direct imprint on the fluctuation of the stress at the wall. They have also found that the PDF collapses for the inner-scaling and follows a log-normal distribution exept in the far tails where some likelihood of sign reversal is found. Their result is shown in figure 3.5.

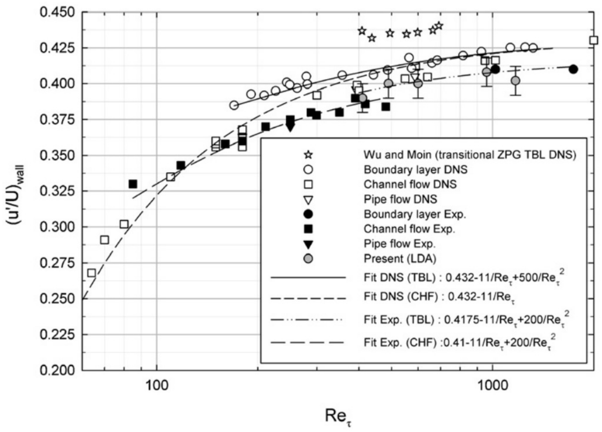

Figure 3.4: Dependency of $\tau^+_{W,\mathrm{RMS}}$ on Re_τ. Based on equation 3.6 $\tau^+_{W,\mathrm{RMS}}$ is equal to $\left(\frac{u_{\mathrm{RMS}}}{u}\right)_{\mathrm{wall}}$. The figure was published by Keirsbulck et al. [43].
[Reproduced from L. Keirsbulck, G. Fourrié, L. Labraga, and M. Gad-el-Hak: Scaling of statistics in wall-bounded turbulent flows *Comptes Rendus Mécanique*, **340**(6):420-433, 2012. DOI: 10.1016/j.crme.2012.02.005 Copyright 2012 Elsevier Masson SAS. All rights reserved.]

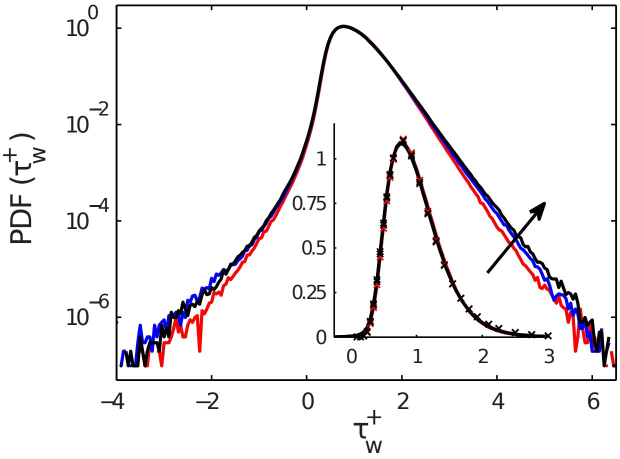

Figure 3.5: PDF of τ^+_W for different Reynolds numbers. The figure was published by Örlü and Schlatter [71].
[Reproduced with permission from R. Örlü and P. Schlatter: On the fluctuating wall-shear stress in zero pressure-gradient turbulent boundary layer flows *Physics of Fluids* (021704), **23**, 2011. DOI: 10.1063/1.3555191. Copyright 2012, API Publisching LLC.]

3.1.2 *Heated channel flow*

Besides the research on the PDF of the wall shear stress and the behavior of several quantities in the channel flow for high Reynolds numbers, also the behavior of a passive scalar within the channel is of interest. The turbulent mixing of fluids, the behavior of species within the flow, and the heat transfer from the wall are of special interest to industry.

Like to the pure channel flow the highly turbulent regime of a passive scalar in a channel flow is currently not reachable using DNS. Even if the Reynolds number is moderate, the Prandtl number $\mathrm{Pr} = {}^{\nu}/_{a}$ of interest can reach values of 10^3 or higher. If the thermal dependency of other quantities is neglected or different species are taken into account the Schmidt number $\mathrm{Sc} = {}^{\nu}/_{\kappa}$ and the Prandtl number are representatives. Here, a is the thermal conductivity and κ the scalar

diffusivity. In this cases, the passive scalar is the property forcing the high resolution of the computational domain. The reason is that for the approximation of the grid resolution not only the turbulent Reynolds number has to be taken into account, instead the product of $\mathrm{Re}_t \cdot \mathrm{Pr}$ is used resulting in $\mathrm{Re}_t \cdot \mathrm{Pr} \sim (L\eta^{-1})^{4/3}$.
Therefore, DNS with scalars is done at low Reynolds numbers. Kawamura et al. [42] have done simulations for $\mathrm{Re}_\tau = 180$ and 395 with Prandtl numbers ranging from $\mathrm{Pr} = 0.025$ to 0.71. On their web database, they provide also results up to $\mathrm{Re}_\tau = 1020$ for $\mathrm{Pr} = 0.71$ as well as $\mathrm{Pr} = 10$ for $\mathrm{Re}_\tau = 395$. They present results for the mean temperature profile, the temperature fluctuation, the temperature budgets and the turbulent Prandtl number.
Similar simulations were done by Schwertfirm and Manhart [87] for $\mathrm{Re}_\tau = 180$ and Pr up to 49. They have shown that for high Prandtl numbers the relationship of the turbulent scalar budgets to each other is changing while the maxima are tending towards the wall. Another interesting fact is that for high Pr the turbulent advection is greater than the production in a specific region. They have also introduced a scaling law for the mean scalar field and the heat transfer coefficient $K^+ = \frac{1}{\mathrm{Pr}} \frac{\partial T^+}{\partial y^+}$, where T denotes the passive scalar.
High Prandtl number simulations up to $\mathrm{Pr} = 2400$ at $\mathrm{Re}_\tau = 150$ were done by Papavassiliou and Hanratty [74] and have been extended to $\mathrm{Pr} = 15000$ by Srinivasan and Papavassiliou [91]. They have used DNS in combination with Lagrangian scalar tracking, where released particles move with the flow in a Lagrangian framework. They discuss the evalulation of the turbulent Prandtl number $\mathrm{Pr}_t = \frac{\nu_t}{\alpha_t}$ to improve simulation models based on an eddy viscosity model. Here, ν_t is the eddy viscosity and α_t the eddy diffusivity.
Besides the improvements based on DNS, You and Moin [106] improve their dynamic global-coefficient subgrid-scale eddy-viscosity model for LES of high Prandtl numbers. They show good comparisons for the mean and the fluctuation profiles of the flow field and the passive scalar for $\mathrm{Re}_\tau = 150$ with $\mathrm{Pr} = 25$ and $\mathrm{Re}_\tau = 300$ with $\mathrm{Pr} = 0.75$. They also show that the model gives reasonably good results for complex geometries.

3.2 LIQUID JETS

Although turbulence within a single phase flow is far from being fully understood, the flow system becomes more complex if two or more immiscible fluids are present. As mentioned in the introduction, the liquid jet exiting into a gas is not only one possible two-phase flow, it is also one of the most interesting flow problems in industrial applications.
Besides the application of fuel injection within an engine, there are multiple other applications as fire fighting, where the area reached by dispersion and dispersion uniformity are mainly interesting, jet cutting, where a thin localized, precise jet without droplet generation is needed, or gas pumps, where the jet and the dispersed fluid are

used to pump a gas by accelerating the surrounding gas efficiently. A further major application is the impinging jet, where a free liquid jet targets a plate normal to the jet axis for cooling of the plate.

The next section describes the liquid jet and the recent publications, while the following section focuses on droplet generation by free liquid jets.

Within this thesis the liquid jet is used as test case for ODT due to its similarity to the channel flow.

3.2.1 *Non-breaking jets*

Although the liquid jet is a flow of great interest the number of publications targeting the continuous jet are sparse. There are multiple publications focussing on the tip of the jet and its breakup, e. g. Ménard et al. [64] or Shinjo and Umemura [89], which is reasonable due to the fact that most investigations are driven by optimizing the fuel injection.

Mansour and Chigier [61] as well as Wolf et al. [95] have done measurements of the mean flow and turbulence within the liquid jet. Their experiment was a jet issuing vertically downward into still air. While Mansour and Chigier have used a pipe with a length of $^{x}/_{D} = 36$ to reach a nearly fully developed pipe flow, where D is the pipe diameter, Wolf et al. have used a channel with an aspect ratio $\frac{2h}{h_s} = 10$ and $\frac{z}{D_h} = 50.6$, where $2h$ is the channel height, h_s the spanwise width of the channel, and $D_h = 4\frac{2 \cdot h \cdot h_s}{4 \cdot h + 2 \cdot h_s}$ is the hydraulic diameter. For further discussions and comparisons between the Wolf data and the data from Mansour and Chigier, following D is also used for the channel height $2h$.

The aim of the measurements by Wolf et al. was to improve the cooling of an impinging jet. As previous publications have discussed, the amount of heat transfer is directly coupled to the turbulence within the jet, wherefore their work focuses on different wire grids and screens within the channel to increase the turbulence at the jet exit. Nevertheless, they have also done measurements without a screen as reference. They have measured the mean and the RMS streamwise velocity profiles at different axial positions up to $\frac{x}{2h} = 30$ for $Re = 23,000$. Furthermore, they have reported the axial development of the turbulence intensity for $Re_B = 23,000$ and $Re_B = 46,000$.

Similar to the findings of Mansour and Chigier, Wolf et al. reported a flattening of the mean profile starting at the free surface. Up to $\frac{x}{2h} = 5$, the flattening is restricted to the surface region $^{y}/_{h} > 0.7$. Reaching $\frac{x}{2h} = 20$ they reported a nearly flat profile. A similar tendency is also seen within the RMS velocity profiles. The decay of turbulent fluctuations starts at the surface while the centerline turbulence stays unaffected. Up to $\frac{x}{2h} = 20$ they have seen a reduction of the streamwise fluctuation velocity to less than 50% of the initial centerline fluctuation velocity. All these results are qualitativly similar to the findings of Mansour and Chigier for a round jet.

Due to a different focus of the publication from Mansour and Chigier they provide more details on the flow and a wider range of Reynolds numbers. They found that the turbulence decay is unaffected by velocity gradients, resulting in a negligible turbulence production within the flow. Furthermore, they concluded that the turbulence becomes isotropic starting at $^{x}/_{D} = 15$ while the relaxation lasts up to $^{x}/_{D} = 20$ for cases with a Reynolds number lower than $\mathrm{Re}_B \approx 17,500$. For higher Reynolds numbers they measured a full relaxation starting at $^{x}/_{D} \approx 3$, wherefore the turbulence decays faster and isotropy is reached earlier. Finally, they found that the turbulence decay follows a linear behavior for a wide range of Reynolds numbers.

The differences between the two studies arise (i) due to the different cross sections and (ii) different phenomena at the surface of the jet. Even if these well documented publications provide insight into the statistics within a circular and a rectangular jet, there is still a need for accurate DNS for both cross sections to clarify the similarities and differences.

3.2.2 *Initial droplet breakup*

Even if the non-breaking jet is desired for some applications, e. g. the liquid film protection of the first wall within fusion energy reactors (Shellabarger et al. [88] or Durbin et al. [24, 25]), most applications involve different conditions of the jet and the droplets. Since the first investigations of breaking liquid jets, especially the group around G. M. Faeth has done a lot of work to characterize the different regimes of breakup.

Their publications report the results of measurements of a round liquid jet issuing vertically downward into still air (Wu et al. [100, 101, 102], Wu and Faeth [98, 99], Dai et al. [17] and Sallam et al. [78, 79]). They distinguish three different breakup mechanisms, Rayleigh breakup, turbulent breakup and bag-shear breakup. They report the associated breakup length, also called column length, measured from the jet exit to the end of the jet column, where the remaining jet breaks into droplets. Furthermore, they have shown that the streamwise velocity of droplets is comparable to the mean streamwise jet velocity while the cross-stream droplet velocity is comparable to the mean cross-stream RMS velocity.

The Rayleigh breakup is valid for small Weber numbers $\mathrm{We} = \frac{\rho_l u_0^2 D}{\sigma} \lesssim 500$ and small Reynolds numbers $\mathrm{Re} = \frac{\rho_l u_0 D}{\mu_l}$, where ρ_l is the liquid density, u_0 the bulk velocity of the jet, σ the surface tension, and μ_l the kinematic viscosity of the liquid. The region is characterized by initial breakup due to increasing surface waves amplitudes finally reaching the centerline. The generated droplets are sparse and their size is comparable to the jet diameter. The location of breakup can be obtained from analysis of the Rayleigh breakup time and the bulk velocity yielding the breakup location x

$$\frac{x}{D} = c_R \sqrt{\mathrm{We}}, \tag{3.7}$$

where c_R is a constant in order of unity influenced by the initial disturbances of the jet surface.

The second region is the turbulent liquid column breakup where the initial jet turbulence irregularly distorts the surface of the jet. These distortions result in the creation of ligaments which afterwards undergo the Rayleigh breakup. Sallam et al. have shown that the breakup length can be derived from the droplet size distribution and is given by:

$$\frac{x}{D} = c_T \sqrt{We}, \tag{3.8}$$

where c_T is another constant in order of unity. This region is valid for $500 \lesssim We \lesssim 30,000$.

The last region is the bag-shear breakup, where liquid turbulence distorts the surface to a much greater degree resulting in strong coupling to the gas phase. The aerodynamic coupling leads to two different phenomena. In the first case the liquid turbulence is fully decayed wherefore large scale aerodynamic coupling creates distortion of the jet, where the jet is breaking in a similar manner as laminar jets in a cross flow. The second case is the shear like breakup where also smaller scale low-energy aerodynamic coupling acts on the surface of the jet. Sallam et al. derived for both cases that the breakup length is independent from the jet Weber number and the length becomes dependent on the density ratio between the liquid and the gas according to

$$\frac{x}{D} = c_B \sqrt{\frac{\rho_l}{\rho_g}}. \tag{3.9}$$

This correlation is valid only if the jet Reynolds number is high enough to be turbulent and the Weber number exceeds roughly $30,000$.

Besides the correlations of the column length, Wu and Faeth [99] have derived a Weber number correlation for the initial breakup position. While the column breakup as derived by Sallam et al. is affected by instabilities at the surface of the jet and the turbulence within the gas phase, the initial breakup, the position of first droplet generation, is only affected by turbulence within the liquid jet. Wu and Faeth have derived that the initial breakup position can be approximated by

$$\frac{x}{D} = c_I We^{-0.67} \approx c_I We^{-\frac{2}{3}}. \tag{3.10}$$

Their measurements show (i) a good comparison to their correlation for $c_I = 2000$ and (ii) are consistent with the measurements by Mansour and Chigier [61], who have shown that the liquid turbulence decays before $^x/_D = 20$ for jets with $Re \leqslant 17,500$ or $^x/_D = 3$ for high Reynolds numbers. In a certain range of Weber numbers, Wu and Faeth have shown that the droplet generation ends before the remaining jet breaks due to surface instabilities or aerodynamic effects. They have obtained the following correlation:

$$\frac{x}{D} = c_E We^{1.68} \approx c_E We^{\frac{5}{3}}, \tag{3.11}$$

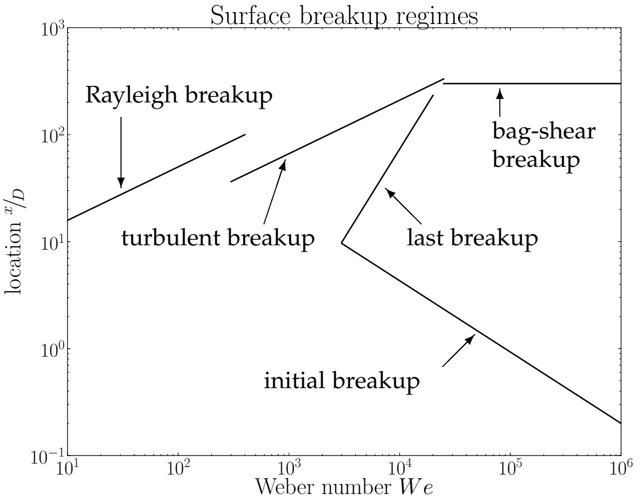

Figure 3.6: Idealized correlations of breakup regimes.

where $c_E = 1.58 \cdot 10^{-5}$ is an empirical coefficient.

From their analysis, they have derived a critical Weber number of $We^* = 2450$ needed to have droplet generation prior to the column breakup. This is close to the intersection point of the initial breakup correlation and the previous correlation at $We \approx 2800$. Nevertheless their measurements show that this critical Weber number is at about $We^* \approx 5200$, where they argue that the difference is a result of their simplified assumptions to derive their correlations. All these correlations are illustrated in figure 3.6.

Since these publications, further investigations have targeted different specific aspects of the breaking liquid jet. These investigations include among others detailed measurements of the creation of ligaments at the surface (Sallam and Faeth [77], C. Dumouchel [23]), improvements of the measurement techniques (Lee et al. [52]), or the liquid jet exiting into a crossflow (Aalburg et al. [6], Sallam et al. [80], Lee et al. [53], or Lubarsky et al. [60]).

Besides these experimental investigations, numerical studies have also been performed. Ménard et al. [64] have developed a simulation tool combining level-set (LS), ghost fluid (GF), and the volume of fluid (VOF) method to accurately track the surface of a liquid jet. Lebas et al. [51] have used this method for simulating the initial breakup of a diesel jet within the atomization regime and have compared the results to an Eulerian-Lagrangian spray atomization (ELSA) model. The atomization regime is part of the bag-shear regime. Also Shinjo and Umemura [89, 90] have simulated the jet. They have focused on the tip of the jet and the ligament creation due to the roll-up at the tip. Their method was a combination of the LS and an improved VOF method called multi-interface advection and reconstruction solver (MARS). The numerical diffusion of the advection scheme, which Ménard et al. [64] handled by using the GF method, was reduced by using the cubic interpolation pseudo-particle (CIP) method.

3.3 SMOKE CLOUD

The simulation of marine stratocumulus clouds is one of the most complex and most interesting flow cases. On the one hand, these clouds mainly influence the Earth's radiative balance, wherefore their prediction is of great interest for weather prediction and global climatology. On an annual mean basis, these clouds exceed a coverage of about 50% (R. Wood [96]) of the subtropical oceans, so accurate prediction of these clouds is essential for climatic simulations. Compared to the ocean, these clouds reflect most of the solar radiation resulting in a net cooling effect.

On the other hand, it is currently impossible to simulate these clouds accurately due to the wide range of spatial and temporal scales. While the global flow structures extend over multiple kilometer and the atmospheric boundary layer is about one kilometer high, the turbulence mixing the moist and the fresh air near the cloud top is smaller than order meters. Also the time scales span multiple orders of magnitude ranging from seconds for the turbulence to weeks for the global flow structures. Furthermore, the interaction of different physical effects within these clouds makes it even more difficult to capture all of them as condensation, evaporation, agglomeration, or movement of water droplets, influence of pollutions, ice generation, interaction of radiation with ice and droplets within the cloud, and so on. Finally, due to the location and the nature of these clouds, measurements are also complex and sparse resulting in a lack of validation data for simulations.

The stratocumulus-topped boundary layer (STBL) consists of two layers, where the lower one is cold, moist and turbulent while the upper one is the warmer and dryer free atmosphere. In between, a relatively thin inversion layer is formed, generating a stable stratification due to the warmer upper layer. The lower layer is well mixed by turbulent convection and is topped by stratocumulus clouds. The turbulence within the lower layer is mainly driven by radiative and evaporative cooling at the top of the cloud resulting in entrainment of fluid parcels from the upper layer into the lower one. Due to this entrainment, the inversion layer moves upwards, where the upward drift velocity is called the entrainment velocity w_e.

$$w_e = \frac{\overline{dh}}{dt} \tag{3.12}$$

Here h is the height of the inversion layer from the surface, which is at about one kilometer. This velocity is several orders of magnitude smaller than the convective velocity of the atmospheric boundary layer.

Comparing the height of the inversion layer to its thickness of a few meters, the inversion layer is very thin showing the mentioned scale range. Evaporation and radiative cooling drive the small scale motions within the inversion layer. These scales are comparable to or even smaller than the inversion layer thickness. This shows again the scale range spanning five orders of magnitude from the smallest scales to the integral scale, which is why simulations are mostly done using LES.

Due to the mentioned lack of detailed validation data, as Bretherton et al. [11] describe, the simulation results are reliable only if the results agree well to the sparse measurements and between independent simulations. One of the first intercomparisons was done by Moeng et al. [66] showing a wide range of agreement but also a great variability in the entrainment of dry air into the cloudy layer. The entrainment is driven by turbulent mixing at the cloud top where the turbulence itself is mainly driven by radiative and evaporative cooling as mentioned before. Moeng et al. also pointed out that there is a great variability among LES models in the prediction of evaporative cooling resulting from different liquid-water profiles. These differences are caused by different calculations of the total water and potential temperature profiles resulting in a variability of simulation setups among the LESs.

Therefore, Bretherton et al. [11] have used a simplified model, the smoke cloud, to analyze the numerical errors caused by different models. The smoke cloud was originally published by D. K. Lilly [57]. In contrast to the stratocumulus cloud, within the smoke cloud the lower layer is filled with a radiatively active, dry smoke. Therefore, turbulence is only driven by radiative cooling at the top.

For comparison, Sayler and Breidenthal [81] have done measurements in a tank as an analogue for the smoke cloud. In this experiment a blue relatively warmer fluid is overlying a colder yellow one and the tank is illuminated from below. The radiation passes through the yellow fluid and is absorbed within the blue one, heating the fluid near the inversion layer. The localized heating generates an unstabel stratification within the blue fluid resulting in turbulent mixing.

Besides generating the initial stratification by temperature, Sayler and Breidenthal also used dextrose within the yellow fluid to generate the initial stratification. Over all test cases they found that the entrainment rate is inversely proportional to the bulk Richardson number $Ri^* = \frac{h^* g'}{w^{*2}}$, where h^* is the height of the convection layer within the cloud, w^* a convective-scale velocity, and $g' = g\frac{\Delta\rho}{\rho_0} = -g\frac{\Delta T}{T_0}$ the effective gravity. One of the major differences between the smoke cloud measurements and stratocumulus clouds is the bulk Reynolds number, which is four orders of magnitude higher than in the experiments.

Based on these experiments, Bretherton et al. concluded that the entrainment rate simulated by LES is strongly coupled to the vertical grid spacing. All simulations overestimated the entrainment to leading order. Even recent LES using a high vertical resolution up to 2.5 meters still overestimates entrainment (Yamaguchi and Randall [105]). Bretherton's simulations also highlight a dependency of entrainment on the advection scheme used. Monotone schemes overestimate the entrainment rate while non-monotone schemes give better results but raise other uncertainties, e. g. negative smoke concentration or temperature overshoots.

Recent developments by Dietze et al. [22] using the LS method for tracking the inversion layer combined with the GF method for setting internal boundary conditions show a significant reduction of errors relative to the results by Bretherton et al. [11]. The error caused by numerical entrainment was reduced by one order of magnitude. At the same time, also uncertainties associated with different advection schemes were reduced by more than a factor of 10.

Schmidt et al. [83] have used ODT to simulate the tank experiment by Sayler and Breidenthal [81]. In contrast to the mentioned LESs, Schmidt et al. are directly simulating the experiment instead of the atmospheric analogue as done by Bretherton et al.. They have reproduced the inverse Richardson scaling for the thermal stratification. For the dextrose forced stratification they could only partly reproduce the inverse scaling. Furthermore, they pointed out some missing measurement details important for the validation of simulation methods. Some of these shortcomes are the unknown absorption within the yellow fluid and the heating of the plexiglas bottom. Sayler and Breidenthal also do not report the time dependency of the Richardson number and the entrainment rate as well as the absorption within the yellow fluid, which isn't zero as expected. Nevertheless, they have reproduced the sensitivity of entrainment rates to molecular transport and more importantly support the tendency of the need for high grid resolution recognized in the context of LES.

Besides the simulation of the smoke cloud case using LES and ODT, De Lozar and Mellado [18] carried out DNSs. Due to the high grid resolution of DNS using realistic flow parameters, they have not simulated the full STBL, instead have simulated the cloud top, a region of the boundary layer of 270 to 540 meters, containing the inversion layer. This has two effects, (i) it makes the smoke cloud case accessible using DNS and (ii) the DNS gives a detailed view into the mechanics involved in the development of the smoke cloud. They have found that the overall radiative cooling, which is equal to the reference buoyancy flux B_0, acts in two ways. B_0 can therefore be divided into the cooling of the cloud bulk Q_{cbl} and secondly the cooling of the inversion layer Q_{inv}. This has two effects; (i) the turbulent mixing within the cloud is only driven by the cooling within the cloud whether it comes from radiation or evaporation and (ii) the entrainment velocity is directly proportional to the cooling of the inversion layer $Q_{inv} = B_0 - Q_{cbl}$.

4

ADDITIONS TO AODT

The results of this thesis are based on the aODT code published by D. Lignell et al. [56]. The following section gives an overview of the code structure before implemented changes for the different cases are explained.

4.1 STRUCTURE OF THE AODT-CODE

The structure of the aODT code is illustrated in figure 4.1 and described next to give an overview of the code. All additional implementations are referenced to line numbers shown in figure 4.1. The code is similar to the BasicODT code which is explained in the BasicODT documentation [47].

Within the ODT implementation there are two different time variables t and t_0. The variable t_0 represents the physical time while $t \geqslant t_0$ represents the eddy trial time. Within each cycle of the *while*-loop (line 7) an eddy is sampled at time t while the flow state is at time t_0. Therefore a correct treatment would be first to calculate the diffusion of the flow from t_0 to t and second to implement the eddy.

This behavior would cause a causality problem due to the fact that the accepted eddy could be rejected due to the change of the flow by the diffusion. This would also neglect the need for the diffusion to time t and therefore again decide whether to accept the eddy. To overcome this problem the accepted eddy is deemed to occur at time t_0 and afterwards the flow is diffused to time t.

The first *if*-clause (line 8) is needed to account for the change of the flow by diffusion. If no eddy was accepted within a certain time lag dt_{CU} between t and t_0, the flow state has to be diffused to minimize the error caused by the time lag.

The grid adaption in line 16 could in principle be skipped but is included to reduce the effort of the diffusion process.

4.2 ADDITIONS FOR CHANNEL FLOW SIMULATIONS

For the simulations up to high Reynolds numbers, a first-order, implicit solver was included. The need for the implicit solver arises due to the adaptivity of the code. This adaptivity causes a very fine grid within regions of a high eddy acceptance rate due to inserting three times the grid within the eddy range by compressing the grid. Furthermore, aODT has the possibility for a much higher grid resolution than needed resulting in an increase of the effort of the first-order, explicit solver already implemented.

The time benefit can be estimated as follows. The number of explicit time steps is $n = \frac{\Delta t}{c \Delta t_{\mathrm{diff}}}$, where Δt is within the interval $[0;\ td \cdot \Delta t_{\mathrm{diff}}]$

```
Initialization
for $N_{reali}$ do
    Initialize realization
    for $N_{stat}$ do
        for $N_{tseg}$ do
            $t_{Mark} = t_{Mark} + t_{End}(N_{stat} \cdot N_{tseg})^{-1}$
            while $(t < t_{Mark})$ do
                if $(t - t_0 \geqslant dt_{CU})$ then
                    Diffusion step for $\Delta t = t - t_0$
                    Adaption of the grid
                    $t_0 = t$
                else
                Sample the next eddy
                if (eddy is accepted) then
                    Implementation of the eddy
                    Adaption of the grid
                    Diffusion step for $\Delta t = t - t_0$
                    Adaption of the grid
                    Raise $\delta t$ to match the oversampling
                    $t_0 = t$
                else
                $t = t + P(\delta t)$
                # P gives an exponential distribution with mean $\delta t$
            Diffusion step for $\Delta t = t - t_0$
            Adaption of the grid
            $t_0 = t$
            Post processing after subinterval
        Post processing after main interval
    Post processing of realization
Post processing
```

Figure 4.1: Structure of the aODT-code. N_{reali} is the number of realizations, N_{stat} the number of averaging periods, and N_{tseg} the number of snapshots within one period. Within each adaption process dt_{CU} is set to $td \cdot \Delta t_{diff}$ where Δt_{diff} is the diffusion time step $\Delta t_{diff} = \Delta x^2_{min}/\nu$ and td a given constant. The time step for the next eddy sampling is sampled from a Poisson distribution P with mean time step δt. Within the eddy sampling, the δt is decreased if the acceptance probability of the eddy is higher than a given value. Due to the coding of aODT in contrast to BasicODT, the implementation of an eddy is part of the eddy sampling process.

and $c \leqslant 0.5$ the Courant Friedrichs Lewy (CFL) number, the stability criterion of the explicit solver. This results in $n = [1; \lceil \frac{td}{c} \rceil]$ explicit solver cycles. As long as the the mean of n is larger than $n_{ie} = \lceil \frac{\Delta t_{imp}}{\Delta t_{exp}} \rceil$, where Δt_{imp} and Δt_{exp} are the computation time for one implicit or explicit solver calculation, the use of the implicit solver is beneficial. Important to note is the dependency of the numerical error of the implicit solver, which is first-order in time, wherefore the error increases with increasing time steps. A second-order Crank-Nicolson solver was also implemented but wasn't used due to the fact that it generated the same results but has a slight increase of the simulation time.
For the presented cases the simulations using the implicit solver are about five times faster than using the explicit one. A direct calculation of the speed-up gives $n_{ie} = 4$, which shows that the use of the implicit solver is beneficial due to the fact that $\overline{n} \approx 20$. The speed-up could be further increased by using the explicit solver for $\Delta t \leqslant n_{ie} \cdot c\Delta t_{diff}$ and the implicit solver otherwise. Up to now, this optimization isn't implemented. Furthermore, it has to be noted that a slight increase in the factor n_{ie} was noticed for increasing grid resolution, which is reasonable because the cost of the explicit solver is $O(N)$ and the Thomas algorithm $O(2N)$. Due to the choice of td and the fact that the mean of n is about 20 to 25, the implicit solver was used for the channel and the smoke cloud cases. For the jet simulations the explicit solver was used due to a higher sensitivity of the flow to numerical errors at the phase boundary.

The second major implementation for the channel flow simulations is the data reduction and the post processing as described in the BasicODT documentation [47]. The data reduction (i) time-integrates the changes caused by each process - eddy implementation, diffusion, adaption - and (ii) calculates the time average of the flow field itself. The first method is implemented around each process by first saving the flow state, then applying the changes due to the process, and finally calculating the changes using the saved state. This is done for the lines 9, 15, 17, and 24. The changes caused by the corresponding grid adaptions are added to the process. An analysis of the numerical diffusion caused by the adaption process shows a negligible influence.
The calculation of time averages is implemented as a second order trapezoidal rule within the diffusion process (line 9, 17, and 24).
The calculation of the mean profiles, the RMS profiles, as well as the first and second order budget terms is implemented in a separate post processing function after the main loop over the realizations. Therefore, the data reduction is (i) a time average within each of the N_{stat} averaging periods and (ii) an ensemble average over the N_{reali} realizations. A detailed discussion of the calculation of the second order budgets (budgets of the turbulent kinetic energy (TKE)) is given by Kerstein et al. [48].

A third part coupled to the implementation of the data reduction was

the implementation and testing of different interpolation schemes. Within aODT, there are two different grids; first the calculation grid (c-grid), which is adaptive and used for all calculations. Due to the constantly changing grid, it is not possible to calculate statistics, wherefore a second static grid (s-grid) was introduced.
The already implemented interpolation scheme was a first order, conservative, constant interpolation (approximation one within figure 2.3), where the value at the cell position was assumed to be the mean value of the cell. Especially for channel flows at higher friction Reynolds numbers this method lead to unphysical oscillations near the wall up to $y^+ \approx 5$. Therefore, some of the methods described in section 2.3.4 have been implemented and tested.
First, a second order trapezoidal rule based on the first derivative at the cell center was tested (approximation two within figure 2.3). This method, as well as all other higher order methods based on a cell center idea have fixed the unphysical oscillations, but lead to unphysical values for specific cases. One example for these cases is given by the liquid jet simulation, which has a high property curvature within the gas near the liquid surface. This high curvature leads to a high slope at a cell center, as illustrated, and an unphysical backflow. Even higher order schemes based on this center idea lead to similar problems. Tests were done up to fourth order cubic interpolation, all showing the same uncertainty.
Therefore, another interpolation scheme with a trapezoidal rule between cell centers was implemented (approximation three within figure 2.3). Compared to the original interpolation scheme it is not conservative. This interpolation scheme provides good results as long as the profile has nearly linear functions between two points, which is nearly realized by the adaption process. A higher order spline interpolation based on third order polynomials was also tested. The higher accuracy of the spline interpolation slows down the code. Therefore, the linear interpolation was used.
In principle, it is possible to reduce the slowdown of the spline interpolation due to the fact that the geometric arrangement of the cell positions is changed only by the mapping and the adaption processes. Therefore, it is possible to pre-calculate this information and update it after each adaption and mapping process within the modified region. Furthermore, as described within section 2.3.4, different interpolation schemes have different advantages, wherefore a detailed analysis of this part of aODT should be addressed by further studies.

4.3 ADDITIONS FOR LIQUID JET SIMULATIONS

For the simulation of a multi-phase case, the code has to track the phase boundaries using an identification marker for the different phases. The latter is realized by an additional variable containing a marker of the phase for each cell. With this variable and the adaptivity of aODT, the phase boundaries could be automatically tracked as the cell faces between two cells with different phase markers. While

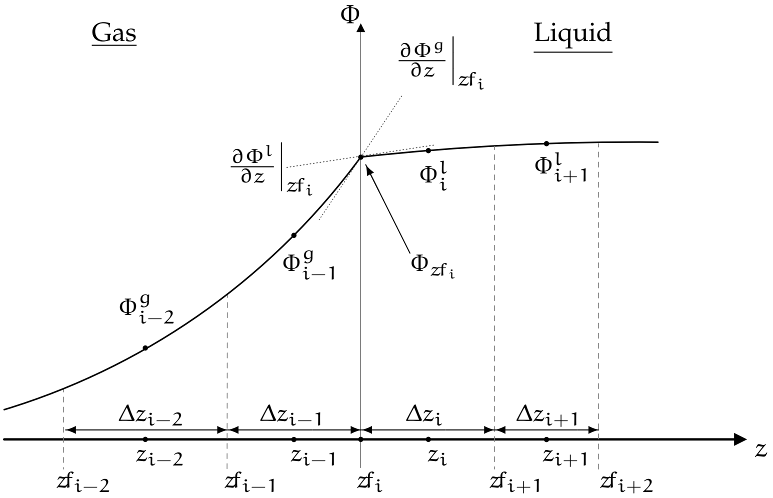

Figure 4.2: Sketch of a phase interface between two immiscible fluids. zf_i are the cell faces, z_i the cell centers, Φ_i the the value of property, with $\Phi \in \{u, v, w, T\}$, and the superscript denotes the liquid l or the gas g. Without loss of generality, the liquid and gas are taken to be representatives for two immiscible fluids. The notation is the same as in figure 2.2 and is used within the implementation of aODT.

the eddy implementation automatically takes care of the phase variable, the adaption and the diffusion process have to be adjusted.

To enable phase boundary tracking, the adaption process as described by Lignell et al. [56] has been modified to check the phase variable in a way that restricts the adaption to a single phase. Nevertheless, this could lead to a problem if a single cell surrounded by different phases fulfills the conditions for adaption. The physical interpretation of this is that, e. g. , two droplets are close enough to each other to agglomerate. This behavior is prevented within the current implementation for the liquid jet, because droplets generated by a two-phase eddy are erased from the line after generation. The erased range is (i) replaced by a constant profile representing the flow state of the cells next to the droplet or (ii) replaced by shifting the domain towards the remaining jet and extending the first or last cell to the corresponding domain boundary.

Also the diffusion process has to be modified for two-phase flows. At the phase boundary two conditions have to be fulfilled; (i) the velocities have to be the same on either side $\vec{u}^l = \vec{u}^g$ and (ii) the fluxes have to be the same $\mu^l \frac{\partial \vec{u}^l}{\partial z} = \mu^g \frac{\partial \vec{u}^g}{\partial z}$, too. The same conditions have to be obeyed for the temperature. This is illustrated in figure 4.2. For the explicit solver, the corresponding fluxes can be calculated using first-order central differences for the gradients resulting in the following equations:

$$\Phi_{zf_i} = \frac{\Phi^l_i + \Phi^g_{i-1} \frac{\Delta z_i}{\Delta z_{i-1}} \frac{\mu^g}{\mu^l}}{1 + \frac{\Delta z_i}{\Delta z_{i-1}} \frac{\mu^g}{\mu^l}} \tag{4.1}$$

$$\frac{\partial \Phi^g}{\partial z} = \frac{\Phi_{zf_i} - \Phi^g_{i-1}}{2\Delta z_{i-1}} \tag{4.2}$$

$$\frac{\partial \Phi^l}{\partial z} = \frac{\Phi^l_i - \Phi_{zf_i}}{2\Delta z_i}. \tag{4.3}$$

Without loss of generality, cell $i-1$ is a gas and i is a liquid cell. The same derivation for the implicit solver gives:

$$a_{i-1} = -\frac{1}{\rho_{i-1}} \frac{1}{\Delta z_{i-1}} \frac{\mu(zf_{i-1})}{z_i - z_{i-1}} \tag{4.4}$$

$$c_{i-1} = -\frac{1}{\rho_{i-1}} \frac{1}{\Delta z_{i-1}} \frac{\mu^g(zf_i)}{\frac{1}{2}\left(\Delta z_{i-1} \frac{\mu_{i-2}}{\mu_{i-1}} + \Delta z_{i-2}\right)} \tag{4.5}$$

$$b_{i-1} = 1 - a_{i-1} - c_{i-1} \tag{4.6}$$

$$a_i = -\frac{1}{\rho_i} \frac{1}{\Delta z_i} \frac{\mu^f(zf_i)}{\frac{1}{2}\left(\Delta z_i \frac{\mu_{i-1}}{\mu_i} + \Delta z_{i-1}\right)} \tag{4.7}$$

$$c_i = -\frac{1}{\rho_i} \frac{1}{\Delta z_i} \frac{\mu(zf_{i+1})}{z_{i+1} - z_i} \tag{4.8}$$

$$b_i = 1 - a_i - c_i. \tag{4.9}$$

Here, μ_i is the viscosity at the cell center of cell i, $\mu(zf_i)$ the interpolated viscosity at the cell face between cell $i-1$ and i, and $\mu^g(zf_i)$ and $\mu^l(zf_i)$ the viscosity at the cell face corresponding to the gas or the liquid, respectively. Because the gas and the liquid viscosity at the interface are undefined, a constant interpolation from the corresponding cell center to the interface is assumed.

Besides the adaption and the diffusion process, also the calculation of the acceptance probability is influenced by the phases. The presented ideas for the change of the calculation are based on unpublished notes (2007) and personal discussions with A. R. Kerstein.

Due to the triplet map implementation, a two-phase eddy, an eddy containing both phases, generates two new surfaces per existing surface within the eddy range. There are two possibilities for two-phase eddies: (i) an eddy partly containing the jet and partly the surrounding air, or (ii) containing the whole jet. In the first case the eddy region contains one surface before the mapping process, while the second one contains two surfaces. Due to the triplet map implementation these number of surfaces is tripled.

Within the following, it is assumed that the eddy contains a part of the jet.

The physical picture of the breakup is that a liquid slab is intersected by the ODT line. This means that a triplet map would result in two distinct slabs of liquid, one containing liquid both inside and outside of the eddy range and one totally within the eddy range. The first

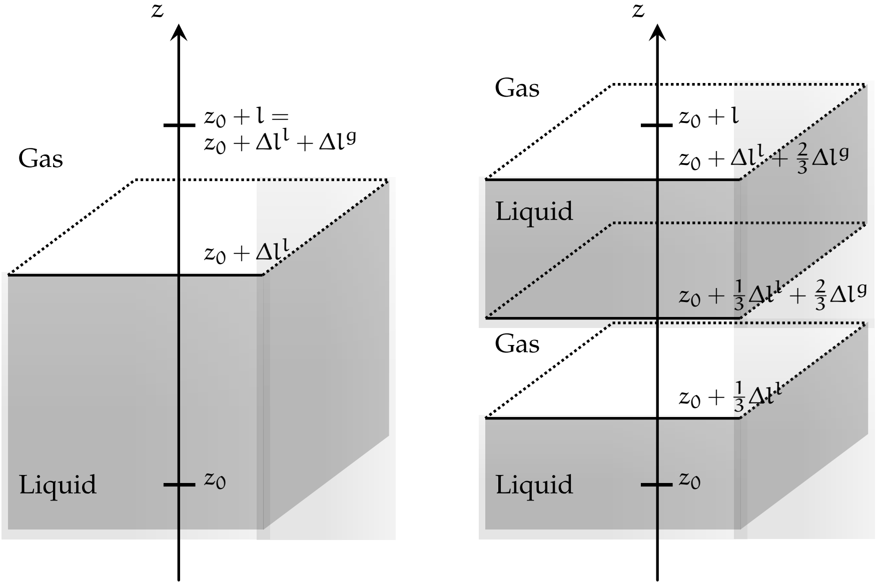

Figure 4.3: The physical idea of droplet generation due to triplet mapping. First, ODT line before eddy implementation, second, the state after the triplet map. Perspectively the reference surface is illustrated.

one is the remaining jet and the second one the ligament. After the ligament is created the secondary breakup occurs, which is not targeted within this thesis. Instead as described earlier, the ligament is erased by shifting the ODT line or replacing the ligament by gas with an uniform velocity equal to the velocity at the endpoints of the inserted interval. This idea is illustrated within figure 4.3.
Before the triplet map implementation, the potential energy per reference surface area stored within the surface can be calculated as $E_{\text{surf}} = \sigma$. After the map the energy is tripled resulting in $E'_{\text{surf}} = 3\sigma$, resulting in:

$$\Delta E_{\text{surf}} = 2\sigma.$$

Due to the two possibilities of breaking eddies mentioned above, the number of surfaces after the triplet map N_{surf} can be introduced. This number is three times the number of surfaces before the map, which is one if the eddy contains only a part of the jet and is two if the whole jet is within the eddy range. Therefore, only $^2/_3$ of the final surface energy is added and the energy change by surface tension can be calculated as

$$\Delta E_{\text{surf}} = \frac{2}{3} N_{\text{surf}} \sigma. \tag{4.10}$$

This energy has to be provided by the available kinetic energy and therefore acts as a sink term within the energy conservation equation (2.13).
Even if this derivation is based on a reasonable physical picture, there is an infinite number of reasonable pictures. One opportunity to take all possible pictures into account is the idea of an isotropic surface as derived by Chiu et al. [14], where each possible orientation of the ODT line compared to the surface is equal likely. Using this idea, a

correction factor $c = 2$ is inserted into equation (4.10), resulting in

$$\Delta E_{surf} = \frac{2}{3} N_{surf} c \sigma. \tag{4.11}$$

4.4 ADDITIONS FOR SMOKE CLOUD SIMULATIONS

The implementations for the smoke cloud case are twofold. First the code has to be adjusted to simulate an additional scalar besides the temperature and secondly the density has to be coupled to the temperature. Buoyancy was implemented using the Boussinesq approximation.
Additionally, the data reduction as explained above was extended for all scalars.

Part II

SIMULATION RESULTS

5

CHANNEL FLOW RESULTS

The first part of this thesis was the simulation of the channel flow as described in section 3.1. The following section gives an overview of the setup of a channel flow simulation and a short discussion about the required simulation time. Further parameters are discussed in appendix C. The discussion concludes with a best practice guide for channel flow simulations.

The next section summarizes the results for friction Reynolds number up to very high values of about $Re_\tau = 6.4 * 10^5$, where the parameters are fitted to give good results for $Re_\tau = 590$. The effects on the law of the wall, the Kármán number, and the additive constant c of the log-law are presented.

In section 5.3, the ODT results for the fluctuations of the wall shear stress are presented and in section 5.4 the influence of a fluctuating forcing pressure gradient is discussed.

Finally, section 5.5 presents the results provided by ODT for a passive scalar.

5.1 SETUP OF CHANNEL FLOW SIMULATIONS

Due to the simplicity of the channel flow, it is the standard test case for all ODT codes. Therefore, the channel flow at $Re_\tau = 590$ is well documented in the BasicODT[1] documentation [47] and compared to the DNS results by Moser and Kim [68]. This comparison was also done for the used adaptive ODT code by Lignell et al. [56], who have used $C = 10$ and $Z = 600$. A detailed discussion of parameters additionally important to aODT is given in appendix C.

As described in the BasicODT documentation, the forcing pressure gradient of the channel flow is directly related to the friction Reynolds number via $Re_\tau^2 = \frac{h^3 \nabla p}{\rho \nu^2}$. Choosing the channel half height h, the density ρ as well as the pressure gradient ∇p to unity, the viscosity can be calculated as the inverse of the Reynolds number. Following the definition of Re_τ and u_τ, this also results in a friction velocity and a wall shear stress of unity.

The simulation time can normally be expressed in terms of the friction time scale $t_\tau = \frac{\nu}{u_\tau^2}$. Schwertfirm and Manhart [87] propose a simulation time for reaching the fully developed channel flow before sampling of $100t^*$, which corresponds to $10\Delta t_B$, where Δt_B is the time needed for transition of the channel flow from a bulk profile u_B. For the previously chosen parameters this would lead to $t^* = \frac{100}{Re_\tau}$, where t^* is the simulation time in physical units. The further discussion and the results shown in section 5.4 show that this estimation doesn't give good results.

---

[1] Available at: https://sites.google.com/site/odtresearch/codes

He and Seddighi [32] also suggests to use $100t^*$ using a different definition of $t^*_{\mathrm{He}} = \frac{h}{u_B}$, where u_B is the bulk velocity of the fully developed channel flow. Their estimation is based on the simulation of the transition from a fully developed channel flow to a higher friction Reynolds number by a sudden change of the pressure gradient. Using this definition and the above-mentioned variables, this lead to $t^* = 100\frac{Re_\tau}{Re_B}$ with $Re_B = \frac{u_B h}{\nu}$. As will be shown in section 5.4, this estimation gives good results for the transition of an ODT simulation starting from a zero profile or a fully developed profile of a lower friction Reynolds number with an order unity factor. The unknown value for Re_B can be estimated using the correlation for the skin-friction coefficient C_f by Schultz and Flack [86] or Zanoun et al. [109] and the definition of C_f.

$$C_f = \frac{\tau_W}{\frac{1}{2}\rho\bar{u}^2} = 2\left(\frac{u_\tau}{u_B}\right)^2 = 2\left(\frac{Re_\tau}{Re_B}\right)^2 \tag{5.1}$$

For the statistics calculation time t_C a meaningful estimation is based on the turnover time of the largest possible eddy. This estimation is difficult due to the stochastic eddy sampling and the dependency of the turnover time on the instantaneous flow profile, which isn't known prior to the simulation. Furthermore, the largest possible eddy is the most unlikely eddy and has a turnover time not representative of the most probable eddy, and thus makes the estimated calculation time inefficiently high. A better estimation, which turned out to give good results but is not based on a theory, is to run the simulation for about $a \cdot 10^5$ accepted eddies, where a is factor of order unity.

Table 5.1 summarizes the setup for the high Reynolds number simulations. The starting profile is a fully developed flow profile of the next lower Reynolds number. The time t^* defines the time simulated to reach a fully developed flow profile of the new Reynolds number. Then statistics gathering begins, continuing for a time t_C. Calculation of the statistics is based on a time average over t_C. Some simulations are also averaged over an ensemble of independent simulations corresponding to the number of CPUs used, resulting in an overall simulation time of CPU number times t_C.
In table 5.2, the setup conditions for the simulations of an oscillating pressure gradient are summarized. The simulation starts from a fully developed flow profile with $Re_\tau = 1280$ and advances the channel flow with a constant pressure gradient for $\Delta t = \frac{T}{20}$, where T is the cycle duration of the pressure fluctuation. Afterwards, the current instantaneous flow profile is saved as the new restart profile for the next realization. After saving, the realization proceeds for two cycle durations and restarts with the saved profile for the next realization. The reason for this procedure is twofold: First, the calculation of the pure channel flow is needed to generate an independent fully developed channel flow profile as starting condition for the oscillating pressure gradient simulation. To erase the dependancies to the starting profile, the profile after the pure channel period is used as the next starting profile. The second reason for this procedure is to analyze the time

Table 5.1: Setup of channel flow for high Reynolds number simulations. t^* is the simulation time before statistics are calculated. t_C is the calculation time for the statistical averaging per CPU. CPUs specifies the number of cores used for the simulation, where the CPUs vary between Intel Xeon E5645 2.40GHz, Intel Core i7-2600 3.40GHz, Intel Xeon E5-1620 3.6GHz, and Intel Xeon E5-2630 2.3GHz. Reali is the number of ODT realizations calculated on each CPU.

No.	Re_τ	ν	t^*	t_C	CPUs /
	[–]	$[m^2/s]$	[s]	[s]	Reali
0	320	$3.125 \cdot 10^{-3}$	10000	300000	1 / 1
1	590	$1.695 \cdot 10^{-3}$	10000	100000	1 / 1
2	640	$1.5625 \cdot 10^{-3}$	10000	150000	2 / 1
3	1280	$7.8125 \cdot 10^{-4}$	10000	60000	5 / 1
4	2560	$3.90625 \cdot 10^{-4}$	10000	60000	5 / 1
5	5120	$1.953125 \cdot 10^{-4}$	10000	10000	5 / 1
6	10240	$9.765625 \cdot 10^{-5}$	100	2000	5 / 1
7	20000	$5.0 \cdot 10^{-5}$	100	500	4 / 1
8	40000	$2.5 \cdot 10^{-5}$	50	20	5 / 1
9	80000	$1.25 \cdot 10^{-5}$	50	10	5 / 1
10	160000	$6.25 \cdot 10^{-6}$	20	20	5 / 1
11	320000	$3.125 \cdot 10^{-6}$	10	10	5 / 1
12	640000	$1.5625 \cdot 10^{-6}$	3	5	4 / 1

development after introducing the pressure fluctuation.
The number of realizations is chosen to ensure an equal measuring time within each measuring period of the pressure fluctuation. The simulation procedure is schematically illustrated in figure 5.1. The initial calculation of the channel flow is needed to ensure an independent flow field at the start of the pressure fluctuation. The first cycle duration of the channel with fluctuating pressure is used to prevent artificial effects of the channel with a constant pressure gradient.

Table 5.2: Setup of the oscillating pressure simulations. T is the cycle duration, $A = \frac{1}{2}(\max(\nabla p) - \min(\nabla p))(\text{mean}(\nabla p)^{-1}$ the amplitude. The number of realizations is chosen to ensure an equal measuring time for a period for each simulation.

Re_τ	T	A	Realisations
1280	1600	0.2	125
1280	800	0.2	250
1280	400	0.2	500
1280	200	0.2	1000
1280	100	0.2	2000
1280	50	0.2	4000
1280	25	0.2	8000
1280	12.5	0.2	16000
1280	6.25	0.2	32000
1280	100	0.1	1000
1280	100	0.3	1000

Finally, table 5.3 summarizes the setup of the heated channel simulations. The setup is similar to the case of Kawamura et al. [42] with a forcing term for the passive scalar of $F_T = \frac{u}{\overline{u}_B}$ and zero boundary conditions, where u is the streamwise velocity and $\overline{u}_B$ the mean bulk velocity. First, simulations for $Re_\tau = 395$ with varying Prandtl number and $Pr = 0.71$ with varying Reynolds number are done to provide a direct comparison to the results from Kawamura et al. [42]. Second, further simulations are done to show the capability of ODT.

5.2 CHANNEL FLOW UP TO VERY HIGH REYNOLDS NUMBERS

Within the introduction to channel flow simulations 3.1 the need for simulations up to very high friction Reynolds numbers is discussed. Due to the one-dimensionality of ODT, the method provides the opportunity to simulate channel flows with a much higher Re_τ than is currently feasible for DNS. Furthermore, the adaptivity of aODT also reduces the computational cost compared to the equidistant calculation of BasicODT, which is the reason for the possibility to simulate channel flow cases up to a friction Reynolds number of about $6 \cdot 10^5$.

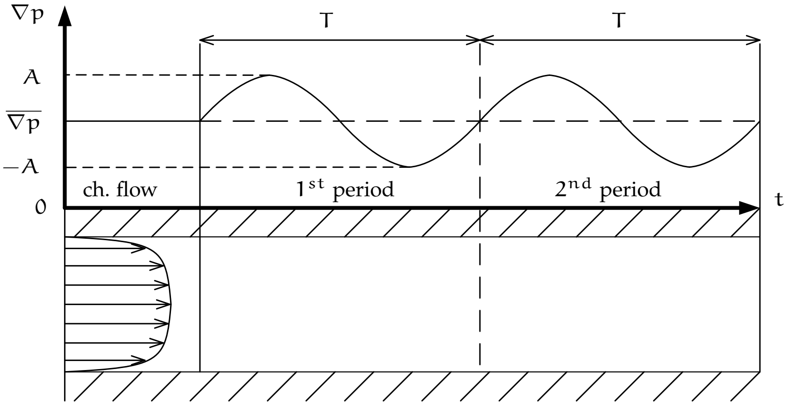

Figure 5.1: Schematic illustration of the simulation with a fluctuating pressure gradient. ∇p denotes the forcing pressure gradient, A the magnitude of the sinusoidal oscillation around the mean pressure gradient and T the cycle duration of the oscillation. The simulation starts from a fully developed flow profile with a simulation of a pure channel flow without oscillation for $\Delta t = \frac{1}{20}T$ to generate a random, fully developed profile. Afterwards, the channel flow with an oscillating pressure gradient is simulated for two periods, where the first one is used to overcome artifacts from the pure channel flow.

Table 5.3: Setup for simulations with a passive scalar. $\mathrm{Pr} = {}^{\nu}/_{a}$ is the Prandtl number, where a is the thermal diffusivity. td is a free adjustable factor determining the maximal number of CFL time steps between two diffusion steps. A detailed description of td is given in appendix C and in the BasicODT documentation [47]. The upper eight simulations are for comparison to DNS data, while the lower ones show the capability of ODT. ODT parameters are chosen to be $C = 10$, $Z = 600$, and $\alpha = {}^{2}/_{3}$

Re_τ	Pr	td	Re_τ	Pr	td
395	0.025	16	395	0.71	16
395	0.71	16	640	0.71	16
395	1.0	16	1020	0.71	16
395	10.0	16	1240	0.71	16
1280	0.025	16	1280	5.0	16
1280	0.2	16	1280	7.0	16
1280	0.71	16	1280	10.0	$16^2 \cdot 4$
1280	1.0	16	1280	20.0	16^3
1280	2.0	16	1280	50.0	$16^3 \cdot 4$

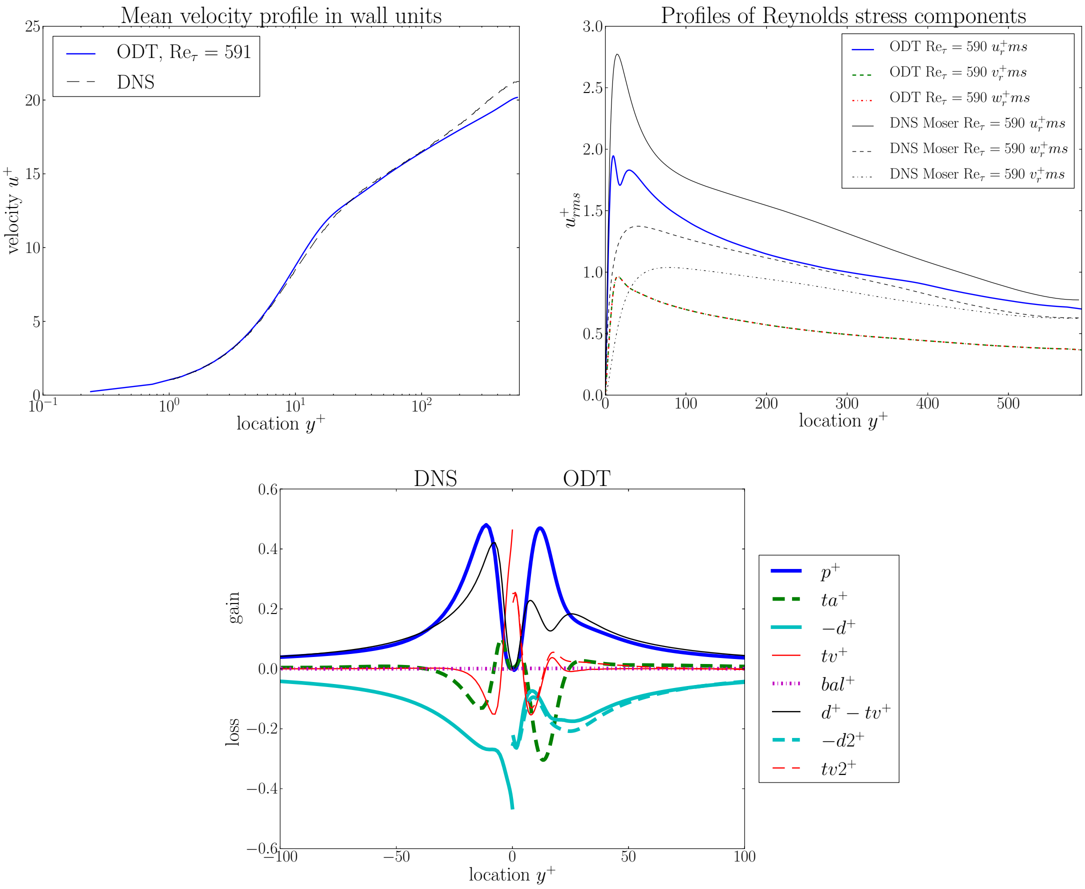

Figure 5.2: Comparison between ODT and DNS for $\mathrm{Re}_\tau = 590$. (i) The mean profile in wall units, (ii) the Reynolds stresses in wall units and (iii) the budget terms of the TKE. As described in the BasicODT documentation [47] and by Schulz et al. [5], within the data gathering of ODT there are two ways to calculate the dissipation and the viscous transport. Both methods are based on the calculation of the combined effect, also illustrated.

5.2.1 *Calibration of channel flow simulations*

Figure 5.2 shows the adjusted results for the channel flow with $\mathrm{Re}_\tau = 590$ and the comparison to the DNS results by Moser and Kim [68]. As already discussed by Kerstein [46], Schmidt et al. [84], and Lignell et al. [56], ODT reproduces the mean flow profile, the fluctuation velocity, and the budgets of the TKE in a meaningful way. Due to the fact that ODT is one-dimensional, it does not provide the capability to reproduce the outer buffer layer at the centerline, which is mainly affected by large scale 3D motions.

Schmidt et al. [84] have shown a reasonable fit even for the law of the wall containing the outer buffer layer for $\mathrm{Re}_\tau = 590$, but maintaining a good fit with increasing Reynolds number requires dependency of both ODT parameters on the friction Reynolds number. Within a channel flow simulation with ODT, there are four possible strategies for the choice of the ODT parameters: (i) to generate a reasonable fit of the viscous layer and a good match of the buffer and the *meso* layer, (ii) to generate a reasonable fit for the viscous layer, the buffer layer and of the constant κ due to a match of the constant region within the

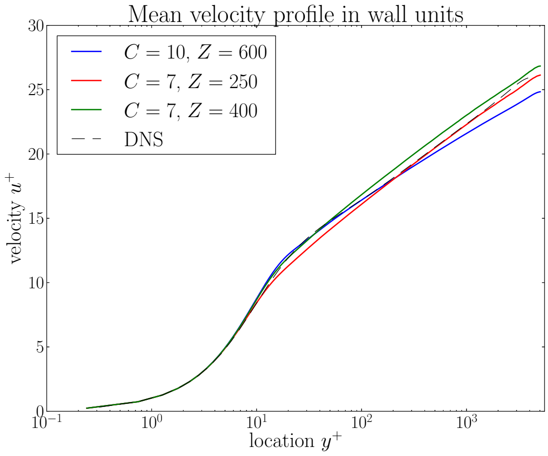

Figure 5.3: ODT modeling strategies for the law of the wall.

γ-plot (see below) resulting in an offset in the logarithmic region of the mean profile, (iii) to generate a reasonable fit of the viscous layer and the logarithmic layer resulting in differences in the buffer and the *meso* layer, or (iv) a reasonable over all fit of the full law of the wall including the outer buffer layer with slight deviations from the DNS. Within the mentioned publications, the first one was unknowingly chosen by fitting the DNS case for $\mathrm{Re}_\tau = 590$ due to interpreting the *meso* layer as the logarithmic part as described in section 3.1. One exception is presented by Schmidt et al. [84] as mentioned before, who have used the last strategie. The second one gives reasonable results with overestimation of the mean velocity within the logarithmic region. The third one instead underestimates the velocity in the buffer and *meso* layer as well as the outer buffer layer. The last possibility combines the second and the third one keeping their advantages and disadvantages. These strategies are illustrated in figure 5.3 except the last one, which could be estimated by eye. Depending on the case, one has to choose which feature has to be prioritized. Within this thesis the first one was chosen to be consistent to previous publications. Even if the results for the mean profile are getting worse for higher Reynolds numbers, the basic behavior could be analyzed. Furthermore, as can be seen in the figure, a change of the Z parameter has no effect to the logarithmic region. Instead it just influences the point of change from the linear region towards the logarithmic one.

As shown in the above-mentioned publications, ODT additionally underestimates the mean fluctuation velocity. In contrast to DNS, the velocities within ODT, with the exception of the mean flow direction, are not physical properties, instead are treated as energy storage containers. Therefore, by construction of the triplet maps and the corresponding treatment of energy conservation there is no difference between the wall normal and the spanwise velocity. This symmetry is broken, if there is a source within one of these directions or the boundary conditions differ from each other. Finally, the budget terms compare well to the results of the DNS.

Within ODT, the calculation of the dissipation and the viscous trans-

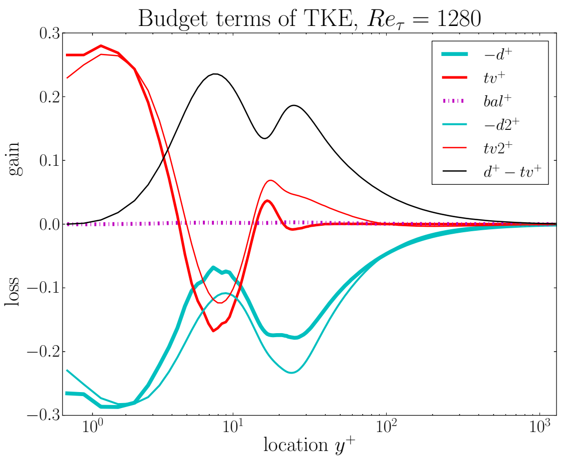

Figure 5.4: Calculation alternatives for dissipation and viscous transport for $\mathrm{Re}_\tau = 1280$. d^+ and tv^+ show the results for the first alternative with a direct calculation of tv. The second alternative with direct calculation of the dissipation using equation (5.2) is shown by $d2^+$ and $tv2^+$. $d^+ - tv^+$ shows the combined effect, which is equal to $p^+ + ta^+$ for a statistically stationary channel flow.

port are based on the gathering of the combined effect of both. One of them is than calculated directly, while the other is based on the combined effect. For example, as it is implemented in BasicODT [47], the viscous transport is calculated via the second derivative of the TKE, while the dissipation is calculated as the combined effect minus the viscous transport. The alternative way is based on a direct calculation of the dissipation using

$$d = \overline{\left(\frac{\partial u_i'}{\partial y}\right)^2} = \overline{\left(\frac{\partial u_i}{\partial y}\right)^2} - \left(\frac{\partial \overline{u}_i}{\partial y}\right)^2 \tag{5.2}$$

as presented by Schulz et al. [5]. The results of both methods are shown in figure 5.4 with slight differences. For higher Reynolds numbers or shorter simulation times, the method based on a direct calculation of the dissipation is more robust. The reason is that the calculation of the dissipation is based on first derivatives, while the direct calculation of the viscous transport is based on a second derivative, which is more sensitive to slight fluctuations. With increasing Reynolds number, the direct calculation of the viscous transport shows high frequency fluctuations, especially at the wall. Nevertheless, if the calculation time is long enough to get rid of these fluctuations, the method with a direct calculation of the viscous transport is preferable, due to slightly better results. A direct calculation of both budgets is also possible but results in a slight deviation from budget balance. A full discussion of the differences of the budgets and their interpretation is given by Kerstein et al. [48], the BasicODT documentation, and Schulz et al. [5].

5.2.2 *Mean velocity profiles at high Reynolds numbers*

Based on these results and a calibration of the ODT parameters to the DNS results of Moser and Kim [68] for $\mathrm{Re}_\tau = 590$, an exten-

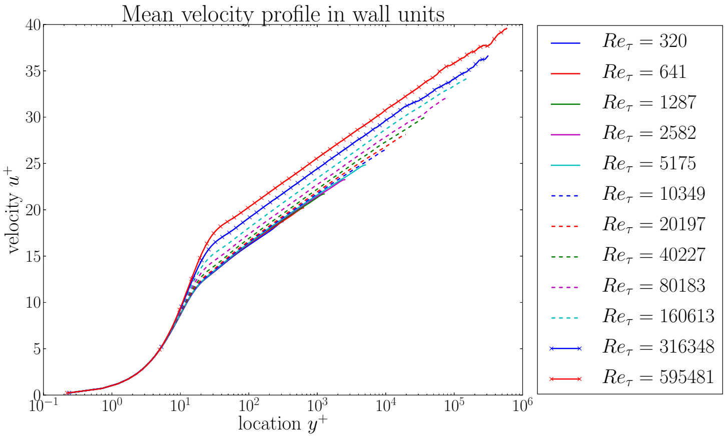

Figure 5.5: Law of the wall up to $\mathrm{Re}_\tau = 6 * 10^5$

sion to higher friction Reynolds numbers is performed. The calibration was tested against a DNS by Lozano-Durán and Jiménez [59] for $\mathrm{Re}_\tau = 4200$ and shows a good comparison (see figure 5.3 blue line).
Figure 5.5 shows the comparison of the law of the wall for all different Reynolds numbers. As it can be seen, the logarithmic region is extended while the viscous sublayer stays constant. With increasing Reynolds number, a shift of the logarithmic region to higher velocities is seen, which is not found in the pipe flow measurements by McKean et al. [63] up to $\mathrm{Re}_\tau = 3 * 10^6$. As explained by Schmidt et al. [84], the ODT model parameter Z directly influences the start of the buffer layer and therefore the y-intercept c of the formulation of the logarithmic region (3.3). This indicates a slight dependency of the parameter Z on the friction Reynolds number.
Figure 5.6 shows the comparison of the ODT results to the theories of a logarithmic law (plot for γ) and a power law (plot for β) as explained by Moser et al. [68]. The first one would show a constant line if the mean flow profile would have a logarithmic region, which isn't seen in this plot for the lower Reynolds number cases. Taking the idea of a leading order logarithmic region as discussed by Panton [73], a Karman constant of about 0.44 could be estimated which is much higher than the value of 0.37 mentioned in section 3.1. For $\mathrm{Re}_\tau \geqslant 2 \cdot 10^4$, this logarithmic region is seen for $y^+ \geqslant 200$, which follows the discussion of Marusic et al. [62] who have concluded from several publications a start for the logarithmic region of $100 \leqslant y^+ \leqslant 600$ with a focus on $200 \leqslant y^+ \leqslant 300$. As explained above, there are several possibilities to choose the ODT parameters so that it is in principle possible to match the Karman constant. This would lead to a good match of the logarithmic region but would also result in a greater discrepancy for the inner buffer layer.
The plot comparing to the power law instead doesn't show a constant region. Also a decreasing line could be estimated for each case, but varies with increasing Reynolds number.

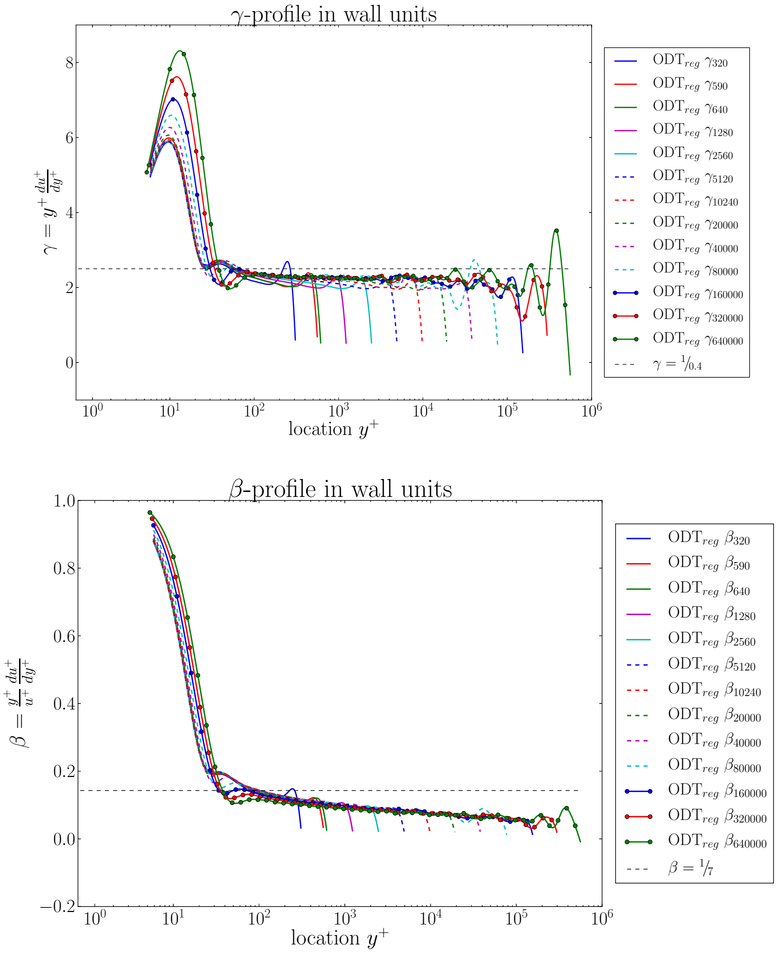

Figure 5.6: Comparison plots for (i) a logarithmic region and (ii) a power law region for the law of the wall. The index `reg` indicates a regression of the based data to get rid of fluctuations due to a too short measuring time.

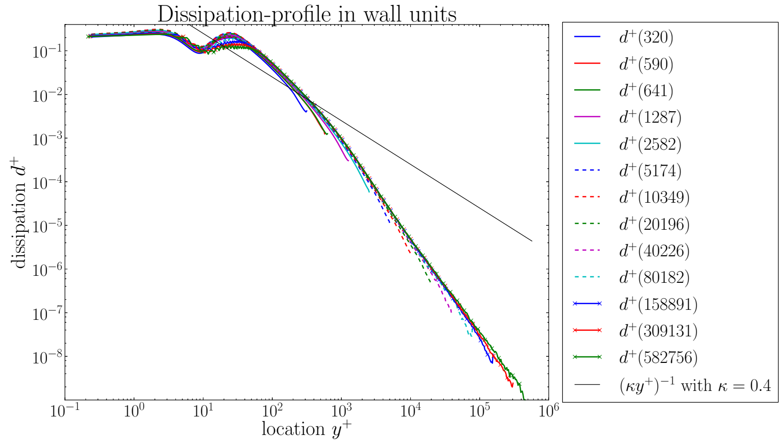

Figure 5.7: Dissipation profiles in wall units up to high Reynolds numbers

5.2.3 *Dissipation profile at high Reynolds numbers*

Another comparison quantity for high Reynolds number simulations is the dimensionless dissipation. As shown by Kaneda et al. [41] for channel flow DNS up to $\mathrm{Re}_\tau = 5120$, the decay of the dissipation for $y^+ > 30$ follows $d^+ = (\kappa y^+)^{-1}$. On the one hand, this plot provides the opportunity to estimate the Kármán constant and, on the other hand, shows that the dissipation converges for higher Reynolds numbers. The corresponding plot is shown in figure 5.7, indicating an overestimation of the dissipation in the region $15 \leqslant y^+ \leqslant 200$ and an underestimation for $y^+ > 200$. Furthermore, the decay is proportional to $d^+ \sim (\kappa y^+)^{-2.1}$, resulting in a much faster decay of the dissipation towards the centerline as expected from DNS. Nevertheless, this plot shows a good convergence for high friction Reynolds numbers.

The faster decay could be a result of the missing 3D information. Especially at the centerline, the 3D effect of large scale eddies, which communicate in the streamwise and the cross-streamwise directions, is neglected by the model resulting in an underestimation of (i) the fluctuation velocity and (ii) the dissipation.

Figure 5.8 shows the production, the dissipation and the turbulent advection in the same way as in the comparison plot for the dissipation. It can be seen that the production follows in a wide y^+ range the decay of $(\kappa y^+)^{-1}$ as known from DNSs. Within the DNS, the counterpart to the production is given by the dissipation, but this is not seen in ODT as mentioned above. This implies that some other term is the counterpart to the production. As can be seen, the production is neutralized by the turbulent advection.

This comparison shows that ODT underestimates the dissipation. The dissipation is mainly driven by steep gradients which are produced due to the mapping process. The underestimation of the dissipation could be decreased by changing the mapping process itself. Possible changes are to replace the triplet map by a quintiplet map or twice-applied triplet map. The first one follows the same idea as the triplet map but instead of using three compressed copies five ones are used where the second and fourth copy are reversed. The latter idea keeps the sampled eddy and uses this eddy as a new candidate for implementation. If it is again excepted a similar behavior as given by nine copies is produced. Both methods could increase the dissipation by steepening up the gradients. Even if the ideas behind these changes are reasonable, tests show that both methods give comparable results as the triplet map showing that this behavior is caused by the one dimensionality of ODT.

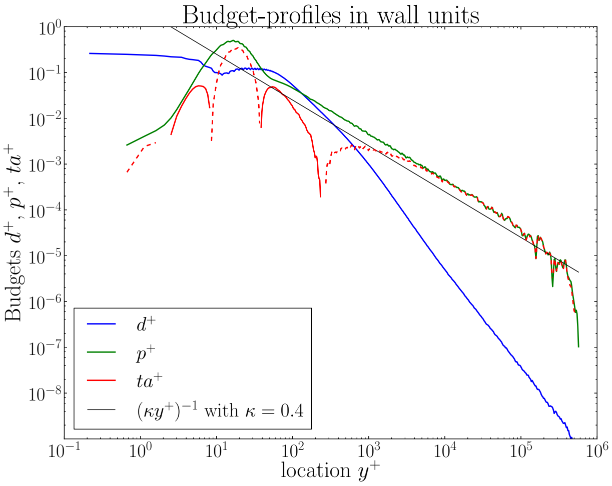

Figure 5.8: Comparison of budgets at $\mathrm{Re}_\tau = 640,000$. The dashed line parts of the turbulent advection are the negative parts of the profile.

5.2.4 *The diagnostic plots for channel flow results*

Figure 5.9 shows both versions of the diagnostic plot from Alfredsson et al. [8] for channel flow DNSs[2], where the data is normalized by the centerline velocity u_∞ in contrast to the original normalization by the free stream velocity which isn't defined in channel flow. Also included is the approximation for TBLs by Alfredsson and an adjusted version. These approximations show that the channel flow also converges for the outer scaling showing a similar tendency as the TBL but with slightly different values. The channel flow corresponding parameters of the parabola $\frac{u_{\mathrm{RMS}}}{u_\infty} = a\frac{\overline{u}}{u_\infty}$ are $a = 0.048$ and $b = 0.26$, resulting in a maximum of $\max\left(\frac{u_{\mathrm{RMS}}}{u_\infty}\right) = 0.0912$ and a position of $\left(\frac{\overline{u}}{u_\infty}\right)_{u,\max} = 0.592 = G$. Comparison to the results for TBLs and pipe flows, $G_{\mathrm{TBL}} = 0.56$ and $G_{\mathrm{pipe}} = 0.52$ respectively, emphasizes the channel flow as the best test case for research of the outer peak. Additionally, the higher maximum also benefits the study in that the outer peak arises for $\mathrm{Re}_\tau \approx 5000$ for the channel flow, while the same behavior for TBLs is first seen at $\mathrm{Re}_\tau \approx 10^4$ (Results from Alfredsson et al. [8]).

The ODT representation of the diagnostic plots are shown in figure 5.10. Again the underestimation of the fluctuation velocity can be seen. Furthermore, in contrast to the DNS results, the tails of the outer scaling neither converge to each other nor show a parabolic behavior. Instead a linear decrease from approximately the second hill[3], which is an ODT specific one discussed by Lignell et al. [56], up to $\frac{\overline{u}}{u_\infty} = 0.95$ can be seen. This is also represented in the second plot by a scaling pro-

---

[2] Online available databases for the following publications are used: Hoyas and Jiménez [34], Jiménez and Hoyas [38], Hoyas and Jiménez [33], del Álamo et al. [21], del Álamo and Jiménez [19, 20], and Moser et al. [68]

[3] The second hill is generated by the forced alignment of near-wall eddies by the wall, wherefore the largest fluctuations occurring at $\frac{1}{3}l$ and $\frac{2}{3}l$ are superposed for the smallest eddies.

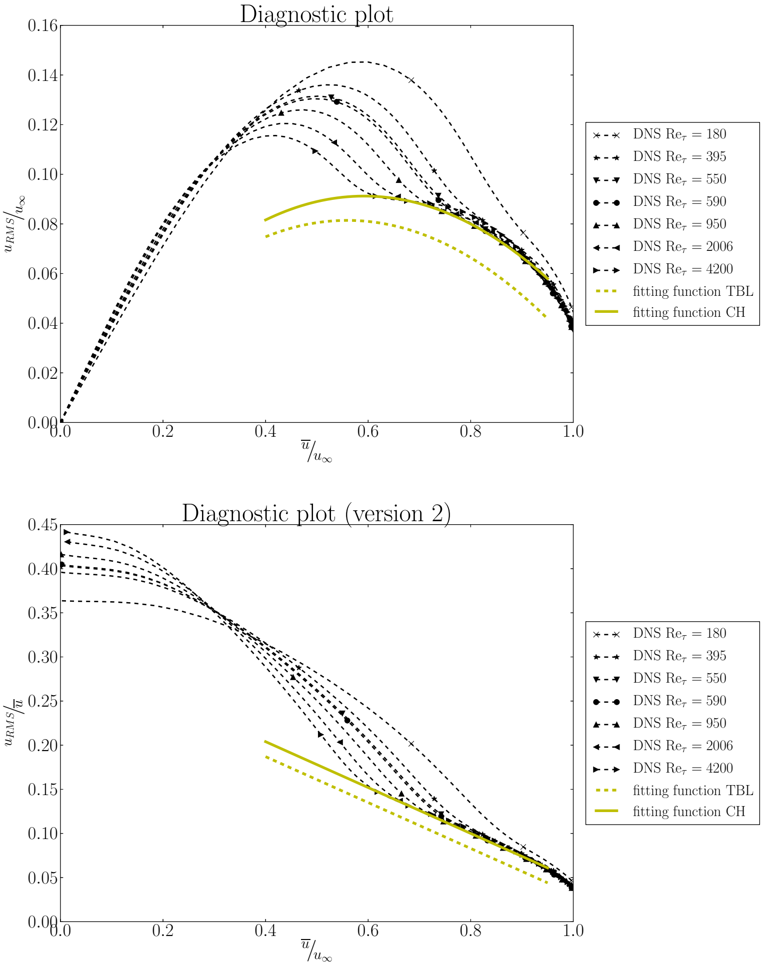

Figure 5.9: Diagnostic plots of channel flow DNS data. The DNS data are from Hoyas and Jiménez [34], Jiménez and Hoyas [38], Hoyas and Jiménez [33], del Álamo et al. [21], del Álamo and Jiménez [19, 20], and Moser et al. [68]

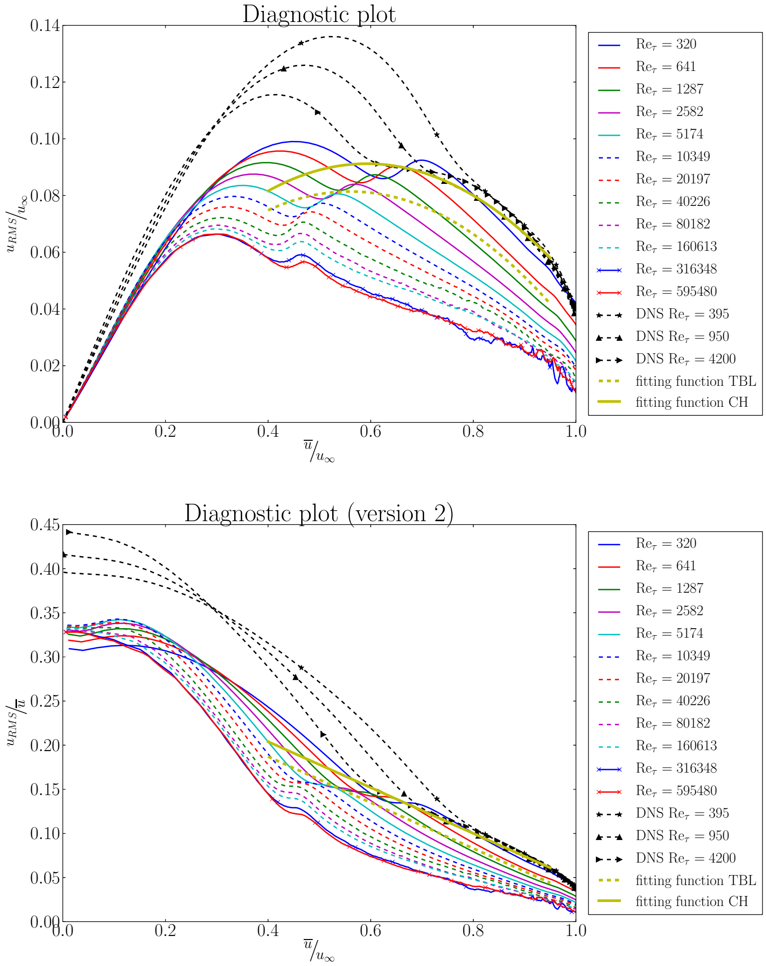

Figure 5.10: Diagnostic plots of channel flow ODT and DNS data

portional to $\frac{u_\infty}{\bar{u}}$. The absence of the outer scaling indicates that ODT doesn't represent the large scale motions in a meaningful way. This isn't surprising, because the large scale motions contain 3D information and interactions with streamwise and spanwise separated fluid elements which are not represented in the 1D formulation of ODT. Within ODT, these large scale eddies are sparse and they are modeled via the mapping process like all other eddies with no interaction with the surrounding flow field, which is an unrealistic assumption. Nevertheless, ODT is currently the only turbulence model to reach such high Reynolds numbers without modeling the smallest scales. New developments based on the first publications of Schmidt et al. [84] (large eddy simulation with ODT as a sub-grid-scale model (LESODT)) and Gonzalez-Juez et al. [31] (one-dimensional turbulence with a 3D coupling (ODTLES)) are intended to overcome these shortcomings of ODT. Further investigations of ODTLES are done e. g. by Schmidt et al. [85] and Glawe et al. [1][30].

5.3 STATISTICS OF THE WALL SHEAR STRESS

New industrial developments create the need for information about more and more details of turbulent flows. One part is the fluctuation of the wall shear stress and its behavior with increasing Reynolds number. The current results are summarized in the publications by Örlü and Schlatter [71] and Keirsbulck et al. [43, 44]. Örlü and Schlatter compare the RMS value of the normalized wall shear stress, discuss discrepancies between different DNS and measurements of TBLs, and show comparisons of the PDF of the normalized wall shear stress for different Reynolds numbers. Keirsbulck's group instead discusses further statistical properties and the Reynolds dependency of wall shear stress.

Figure 5.11 shows the results of ODT for the simulations listed in table 5.1. As expected from measurements by Keirsbulck et al. [43], the results show a slight increase up to a maximum of about 0.327 while the analysis by Keirsbulck gives a theoretical maximum of 0.432, also represented by the fit $\tau^+_{W,RMS} = 0.432 - \frac{11}{Re_\tau}$ of the DNS data. The shifted ODT results show a good comparison to the theoretical curve in the range of $600 \leqslant Re_\tau \leqslant 2 \cdot 10^4$. The discrepancy at the lower and upper end of the Reynolds numbers range as well as the shift can be explained by ODT itself. The lower one is the result of the formulation of ODT, which is constructed for highly turbulent flows and therefore overestimates the fluctuations at the wall. The upper discrepancy instead is the result of the too short simulation time, which results in an underestimation of large eddies. More accurate results would be calculated by using the turnover time of the largest possible eddy as an estimation for the averaging time instead of the described simulation time based on the number of accepted eddies as described in section 5.1. The underestimated, large eddies would increase or decrease the velocity at the walls and therefore would raise the upper and lower tail of the PDF. The shift of the curve can be explained by

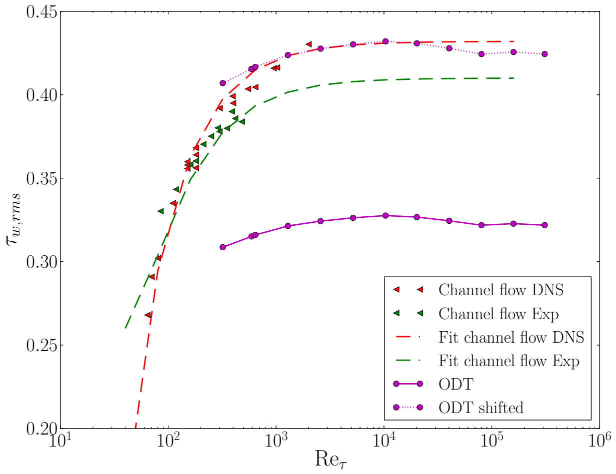

Figure 5.11: $\tau_{W,\mathrm{RMS}}$ as function of the friction Reynolds number. The ODT results are shifted to match the theoretical maximum from the analysis of Keirsbulck et al. [43]. The fitted curves from Keirsbulck follow $0.432 - \frac{11}{\mathrm{Re}_\tau}$ and $0.41 - \frac{11}{\mathrm{Re}_\tau} + \frac{200}{\mathrm{Re}_\tau^2}$ for the channel flow DNS results and measurements respectively.

the absence of 3D information of large flow structures, which would also generate negative wall shear stresses due to local flow reversals or more probably high stresses due to local flow accelerations.

Figure 5.12 shows the PDF of the wall shear stress for different friction Reynolds numbers. The ODT results are scaled to match the maximum of the DNS. As can be seen, ODT underestimates the PDF for higher wall shear stresses in the range $1 \leqslant \tau_W \leqslant 2.5$. This is the result of missing the acceleration due to large 3D motions. Also seen is the total absence of the negative part and the underestimation of the lower region of τ_W. This is also caused by neglecting 3D large scale motions which in this case cause flow reversal or deceleration of the flow.

Also seen is the tendency of a slight increase of the tails of the PDF with increasing Re_τ as explained by Örlü and Schlatter [71]. A deviation from this trend is seen for $\mathrm{Re}_\tau \geqslant 4 \cdot 10^4$ which was explained before.

5.4 INFLUENCE OF AN OSCILLATING FORCING PRESSURE GRADIENT

This section summarizes the results for the simulations of the channel flow with an oscillating forcing pressure gradient. The aim of these simulations is to influence the PDF of the wall shear stress. The setup of the simulations is described in section 5.1. Due to the lag of comparison DNS cases, another simulation with a sudden increase of the pressure gradient following the description of He and Seddighi [32] was also done and will be described first.

The setup is similar to the simulation of an oscillating pressure gradient, stating with a pure channel flow at $\mathrm{Re}_\tau = 320$ and simulating for a period ΔT, saving the instantaneous profile as the new starting

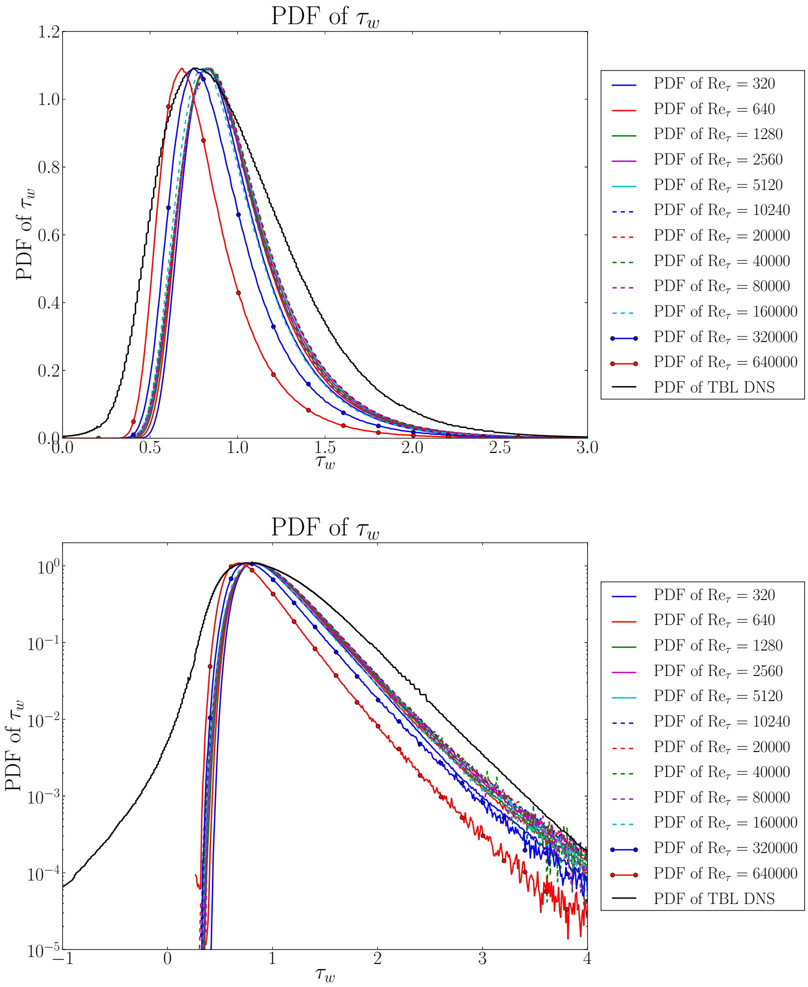

Figure 5.12: PDF of τ_W for different Re_τ. ODT results are individually scaled to match the maximum of the DNS results. The mean scaling factor is 0.658.

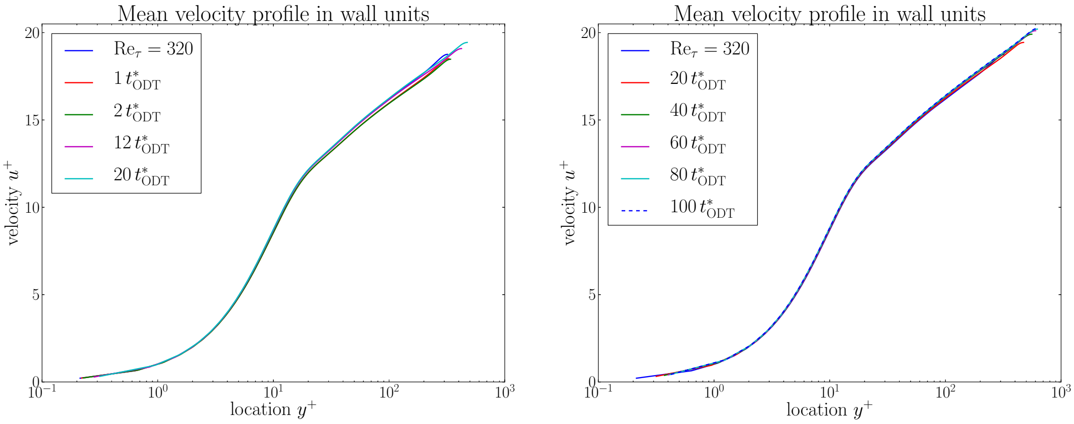

Figure 5.13: Mean profiles in a transient channel flow from a fully developed state at $\mathrm{Re}_\tau = 320$ up to $\mathrm{Re}_\tau = 640$. Left, detailed view to the first $20\,t^*_{\mathrm{ODT}}$, with $t^*_{\mathrm{ODT}} = 0.2s$ resulting in factor $\frac{0.2s}{t^*_{\mathrm{He}}} \approx 7$. Right, law of the wall at specific time steps.

profile for the next realization. After saving, the pressure gradient is increased by four which is the corresponding one for a doubled Reynolds number. The simulation resumes until a full developed channel flow with $\mathrm{Re}_\tau = 640$ has been reached. Afterwards, the next realization starts form the saved instantaneous profile calculating the pure channel flow at the lower Reynolds number.

Figure 5.13 shows the results for the law of the wall at certain times in the transient flow. Here t^*_{ODT} is 0.2s resulting in a factor $\frac{t^*_{\mathrm{ODT}}}{t^*_{\mathrm{He}}} \approx 7$, which is consistent with the mentioned order unity in section 5.1. As can be seen for the curve $1\,t^*_{\mathrm{ODT}}$, the sudden increase of the pressure gradient results in a decrease of the logarithmic region. This is reasonable due to the lag of information transport to the wall, wherefore within the viscous region the wall shear stress increases faster than the flow is accelerated at the centerline resulting in a decrease of u^+ in the center region not directly coupled to the wall. This effect is also seen by He and Seddighi [32] but to a greater degree. Up to $20\,t^*_{\mathrm{ODT}}$ the deviation from the ideal law of the wall vanishes and the flow shows profiles comparable to the law of the wall profiles for different Reynolds numbers. The same behavior can be seen for all profiles up to the final fully developed profile. This contradicts the results from He and Seddighi who have identified three different stages of development of the channel flow with increasing Reynolds number. In contrast to the DNS, ODT doesn't have the capability to simulate 3D structure present in the transient channel flow.

This shows that ODT does not capture all effects present in the transient channel flow, which isn't surprising due to the fact that He and Seddighi identified similar behavior as found in the transition of a channel from a laminar to a turbulent flow, which cannot be captured by ODT. For ODT a much better comparison case would be the transition at higher Reynolds numbers where the flow is fully turbulent without similarities to a laminar flow as is the case for $\mathrm{Re}_\tau = 180$ which is not the common range of application of ODT.

Nevertheless, it is noticeable that ODT gives a transition time within a factor of 7.

A more realistic case is the channel flow with a fluctuating pressure gradient. In contrast to the He and Seddighi case, in which the pressure gradient increases by a factor of 5.2, for the following case the pressure gradient has a continuous change with an amplitude of maximal $A = 0.3$ resulting in a change of the friction Reynolds number in the range $[0.87 \cdot Re_\tau; 1.2 \cdot Re_\tau]$.

Figures 5.14 and 5.15 show the PDFs of τ_W for a cycle time of $T = 25s$ and $T = 400s$, respectively. It can be seen that for increasing pressure gradient, the maximum of the PDF is decreasing and the PDF itself is broadening. This is reasonable due to the acceleration of the flow, especially at the wall, and therefore an increase of the probability of higher τ_W. For decreasing pressure gradient, the PDF is getting narrower and the maximum is increasing, which is the result of the deceleration of the flow, resulting in a higher probability of small flow gradients at the wall. Furthermore, it can be seen that for higher cycle durations, this effect is stronger due to a better capability of the flow to react to the change of the pressure gradient.

The described effects are also seen in the figures 5.16. For a cycle duration of $T = 25s$, the mean PDF of the simulation is the same as that of the channel flow without oscillation, resulting in no effect on the mean properties of the PDF. In contrast, the mean PDF of the higher cycle duration simulation shows a significant difference. The most probable values $(0.75 \leqslant \tau_W \leqslant 1.25)$ are decreased while the lower values $(0.4 \leqslant \tau_W \leqslant 0.75)$ become more probable. There is also a slight increase for values higher than $\tau_W = 1.25$. This indicates that the RMS value of τ_W is increasing while the mean value remains constant.

The comparison of the two illustrations of the PDFs for different periods within the simulation shows that, while for $T = 400s$ the extrema of the sinusoidal response are represented by the PDF of the corresponding periods, the PDFs of $T = 25s$ are not sorted in the same manner. This suggests a time shift in the sinusoidal response of the PDF of τ_W.

The time shifts are summarized in table 5.4. As already estimated from the PDF for $T = 400s$, the shift is nearly zero. Meaning that the flow has enough time to react to the oscillation of the pressure gradient. Due to this fact, the bounding PDFs of $T = 400s$ within figure 5.16 are the boundaries for modification of the PDFs due to an oscillating pressure. This is supported by the simulations with $T = 800s$ and $T = 1600s$, which give the same results, and can be explained by the results for the PDF of τ_W for different friction Reynolds numbers shown in figure 5.12. If the cycle duration is further increased, the flow has more time to react to a change of the pressure gradient. This

Table 5.4: Time shift of sine function response of the τ_W statistic for an oscillating pressure gradient

T in [s]	6.25	12.5	25	50	100	200	400	800	1600
$20\,\frac{\Delta t}{T}$	3.9	3.75	3.4	2.45	1.45	0.6	0.05	−0.15	−0.3

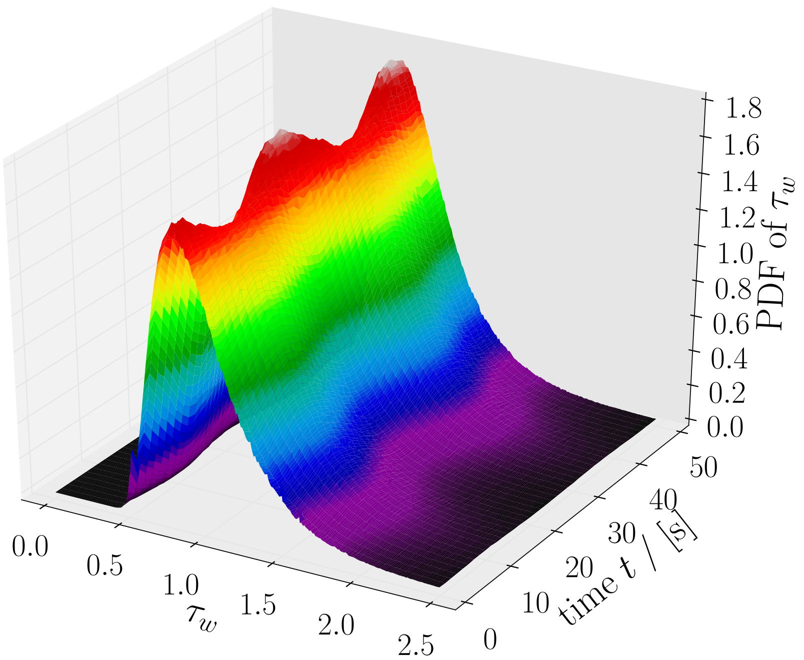

Figure 5.14: 3D-PDF plot of τ_W for $T = 25s$ within a channel flow with $Re_\tau = 1280$.

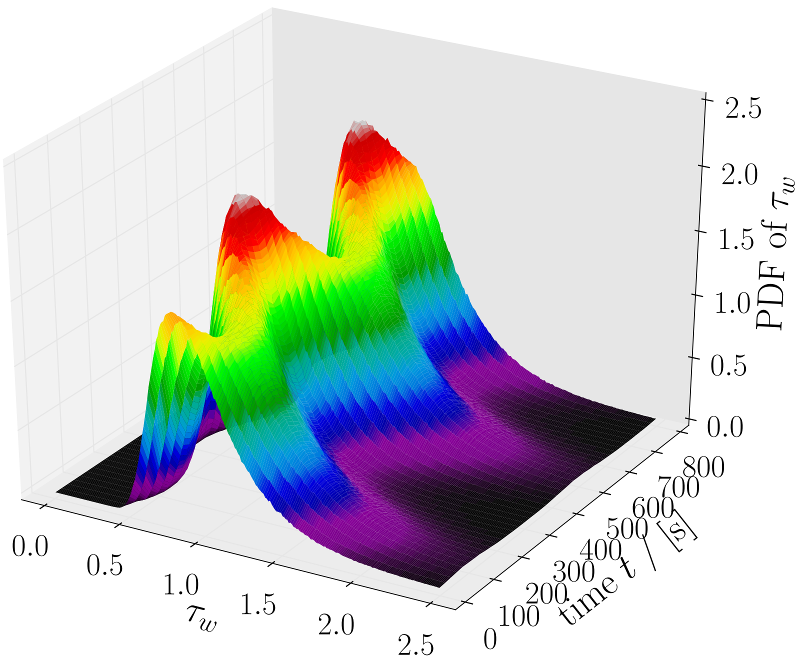

Figure 5.15: 3D-PDF plot of τ_W for $T = 400s$ within a channel flow with $Re_\tau = 1280$.

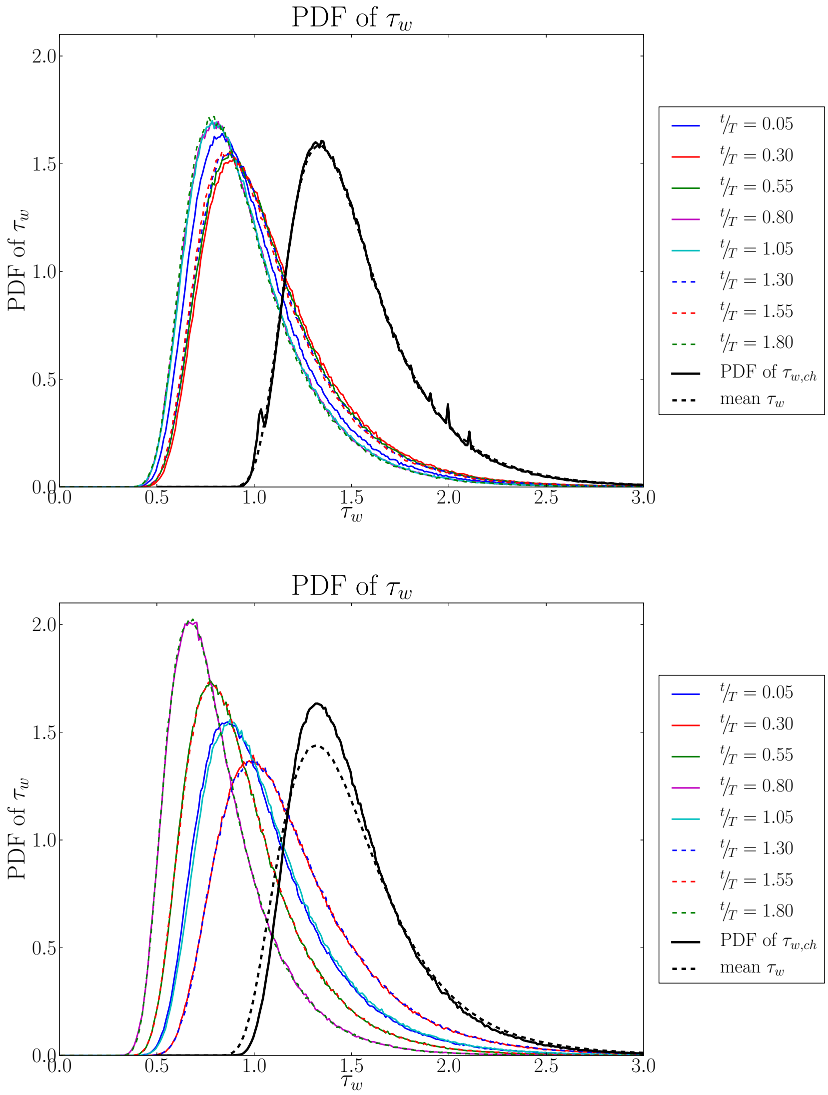

Figure 5.16: PDF of τ_W for $T = 25$s and $T = 400$s. The mean PDF and the PDF of the channel flow are shifted by $\Delta\tau_W = 0.5$. The peaks in the $\tau_{W,ch}$ profile of the upper figure are artifacts of a too short measuring time for the channel flow, resulting in too much sensitivity to the starting profile.

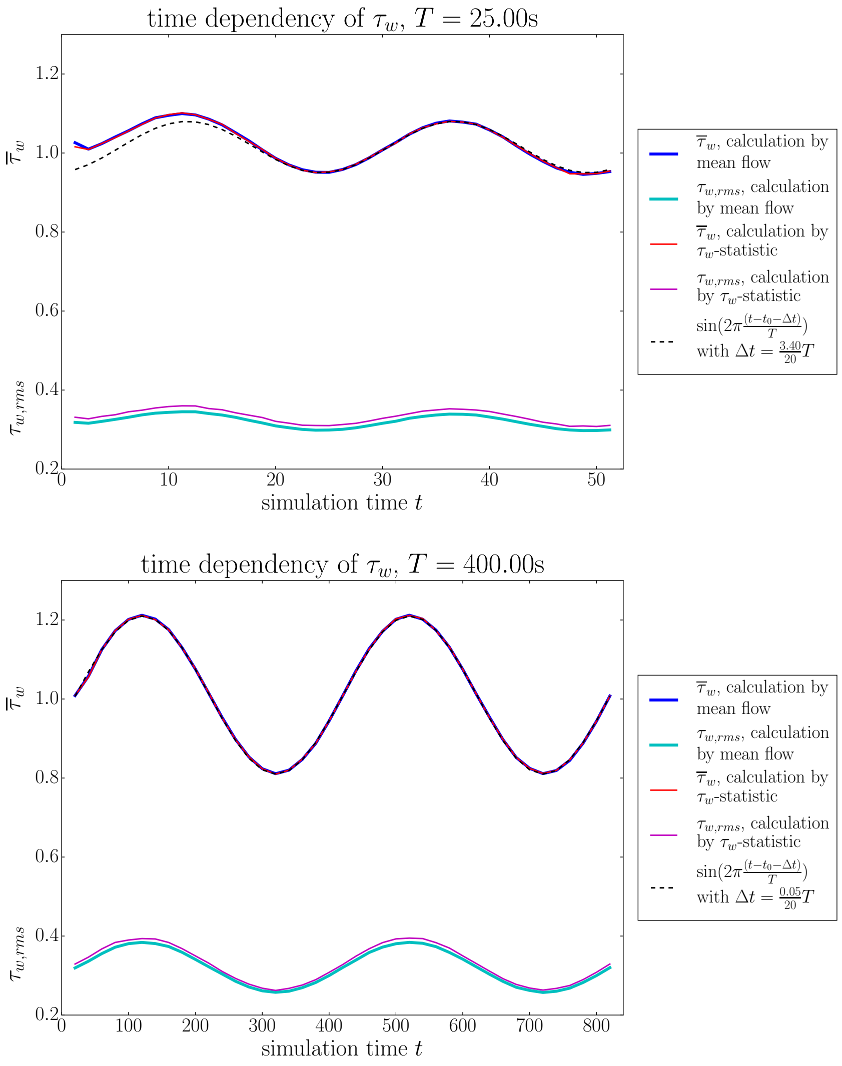

Figure 5.17: Time dependency of $\overline{\tau}_W$ and $\tau_{W,RMS}$ for $T = 25s$ and $T = 400s$. Also included is a sine function to illustrate the time shift of the response of τ_W to the oscillating pressure.

results first in a similar behavior as for $T = 400s$, and later on in an equivalent effect as for increasing or decreasing the friction Reynolds number. The negative time shift presented in table 5.4 for $T = 800s$ and $T = 1600s$ is an effect of the chosen measuring period length. For an increased number of measuring periods per cycle duration, this shift tends to zero.

Within figure 5.17, the mean and the RMS value of the wall shear friction are shown. Additionally, a fitted sine curve to show the time shift is also included. For both of the values shown, two methods for the calculation are compared. First, the mean wall shear stress is calculated via derivative of the mean flow at the wall, where the mean flow profile is calculated as the time average over the period and an ensemble average over the realizations. The second calculation method is based on the PDF of τ_W gathered during each period and over all realizations. It can be seen that both methods show the same results as expected.

The RMS values are also calculated (i) by the mean flow following the

definition in equation (3.6) and (ii) from the PDF. In contrast to the mean value of τ_W, the RMS values show a difference between the two calculation methods. This difference is also seen for a pure channel flow simulation. It could be the result of the calculation of $\tau_{W,RMS}$ following equation (3.6), because the calculation is done for the nearest point to the wall rather than as the limit value at the wall. One interesting fact is that for higher cycle durations the difference is decreasing in regions where the flow is slowed down by a decrease of the forcing pressure gradient.
A variation of the magnitude at $T = 100$s shows similar modifications of the PDF as given by an increase of the cycle duration. This is shown in figure 5.18 for three different magnitudes $A \in (0.1;\ 0.2;\ 0.3)$. In contrast to the variation of the cycle duration it is not bounded by the PDFs given by figure 5.16 for $T = 400$s. Furthermore, the time shift stays constant and only the magnitude of the oscillation of $\overline{\tau}_W$ is increased as expected. This provides the opportunity to replace a simulation with a specific cycle duration by another one with a different T and an adjusted magnitude of the fluctuation as indicated by the cases with (i) $T = 25$s and $A = 0.2$ and (ii) $T = 100$s and $A = 0.1$.

5.5 HEATED CHANNEL FLOW WITH A LARGE VARIATION OF PRANDTL NUMBER

Up to now, only results with a focus on the velocity and the turbulence within the flow of the channel are presented. But this is only one part of the industrially interesting channel flow. Another one is the behavior of a passive scalar within a turbulent flow, i. e. the temperature for heat absorption at the wall or an impurity for separation. Even if the temperature directly influences the density and the viscosity of the flow, it is often treated as a passive scalar. Therefore, this section concludes the results for the behavior of a passive scalar. The performed simulations are summarized in table 5.3.
Figure 5.19 shows the results of the simulations varying the Reynolds number and keeping the Prandtl number constant at $Pr = 0.71$. As was expected from the results of the channel flow for high Re_τ from section 5.2, the mean velocity profile is reproduced with deviations at the outer buffer layer. As good as the velocity profiles are, the mean temperature profiles show a deviation in the slope of the logarithmic region.
To study the dependency of the slope of the logarithmic region on the forcing term of the passive scalar and the parameter α, five additional cases are done as summarized in table 5.5. The results are shown in figure 5.20. As expected, case F shows the same results for the u-velocity and the passive scalar T, due to identical simulation. Cases C and D show the effect of changing (i) the right hand side function of T and (ii) the parameter α respectively. For case C the slope of the logarithmic region of T is increasing, while the profile of u^+ stays constant. This is the result of a non-uniform forcing, which is greater than unity in the center of the flow and tends to zero at the wall. In

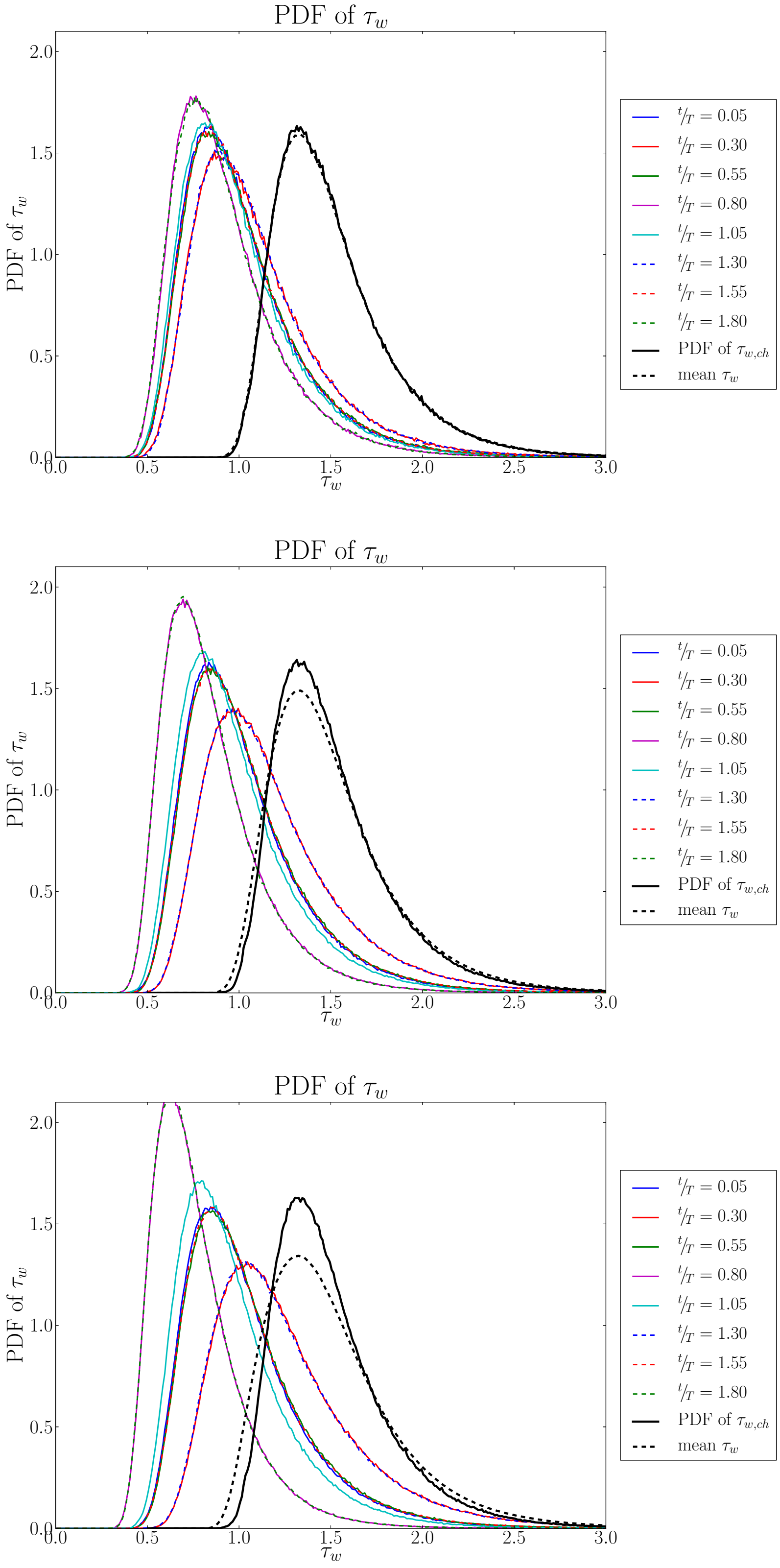

Figure 5.18: PDF of τ_W for $T = 100s$ and $A \in (0.1;\ 0.2;\ 0.3)$. The mean PDF and the PDF of the channel flow are shifted by $\Delta\tau_W = 0.5$. The profile for $A = 0.1$ shows nearly the same results as the one given in figure 5.16 for $T = 20s$.

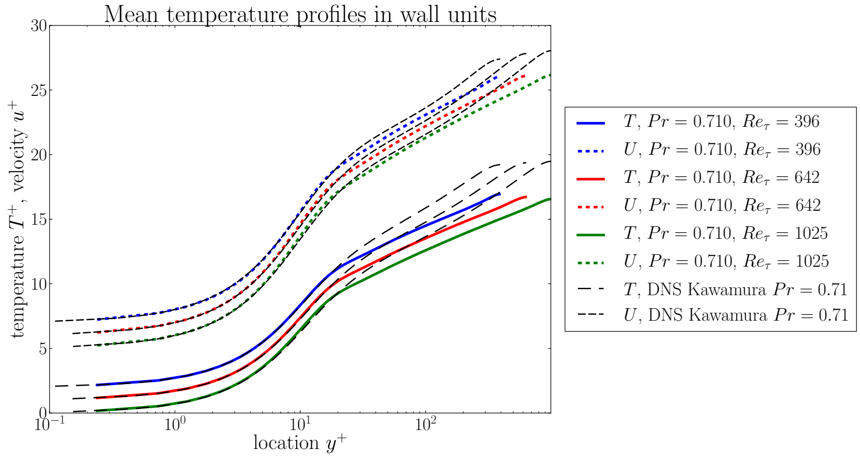

Figure 5.19: Law of the wall of a passive scalar with $\mathrm{Pr} = 0.71$ compared to DNS results by Kawamura et al. [42]. The velocity profiles are shifted by +5. For better comparison, the cases for $\mathrm{Re}_\tau = 395$ and 640 are also shifted by +2 and +1, respectively.

Table 5.5: Setup for additional simulations with a passive scalar. The first case A is the same as mentioned in table 5.3. The additional cases are mentioned below the line. *Forcing* describes whether the right hand side term of the passive scalar equation is as described by Kawamura et al. [42], or whether it is equal to the pressure gradient within the momentum equation. α is the ODT parameter describing the redistribution of energy among the velocity components.

Case	Re_τ	Pr	Forcing	α
A	1280	1.0	$^{u}/_{\bar{u}_B}$	$^2/_3$
B	1280	1.0	$^{u}/_{\bar{u}_B}$	$^1/_3$
C	1280	1.0	$^{u}/_{\bar{u}_B}$	0
D	1280	1.0	1	$^2/_3$
E	1280	1.0	1	$^1/_3$
F	1280	1.0	1	0

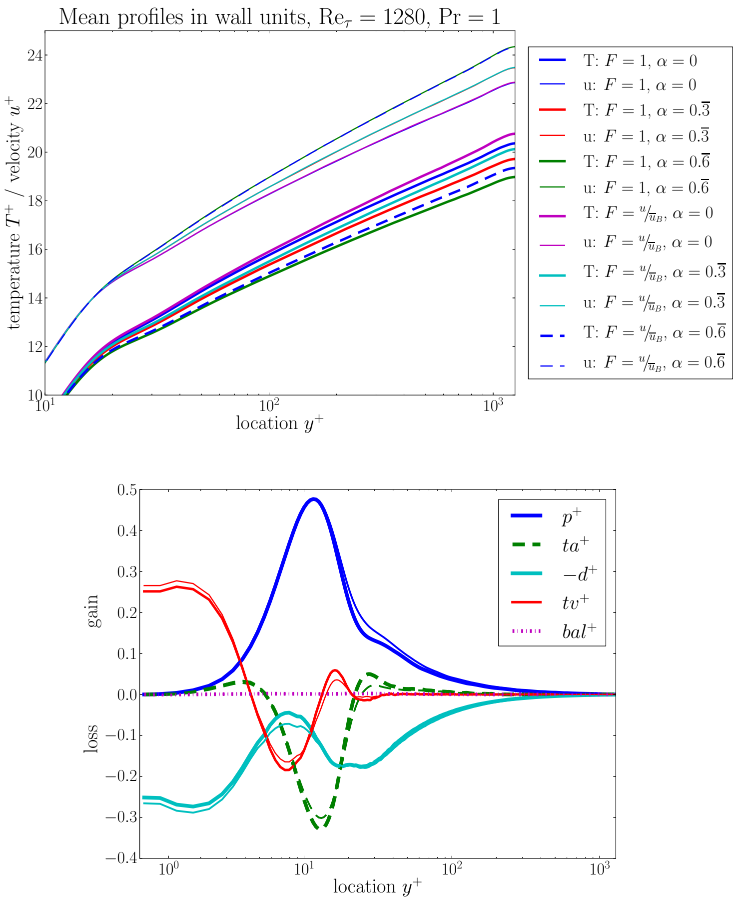

Figure 5.20: The upper figure shows the logarithmic region of the ODT profile for the velocity and the passive scalar. The curves for the velocity are shifted by 2.5. The lower figure shows the influence of α on the budget terms of TKE. The thick lines are calculated with $\alpha = 0$ and the thin lines with $\alpha = {}^{2}/_{3}$.

case D the slope of the logarithmic region of u is increasing, while the one of T^+ is decreasing. In this case, the redistribution of kinetic energy due to the kernel addition has the same effect as reducing the ODT parameter C, resulting in fewer accepted eddies, a reduction of turbulent and viscous transport and the decreasing of the slope of T^+. The budget reduction is also seen in the figure showing the budgets, where both transport budgets show a reduction for $y^+ > 5$. On the other hand, the energy redistribution generates turbulence in the velocity components v and w resulting in an increase of the dissipation, especially near the wall for $y^+ < 15$. Taking into account that the DNS results from Kawamura et al. [42] for $\mathrm{Re}_\tau = 395$ and $\mathrm{Pr} = 1$ show nearly the same results for the law of the wall for the equivalent of case A, the conclusion for ODT with $\alpha = {}^{2}/_{3}$ has to be that the kernel addition overestimates the redistribution among the velocity components. Therefore, this case contradicts the common use of $\alpha = {}^{2}/_{3}$ for the channel flow, which was an outcome from the analyze of the homogeneous turbulence. Due to the fact that any value of α within its range of $[0; 1]$ follows the idea of *tendency to isotropy*, a different value would give better results for at least the passive scalar simulation resulting in a further adaption of the parameters C and Z. Furthermore,

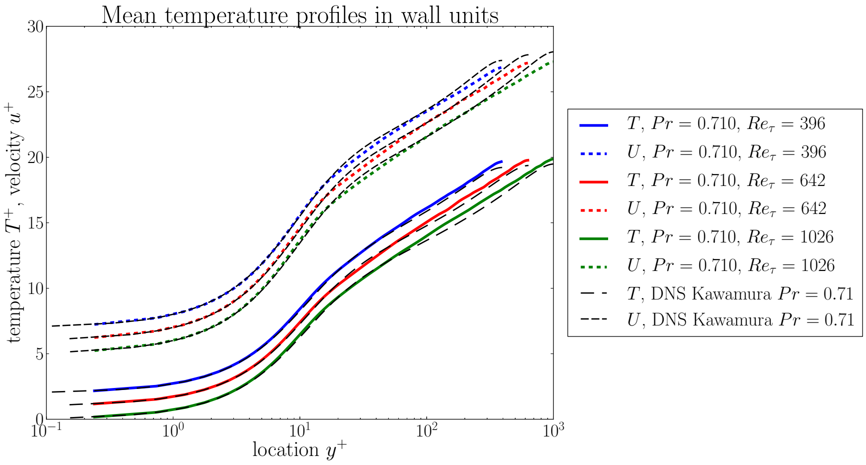

Figure 5.21: Law of the wall of a passive scalar with $\mathrm{Pr} = 0.71$ compared to DNS results by Kawamura et al. [42]. The velocity profiles are shifted by $+5$. For better comparison, the cases for $\mathrm{Re}_\tau = 395$ and 640 are also shifted by $+2$ and $+1$, respectively.

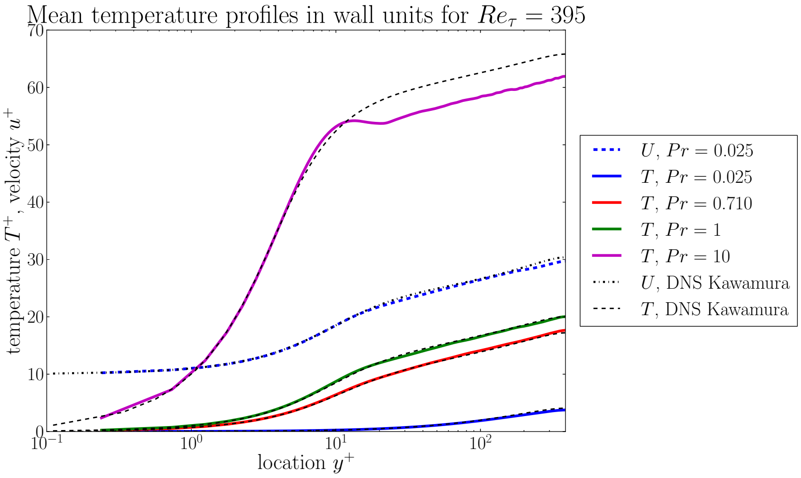

Figure 5.22: Passive scalar law of the wall for different Prandtl numbers. All ODT velocity profiles are identical, wherefore the profile is only shown for $\mathrm{Pr} = 0.025$. The velocity profile is also shifted by $+10$. The black dashed lines show the corresponding DNS results.

this case shows that the factor α has a major influence on the results, which is also highlighted by the results of Kerstein et al. [48], who have got best results with $\alpha = 1$ for the free shear flow and the wake simulation instead of $\alpha = {}^2\!/_3$ from the studies of the homogeneous turbulence.

Figure 5.21 shows the same cases as within figure 5.19 with adjusted parameters using $C = 5.5$, $Z = 350$, and $\alpha = {}^1\!/_6$. As can be seen the profiles for the mean velocity and the temperature are reproduced. The parameters are adjusted to give a good over all comparison for $\mathrm{Re}_\tau = 395$ and $\mathrm{Pr} = 1$.

A comparison of the passive scalar simulations for different Prandtl numbers is shown in figure 5.22. As already presented by Schwertfirm and Manhart [87] and Kawamura et al. [42] the profiles are increasing as expected. A comparison to DNS results from Kawamura

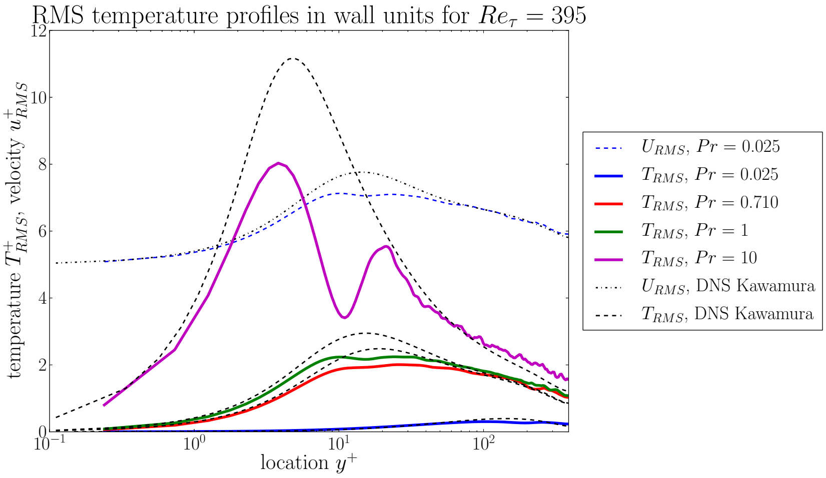

Figure 5.23: Mean fluctuation of a passive scalar for different Prandtl numbers. All ODT velocity profiles are identical, wherefore the profile is only shown for $\mathrm{Pr} = 0.025$. The RMS velocity profile is also shifted by +5. The black dashed lines show the corresponding DNS results.

for $\mathrm{Re}_\tau = 395$ shows a very good agreement for the viscous layer for all Prandtl numbers. Also the logarithmic layer is reproduced for lower Prandtl numbers up to $\mathrm{Pr} = 1$. Cases with higher Prandtl numbers show also the same slope within the logarithmic layer. The shift is a result from the ODT mechanism itself. Similar to the double-hill uncertainty shown within the RMS curves for the velocity fluctuations (compare figure 5.2 upper left), this shift is a ODT specific result not found in DNS.

The double-hill structure is in the range $9 \leqslant y^+ \leqslant 25$. Taking into account that ODT is not capable to simulate this region accurately, ODT generates reasonable good results for the mean profiles within the range of DNS comparable cases.

These good agreement is also seen in the results for the RMS velocity and temperature fields shown in figure 5.23. For the velocity fluctuations the known underestimation within the range $7 \leqslant y^+ \leqslant 50$ is seen. In contrast to the previous results for high Re_τ simulations, the fluctuation profile for $y^+ > 50$ shows a better agreement to the DNS results. Even if the profile is improved ODT has not the capability to reproduce the outer hill seen for higher Reynolds numbers. Due to the fact that this improvement is caused by a change of α, the lateral and wall normal fluctuation velocities are reduced and show worse results. Nevertheless, within a channel flow the turbulent kinetic energy is mostly effected by the streamwise velocity fluctuations wherefore this component is most important.

As the velocity fluctuations, also the temperature fluctuations show a good agreement for all Prandtl numbers, while the same underestimations are seen. Comparing the temperature fluctuation profile with the velocity fluctuations, it can be seen that the double-hill structure of ODT is moved towards the wall for higher Prandtl numbers. This is reasonable due to the fact that in ODT eddies are tested and accepted everywhere, especially at the wall. Therefore, the same behavior as for the velocity fluctuations is also seen for the temperature. Within the velocity field, fluctuations due to an accepted eddy, which is totally within the viscous layer, they are more or less instantly diffused, while the imprint within the temperature field is still present due to the lower diffusion coefficient. This leads to the same double-hill structure as within the velocity field, as described by Lignell et al. [56], but for smaller wall distances. The same logic but the other way round could be done for lower Prandtl numbers also showing the double-hill structure.

Figure 5.24 shows the budget terms of the equation for scalar variance $\overline{T'^2}$, which can be derived in a equivalent way as shown for the TKE budgets in section 2.3.3. The budgets are normalized with $\frac{u_\tau^2 T_\tau^2}{\lambda}$. The upper left subfigure shows the results for $\mathrm{Pr} = 0.025$. It can be seen that the production is the major budget term for $y^+ > 20$ and is nearly equal to the dissipation, indicating that nearly every fluctuation is instantly dissipated. A slight amount of scalar variance is moved towards the wall by viscous transport resulting in a balance of viscous transport and dissipation.

Starting from $\mathrm{Pr} = 0.2$ the dissipation shows the ODT typical shape with a minimum at about $y^+ = 10$. This local minimum is moving towards the wall for increasing Prandtl number. Also the other budgets show the known shape except from the turbulent and viscous transport which are negative for $12.5 < y^+ < 100$ and $7.5 < y^+ < 50$, respectively, and zero afterwards. This shows that for low Prandtl numbers the transport moves the scalar variance only towards the wall. A full discussion of all budgets of the TKE is given by Kerstein [46] or Schulz et al. [5].

The subplot for $\mathrm{Pr} = 0.71$ first shows positive regions for the transport budgets not attached to the wall resulting in a move of T'^2 away from the production area, both to the wall and towards the centerline. Additionally, the advective transport is coming up to be the major counterpart to the production within the buffer layer. This trend is increased for higher Prandtl numbers. Again, the dissipation is equal to the production for $y^+ > 50$ showing that all scalar variance is dissipated at the same position without any movement.

As described by Schwertfirm and Manhart [87] and reproduced by ODT the turbulent advection becomes more important than the production, first for the region[4] $20 < y^+ < 30$ and later on for the whole flow except the wall attached region up to about the middle of the buffer layer. This shows that for high Prandtl numbers there is no production of T'^2 in that region and scalar *energy* is only transported there by turbulent movement. In the range of the presented simulations the passive scalar has a constant value of fluctuations for $y^+ > 60$.

As the results for the high Reynolds number simulations of the pure channel flow show, it is in principle possible for ODT to simulate such high Re_τ cases. Also the Prandtl number can be increased to high val-

---

[4] This starting point is also seen in the DNS so that ODT can reproduce this effect in a meaningful way.

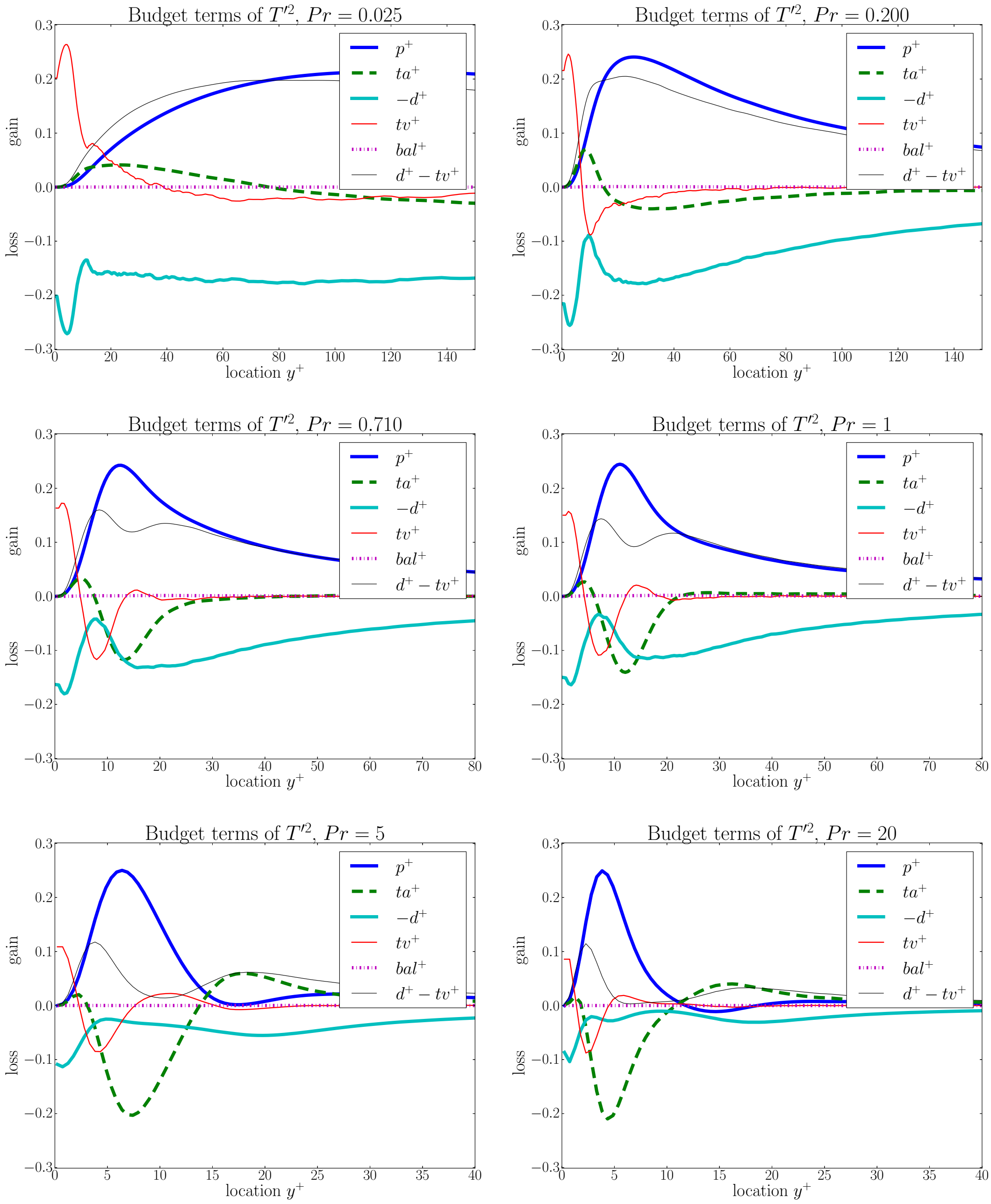

Figure 5.24: Comparison of T'^2 budgets for different Prandtl numbers with $Re_\tau = 1280$. p is the production, ta the turbulent advection, d the dissipation, tv the viscous transport and bal the balance of budgets. Additionally the combined effect of tv and d is given showing the typical two-hill structure of ODT except for $Pr = 0.025$.

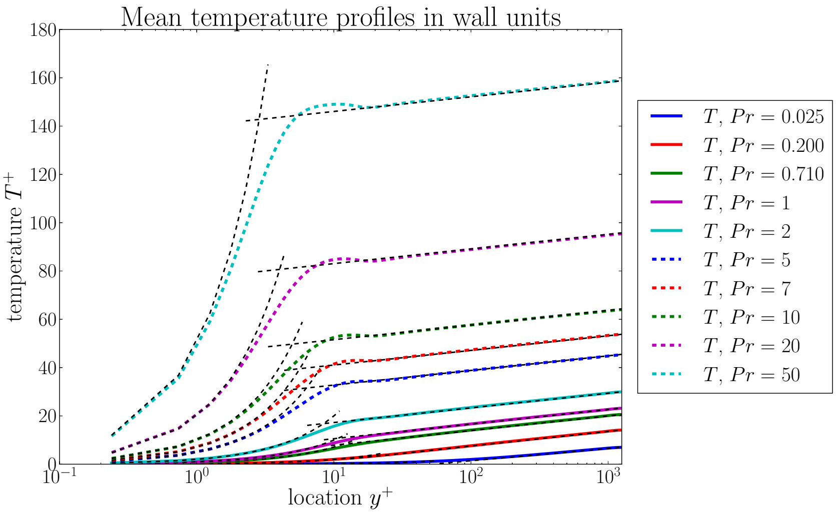

Figure 5.25: Passive scalar law of the wall for different Prandtl numbers. The black dashed lines show (i) the linear layer $T^+ \sim y^+$ and (ii) the logarithmic layer $T^+ = \frac{1}{\kappa}\ln(y^+) + B$ with $\kappa = 0.38$.

ues. Figure 5.25 shows the results for high Prandtl numbers. As expected from the results shown in figure 5.22 the profiles are increasing with increasing Prandtl number. As the dashed lines show the linear layer is always reproduced. The discrepancy seen for $\mathrm{Pr} = 50$ is an artifact from the under-resolved statistics grid[5]. Also the logarithmic region is well defined by the known approximation giving a constant κ of 0.38 as for the velocity. The difference in κ to $\kappa_{SM} = 0.27$ published by Schwertfirm and Manhart [87] and $\kappa_K = 0.43$ by Kawamura et al. [42] is a result of a wrong indication of the logarithmic region as discussed previously for high Reynolds numbers. Furthermore, it is non-trivial that ODT shows the same constancy of κ as within the mentioned publications.

As already mentioned, ODT generates a local maximum for $\mathrm{Pr} > 1$. The overshot is on the one side bounded by a fixed value of $y^+ \approx 20$. The lower bound instead is constantly decreasing broadening the overshot region. The fact that this region is nearly the same as the buffer zone, it is a further indication that ODT misses some phenomena within this region.

5.6 SUMMARY OF CHANNEL FLOW RESULTS

Within the chapter about the channel flow, several cases are analyzed. First the pure channel flow was simulated up to very high friction Reynolds numbers showing that ODT has the capability to reach industrial interesting regions. Besides the mean flow, the fluctuation velocity and the budget terms profiles also further statistics are calculated. The PDF of the wall shear stress compares good to results

---

[5] Within aODT there are two different grids. The first one is the adaptive grid as introduced by Lignell et al. [56] for the simulation, while the second one is used for the statistics calculation to provide a non-changing grid.

generated by DNS.

A further discussion about the outer peak within the fluctuation velocity profile shows that ODT misses this effect. It is concluded that the outer peak is generated by medium to large scale turbulence also modeled within ODT but ODT misses the streamwise and lateral information exchange. Summarizing a lot of DNS data, the same parabolic approximation within the diagnostic plot as presented by Alfredsson et al. [8] is also presented for the channel flow. Due to different parameters of this parabola, the channel flow is identified to be a better test case for analyzing the structures of the outer peak due to a more significant generation of the outer peak for the same friction Reynolds number compared to TBL.

A further, time developing test case using a fluctuating pressure gradient is presented. It shows on the one hand, that ODT has the capability to simulate time developing flows, and on the other hand, that a fluctuation of the pressure gradient periodically changes the PDF of the wall shear stress but the mean stress keeps the same. This shows that a modulation of the driving pressure gradient seems to be neither advantageous nor disadvantageous for the wall shear stress. This has to be verified by DNS.

Also a for ODT more critical test case presented by He and Seddighi [32] was tested. It is shown that ODT needs within an order unity factor the same time to reach the new full developed state. The fact that the test case was performed at low Reynolds numbers, where structures comparable to laminar flows are present, is critical for ODT. For comparison to ODT a similar test case with a sudden increase of the pressure gradient or a fluctuating pressure gradient at higher Reynolds numbers would be advantageous and would target the range of application of ODT.

The results for the heated channel simulations show good agreement to DNS results and have given a better insight into the role of the parameter α for channel flows. It is shown that $\alpha = 1/6$ gives better results than $\alpha = 2/3$, which has been an outcome from homogeneous turbulence. For cases with a distinct flow direction as within the channel flow $\alpha = 1/6$ should be preferred as long as passive scalars are simulated. Otherwise, the ODT parameters C and Z can be adjusted to compensate the differences generated by a different α.

The good agreement of the ODT results are advantageous in two ways. First, the heat transfer simulation within channels for industrially relevant conditions is possible. Second, due to the implementation of aODT, it is possible to (i) simulate buoyant active scalars within the same range of Prandtl and or Schmidt numbers and (ii) to simulate the channel with a viscosity dependent on scalars such as temperature.

Concluding, it can be said that ODT is valuable for studies of complex physics within the channel flow. To overcome the already known and the newly noticed shortcomes, ODT could be used as a sub grid model for LES or as a stand-alone 3D implementation. Both methods, LESODT and ODTLES, are presented by Schmidt et al. [84] and [85], respectively.

6 RESULTS FOR THE LIQUID JET

As described in the introduction, the simulation of a turbulent, two-phase flow is one of the most complex and challenging problems. The next section summarizes the setup as well as the results of the simulations for non-breaking and breaking jets.

The non-breaking, rectangular jet case was chosen due to the simplicity of the case. It is an ideal test case to analyze the turbulence at a free-slip boundary. The results are compared to experiments of Wolf et al. [95] and are already published by the author [5].

Based on these simulations, the breakup model, as described in section 4.3, was used to simulate the first and last breakup. The results are presented in section 6.3 and are compared to measurements from Wu et al. [99] and Sallam et al. [79]. Further investigations based on these developments by Movaghar et al. [4] (including the author) are discussed in section 6.3.3.

6.1 SETUP OF LIQUID JET SIMULATIONS

The liquid jet simulations are setup in a similar way as the simulations with a fluctuating pressure gradient and the setup is illustrated in figure 6.1. The simulation starts from a fully developed channel flow profile of water at standard conditions with a bulk Reynolds number $Re_B = 23,000$, a channel height $D = 10.2\,\mathrm{mm}$ and a bulk velocity $u_B = 2\,{}^{m}\!/_{s}$. The channel flow is simulated for $t_{channel} = 5\frac{D}{u_B}$ to ensure an independent flow profile. At this point, the current flow profiles are saved as new restart profiles for the next realization. After saving, the boundary conditions of the current realization are changed from no-slip of the channel flow to a free-slip boundary condition and the simulation is proceeded. When the realization has finished, the next simulation starts using the saved channel flow profiles.

For comparison to the measurements by Wolf et al. [95], the axial position of the temporal jet is calculated using the jet time t_{Jet}, which starts at the outlet of the jet, and the bulk velocity of the jet,

$$x = t_{Jet} \cdot u_B. \tag{6.1}$$

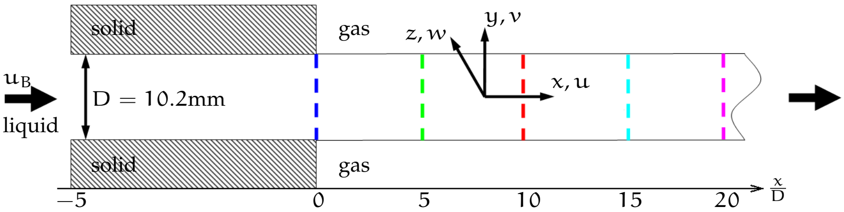

Figure 6.1: Illustration for the simulation of liquid jets.

For verification of the free-slip assumption, further simulations with surrounding gas at standard conditions are done. For these simulations, the boundary condition is not changed, instead the simulation domain is extended by a factor of three, where the newly generated domain part is treated as air at standard conditions. The boundary condition for the surrounding air is chosen to be free-slip. Sampled eddies containing both phases are prohibited.

The simulations of the breakup are done using surrounding air. In contrast to the simulation of the non-breaking jet with surrounding air, two-phase eddies are allowed. In this regard, due to the nature of the triplet map, each accepted, two-phase eddy generates at least one droplet. As described in section 4.3 the droplet is erased from the line after generation. The reason for erasing the droplet is that ODT lacks a suitable capability to simulate the secondary breakup or the droplet propagation. Further investigations could address this fact by coupling existing 3D tools using droplet statistics to simulate the droplet propagation and to recouple the droplet influence on the gas phase back to the ODT line.

All simulations for the non-breaking and the breaking liquid jet are summarized in the tables 6.1 and 6.2.

6.2 RESULTS FOR THE NON-BREAKING LIQUID JET

This section concludes the results of the non-breaking liquid jet simulations. First a detailed parameter study is presented before the results as published in [5] are discussed.

6.2.1 *Parameter study for the liquid jet*

Within this section the influence of the ODT parameters is discussed. For verification of the ODT results, the turbulence intensity is used as described in the following section and discussed in section 6.2.3.

As mentioned in section 6.1 the ODT parameters are varied around $C = 12.5$ and $Z = 50$, which give the best fit for the first simulations compared to the measurements from Wolf et al. [95] as presented in the paper [5].

Figure 6.2 left shows the influence of the C parameter. As can be seen, with decreasing C the decay region is shifted farther downstream while the overshoot is slightly decreased. This is reasonable due to the fact that the acceptance probability, which is scaled by C, decreases. The decay of the overshoot is a result of the dissipation, which has more time to act on a profile, thus reducing turbulent fluctuations. With increasing C the decay region is shifted upstream and the slope of the decay region is increased. As this figure shows, the best comparison is achieved by using $C = 10$ in case of $Z = 50$ giving a match of the measurement results for $9 \leqslant {}^{x}/_{D} \leqslant 16$. Even if this region is matched, the slope of the decay region is underestimated by ODT giving a hint that (i) the dissipation is underestimated, (ii) the production overestimated, or (iii) the turbulent advection is wrong in

Table 6.1: Setup of non-breaking liquid jet simulations. All simulations are done using 5000 realizations. For the simulation with the surrounding air the ODT line is extended by a factor of three and two-phase eddies are prohibited. The boundary condition of the air is free-slip.The simulation number 6 is the standard case and is the same for all studies.

No.	C	Z	Re_B	comments
1	1.0	50	23,000	
2	2.5	50	23,000	
3	5.0	50	23,000	
4	7.5	50	23,000	
5	10.0	50	23,000	
6	12.5	50	23,000	
7	15.0	50	23,000	
8	17.5	50	23,000	
9	12.5	1	23,000	
10	12.5	2	23,000	
11	12.5	5	23,000	
12	12.5	10	23,000	
	12.5	50	23,000	same as No. 6
13	12.5	100	23,000	
14	12.5	250	23,000	
15	12.5	400	23,000	
16	12.5	50	11,500	
17	12.5	50	17,250	
	12.5	50	23,000	same as No. 6
18	12.5	50	34,500	
19	12.5	50	46,000	
20	12.5	50	57,500	
21	12.5	50	69,000	
22	12.5	50	23,000	surrounding air

Table 6.2: Setup of breaking liquid jet simulations. The channel flow part was simulated using $C = 6.73$ and $Z = 288$. For the jet part $C = 12.5$ and $Z = 50$ are used. The jet was surrounded by air at standard conditions. The channel flow was simulated for $t^* = 0.4\text{s}$ and the jet for $t_C = 2.04\text{s}$, corresponding to $^{x^*}/_D = 7.84$ and $^{x_C}/_D = 400$. The simulations are averaged over 1000 realizations.

Re_B	11,500	17,250	23,000	34,500	46,000
We			$2.5 \cdot 10^3$		
			$5.0 \cdot 10^3$		
	$1.0 \cdot 10^4$	$1.0 \cdot 10^4$	$1.0 \cdot 10^4$	$1.0 \cdot 10^4$	$1.0 \cdot 10^4$
			$2.0 \cdot 10^4$		
			$4.0 \cdot 10^4$		
			$8.0 \cdot 10^4$		
	$1.6 \cdot 10^5$	$1.6 \cdot 10^5$	$1.6 \cdot 10^5$	$1.6 \cdot 10^5$	$1.6 \cdot 10^5$
			$3.2 \cdot 10^5$		
			$6.4 \cdot 10^5$		
			$1.28 \cdot 10^6$		
	$2.56 \cdot 10^6$	$2.56 \cdot 10^6$	$2.56 \cdot 10^6$	$2.56 \cdot 10^6$	$2.56 \cdot 10^6$
			$5.12 \cdot 10^6$		
			$1.0 \cdot 10^7$		
			$2.0 \cdot 10^7$		
	$4.0 \cdot 10^7$	$4.0 \cdot 10^7$	$4.0 \cdot 10^7$	$4.0 \cdot 10^7$	$4.0 \cdot 10^7$
			$8.0 \cdot 10^7$		
			$1.6 \cdot 10^8$		
			$3.2 \cdot 10^8$		
	$6.4 \cdot 10^8$	$6.4 \cdot 10^8$	$6.4 \cdot 10^8$	$6.4 \cdot 10^8$	$6.4 \cdot 10^8$
			$1.28 \cdot 10^9$		

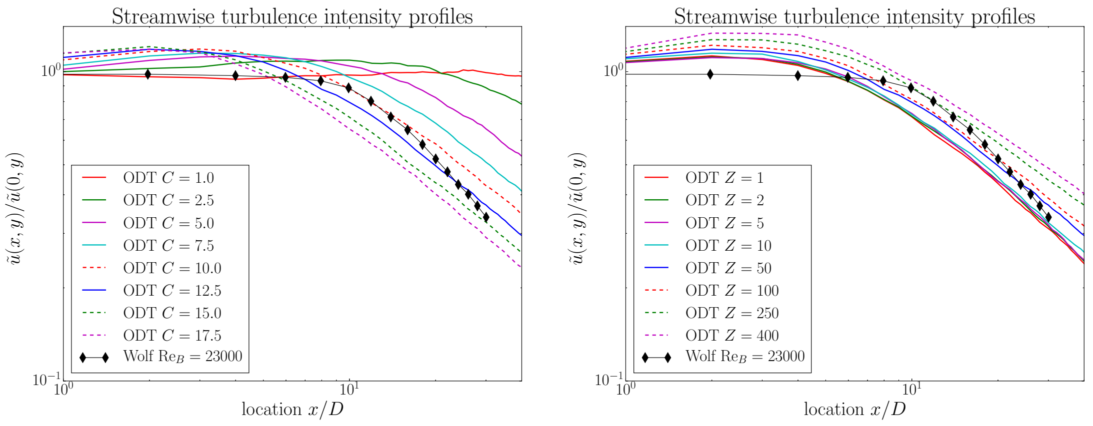

Figure 6.2: Parameter study for liquid jet simulations. Within the left figure the ODT parameter C has been changed, while Z is constant at 50. In the right figure the parameter Z was varied with constant $C = 12.5$.

the centerline region. Within this region the turbulence intensity is decaying exponentially wherefore it is linear within this double logarithmic presentation. Within the following this region is named the *'linear decaying'* region.

In the right figure the variation of Z is shown. For decreasing Z the profiles converge toward a lower bound represented by the curves for $Z = \{1, 2, 5\}$. Also the curve for $Z = 10$ shows nearly the same results with slight deviations to higher values. This shows that for $Z \leqslant 10$ all relevant eddies are accepted and the results become independent from Z for the choice of $C = 12.5$. Furthermore, with decreasing Z the slope of the decay region is increased. Even if the slope is increased, the measured slope by Wolf [95] is not matched. This could be a result of the missing 3D interaction represented by the underestimation of the fluctuation velocities typically present in ODT simulations. As this results show, the best match is given by using $Z = 250$ in case of $C = 12.5$. This parameter set gives a match of the measurements for $9.5 \leqslant x/D \leqslant 14$.

These two studies show that the optimization of the parameters is not trivial. Due to the fact that both parameters influence (i) the slope of the decay region and (ii) the spatial position, it is possible to represent the jet for each choice of C or Z. Furthermore, this shows that there if a functional correlation between both parameters. Figure 6.3 shows three different pairs of parameters all matching the measurements in the range $9 \leqslant x/D \leqslant 15$ with slight differences in the slope of the decay region simulated by ODT. While the parameter pair $\{C; Z\} = \{7.5; 5\}$ has the steepest slope in the decay region, the case with $\{12.5; 250\}$ also matches the the profile for $\frac{2y}{D} = 0.6$. Nevertheless, all simulations show a much too flat decay region.

As the variations of C and Z show, it is possible to generate steeper slopes by increasing C and decreasing Z. Therefore, it could be possible to match the slope of the decay region. This case would show a too early decay giving a hint that there are systematic differences between the ODT case and experiments. One possible difference is the sudden change of the pressure gradient where a gradual change could be more realistic. Another difference could be the change of parameters wherefore the turbulence structure is changed at the jet exit. Further modeling within ODT could target these issues.

Figure 6.4 compares the standard case using $C = 12.5$, $Z = 50$, and free-slip boundary conditions to the one with surrounding air. The simulation was done to verify the assumption that the interface of a non-breaking jet can be simulated as a free-slip boundary condition. As the figure shows, the results are nearly identical. A detailed discussion of this case is given in section 6.2.5.

Further simulations varying the maximum and the minimum cell size possible for the adaption process were done and show no recognizable differences.

As this parameter study shows, there is a functional correlation between C and Z, wherefore the optimal parameter pair depends on the issue. The further study of the liquid jet is done using $\{C; Z\} = \{10; 50\}$. Due to the code development, the analyses of the breaking jet is done

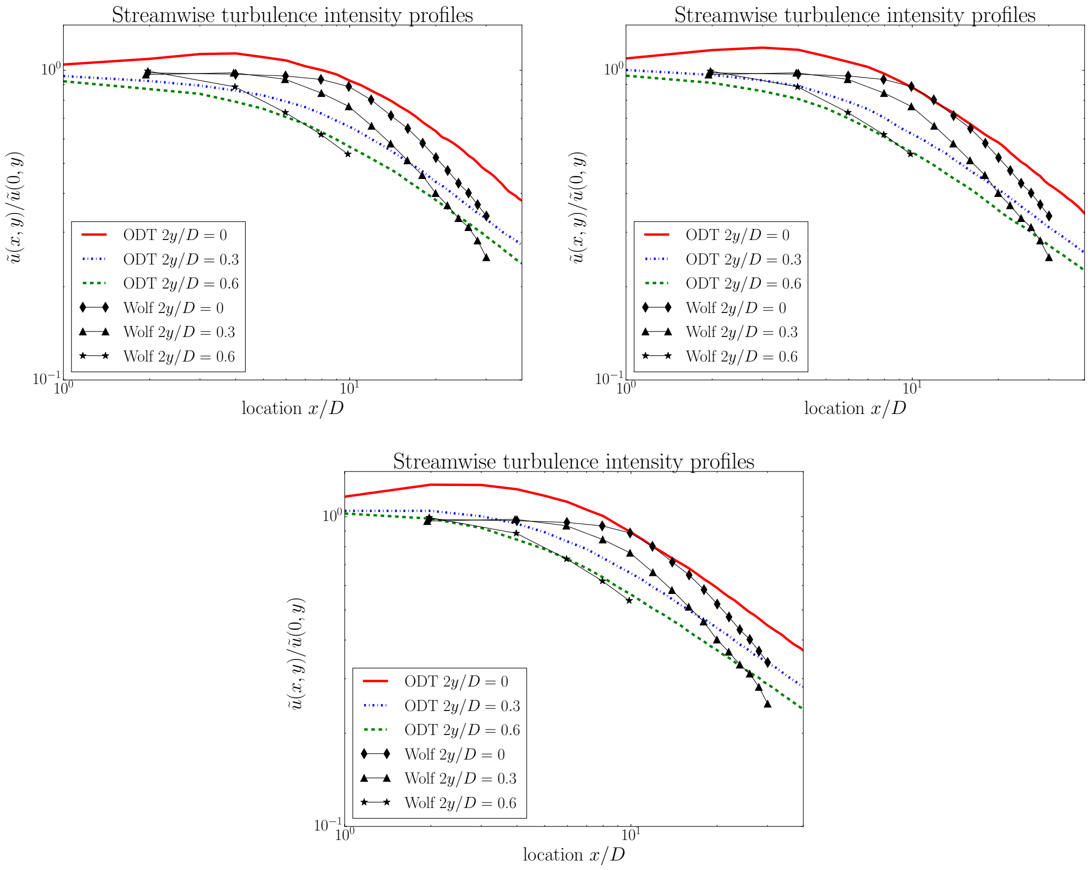

Figure 6.3: Comparison of the turbulent intensity to measurements at different lateral positions. From top left to bottom, the parameter pairs {C; Z} are {7.5; 5}, {10; 50}, and {12.5; 250}

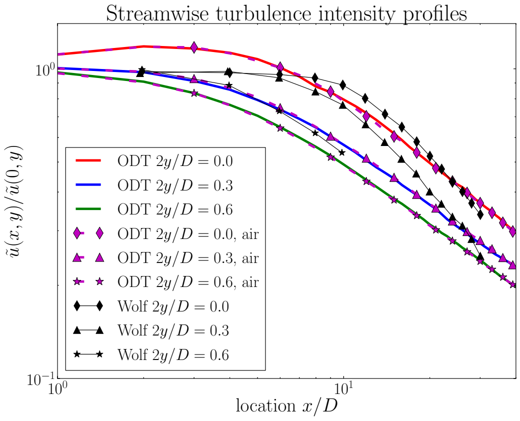

Figure 6.4: The figure shows a comparison of the standard jet simulation No. 6 compared to a simulation with surrounding gas.

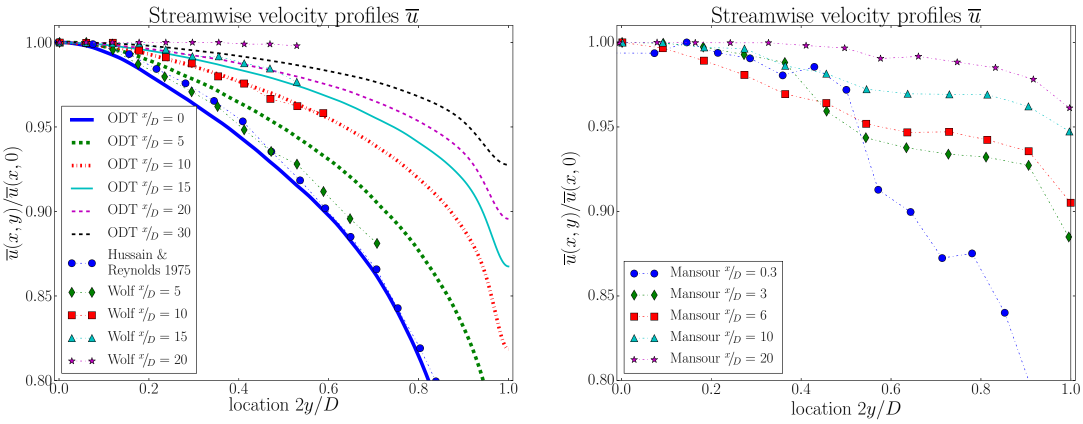

Figure 6.5: Left: Streamwise mean velocity profiles of the rectangular liquid jet. Right: Streamwise mean velocity profiles of the cylindrical liquid jet measured by Mansour and Chigier [61]

using the parameters $\{12.5; 50\}$ as presented in a paper published by the author [5].

6.2.2 *Mean and fluctuation velocity profiles*

While analyzing a new flow case, the most important profiles are the mean and the fluctuation velocity profiles. Therefore, these profiles are compared first at specific locations $^{x}/_{D} = \{0,\ 5,\ 10,\ 15,\ 20\}$ (compare figure 6.1) downstream of the jet exit, where the origin is located at the centerline of the jet exit. Even if these profiles are the most important, the ODT parameters are not chosen to best fit these profiles, instead are matched to reproduce the *'linear decay'* region of the turbulence intensity at the centerline as explained in the next section.
Figure 6.5 left shows the normalized results for different mean flow profiles of the jet simulation using $C = 10$ and $Z = 50$ for the jet part. The foregoing channel is simulated with $C = 7$ and $Z = 400$. The parameters for the channel flow are chosen to reproduce a good overall fit of the mean flow profile instead of a fit of the logarithmic region as described in section 5.2.1. The profiles are normalized with the mean flow velocity at the centerline at the same downstream position.
As can be seen, the profile at the jet exit, which is the same as the mean channel flow profile, reproduces the results measured by Hussain and Reynolds [35] and Wolf et al. [95]. The best fit is produced for the profiles at $^{x}/_{D} = 10$ and 15. The discrepancy in the profile at $^{x}/_{D} = 5$ can be explained by the missing 3D motion of ODT at the exit, where the sudden change from a no-slip boundary condition to a free stream causes 3D motions. The profile at $^{x}/_{D} = 20$ is flatter than simulated by ODT. This shortcoming of ODT was already discussed by Gonzalez-Juez et al. [31] showing that ODT underestimates the turbulent transport in the streamwise and cross-streamwise directions at the free surface resulting in a much slower equalization of the mean flow. They have also shown that ODTLES can improve this by simulating the missed physical transports.

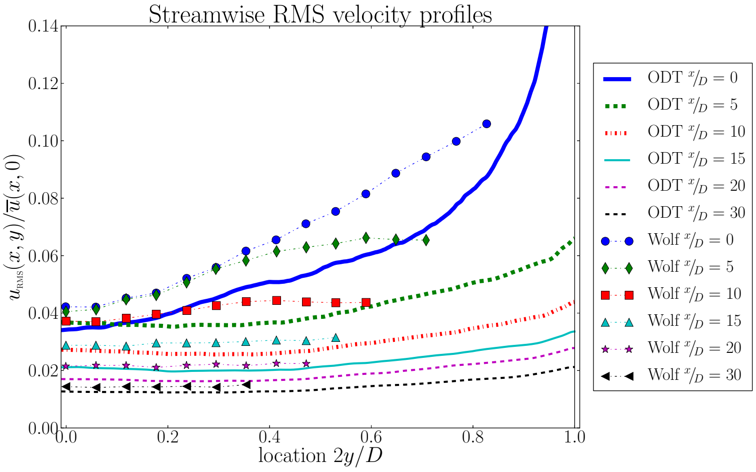

Figure 6.6: Streamwise fluctuation velocity profiles of the planar liquid jet.

This is also supported by the measurements from Mansour and Chigier [61] for a round liquid jet. Their results for the mean velocity profiles are shown in figure 6.5 right. As can be seen, the profiles for $^x/_D = \{3,\ 6,\ 10\}$ show a plateau for $0.55 \leqslant \frac{2y}{D} \leqslant 0.9$. This reflects the high amount of turbulence at the surface generating the equalization at the surface. Farther downstream, this plateau acts on the centerline region producing the tendency to a flat profile.

Figure 6.6 shows the results for the fluctuation velocity. The profile at the jet outlet reflects the underestimation of the fluctuation velocity typical for ODT channel flow simulations. While the measurements show for the normalized values a streamwise constancy of the RMS velocity for the centerline region ($\frac{2y}{D} \leqslant 0.4$) and a decay to a plateau for the outer region ($\frac{2y}{D} \geqslant 0.6$) up to $^x/_D = 5$, the ODT results show a decay in nearly the whole profile. The increase at the centerline is a result of increasing C and decreasing Z which increases the overall acceptance probability and reduces the energy threshold of an eddy wherefore more eddies are accepted.

Farther downstream, the RMS velocity profiles show a decay constant for the whole profile. The measurements instead show that the region of the plateau is decreasing more rapidly and spreading towards the centerline while within the inner region only a slight decay is seen from $^x/_D = 5$ to 10. Afterwards, similar to the ODT results, a constant decay is also seen for the measurements.

These results reflect the structure of ODT not capturing systematic differences in the turbulence structure near the wall or a free surface and the turbulence near the centerline. Nevertheless, ODT provides the opportunity to reach flow conditions incalculable by other techniques or costly so that no parameter studies are feasible.

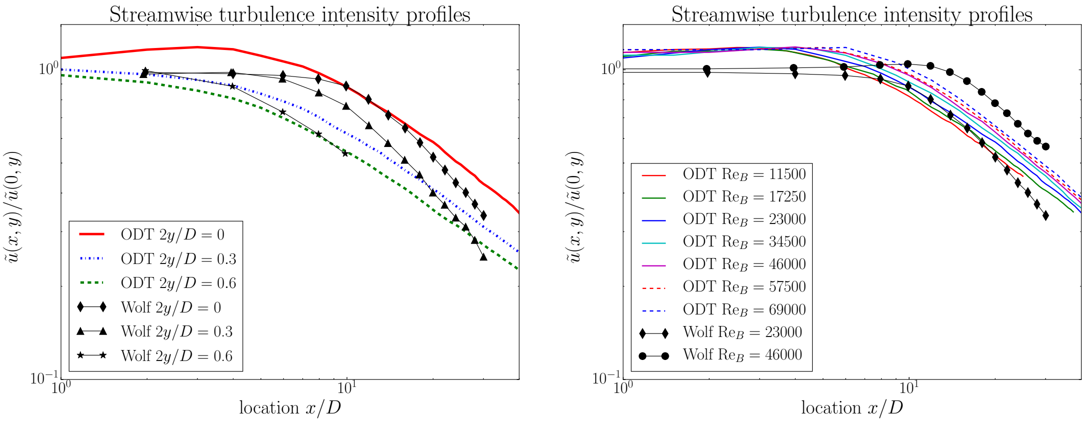

Figure 6.7: Streamwise turbulence intensity of a rectangular liquid jet compared to measurements from Wolf et al. [95]. Left: Turbulence intensity for $Re_B = 23,000$ and different lateral positions. Right: Turbulence intensity at the centerline for different Reynolds numbers ranging from $Re_B = 11,500$ to $69,000$.

6.2.3 *Turbulence decay of a liquid jet*

As described in the previous section, the mean flow profiles and the profiles of the RMS velocity are the most important profiles to compare simulations to measurements. In the specific case of ODT, which has reasonable discrepancies in modeling the 3D effects at the outlet and the turbulence structure at the free surface, the behavior at the centerline is least affected by these two effects. Therefore, the ODT parameters should be chosen to best fit the turbulence intensity decay at the centerline.

Figure 6.7 left shows the turbulence intensity $\tilde{u}$ at the centerline for the jet simulation with a bulk Reynolds number $Re_B = \frac{D \cdot u_B}{\nu} = 23,000$, where the turbulence intensity is calculated as $\tilde{u} = \frac{u_{RMS}}{\bar{u}}$. As already shown within the parameter discussion (section 6.2.1) none of the tested parameter pairs reproduces the *'linearly decaying'* region starting at $^x/_D = 15$. Even the tested simulations using the lowest Z value and the highest C value have not reached the same slope as the measurements. Therefore the case showing the best comparison was chosen.

As already expected from the fluctuation velocity profiles, the measurements show a faster decay. One reason could be that ODT underestimates the dissipation. Another one could be that the droplet generation, which is present within the experiments and is neglected by this jet simulation, extracts great amounts of TKE from the jet - especially at the start of the jet - wherefore the rest is dissipated more effectively.

Besides these shortcomings of ODT, it shows also a *'linearly decaying'* region starting at $^x/_D \approx 15$. The range from $9 \leqslant {}^x/_D \leqslant 15$ is matched by the simulation. Also the profile for $\frac{2y}{D}$ compares well. As shown in figure 6.3 it is possible to match the measurements for $\frac{2y}{D}$, but the uncertainties at the boundary within ODT have to be kept in mind.

The ODT results for $\frac{2y}{D} = 0.3$ show a much too early decay and miss the constancy of this profile up to $^x/_D = 5$. This was already expected from the fluctuation velocity profiles in figure 6.6 showing that ODT does not capture the constancy of the RMS profiles for $\frac{2y}{D} \leqslant 0.4$. The reason for this behavior could be the sudden change of the ODT parameters C and Z at the jet exit. This results in the acceptance of more eddies wherefore (i) more energy is shifted from the u_{RMS} velocity towards the other ones reducing the amount of u_{RMS} and (ii) the dissipation is increased due to more fluctuations caused by these additional eddies. A second reason could be the sudden vanishing of the pressure gradient wherefore the source term driving the flow within the channel vanishes. A more realistic behavior in this manner could be established by gradually adapting these parameters, but needs additional assumptions and modeling, wherefore it has not been attempted.

Figure 6.7 right shows the results for different bulk Reynolds numbers ranging from $Re_B = 11{,}500$ to $Re_B = 69{,}000$. As can be seen, the slope of the decay region is constant for all Reynolds numbers. Similar to the measurements from Wolf et al., the decay regions themselves are shifted farther downstream with a lower shift distance than given by the measurements. Furthermore, the overshoot region within ODT also stays constant, while the measurements show an increase to similar values as shown by ODT.

6.2.4 *Budget terms within the liquid jet*

This section summarizes the results for the TKE budgets of the liquid jet. Figure 6.8 shows the budgets for different streamwise positions $^x/_D \in \{5, 10, 15, 20, 30, 40\}$ (upper left to lower right). The budgets are normalized by the bulk TKE q_B divided by the jet time t_{Jet}, where the local TKE expressed per unit mass is calculated by $q = \frac{1}{2}\left(u'^2 + v'^2 + w'^2\right)$. The choice of the mean TKE for normalization is based on the fact that the TKE within the jet is decaying exponentially wherefore also the budgets have to decay in the same manner. The choice of the jet time is empirically giving mostly constant budget shapes within the *'linearly decaying'* region for $^x/_D \geqslant 15$.

As can be seen, the production and the dissipation are the major budget terms within the jet. The production can be approximated by two lines, where the first one starts at the boundary up to the top of the triangle - the boundary line - and the second decreases to zero at the centerline - the center line. Up to $\frac{x}{D} = 15$ this triangle top is increasing and moves slightly towards the centerline while the slope of the boundary line is nearly constant. This corresponds to the range where the turbulence intensity has not reached the *'linearly decaying'* part. Afterwards the shapes of the budgets stay constant except for the boundary line, which is slightly moving forward towards the centerline. The dissipation shows a similar tendency balancing the production.

While the viscous transport is nearly zero except in a thin boundary layer, the advective transport shows an increasing trend giving a loss

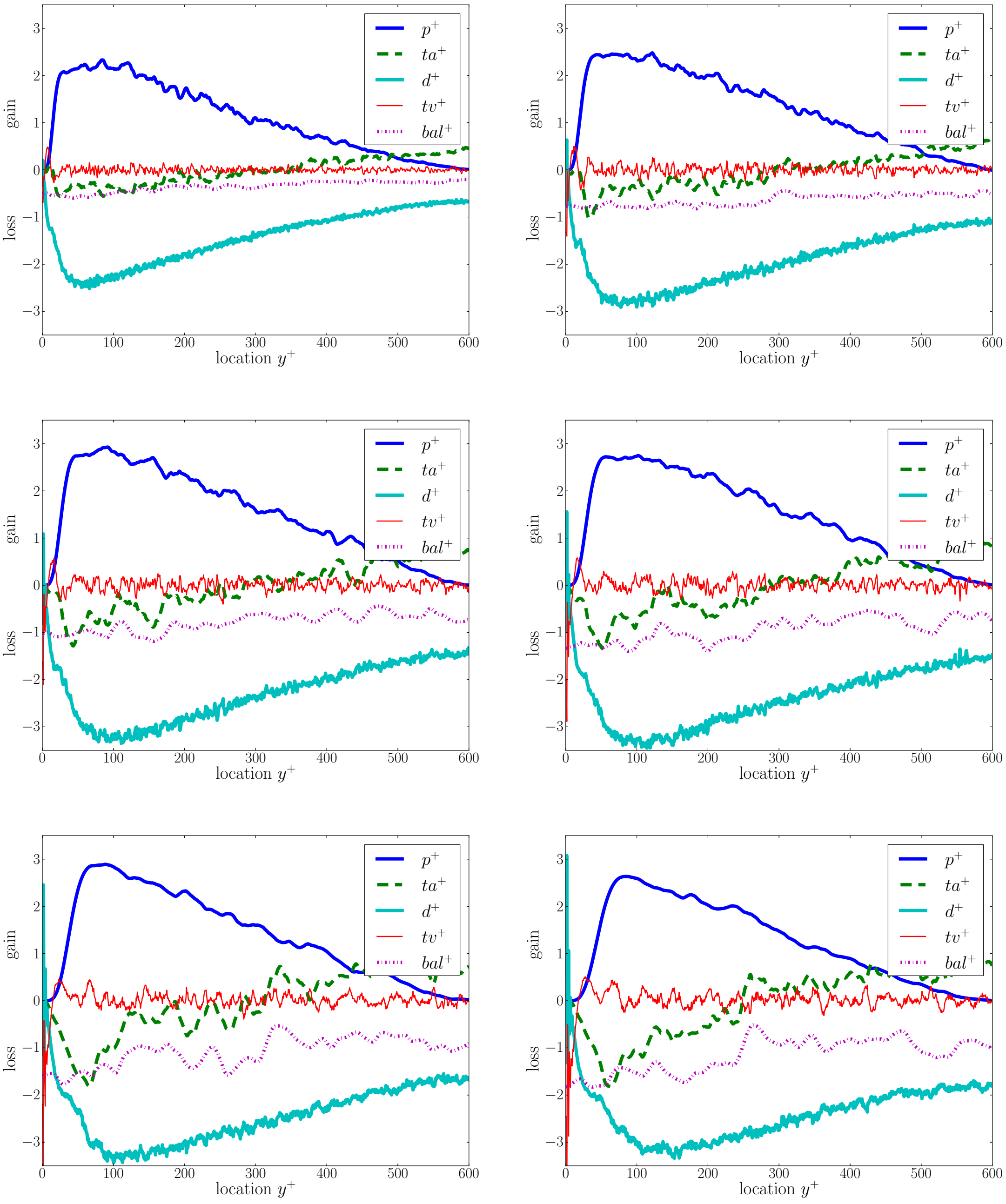

Figure 6.8: The figures show the TKE budgets within the liquid jet simulation for different streamwise positions $\frac{x}{D} \in \{5, 10, 15, 20, 30, 40\}$ (upper left to lower right in reading order). The budgets are normalized with the bulk TKE q_B divided by the time since the outlet of the jet t_{Jet}.

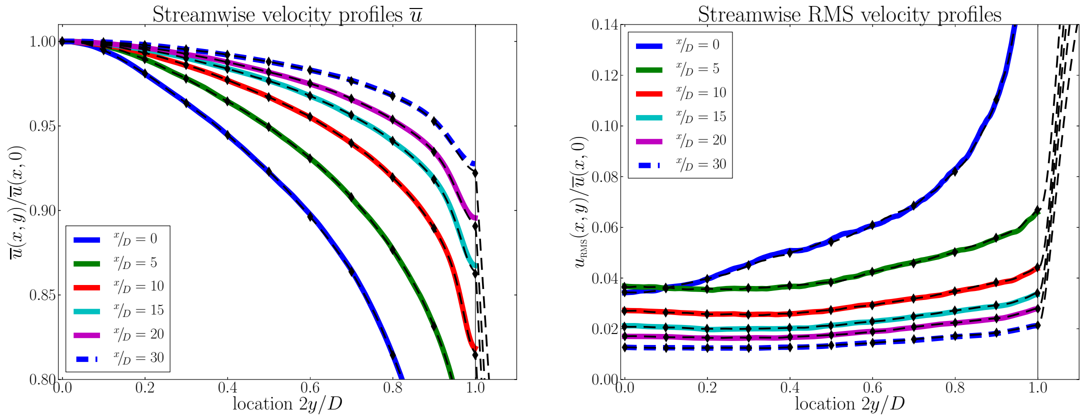

Figure 6.9: Simulation results for a liquid jet with surrounding air compared to previous jet simulations with a free-slip boundary condition. the left figure shows the mean velocity normalized by the current centerline velocity. The right figure shows the fluctuation velocity normalized in the same way as the mean flow. The black dashed lines with markers show the corresponding data of the simulation with the surrounding gas. The thin black vertical line illustrates the jet surface or the boundary.

for $y^+ \leqslant 300$ and a gain elsewhere. First, up to $\frac{x}{D} = 10$, the slope of this trend is increasing and afterwards levels off, showing a steady advective transport of TKE towards the centerline.

Collectively the budgets show an overall loss of TKE. This loss is continuously slightly increasing. As expected from the trend of the turbulence intensity decay in figure 6.7, the loss is nearly constant.

6.2.5 *Influence of the surrounding gas*

As already shown in the parameter study, the case using the surrounding gas shows the same results for the turbulence intensity as the standard case with free-slip boundary conditions. This section compares also the mean and the fluctuation velocity profiles.

From the theory of section 4.3 the gradient within the liquid phase has to be $^{\mu_l}/_{\mu_g}$ times less than the one in the gas phase, which results in a factor of 52 for a water jet in still air at standard conditions. Especially at the beginning of the jet, where the gradient in the gas phase is very steep, the deviation from the free-slip boundary condition is great.

Taking into account that ODT lacks the capability to simulate the 3D effects at the outlet, the error caused by the inaccurate boundary condition can be neglected. On the other hand, a free liquid jet in still air generates a coflow not considered in these simulations, which reduces the velocity gradient in the gas phase, mitigating the inconsistency of the free-slip boundary condition.

Figure 6.9 shows the mean and the fluctuation velocity profiles compared to the standard case. As can be seen, the velocity gradients at the surface show a discontinuity as expected. Furthermore, the velocity profiles show a slight deviation at the boundary for $^x/_D > 5$. The surrounding gas shows slightly lower velocities which result from the

inertia of the surrounding gas. Therefore the gas has to be accelerated wherefore kinetic energy is diffused from the liquid to the gas reducing the velocity of the liquid. Within the case of a free-slip boundary this effect is neglected wherefore the velocity has to be higher.
This raises another possibility for the difference within the velocity profiles compared to measurements. Within an experiment the jet generates a coflow, which has approximately the same velocity as the jet. Therefore the decelerating effect of the gas is not present instead an opposite effect is expected.
In contrast to the mean velocity profiles, the fluctuation velocity profiles show no deviation between both cases.
This comparison shows that the assumption of a free-slip boundary condition is a good approximation for a non-breaking jet.

6.3 TURBULENT BREAKUP OF A FREE LIQUID JET

Besides the mean flow structure and the turbulence within the free liquid jet, the breakup mechanisms are of major interest. Due to the complexity of tracking the accurate surface position and the 3D flow properties at the interface, it is extremely challenging to do full DNSs of the liquid jet even at low Reynolds numbers. Therefore, most commercial codes use measured droplet distributions and breakup scenarios to emulate correct structures.
The following sections summarize ODT results for a breaking liquid jet. As for the non-breaking jet, which could be coupled with a 3D solver to overcome the uncertainties at the outlet and the free surface not captured by ODT, the breaking jet simulations are also viewed as input to a 3D solver using the droplet generation as an input and feeding the gas flow back to ODT.
Here, to exclude the additional complexity of coupling ODT to a 3D solver, the simulations are done using the same setup as for the non-breaking liquid jet with surrounding gas as presented in the previous section with the opportunity to accept two-phase eddies. As described in section 4.3, each accepted eddy is generating one droplet, as long as the eddy region does contain only one of the two phase boundaries of the remaining jet. Otherwise it would generate three compressed copies of the original jet.
In the case of generating one droplet, the droplet itself is erased from the line, as described in section 4.3, because ODT does not provide a suitable capability to track the droplet. The remaining jet is therefore reduced by the droplet size. This treatment causes additional uncertainties - such as the acceleration effect of the gas phase due to the droplets - in addition to the ones already mentioned for the non-breaking liquid jet. If an eddy contains both phase boundary points and therefore would generate three compressed copies of the jet, the simulation is stopped, the statistics of the prior droplets are saved, and the time is treated to be the time of the *jet core* breakup. The *last* breakup instead terms the last breaking eddy right before the jet core breakup or the end of the simulation. The *initial* breakup is the first

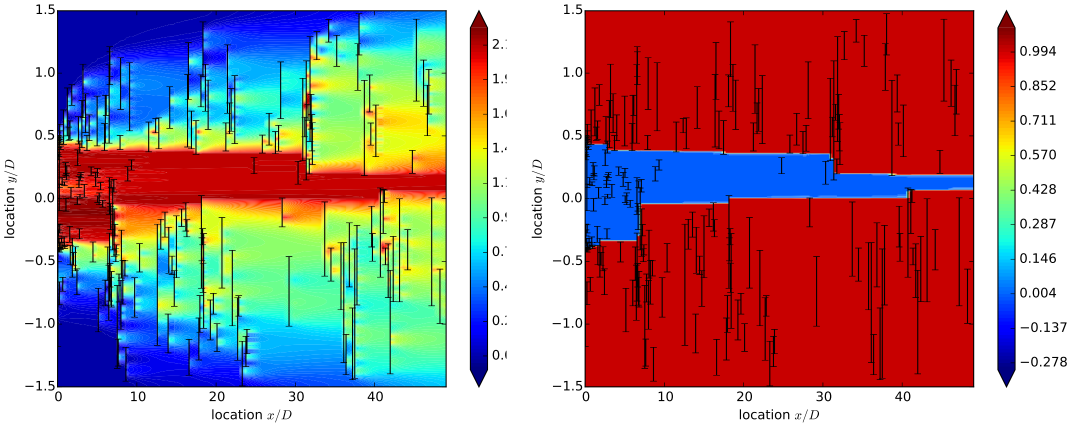

Figure 6.10: Exemplary realization of the breakup simulation. The jet is simulated with $\mathrm{Re}_B = 23,000$ and $\mathrm{We} = 1.28 \cdot 10^6$. The error bars indicate the streamwise location ${}^x/_D$, the lateral position y_0 and the size l of an eddy. The coloring in the left figure indicates the mean velocity, where *red* corresponds to $2\frac{m}{s}$ and *blue* to $0\frac{m}{s}$. In the right figure the coloring indicates the the phase, where *red* corresponds to the liquid and *blue* to the surrounding gas.

accepted two-phase eddy.

Keeping the uncertainties in mind, the following sections present the results provided by ODT. First the initial and last breakup will be discussed before additional statistics about the droplet size distribution and the energy of breaking eddies are discussed.

6.3.1 *Initial and last breakup*

Based on the non-breaking, rectangular, liquid jet the simulation of the jet breakup is done. The simulations are done without any modeling of further physical effects influencing the breakup. The droplet regions are replaced by gas phase with a velocity equal to the surface velocity of the droplet, which is equal on both sides due to the nature of the triplet map. This treatment emulates the gas acceleration effect of the droplets in a slight way, rather than erasing the droplet by shifting the cells.

Figure 6.10 shows one exemplary realization of the breaking liquid jet simulation with a bulk Reynolds number of 23,000 and a Weber number $\mathrm{We} = \frac{\rho_l D u_B^2}{\sigma} = 1.28 \cdot 10^6$, where ρ_l is the density of the liquid and σ the surface tension. The figure is colored by the mean streamwise velocity and the error bars illustrate the time t_{Jet}, location y_0 and size l of an accepted eddy, where the time of the simulation is converted to a streamwise location using $x = t_{\mathrm{Jet}} u_B$. The right figure shows the corresponding phases, where the liquid is illustrated by the *blue* region.

Within the first 10 jet diameters the velocity within the jet is nearly equalized, which is in agreement to the results of the non-breaking jet. Furthermore, most liquid eddies - eddies totally within the liquid phase - are within the same range. On both surfaces, the accelera-

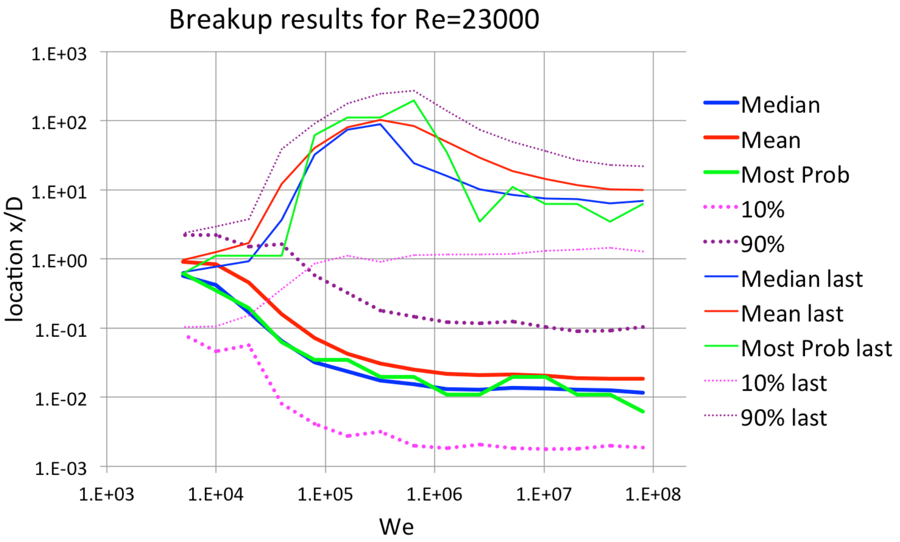

Figure 6.11: Dependence of initial and last breakup location on the Weber number. The thick lines indicate the initial breakup, the thin lines the last breakup. The dotted lines indicate the bandwidth of fluctuations of the breakup location. E. g. the 10% curve indicates that 10% of the realizations have shown an earlier breakup. The data are simulations with 1000 realizations.

tion of the gas phase can be seen, especially around $^{x}/_{D} = 25$ on the lower side of the jet. The acceleration of the gas phase generates velocity gradients which drives further eddies within the gas phase. At $^{x}/_{D} \approx 7$ lower side and $^{x}/_{D} \approx 33$ upper side some exemplary breaking eddies occur, reducing the remaining core jet. The generated droplets are erased from the ODT line as explained in the previous section.

For comparison to experiments especially the initial and the jet core breakup are of major interest, where the initial breakup is the location of the first droplet. The jet core breakup position is the position where no remaining jet is present and the jet is fully dispersed. Figure 6.11 shows the ODT statistics of the initial and last breakup position illustrated by thick and thin lines, respectively. The solid lines show the mean, median and most probable breakup location. The great variability of the breakup position is illustrated by the 10% and 90% lines showing the distance from the jet exit where at least 10% (or 90%) of the realizations have already had an initial breakup. This variability is also illustrated in figure 6.12. The lines for the median and the most probable breakup position are similar for the initial breakup, while the mean breakup position shows a later breakup. All curves show for the initial breakup a decrease up to We $\approx 10^6$ and a constancy afterwards. This is reasonable due to the fact that with increasing Weber number the threshold for a breaking eddy decreases until it is negligible and every eddy could generate a droplet.

Within the stage of development of ODT used for the breakup analysis, the simulation of the final breakup was not possible for every Weber number due to the fact that the Rayleigh breakup mechanism was not implemented. This missing mechanism provides the possibility of a jet generating no final breakup due to a too high surface tension

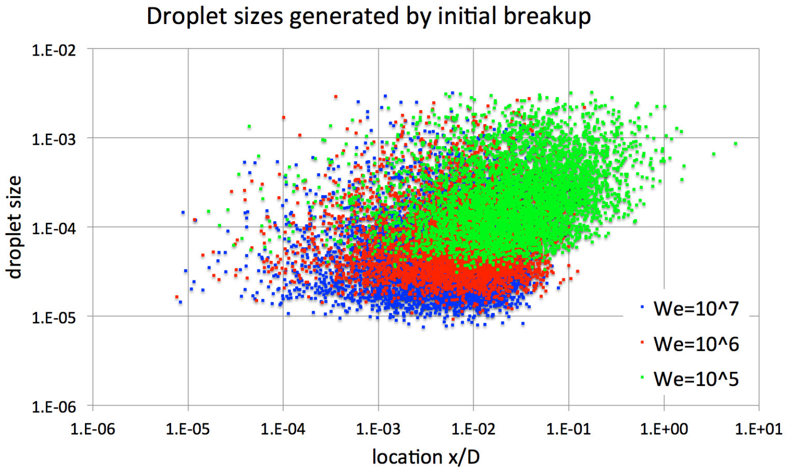

Figure 6.12: Droplet size and location of initial breakups for different Weber numbers. The simulations are done for jets with $\mathrm{Re}_\mathrm{B} = 23,000$ and 1000 realizations.

energy needed to generate further droplets and the final breakup. This possibility increases with reducing Weber number. Even if no final breakup is present, the last occurred breakup could be analyzed. For high Weber numbers the last breakup converges against the final breakup. On the other side, for lower Weber numbers within the range $5 \cdot 10^3 \leqslant \mathrm{We} \leqslant 1.5 \cdot 10^4$ Wu and Faeth [99] have reported a last and a final breakup, where the final breakup is a Rayleigh breakup. For higher Weber numbers, the curve for the last breakup converges against the Rayleigh breakup. For lower Weber numbers, last breakup converges to the initial breakup. Prior to the lowest Weber number at which an initial breakup occurs, Wu and Faeth have only measured the Rayleigh breakup.

Within ODT a similar tendency is seen. For lower Weber numbers the last breakup converges to the initial breakup. Afterwards it increases to a maximum. For higher Weber numbers, the last breakup again decreases until it converges to a constant value. The variability of the most probable last breakup position will be explained later on.

As already mentioned, figure 6.12 shows the droplet size and the location of the initial breakup for three different Weber numbers. The results show a variability of the initial breakup position ranging over about four orders of magnitude. Even if the unlikely ones are excluded, the variability still ranges over two orders of magnitude, which was also shown in the previous figure. Within the measurement results from Wu and Faeth [99], there is no information about the variability of the initial breakup position. Furthermore it is not mentioned whether their results show the mean, median or most probable breakup position. This should be targeted by further investigations.

On the other side, figure 6.12 shows the droplet size of the breaking eddies. It is clearly seen that with increasing Weber number the droplet size distribution is getting broader. This can be explained by the reduced threshold energy from surface tension wherefore also

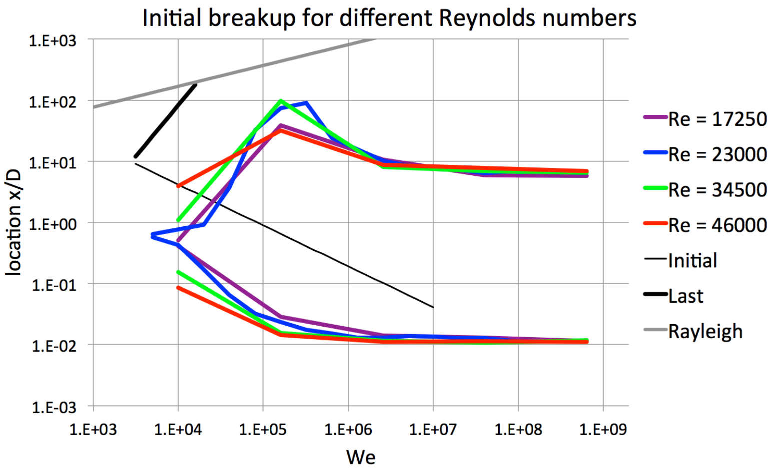

Figure 6.13: Breakup locations for different Reynolds numbers. The theoretical curves are presented by Wu and Faeth [99]. All simulations are done with 1000 Realizations.

smaller eddies, which have normally less available kinetic energy to be removed, have enough energy to overcome this threshold.

Figure 6.13 shows the initial and last breakup results for different jet Reynolds numbers compared to the theoretical curves from Wu and Faeth [99]. The initial as well as the last breakup curves show the same results independent of the Reynolds number. This is consistent to the measurements from Wu and Faeth who have also noted this independence. Compared to the theoretical curves, the initial breakup is one order of magnitude lower than within the experiments.

One reason for this too early breakup could be unphysical large eddies. At the moment the jet simulation starts, all eddy sizes are allowed. Within an experiment at least the gas phase eddies are restricted in size depending on the distance from the jet exit. For ODT this location corresponds to the time since the start of the jet simulation. On the other side, within ODT eddies are energetically accepted or rejected depending on (i) the eddy size and (ii) the turnover time. The missing of some kind of eddy suppression leads possibly to the acceptance of eddies with a turnover time larger than the jet time, which corresponds to eddies larger than possible within an experiment. Including some kind of eddy suppression would shift the curves to higher values of $^{x}/_{D}$. The eddy suppression would prohibit all breaking eddies, which have enough energy to overcome the surface tension, until the turnover time is smaller than the jet time times a constant parameter.

This would also shift the last breakup upwards, which could possibly lead to later last breakups than measured within experiments. Therefore, a modeling of the Rayleigh breakup is needed.

6.3.2 *Additional statistics*

Within ODT simulations of the breaking jet, further statistics could be gathered. Figure 6.14 shows the PDFs of the breakup location of

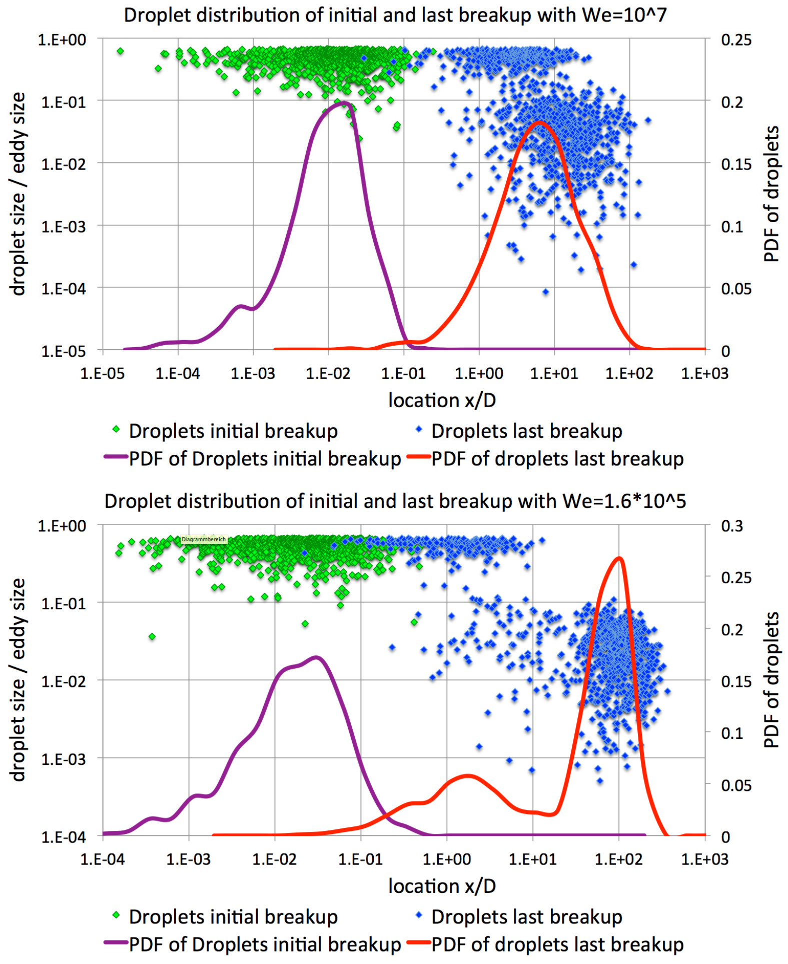

Figure 6.14: Fraction of droplet size on the corresponding eddy size for the initial and last breakup for two different Weber numbers. The lower figure shows the uncertainty of defining the most probable breakup position for the last breakup.

the initial and the last breakup. Furthermore, the quotient of droplet size divided by the eddy size of the droplet generating eddy is also shown. The droplet size is directly coupled to the liquid part within the eddy range prior to the mapping process. Therefore the droplet fraction can be calculated from the liquid part prior to the mapping. This shows that most initial breakups are generated by eddies with a liquid fraction of 50% or more. Due to the negligible kinetic energy within the gas phase, it could be said that these eddies are driven by the turbulence within the jet.

On the other side, the results for the last breakup show two separated clouds of liquid fractions. One cloud corresponds to the liquid driven eddies similar to the initial breakup, while the other cloud shows liquid fractions smaller than about 20%. Due to the small liquid fraction, the needed energy to overcome the surface tension threshold has to be mainly provided from the gas phase wherefore these eddies could be treated as aerodynamically driven last breakups.

This theory is supported by the corresponding figure for $\mathrm{We} = 160,000$, where the second cloud is shifted to higher $^{x}/_{D}$ values. Due to the increased threshold surface tension energy, first it is not possible for

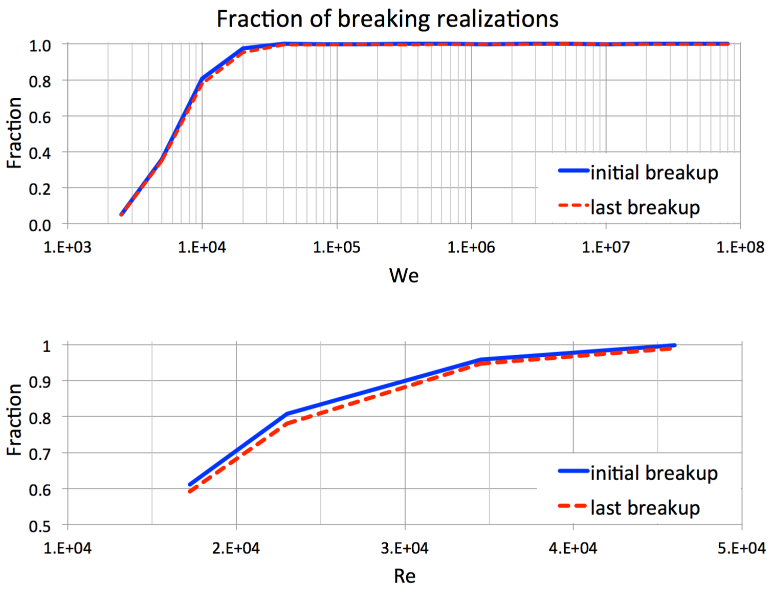

Figure 6.15: Fraction of realizations within a simulation showing an initial and last breakup. The upper figure shows the dependency on the Weber number, the lower one on the bulk Reynolds number. Realizations having exact one droplet are considered to have no last breakup.

the gas phase to provide enough energy to overcome this threshold. The gas shear has to develop first before large eddies could provide enough available kinetic energy for a breakup. Therefore, the aerodynamically driven breakups are shifted to greater values of $^x/_D$. Furthermore, this figure also explains the great fluctuation for the most probable breakup location within figure 6.11. Within the simulation with $\mathrm{We} = 160,000$ it is possible to calculate two different most probable breakup locations, one for the breakups driven by turbulence within the fluid and one for the aerodynamic driven breakups. Within experiments the breakups at too large distances from the jet exit are unphysical due to the fact that the remaining jet would have become unstable and a Rayleigh breakup would have happened. Therefore, as long as no mechanism modeling the Rayleigh breakup is implemented, the results for the last breakup have to be treated carefully.

Within the ODT simulation, especially for low Weber numbers, not every realization has an initial breakup. Some of the realizations that show an initial breakup then have no further breaking eddy so that only one droplet is generated by this realization. Figure 6.15 shows the fraction of realizations generating an initial and a last breakup depending on the Weber number. It can be seen that between 2000 and $10,000$ the probability of a realization showing an initial breakup decreases to nearly zero. Even if it is possible to have an initial breakup for lower Weber numbers it is unlikely below $\mathrm{We} = 3000$. This is in good agreement with the measurement from Wu and Faeth, who have found a boundary for initial breakups at about $\mathrm{We} = 5000$.
The lower part of figure 6.15 shows the percentage of realizations with an initial breakup depending on the Reynolds number at $\mathrm{We} =$

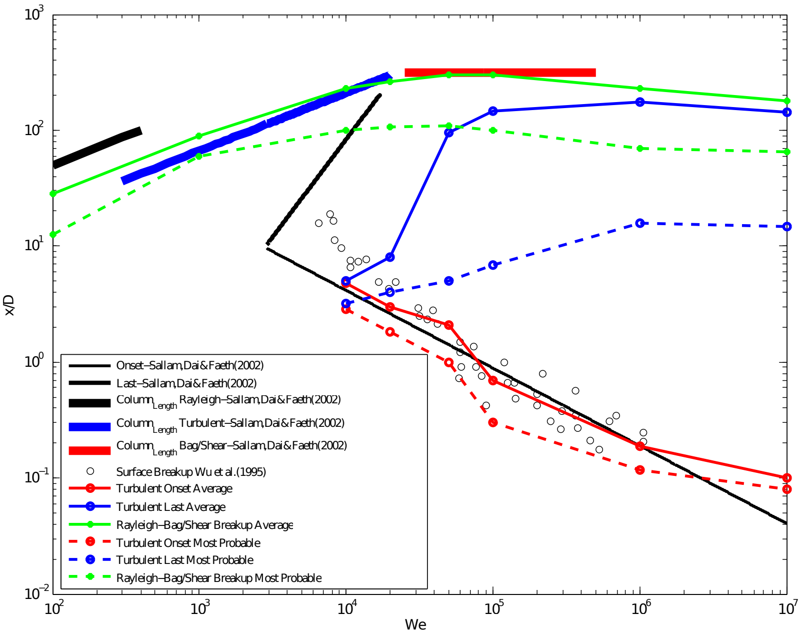

Figure 6.16: Initial, last, and Rayleigh breakup results of ODT compared to measurements from Wu and Faeth as presented by Movaghar et al. [4]. Simulations are done using a large eddy suppression depending on the jet time t_{Jet}.

10,000. This shows that with increasing Reynolds number the number of realizations having an initial breakup increases. This and the fact that for higher Reynolds numbers the gap between initial and last breakup increases as shown in figure 6.13 suggests a shift of the lower Weber number bound to lower Weber numbers for increasing Reynolds number. Within the experiments such a behavior is not reported. Perhaps this behavior is prevented due to including of some kind of large eddy suppression. Further studies should target this behavior.

6.3.3 *Further investigations*

Since the first investigations of the breakup model within ODT, further developments are pursued by A. Movaghar at the department of applied mechanics, Chalmers University of Technology in Sweden, in cooperation with the author. The further development targeted first the implementation of a Rayleigh breakup mechanism and a suppression of unphysical large eddies. The results are summarized by A. Movaghar et al. [4] and are briefly presented here.

Figure 6.16 shows the simulation results including the Rayleigh breakup mechanism and a suppression of unphysical large eddies. Here, “Onset” terms the initial breakup. As can be seen, the large eddy suppression shifts the initial breakup position to higher $^x/_D$ values, as it was expected in section 6.3.1. Even if this mechanism acts on the results, there is still an uncertainty in defining a comparison values - most probable, mean value, or median value - due to the lack of that information for the experiments. Also the slope of the last breakup curve compares well to the theoretical curve from Wu and Faeth [99]. Illustrated by the thin green lines are the results of the Rayleigh breakup modeling, which is described in detail by Movaghar et al. [4]. These lines show a good agreement to the measurements (termed as "column length") (i) for the low Weber number Rayleigh breakup (thick black line), (ii) the moderate Weber number turbulent breakup theory (thick blue line), and (iii) the high Weber number bag/shear breakup theory (thick red line) as derived by Sallam et al. [79].

Within section 6.3.1 it is shown that the last breakup results show a maximum at $We \approx 30,000$. As discussed, due to the implementation of the suppression of large eddies without including the Rayleigh breakup model these last breakup lines would shift to larger values of $^{x}/_{D}$. This could possibly result in the fact that the ODT results show a later last breakup than seen in experiments. As the results from Movaghar et al. show, this maximum is not seen, wherefore the Rayleigh breakup is needed to limit the $^{x}/_{D}$ value for the last breakup. Furthermore, this arises the possibility that for higher Weber numbers not a constant line is seen, instead a slight decrease similar to the previous results in figure 6.13 could be present. A hint for this assumption is the slight decrease seen by the results from Movaghar et al..

6.4 DISCUSSION OF LIQUID JET RESULTS

Within this chapter, the ODT results for a liquid jet exiting into still gas and the breakup results are presented. In section 6.2 a parameter study is presented showing that for a best fit of the measured turbulence intensity there is a functional correlation between both ODT parameters. Further studies including the grid restriction parameters of the grid adaption and the surrounding gas compared to a free-slip boundary are discussed. While the grid parameters have no influence on the results showing that the grid is well resolved, a slight difference between a free-slip boundary condition and a surrounding gas shows a different behavior at the surface of the jet. Even if ODT has by construction shortcoming in simulating free-slip boundary conditions, it is shown and discussed in section 6.2.5 that the free-slip boundary condition is a good approximation.

In sections 6.2.2 and 6.2.4 the mean profiles and the budget terms are presented. The mean profiles are compared to measurements showing a good agreement for the center part of the flow and differences at the surface. These differences were already discussed by Gonzalez-Juez [31] showing that ODTLES improves the simulation of free-slip surfaces due to capturing 3D interactions. Within the RMS velocity profiles the differences are also present showing the reason for the differences in the mean flow profiles. While within the measurements, the RMS profiles start to decay at the surface and stay constant in the center region of the flow, ODT shows a nearly constant decay for the whole jet. Reasons for this discrepancy are discussed and two possible solutions are presented; (i) smoothing out the sudden change of the pressure gradient within the flow and (ii) adapting the ODT parameters, which are changed between the channel and the jet part of a realization.

For the budget terms a self similar scaling was found for the streamwise locations within the region of *'linearly decaying'* turbulence intensity. Furthermore, the budget terms support the discussions of the mean and RMS streamwise velocities. Direct comparisons to measurements or DNS results are not done due to the lack of this information.

As a second part, the initial and last breakup are simulated. In a first step, the results show differences between the mean, median and most probable breakup position. Keeping the discrepancies from the liquid jet simulations in mind, the breakup results show good representation of the measurements even if the initial and last breakup positions are too far upstream. The reasons for this behavior are discussed. Further developments by A. Movaghar et al. [4] (i) modeling the Rayleigh breakup and (ii) suppressing unphysically large eddies show that the suggested modelings improve the results as expected.

Analyses of the breakup position, the droplet size and the ratio between the droplet and the eddy size have shown two different mechanisms for the last breakup. One mechanism is based on turbulent structures within the fluid, while the other is driven by aerodynamic turbulence. As expected, these two mechanisms show a dependency to the Weber number. Due to the fact that this analysis was done prior to the implementation of the Rayleigh breakup mechanism and the eddy suppression, this analysis should be repeated.

Based on these first studies, further investigations are valuable. Improvements targeting the shortcoming of the jet simulation as basis for the breakup should have a major focus. Here detailed measurements and comparing DNSs are needed. Nevertheless, due to the good comparisons between measurements and ODT results for the breakup, figure 6.16, further parameter studies could be done.

7

SIMULATION OF THE SMOKE CLOUD

Up to now, all test cases are focused on a specific flow direction and are chosen to analyze one specific problem within the flow like the turbulence within the channel, the influence of the free-slip surface on the development of a free jet or the influence of the surface tension on the initial breakup and the column length. Furthermore, all of these flows are more or less coupled to the standard test case of ODT, the channel flow.

The following test case, the smoke cloud, has in contrast no determining flow direction, but instead is focused on buoyancy-driven turbulence like in Rayleigh-Bénard convection [13, 40]. The smoke cloud case is a model for real clouds where the cloud itself is marked by a passive scalar, which is unity within the cloud and zero above. This scalar mainly influences the cooling region and therefore forces a previously stably stratified flow to become unstable. The unstable stratified flow than generates turbulence by converting potential energy into kinetic energy. Furthermore, the generated turbulence mixes the smoke scalar and therefore directly influences cooling of the cloud.

This counterplay between the smoke scalar and the temperature is the main focus of the following study. A detailed introduction to the case is given by Bretherton et al. [11]. Compared to a real cloud case, the smoke cloud excludes additional complexity by not modeling the humidity of the gas and the cooling and heating produced by evaporation and condensation, respectively. These additional phenomena could be a topic for further investigations of ODT in this area.

The following section describes the setup of the smoke cloud case within ODT as presented for DNS by Lozar and Mellado [18] and specifies the parameters of all simulations presented in this thesis. Afterwards, in section 7.2 the results without any further modeling are presented before the influence of the chosen large eddy suppression method (LESM) is discussed. Parameter studies are done for the ODT parameters C and Z as well as the parameter b_{LESM} of the *Time*-LESM. In section 7.3 a further modeling approach that introduces the influence of large scale motions at the top of the cloud not captured by ODT is presented. The results for the chosen ansatz and the influence of the additionally introduced parameter are discussed.

7.1 SETUP OF THE SMOKE CLOUD SIMULATIONS

Within ODT the smoke cloud case is set up using two additional scalars fields, the temperature and the smoke, where the temperature is buoyantly active in regard to the influence of eddy acceptance and the smoke scalar is passive. The temperature is indirectly active due to a coupling to the density of the flow using the Boussinesq approximation with a reference temperature T_0.

$$\rho(T) = \rho_0 - \frac{T - T_0}{T_0}\rho_0 \tag{7.1}$$

Even if the density is non-constant, the ODT formulation for constant properties is used instead of the one presented by Ashurst and Kerstein [9]. This follows the Boussinesq approximation (7.1), where the variation of the density is only taken into account within the buoyancy term, which is represented in the calculation of the eddy acceptance probability (2.22).
The initial profiles for the temperature and the smoke scalar are set up as presented by Lozar and Mellado [18]

$$T(z) = \frac{\Delta T}{2}\left[1 + \tanh\left(\frac{z - z_0 - \theta}{\Theta}\right)\right] + T_0 \tag{7.2}$$

$$f(z) = \frac{1}{2}\left[1 - \tanh\left(\frac{z - z_0}{\Theta}\right)\right], \tag{7.3}$$

where z_0 is the position of the cloud top, Θ the thickness of the hyperbolic tangent profile around z_0, θ the upward shift of the temperature profile, and $\Delta T = \frac{\Delta b\, T_0}{g}$ is the initial temperature difference. Due to personal communication with A. Lozar, for all simulations the thickness Θ is chosen to be $0.1171875\,\Lambda$ to be consistent with the presented results by Lozar and Mellado [18] in contrast to their mentioned $\Theta = 0.1\,\Lambda$, where Λ is the optical depth for radiation of the smoke cloud. The offset is $\theta = 0.05\Lambda$. Different values for $\theta \in [-0.1; 0.1]$ are tested but show, as expected, no influence on the results of the self-similar region, wherefore their presentation is skipped.
Before starting the simulation, the initial temperature field is modified by integrating the effect of the cooling by the smoke profile for $2t_0$ without turbulent mixing and diffusion, where $t_0 = \left(\frac{\Lambda^2}{B_0}\right)\hat{}\,(^1/_3)$ is the reference time. B_0 is the reference buoyancy flux given by radiation:

$$B_0 = \frac{F_0 g}{\rho_0 c_p T_0}. \tag{7.4}$$

Here F_0 is the energy exchange of the cloud with the atmosphere, ρ_0 the reference density, and c_p the heat capacity at constant pressure. The velocity profiles are initialized by a random fluctuation with $\overline{\Phi} = 0$ and $\Phi_{RMS} = 10^{-12}$.

Table 7.1 concludes the simulations presented in the following section. The Z parameter of ODT is set to 10. Further simulations varying Z from 1 to 100 show no significant differences wherefore the study is not presented.
Multiple LESMs are tested. The *Thirds* LESM restricts the acceptance of an eddy to those eddies, for which each of the three thirds of the eddy would be an acceptable eddy. The *TwoThirds* LESM is similar to the previous one but a bit less restrictive. The method allows also eddies which have only two of the thirds generating an acceptable

Table 7.1: Setup of smoke cloud simulations.

No.	C	LESM	b_{LESM}
1	5.0	no LESM	—
2	10.0	no LESM	—
3	10.0	Thirds	—
4	10.0	TwoThirds	—
5	10.0	Time	0.1
6	10.0	Time	0.5
7	10.0	Time	1.0
8	10.0	Time	5.0
9	10.0	Time	10.0
10	30.0	Time	1.0
11	50.0	Time	1.0

eddy. The *Time* LESM does not restrict eddies by their acceptance, but instead restricts the eddies based on their turnover time τ calculated individually for each eddy based on the current flow state. An eddy is rejected if the simulation time is less than $\tau \cdot b_{\text{LESM}}$, where b_{LESM} is a freely adjustable parameter. The *Fraction* LESM, where the eddy size is restricted to a fraction of the domain size, was not tested due to the similarity to the choice of the largest possible eddy size l_{max}.

Table 7.2 specifies the simulation with the extra shear energy E_{es} in the eddy rate expression (2.22). The motivation for the extra shear and the results are discussed in section 7.3.

7.2 RESULTS FOR THE SMOKE CLOUD

As already mentioned for the jet simulations, while analyzing a new test case the most important comparison is given by the mean profiles. For the smoke cloud case the most important profile is the one for the smoke scalar due to the fact that it mainly influences the buoyancy, which drives the turbulence within the cloud.

Figure 7.1 shows the mean profiles of the temperature and the smoke scalar. The left figure shows the whole simulation domain, while the right one gives a detailed view to the inversion region, the region around the inversion point z_i, where z_i is defined by zero buoyancy. As the first one shows, ODT overestimated the depth for the turbulent mixing region. This is due to the fact that each eddy could be accepted if the energy is positive. This leads to a too fast downwards propagation of turbulence due to medium and large eddies, wherefore it is reasonable to use some kind of eddy suppression. Depending on the LESM, the influence could be various and is discussed later. Furthermore, ODT shows a very sharp profile next to the inversion point in contrast to a smooth minimum in the DNS profile. One explanation for this difference could be the horizontal averaging within the DNS, which would smooth down the sharp minimum in the buoyancy pro-

Table 7.2: Setup of smoke cloud simulations containing the extra shear term. C_{SM} is a parameter determining the amount of the added shear in the rate expression.

No.	C	LESM	b_{LESM}	C_{SM}
12	30.0	no LESM	—	0.0
13	30.0	no LESM	—	0.1
14	30.0	no LESM	—	0.2
15	30.0	no LESM	—	0.5
16	30.0	no LESM	—	1.0
17	30.0	no LESM	—	2.0
18	30.0	no LESM	—	5.0
19	30.0	Time	1.0	0.0
20	30.0	Time	1.0	0.1
21	30.0	Time	1.0	0.2
22	30.0	Time	1.0	0.5
23	30.0	Time	1.0	1.0
24	30.0	Time	1.0	2.0
25	30.0	Time	1.0	5.0

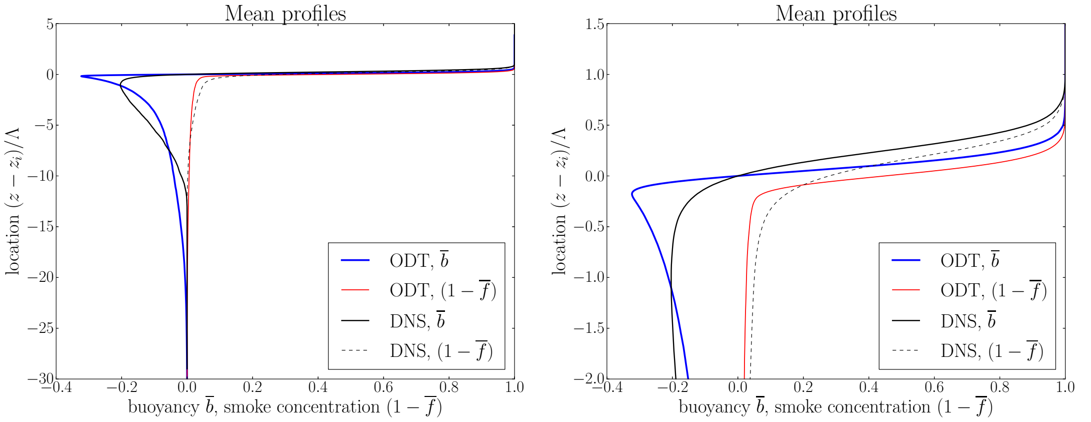

Figure 7.1: Mean profiles of smoke cloud simulation with $C = 10$, $Z = 10$ and no LESM (case No. 2) compared to DNS results by Lozar and Mellado [18].

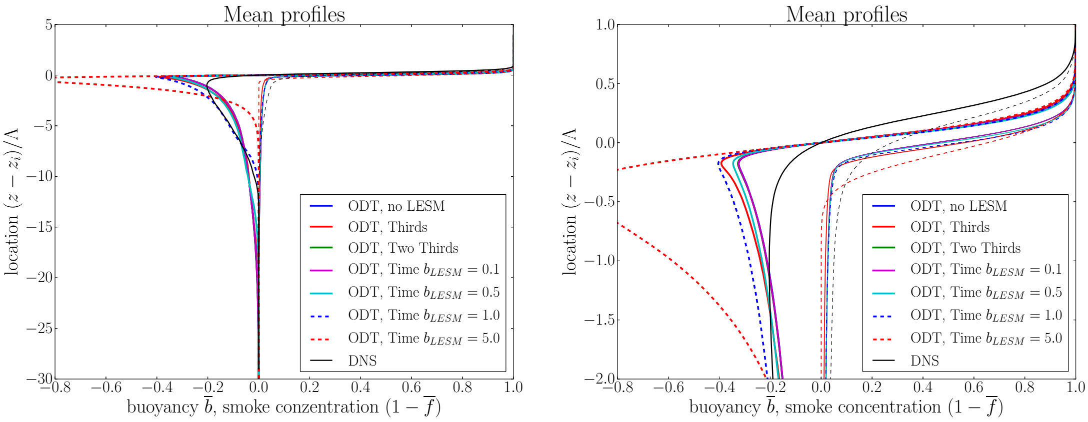

Figure 7.2: Comparison of mean profile of the smoke cloud simulation with $C = 10$, $Z = 10$ for different LESM (cases 2 to 8) compared to DNS results by Lozar and Mellado [18]. The thick lines are the temperature profiles, the thin ones the smoke scalar.

file. Another reason could be the higher turbulence level within the mixing region.

The latter reason in contrast to the first one is supported by the detailed view showing a smoother profile for the temperature as well as for the smoke scalar below and above the inversion point. The smoother profile for the smoke scalar also influences directly the temperature wherefore the sharp profile within ODT forces a more localized cooling than given within the DNS. This localized cooling again is supporting the sharp profile and therefore generates a much greater resistance for eddies ranging into the stably stratified region. Therefore, as mentioned above, the main focus has to be the smoke scalar profile and analysis of the behavior of this profile for different changes in parameters and models.

A further reason for the difference in the profiles could be the horizontal averaging for the calculation of the cooling. In contrast to the ODT simulations, where the cooling is calculated based on the instantaneous profile, within the DNS the cooling is based on a horizontally averaged smoke scalar profile. Due to the fact that this averaging is currently impossible within ODT, the cooling is based on the instantaneous profile resulting in a more localized cooling and a sharper temperature profile.

Besides the differences near the inversion point, the DNS results show linearly decreasing temperature for $-10 \leqslant \frac{z-z_i}{\Lambda} \leqslant -2$. Even though the region near z_i shows great differences, the turbulence within ODT also tends towards a linearly decreasing temperature shown for $-20 \leqslant \frac{z-z_i}{\Lambda} \leqslant -5$.

The next figures 7.2 show the comparison of different LESMs for $C = 10$ and $Z = 10$. The free parameter b_{LESM} of the *Time* LESM is described in the previous section. While most of the simulations show nearly the same results within the view of the whole domain, the simulations with the *Time* LESM using $b_{LESM} = [1.0; 5.0]$ show a significant difference. The one with $b_{LESM} = 5.0$ shows a turbulence depth of about $\frac{z-z_i}{\Lambda} = -5$ which is less than the DNS value. Furthermore, it

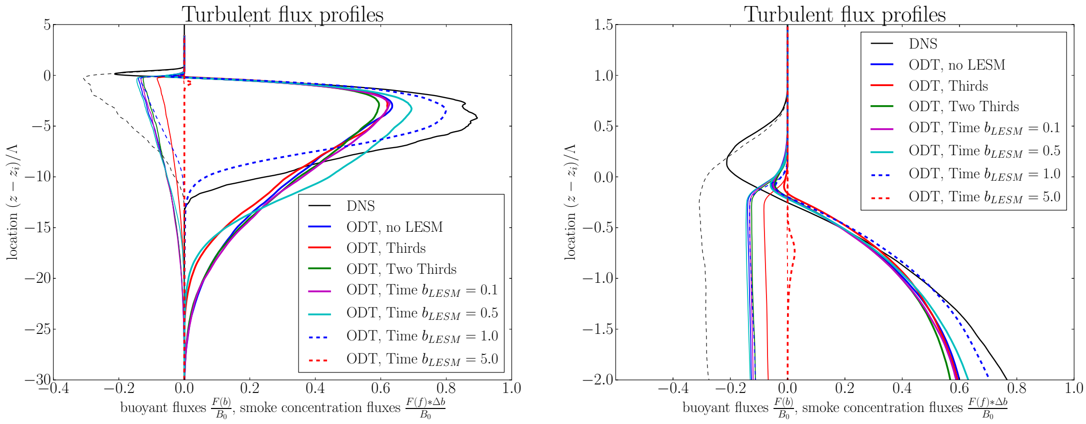

Figure 7.3: Comparison of turbulent flux profile of the smoke cloud simulation with $C=10$, $Z=10$ for different LESM (cases 2 to 8) compared to DNS results by Lozar and Mellado [18]. The left figure shows the whole simulation domain, while the right one shows the region around the inversion layer. The thick lines are the fluxes of the buoyancy (mostly positive values), the thin ones the fluxes of the smoke scalar (all negative values).

shows a sharp peak at the minimum in the temperature field suggesting that nearly no turbulence is present. Compared to the simulations with $b_{LESM}=0.1$, 0.5, and 1.0 these profiles show that the *Time* LESM using $b_{LESM}=5.0$ is too restrictive. In contrast $b_{LESM}=1.0$ shows nearly the same turbulence depth as the DNS and also matches the linearly decreasing region of the temperature.

The detailed view of the mean profiles shows slight differences between the model variants. As already seen in the left figure, the simulation with $b_{LESM}=1.0$ shows slightly lower temperatures than the other simulations except the one with $b_{LESM}=5.0$. The simulations without LESM, using the *Two Thirds*, or the *Time* LESM with $b_{LESM}=0.1$ show the same results. The *Thirds* and the *Time* LESM with $b_{LESM}=0.5$ show the same results for $\frac{z-zi}{\Lambda}\leqslant-1.2$. Near the inversion point the *Thirds* simulation tends towards the *Time* LESM with $b_{LESM}=1.0$. This suggests that the *Thirds* method is more restrictive in the region near the inversion point, which is reasonable due to the positive stratification and therefore the rejection of an eddy with a third lying in this region.

A comparison of the smoke scalar profiles show that the LESM has no significant influence on the profiles except the *Time* LESM with $b_{LESM}=5.0$. All methods give too few eddies mixing the stable stratified region. More mixing there would generate a smoother profile. This is also supported by the profiles of the turbulent fluxes shown in figure 7.3. As the detailed view of the turbulent transport shows, the profile for the turbulent transport of the smoke scalar is qualitatively the same but scaled by a half and shifted downwards. Furthermore, the profile for the *Thirds* LESM is less than the others, supporting the idea that the method is more restrictive than the others. The nearly zero flux profiles for the *Time* LESM using $b_{LESM}=5$ show that the choice of $b_{LESM}=5$ is too high. The same trend as for the smoke scalar is also seen in the turbulent transport of the temperature. Near

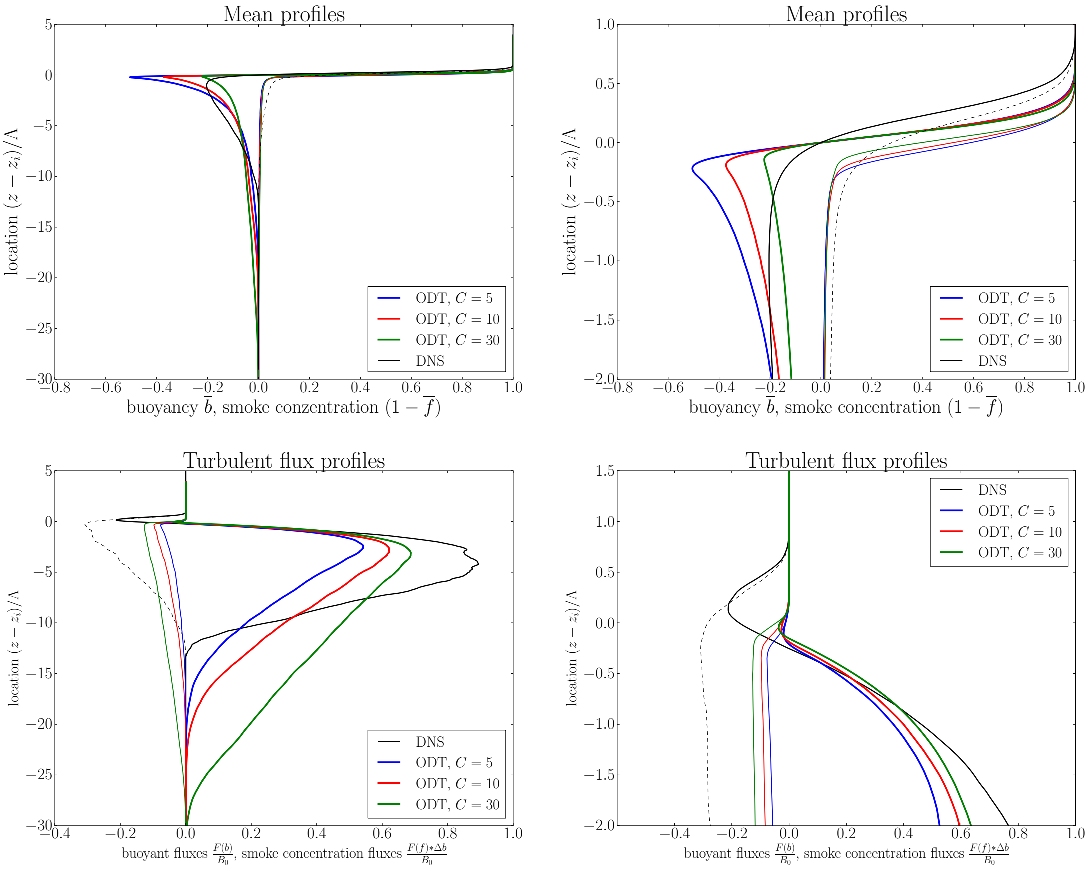

Figure 7.4: Comparison of the profiles for different C parameters (cases 1, 2, and 12). The thick lines are the profiles of the temperature, the thin ones for the smoke scalar. The right figures show the hole domain and the left ones the zoomed region around the inversion point.

the inversion point $-0.25 \leqslant \frac{z-zi}{\Lambda} \leqslant 0.75$ the turbulent transport is underestimated by ODT. This and the mentioned results for the smoke transport show that ODT is too restrictive for eddies mixing the stably stratified region at the cloud top. This also suggests that ODT misses some kind of energy providing 3D mechanism overcoming the threshold of the positive stratification. One possible mechanism is discussed in the next section.

The region below $\frac{z-zi}{\Lambda} = -0.25$ shows nearly the same profiles for the turbulent transport for the different LESMs. Again the more restrictive character of the *Thirds* LESM is seen (i) in the mentioned underestimation of the turbulent transport of the smoke scalar and (ii) in the slightly lower turbulent mixing depth. Also the *Time* LESMs with $b_{\text{LESM}} = [0.5; 1.0]$ show different profiles. While the one with $b_{\text{LESM}} = 0.5$ has a turbulent mixing depth comparable to the *Thirds* method, the one with $b_{\text{LESM}} = 1.0$ gives the same depth as the DNS. Therefore, the *Time* LESM is used for further simulations.

Figure 7.4 shows the dependency of the results on the ODT parameter C using no LESM. As expected, increasing C results in increased turbulent mixing represented by an increase of the turbulent fluxes. The improved mixing also increases the temperature due to a faster vertical transport. Also the mixing depth is increased. The increased acceptance probability also allows more small eddies near the inversion point, wherefore the smoke scalar is more rapidly transported downward resulting in (i) a higher gradient within the smoke profile and (ii) a smaller gap between the temperature and the smoke scalar profile.

The increased temperature profile below the inversion point also affects directly eddies ranging in the stable stratified region. Due to the improved mixing, small eddies get less energy from the negatively stratified part than needed to overcome the positively stratified part, where the negatively stratified part ranges from the minimum within the buoyancy profile downwards and the positively stratified region upwards.

Combining the results from the variation of the LESM and the parameter C the best choice is the *Time* LESM using $b_{\text{LESM}} = 1.0$ and $C = 30$. Even if there are two possible parameters to influence the turbulent transport and the mixing depth, the results show a too little mixing near the inversion point. Therefore, the following section introduces an additional model energy confined to the inversion region of the turbulent transport of the smoke scalar.

7.3 SMOKE CLOUD SIMULATIONS WITH ADDITIONAL SHEAR FORCING MODEL FORMULATIONS

As the results from the previous section show, there is a difference in the advective transport of the smoke scalar compared to the DNS results. With the ODT parameter C the amount of turbulent transport can be modified, resulting in an increase of transport by increasing C. Furthermore, the parameter b_{LESM} of the time LESM and the parameter C both influence the mixing layer depth, wherefore the parameter C can be used to adjust the amount of turbulent transport and b_{LESM} to adjust the mixing layer depth.

Nevertheless, there is still a gap between the results for the turbulent transport of the smoke scalar. This gap is a result of too little entrainment of dry air at the top of the cloud due to the stable stratification at the top of the cloud. Within ODT, the amount of dry air entrainment is a result of the viscous diffusion and the amount of turbulent entrainment, relative to the DNS results, is by a factor of two too low. Therefore, several implementations of extra shear to overcome the stable stratification at this point are tested. The idea behind the extra shear is the emulation of large scale 3D motions providing the turbulence at the cloud top with extra kinetic energy not captured by ODT. This idea is similar to the plume structures in Rayleigh-Bénard convection, where a horizontal flow exists where the up and down drafts meet the wall boundary layers.

The first implementations had the problem of (i) providing no change in the results or (ii) having a too large impact resulting in a linearly stratified flow instead of the normal cloud top with a thin inversion layer.

The currently used model is illustrated in figure 7.5. It generates the

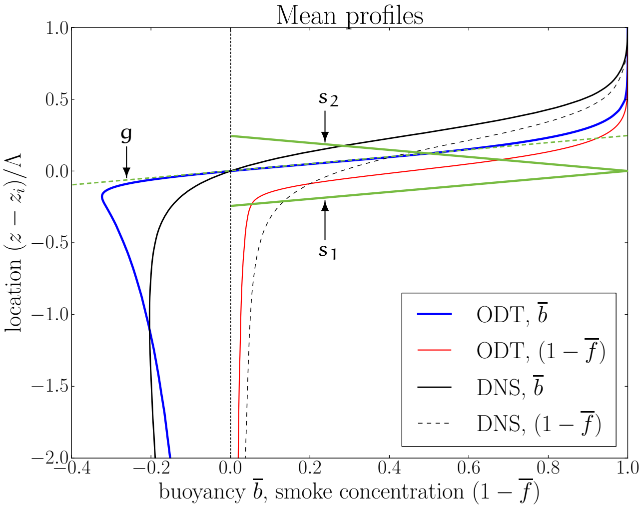

Figure 7.5: Illustration of the extra shear model for smoke cloud simulations. The jet models the kinetic energy stored in large scale 3D motions similar to the shear above plume structures in Rayleigh-Bénard convection. g denotes the maximal gradient of the temperature profile. s_1 and s_2 illustrate the velocity profile used to calculate the extra shear energy, where s_1 is parallel to g and s_2 has the same but opposite slope as g. While the jet width is calculated based on the starting profile after cooling for $2t_0$, the maximum of the jet is always oriented at the time-varying position z_i.

extra shear based on a triangular jet located around the local inversion point z_i. The width of the jet is defined by the greatest slope of the normalized, initial buoyancy profile $b^+ = \frac{g(T-T_0)}{T_0 \Delta b}$ near the inversion point after cooling for $2t_0$. This gives a limited additional jet treated as kinetic energy at the cloud top. This is supported by the DNS results from Lozar and Mellado [59], which show a thin localized peak within the horizontal RMS velocities not reproduced by ODT. This is discussed in the following section.

The inversion point z_i is defined to be the first point with zero buoyancy starting at the top of the simulation domain. Due to the stochastic behavior of ODT, the location of the jet is changing, while the width stays constant. The peak velocity of the horizontal jet is scaled by an additional parameter C_{sc}.

For the calculation of the rate expression, only the jet region part of the eddy region is taken into account as it is also done for the ODT velocity profiles. Therefore, only eddies ranging in the stable stratified region get an effect from this additional shear energy ΔE_{es}. Due to the fact that this extra shear is only used within the eddy rate expression, there is a possibility for negative radicands in the calculation of c_i within equation (2.18). To overcome this problem, the kernel addition is skipped wherefore the energy conservation is no longer obeyed. This is an arbitrary choice. Another possibility is to add the minimum extra shear $\Delta E'_{es} = \Delta E_{kin} - \Delta E_{pot} \leqslant \Delta E_{es}$ to ensure each square root to be positive wherefore equation (2.18) becomes:

$$
\begin{aligned}
c_i = \frac{27}{4l}\Bigg(&-u_{K,i} \\
&+\mathrm{sgn}(u_{K,i})\sqrt{u_{K,i}^2 + \alpha\sum_j T_{ij}u_{K,j}^2 - \frac{8}{27}\frac{1}{\rho_0 l}\frac{(\Delta E_{pot} + \Delta E'_{es})}{3}}\Bigg).
\end{aligned}
\tag{7.5}
$$

Both methods are adding energy to the system. While the first one keeps the kinetic energy constant, instead of reducing it by the amount of available energy, it adds potential energy to the system due to the generation of unstably stratified regions. The second method also adds potential energy but subtracts the amount of kinetic energy, which is available. Therefore, the second method adds less energy to the system than the first one.

Figure 7.6 shows the effect of the extra shear model on the turbulent fluxes using the method skipping the kernel addition. On the one side, a variation of the parameter value up to $C_{sc} = 0.3$ has no effect on the results. On the other side, values greater than $C_{sc} = 0.9$ show huge differences best seen in the results for the molecular fluxes. Instead of one region with molecular flux two regions are present, indicating a plateau within the temperature and the smoke profiles. This is confirmed by the mean profiles (figure 7.7) showing these plateaus in the profiles resulting in no molecular flux in this region. Furthermore, the profiles of the turbulent fluxes are different and not comparable to the DNS results.

The best comparison for the flux profiles is achieved by values $0.5 \leqslant C_{sc} \leqslant 0.7$. While the turbulent buoyancy flux shows good results for $\frac{z-zi}{\Lambda} < 0$ the turbulent smoke flux is still too small in the region $-5 \leqslant \frac{z-zi}{\Lambda} \leqslant 0$. For $0 \leqslant \frac{z-zi}{\Lambda} \leqslant 0.75$ both turbulent fluxes are still underestimated, indicating that the positive stratification is too strong to be overcome by the kinetic energy of an eddy. Also the molecular fluxes reflect the steep gradient by localizing the flux in a smaller region than shown within the DNS.

As the fluxes suggest, the mean profiles show steeper gradient than the DNS. This shows that the model of the extra shear jet improves the results but also shows that there are other phenomena not captured by ODT. One possible phenomenon is the horizontal molecular flux equalizing the inversion thickness. Likewise the turbulent horizontal fluxes are neglected by ODT. Both shortcoming of ODT result from the 1D formulation, wherefore the phenomena of undulation of the inversion layer is not simulated by ODT. Even if the stochastic character of ODT generated a similar phenomenon as the undulations the resulting horizontal fluxes are neglected.

Up to now the model discussion and all comparisons are done for the case with $Re = 800$ and $Ri = 10$. Figure 7.8 shows the results for $Re = 1600$ and $Ri = 57$ using the adjusted parameters $C = 30$, $Z = 30$, the *time* LESM with $b_{LESM} = 1.0$, and $C_{sc} = 0.6$. The simulation of

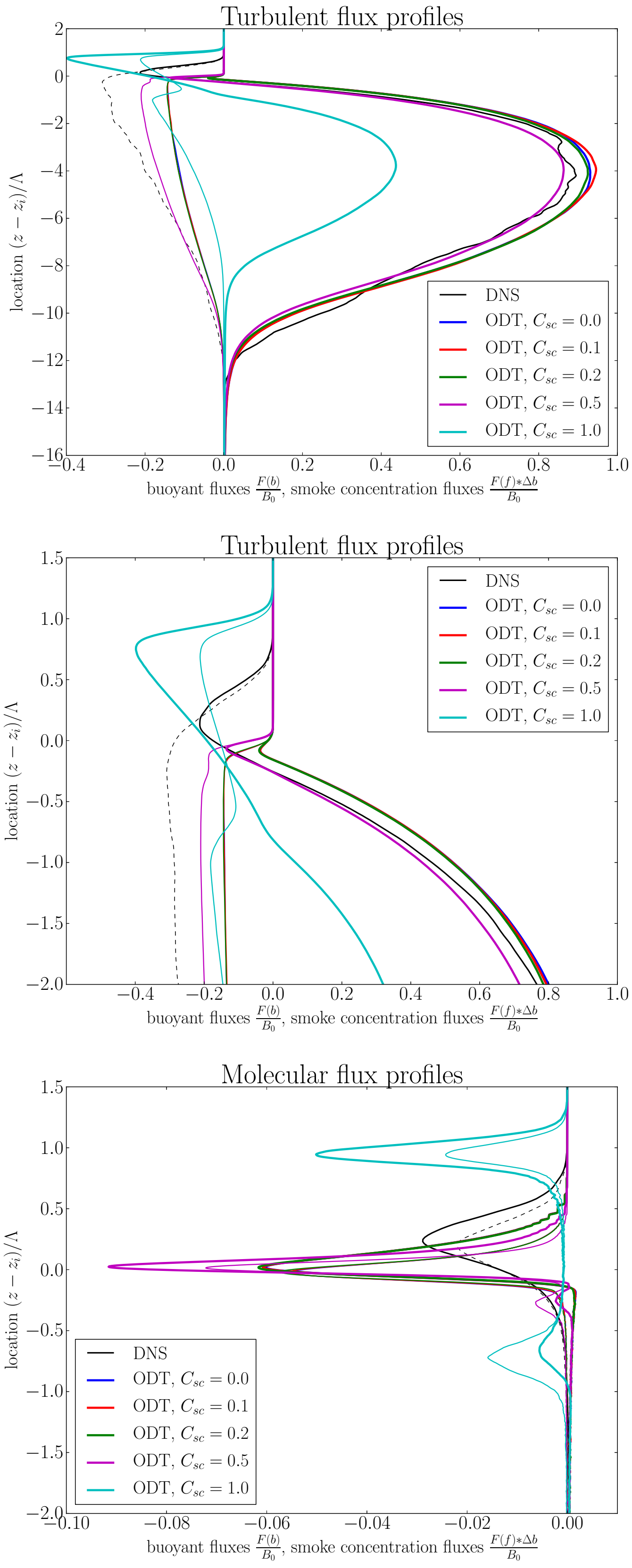

Figure 7.6: Turbulent flux dependency on extra shear term from jet modeling at the cloud top (cases 19 to 23). The first figure shows the turbulent transport in the whole domain, while the second one shows the inversion region. The third figure shows the corresponding viscous fluxes. The thick lines are the fluxes of the buoyancy, the thin ones the fluxes of the smoke scalar.

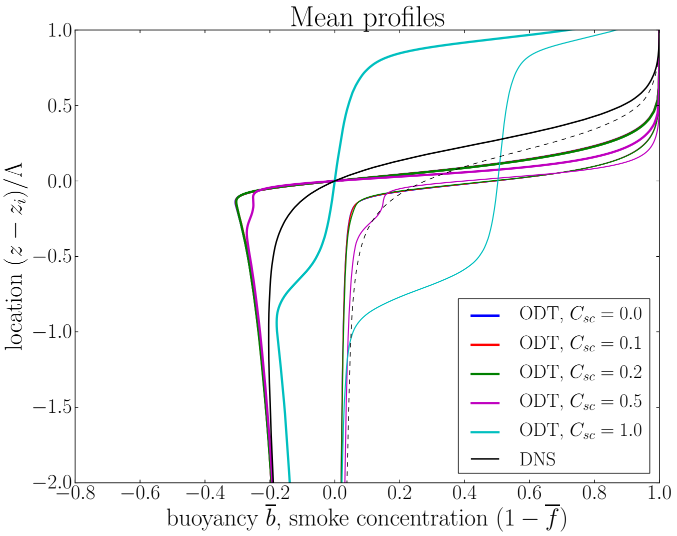

Figure 7.7: Dependency of mean buoyancy and smoke scalar to extra shear term from jet modeling at the cloud top (cases 19 to 23).

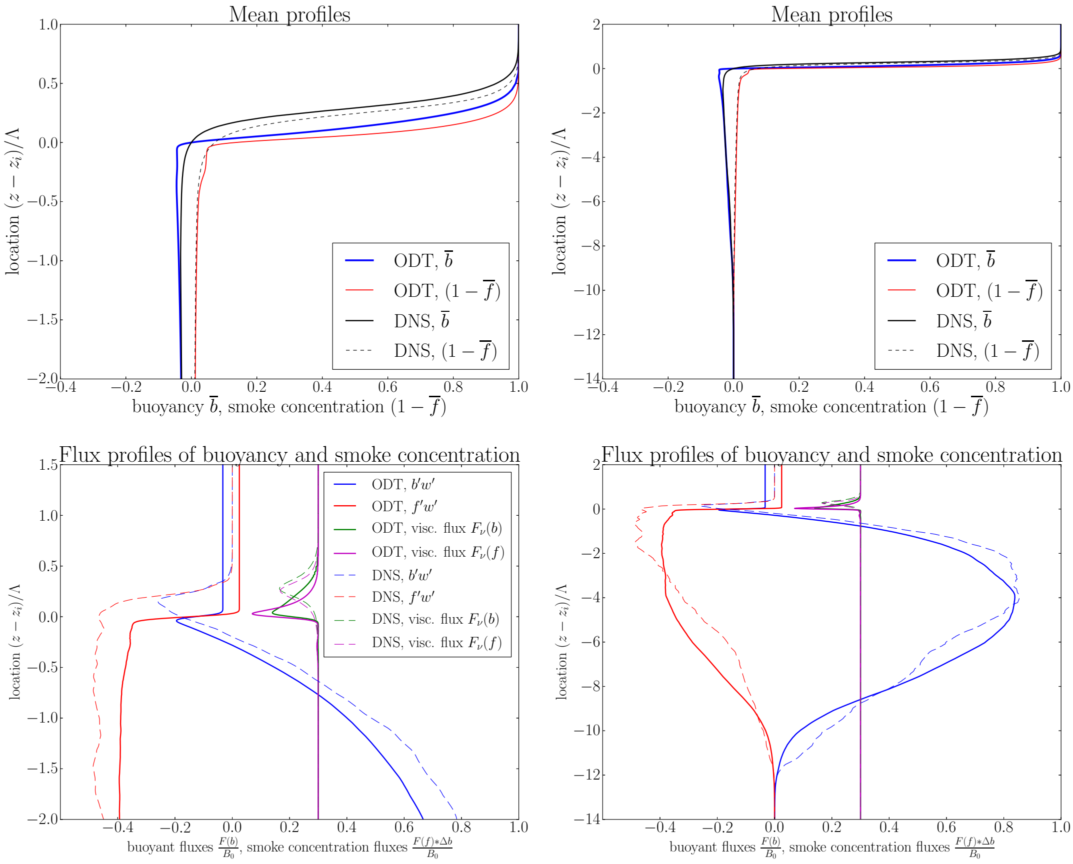

Figure 7.8: Results for the smoke cloud simulation at higher dimensionless parameters; Re = 1600, Ri = 57. The legend for the lower right figure is the same as in the lower left figure. The molecular fluxes are shifted by 0.3. The non-zero profiles for the turbulent fluxes for $\frac{z-zi}{\Lambda} > 0$ are a result of the used non-conservative interpolations as described in section 4.2

this case is interesting due to the fact that the undulations are low, wherefore the effect of horizontal fluxes are reduced.
As the mean profiles show, there is still a difference near the minimum of the buoyancy profile. In contrast to the DNS results ODT shows a buckling and a steep gradient. Nearly the same is also seen for the smoke profile. For the upper part of the mean profiles for $\overline{b} > 0.4$ (and $1 - f > 0.4$) the ODT results show nearly the same shape as the DNS results except for a vertical shift of about 0.2Λ. Comparing the whole simulation domain, ODT gives a very good comparison to the DNS results.
Also the flux profiles compare well to the DNS results. As expected from the mean profiles, the viscous fluxes are higher near the buckling and afterwards tend to DNS results. Similar to the results for the lower Reynolds number case, the turbulent flux profiles[1] again decrease to zero much earlier than the DNS fluxes. This shows that besides the undulations, there are other 3D effects at the region near the inversion point $-0.2 \leqslant \frac{z-zi}{\Lambda} \leqslant 0.2$ not captured by ODT. Nevertheless, again comparing the whole simulation domain, the profiles for the turbulent fluxes are very good approximated by the ODT results.

7.4 VELOCITIES WITHIN THE SMOKE CLOUD SIMULATION

As seen within all previous cases, the channel flow as well as the jet, also within the smoke cloud case the fluctuation velocities are underestimated. Furthermore, due to the lack of a distinct flow direction, all velocity components are just energy holding containers. Even the initialization as described within section 7.1 does not give the velocity components a kinematical meaning due to setting the velocities to zero. The only mechanism generating velocity fluctuations is therefore the kernel addition within the eddy process, which distributes the final available energy to the velocity components. An eddy within this initialized field has no kinetic energy and the only source of energy is the unstable stratification and therefore available potential energy.
The redistribution of the freed potential energy is arbitrary. To give the vertical velocity component w a specific role, this velocity component is the preferred one to gain kinetic energy. This is reasonable as a reflection of the descent of heavier fluid parcels. Therefore the energy redistribution used for freed potential energy is $(u; v; w) = \frac{1}{4}(1; 1; 2)$. In contrast, if the eddy lifts heavier parcels over lighter ones, the needed potential energy is gathered equally from each velocity component $(u; v; w) = \frac{1}{3}(1; 1; 1)$ resulting in the formulation used within the derivation in section 2.2.2 and appendix A.
Figure 7.9 shows the normalized profiles of the horizontal and the vertical RMS velocities, $u_{\mathrm{RMS}} = \sqrt{u'^2 + v'^2}$ and $w_{\mathrm{RMS}} = \sqrt{w'^2}$ respectively. The velocities are normalized using the convective reference flux B_{ref} as described by Lozar and Mellado [59] to generate self-similar pro-

---

[1] The non-zero value for the turbulent fluxes are a result of the used non-conservative interpolation. The constant profiles for $\frac{z-zi}{\Lambda} > 0.05$ have to be treated as zero.

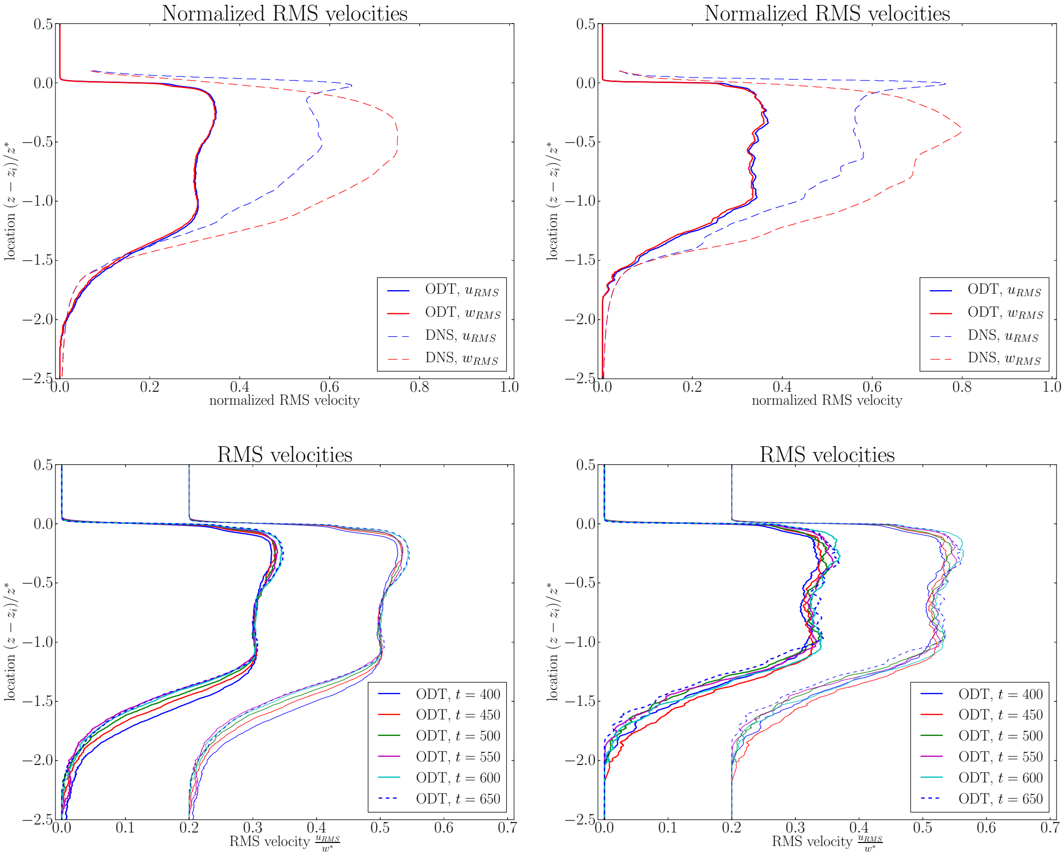

Figure 7.9: Results for the fluctuation velocity profiles normalized by B_{ref}. The left figures shows the results for $\mathrm{Re} = 800$, $\mathrm{Ri} = 10$ and the right ones for $\mathrm{Re} = 1600$, $\mathrm{Ri} = 57$. The upper ones show the comparison to DNS results, while the lower ones show the time self-similarity of the ODT simulations. Within the lower figures, the thick lines are the u_{RMS} profiles and the w_{RMS} are shifted by 0.2. u_{RMS} is the horizontal velocity component. Within ODT the freed potential energy is distributed among the velocity components by $\frac{1}{4}(1;1;2) = (u;v;w)$

files. The reference flux is defined by the two cooling components within the system; (i) the cloud-bulk cooling Q_{cbl} below the inversion point and (ii) the cooling of the inversion layer Q_{inv}. The instantaneous cloud-bulk cooling is the time derivative of the integrated mean buoyancy up to the cloud top, indicated by the inversion point. The inversion layer cooling instead is calculated the same way but starting at the inversion point.

$$\begin{aligned} -B_0 &= \frac{\partial}{\partial t}\int_0^{zi} b(z)\,dz + \frac{\partial}{\partial t}\int_{zi}^{\infty} b(z)\,dz \\ &= Q_{cbl} + Q_{inv} \end{aligned} \tag{7.6}$$

Lozar and Mellado [59] define the reference flux as the time averaged cloud-bulk cooling

$$B_{ref}(t) = -\frac{1}{t-t_0}\int_{t_0}^{t} Q_{cbl}(\tau)\,d\tau\,. \tag{7.7}$$

Using this definition of the reference flux, the reference length and the reference velocity can be calculated as follows:

$$\begin{aligned} z^* &= \frac{1}{B_{ref}}\int \overline{w'b'}\,dz \\ w^* &= \left(B_{ref}\,z^*\right)^{1/3}\ . \end{aligned} \tag{7.8}$$

As the results show, ODT underestimates the fluctuation velocities by a factor of two, even if the extra shear is added resulting in an increase of turbulent kinetic energy near the inversion layer. This could be one reason for the sharp inversion profiles described in the previous section due to the fact that also the available turbulent kinetic energy for eddies is therefore underestimated by a factor of four.
Besides the underestimation, ODT shows the same amount of fluctuation velocities for the horizontal and the vertical velocity components. In contrast, the DNS results show that the vertical component fluctuations are higher than the horizontal ones except in a localized zone near the cloud top. On the one side, this shows that the chosen redistribution of energy gives too little energy to the vertical velocity components. A better, but not tested, redistribution would be $\frac{1}{5}(1;1;3)$ or $\frac{1}{9}(2;2;5)$. On the other side, this shows that the used extra shear model is reasonably emulating the location of the peak in the horizontal velocity components and suggests a further modeling of the underestimation of velocity components.
Nevertheless, as two cases shown in figure 7.9 show, ODT reproduces the self-similarity shown by the DNS. Due to the limitations of DNSs to moderate Reynolds and Richardson numbers, this reproduction of self-similarity provides the opportunity to use ODT to extend the range of simulated dimensionless parameters. Furthermore, the reduced effort of ODT also provides the opportunity to include further physical mechanisms present within a real cloud, e. g. evaporation.

7.5 ENTRAINMENT RATES

As described in section 3.3, LESs are overestimating the entrainment velocity due to a too coarse grid resolution around the inversion. This is not the fact within ODT suggesting a good representation of this velocity by ODT. Furthermore, as De Lozar and Mellado [18] describe, the entrainment rate is mainly depending on the difference between introduced cooling, which is equal to the buoyancy flux B_0, and cooling of the cloud bulk Q_{cbl}. Due to the fact that both values are represented within ODT - B_0 due to the implementation of source term within the model and Q_{cbl} due to the meaningful reproduction of the turbulent buoyancy flux $\overline{w'b'}$ - also the cooling of the inversion layer Q_{inv} is reproduced. As De Lozar and Mellado have shown, the entrainment rate for STBL can be calculated using the cooling of the inversion layer Q_{inv}.

$$w_e = -\frac{Q_{inv}}{\Delta b} \tag{7.9}$$

Furthermore, they have shown that there are three contributions for the inversion cooling affecting the entrainment velocity, (i) the cooling due to turbulent transport B_{turb}, (ii) the cooling due to viscous transport B_{visc}, and (iii) the direct cooling B_{dc}.

$$Q_{inv} = \underbrace{\left(\overline{w'b'}\right)|_{zi}}_{B_{turb}} \underbrace{-\kappa_T \left(\overline{\frac{\partial b}{\partial z}}\right)\Bigg|_{zi}}_{B_{visc}} \underbrace{-B_0\left(1-e^{-\tau(zi)}\right)}_{B_{dc}} \tag{7.10}$$

While in the DNS the cooling due to viscous transport can be neglected, within ODT the cooling of the inversion is not only generated by turbulent fluxes and direct cooling. As the figures show, within ODT B_{turb} is underestimated, while B_{visc} is overestimated. The amount of direct cooling is coupled to the smoke profile via $\tau(z_i)$. This shows again that the results strongly depend on the reproduction of the mean smoke profile, wherefore an improvement of the mean smoke profile would directly improve B_{dc} and B_{visc} and indirectly B_{turb}.
Nevertheless, due to the reproduction of Q_{cbl}, using the approximation for the entrainment velocity derived by De Lozar and Mellado

$$w_e = \frac{F_0}{\rho_0 c_p \Delta T}\left(0.175 + \epsilon\frac{\delta_i}{\Lambda}\right) \tag{7.11}$$

ODT also reproduces the entrainment velocity as shown in table 7.3. In this equation ϵ is a constant scaling the dependence of the direct cooling on the inversion thickness δ_i.

Table 7.3: Entrainment velocities simulated by ODT.

Case	ΔT	ϵ	$\frac{\partial z_i}{\partial t}$	equation (7.11)
$Re = 800$, $Ri = 10$	1.75 K	0.3	$6.9\,\frac{mm}{s}$	$5.6\,\frac{mm}{s}$
$Re = 1600$, $Ri = 57$	10 K	0.39	$1.48\,\frac{mm}{s}$	$1.52\,\frac{mm}{s}$

7.6 DISCREPANCIES BETWEEN ODT SIMULATIONS AND DNSS

Within this section the main discrepancies between the DNSs from Lozar and Mellado [18] and the presented ODT simulations are discussed.

As described by Lozar and Mellado the cooling within the DNS is based on a horizontally averaged profile. Due to the calculation of independent realizations within ODT it is impossible to calculate an ensemble average representing the horizontal average for each time step. Even if all realizations are calculated simultaneously so that a ensemble average is possible, due to the stochastic character of ODT and the therefore non-synchronized diffusion steps, the calculated mean profiles would have a time lag. Besides the described time lag, this would also result in a huge amount of memory to keep track of the ODT lines and their statistics.

Therefore, within ODT radiative cooling is based on the instantaneous profile. This could be a reason for the steeper gradients within the mean buoyancy and smoke profiles of ODT. The horizontal average within the DNS broadens the area of direct cooling resulting in a flatter profile.

To emulate this behavior, it is possible to use a predefined mean profile for calculating the cooling. Although this is closer to the modeling within the DNS it raises further uncertainties within ODT. On the one hand there is the question how to define the used mean profile. On the other hand, how should the profile be moved upwards? These two uncertainties could have a direct influence on the results.

A further uncertainty based on the different implementations of the direct cooling is introduced by the horizontal average for the calculation of the results. Resulting from the broader cooling it is possible that also the mean profiles are smeared out due to the horizontal averaging. This could be overcome by calculating the horizontal average after shifting each vertical profile based on its individual inversion layer position $z_i(x, y)$. This could possibly result in steeper gradients.

Another discrepancy is introduced by the current implementation of the data averaging, which is based (i) on an ensemble average over all realizations and (ii) on a time average over $\Delta t = 50\,\mathrm{s}$. Currently not implemented in the aODT code is a more accurate statistics calculation method that is based on snapshots at discrete time steps as presented by Schulz et al. [5]. Even if this procedure is more accurate, as shown by Schulz et al., the calculation based on the time and ensemble average is as accurate as the snapshot ensemble average as long as the time step for averaging is short enough.

7.7 DISCUSSION OF SMOKE CLOUD SIMULATIONS

Within this chapter the ODT results for the smoke cloud case representing the STBL are presented and compared to DNS results by De Lozar and Mellado [18]. Instead of the full boundary layer only the region around the inversion layer was simulated.

First a simulation using no specific models was done showing that ODT overestimates the turbulent depth of the mixing zone. An analysis of different LESM show that the *Time* LESM produces reasonably good results using a model factor $b_{\mathrm{LESM}} \approx 1.0$. This method restricts the acceptance of eddies to those whose turnover time is comparable to the simulation time. This is reasonable due to the fact that the eddy size, which is directly coupled to its turnover time, is linearly growing in time.

Further parameter studies for the ODT parameters C and Z were done. Similar to the results from Schmidt et al. [83] it could be shown that the results are independent of Z and that $C = 30$ gives good reproduction of the turbulent buoyancy flux. Nevertheless, the turbulent smoke flux was still underestimated, wherefore an additional extra shear model around the inversion point zi was introduced.

Another parameter study for the shear model parameter C_{sc} was done. It turned out that the parameter which scales the maximal velocity of the introduced horizontal jet $C_{sc} \in [0.5; 0.7]$ is comparable to the peak within the DNS profiles showing the horizontal fluctuation velocity. Nevertheless, ODT still underestimates the turbulent mixing around the inversion point $-0.2 \leqslant \frac{z-zi}{\Lambda} \leqslant 0.7$ resulting in a too small inversion thickness. The same tendencies are also recognized for the simulation using higher initial Reynolds and Richardson numbers.

The comparisons of the fluctuation velocities show a tendency to self-similar profiles (i) in time and (ii) for different cases as presented by DNS. Within ODT the freed potential energy has to be stored within the velocity components. Within the work of this thesis two redistributions were tested. It is shown that a non-equal distribution shows similar tendencies between the vertical and horizontal fluctuation components. This could be further improved by using the suggested alternative distributions.

Finally, the entrainment velocity is discussed. It is shown that ODT reproduces the entrainment even if the representation of the inversion layer is inaccurate. It is further discussed that all further investigations should target an improvement of the mean smoke profile due to a strong dependency of all other profiles and the derived quantities on the mean smoke profile.

Part III

CONCLUSION

8

CONCLUSION

As described in the introduction, the challenges for computational fluid dynamics (CFD) are multiple. The cost for DNSs is currently unaffordable for most industrial applications, wherefore the need for modeling rises. This fact provides three different research directions for improvement; (i) the optimization of DNS codes and computers, (ii) the improvement of existing modeling strategies such as RANS and LES, or (iii) the development of totally new modeling strategies. The here presented one-dimensional turbulence (ODT) model belongs partly to the third and partly to the second group. On the one hand it is a new modeling strategy, which has to be validated, and on the other hand it is an existing strategy, which has to be optimized.

Within this thesis both parts are done. On the one hand ODT has been improved to simulate the channel flow as a representative for turbulent wall-bounded flows (TWBF) up to Reynolds numbers of industrial size. On the other side, it is validated against the passive scalar transport in a channel, pressure fluctuation in a channel, the simulation of free-slip boundaries represented by a free liquid jet, the breakup of droplets and the smoke cloud simulation. All these flows target specific physical problems that might be present in an industrial flow. The passive scalar transport is e. g. a representative for the heat transport or the transport of species and impurities. The free-slip jet flow is a representative for all flows with two immiscible fluids and the turbulence interaction at this surface. The jet breakup is by itself an interesting effect for industry. And the smoke cloud simulation is a representative for stratified flows.

Within chapter 5 the results of the channel flow based simulations were presented. It was shown that ODT reaches friction Reynolds numbers up to $\mathrm{Re}_\tau = 500,000$, which is relevant for a lot of industrial applications. It was further shown that ODT misses the effect of large scale interactions in the streamwise and cross-streamwise directions wherefore it should be coupled to 3D simulations providing these information. This shortcoming was discussed in case of the fluctuation velocities using the diagnostic plot from Alfredsson et al. [8] and the budgets of the turbulent kinetic energy.

The results based on the pure channel flow are used to simulate the channel flow with a passive scalar. The results are compared to DNS data from Kawamura et al. [42] and Schwertfirm and Manhart [87]. It was shown that ODT has the capability to reproduce these results and can extend the range of application to industrial flows.

As a last case based on the channel flow, ODT has been used to simulate the channel flow with a fluctuating pressure gradient. Due to the lack of a direct comparison case, a similar but more challenging case presented by He and Seddighi [32] was used. It turned out that ODT doesn't reproduce the detailed effects of this case but reproduces the adaption time within an order unity factor. The simulation of the case with a fluctuating pressure gradient was done to influence the wall shear stress. As the results show, the PDF of the wall shear stress varies between the different cases but the mean wall shear stress stays constant.

In chapter 6 the results of the non-breaking and breaking liquid jet are presented. The jet results are compared to measurements from Wolf et al. [95] showing comparable results for the mean and fluctuation velocity. Discrepancies at the wall are discussed and it turned out, that they are intrinsic in ODT due to neglecting 3D motions at the wall. Further analysis of the turbulent kinetic energy budgets show for the used normalization a self similar behavior for distances from the jet exit greater than $^x/_D = 15$.

Based on the non-breaking jet simulations, the droplet generation was simulated. The results show a great variation for the initial and last breakup position and therefore an uncertainty of the definition of the initial breakup position. Even if the measured positions are at too low $^x/_D$ values, the results give similar trends. The Weber number boundary for having a initial breakup was reproduced and a physically meaningful trend for high Weber numbers was observed. Also the constancy of the last breakup was reproduced for $\mathrm{We} \geqslant 10^7$. Further investigations by A. Movaghar in cooperation with the author have improved the comparability.

Analyses of the droplet distribution have shown that two different effects causing the last droplet are present. On the one hand droplets are generated by turbulence driven by the liquid turbulence within the jet. On the other side droplets are generated by aerodynamic turbulence. It is shown that the aerodynamically driven droplets depend on the Weber number while the droplets generated by liquid turbulence are only less affected.

As a last test case the smoke cloud emulating the top of a stratocumulus topped boundary layer (STBL) was chosen. The results are presented in chapter 7. First, parameter studies for both ODT parameters and the large eddy suppression method (LESM) were done. It turned out that ODT reproduces major effects of the DNS from De Lozar and Mellado [18] but underestimates the turbulent transport of the smoke scalar. This results in a too sharp smoke profile wherefore (i) the cooling is too localized and (ii) the buoyancy profile is too sharp. Further modeling of the peak in the horizontal fluctuation velocity improves the comparability but there are still discrepancies within the results.

A further discussion of the fluctuation velocity profiles show similar to the DNS results a self similarity in time and for different Reynolds numbers. Also the entrainment velocity is reproduced, which is reasonable for ODT as the discussion of the derivation from De Lozar and Mellado [18] shows.

Summarizing, it could be said that ODT is a valuable simulation model. It provides detailed results for specific cases and can reach dimensionless parameters comparable to industrial sizes. Furthermore, it provides the opportunity for parameter studies, where other approaches are too costly or inaccurate. It further provides insight into detailed

turbulent statistics without modeling the smallest scales.
ODT also has shortcomings due to neglecting major parts of 3D motions. They could be compensated by coupling to large scale 3D simulations as it is done in two distinct ways by ODTLES and LESODT.

9

OUTLOOK

Within this chapter some ideas for further investigations are presented. They target on the one hand improvements within ODT and analysis of ODT results and on the other hand ideas for further measurements and DNSs.

As the results of the pure channel flow and the channel flow including a passive scalar show, further investigations of ODT in this area are not needed. Here the coupling to 3D large scale simulations is needed to include the missed effects as it is done e. g. by Glawe et al. [30]. For the passive scalar simulation at very high or very low Prandtl or Schmidt numbers further investigations could target the optimization of the implementation of the diffusion process within ODT, which becomes costly in these regimes. This could be the separation of grids for velocities and the passive scalar. Additional test cases as the Couette flow with a passive scalar or the channel flow with passive scalar flux equal on both walls as presented by Schwertfirm and Manhart [87] could yield further insights into the behavior of a passive scalar.

For the simulation with a fluctuating pressure gradient, further DNS simulations are needed. For ODT it is essential that these simulations are at moderately high friction Reynolds numbers where no laminar similarity exists as is the case for $\mathrm{Re}_\tau \approx 180$. Furthermore, the fluctuation range of the pressure should be limited so that no back flow is generated.

Further investigations for the jet simulation should target the shortcomings of ODT at the wall. A further coupling to 3D large scale simulations would also be beneficial. These two major topics target the two greatest problems of ODT simulating the non-breaking jet. The first one targets the anisotropy at the free-slip wall while the second targets the large scale interactions present in the streamwise direction. Furthermore, also DNSs and measurements are needed to provide detailed information for validation of ODT.

In case of the jet breakup, detailed measurements of the initial breakup location are needed. It is currently unclear if the data presented by Wu and Faeth [99] is the mean, median or most probable breakup position.

All further investigations for the smoke cloud should target an improvement of the mean profile of the smoke scalar due to the strong coupling to the buoyancy profile and all derived statistics. Compared to the DNS results from De Lozar and Mellado [18], within the DNS the radiative cooling is based on the horizontally averaged smoke profile. In contrast to that, within ODT the cooling is based on the instantaneous profile due to the missing horizontally averaged information, which is by construction unfeasible within ODT. A possible emulation of this could be done by using a fixed predefined mean smoke profile, which moves upwards based (i) on a given entrainment velocity or (ii)

by fixing it to a certain point within the profiles, e. g. $b(z_{\text{fix}}) = 0.5$.
Besides this improvement of representation of this DNS case by ODT, it is also possible to include further models targeting the evaporative cooling. As Bretherton et al. [11] have written within the introduction, the smoke cloud case was chosen to exclude the uncertainties within different evaporation models. Due to the possibility to implement these models easily within ODT detailed comparison studies could be done.
Finally, due to the 1D formulation of ODT and the adaptivity of aODT, it is possible to simulate the smoke cloud including the lower surface boundary. Further studies should also target the effect of this lower boundary on the entrainment velocity.

Part IV

APPENDIX

A

DERIVATIONS OF ODT

Within this appendix a detailed derivations of the main equations of ODT and aODT from section 2.2 is given. For simplicity this is done first for ODT and afterwards the changes for aODT are highlighted. Finally the equations from aODT are verified to the ODT equations by specifying to constant density.

A.1 ODT

First the kinetic and potential energy change due to a mapping process are calculated using the Boussinesq approximation. Throughout this derivation, the potential energy is a placeholder for any potential energy. Also the model energies ΔE_{mod} introduced in section 2.2.2 follow the same derivation except the fact that model energies get another constant c_{mod} determining if the model energy is taken into account during the calculation of the energy redistribution constants c_i (equation (2.18), (A.14), or (A.24)).

$$\begin{aligned}
\Delta E_{kin,i} &= \frac{\rho_0}{2} \int \left([u_i(f(z)) + c_i K(z)]^2 - [u_i(z)]^2 \right) \mathrm{d}z \\
&= \frac{\rho_0}{2} \int \left([u_i(f(z))]^2 + 2u_i(f(z)) c_i K(z) \right. \\
&\qquad \left. + c_i^2 K^2(z) - [u_i(z)]^2 \right) \mathrm{d}z \\
&= \rho_0 \int u_i(f(z)) c_i K(z)\, \mathrm{d}z + \frac{\rho_0}{2} \int c_i^2 K^2(z)\, \mathrm{d}z \\
&= \rho_0 l^2 u_{K,i} c_i + c_i^2 \frac{\rho_0}{2} l^3 KK \\
&= \rho_0 l^2 u_{K,i} c_i + c_i^2 \rho_0 l^3 \frac{2}{27}
\end{aligned} \tag{A.1}$$

$$\begin{aligned}
\Delta E_{pot} &= g \int [\rho(f(z)) z - \rho(z) z]\ \mathrm{d}z \\
&= g \int [\rho(f(z)) z - \rho(f(z)) f(z)]\ \mathrm{d}z \\
&= g \int \rho(f(z)) K(z)\, \mathrm{d}z \\
&= g l^2 \rho_K,
\end{aligned} \tag{A.2}$$

where $f(z)$ and $K(z)$ are defined in sections 2.2.1 and 2.2.2 and $KK = \frac{1}{l^3} \int K^2(z)\, \mathrm{d}z = \frac{4}{27}$.
For the kinetic energy change the identity $\int [u_i(z)]^2\, \mathrm{d}z = \int [u_i(f(z))]^2\, \mathrm{d}z$ is used, which is a consequence of momentum conservation shown below.
Using the Boussinesq approximation $\frac{T - T_0}{T_0} = -\frac{\rho - \rho_0}{\rho_0}$ and the definition of the buoyancy b, the potential energy change can be expressed

by the buoyancy instead of the density. Within the implementation of aODT the density formulation is used.

$$\begin{aligned} b &= g\frac{T-T_0}{T_0} && \text{(A.3)} \\ &= -g\frac{\rho-\rho_0}{\rho_0} \qquad \rightarrow \quad \rho = \rho_0 - \frac{\rho_0}{g}b \\ \Delta E_{pot} &= -\rho_0 \int b(f(z))z - b(z)z\,dz \\ &= -\rho_0 l^2 b_K && \text{(A.4)} \end{aligned}$$

Momentum conservation requires:

$$\begin{aligned} \int u_i(z)\,dz &= \int u_i(f(z))\,dz \\ &= \int u_i(f(z)) + c_i K(z)\,dz, && \text{(A.5)} \end{aligned}$$

wherefore

$$c_i \int K(z)\,dz \equiv 0. \tag{A.6}$$

Energy conservation requires:

$$\begin{aligned} \Delta E &= \sum_i \Delta E_{kin,i} + \sum_{pot} \Delta E_{pot} = 0 && \text{(A.7)} \\ &= \sum_i \left(\Delta E_{kin,i} + \frac{1}{3}\left[\sum_{pot} \Delta E_{pot}\right]\right), \end{aligned}$$

where $\sum\limits_{pot}$ symbolizes the summation over all possible potential energies and $\sum\limits_i$ the summation over all three velocities.
Due to the fact that the summation of all energy parts has to be conserved, a redistribution of energy can be introduced as follows.

$$\Delta E = \sum_i \left(\Delta E_{kin,i} + \frac{1}{3}\left[\sum_{pot} \Delta E_{pot}\right] - \Delta E_{redist,i}\right) \tag{A.8}$$

$$\Delta E_{redist,i} = -\alpha \frac{27}{8}\rho_0 l \sum_j u_{K,j}^2 T_{ij} \tag{A.9}$$

$$\sum_i \Delta E_{redist,i} \equiv 0 \qquad\qquad T_{ij} = \begin{cases} -1 & \text{if } i = j \\ \frac{1}{2} & \text{if } i \neq j \end{cases}$$

$$\begin{aligned} \Delta E_i = {} & \rho_0 l^2 c_i u_{K,i} + \frac{2}{27}\rho_0 l^3 c_i^2 + \frac{1}{3}\left[\sum_{pot} \Delta E_{pot}\right] \\ & - \alpha \frac{27}{8}\rho_0 l \sum_j u_{K,j}^2 T_{ij} && \text{(A.10)} \end{aligned}$$

Also as mentioned in the beginning of this section, within the formulation of $E_{kin,i}$ the model energies ΔE_{mod} are missed, wherefore they are added here using the corresponding constants c_{mod}.

$$\begin{aligned}\Delta E &= \sum_i \left(\Delta E_{kin,i} + \frac{1}{3}\sum \Delta E_{pot} + \frac{1}{3}\sum c_{mod}\Delta E_{mod} - \Delta E_{redist,i}\right) \qquad \text{(A.11)}\\ &:= \sum_i \Delta\widetilde{E}_{kin,i}\,,\end{aligned}$$

where $\sum$ indicates the summation over all potential and model energies.

One example of such a model energy is the viscous damping $c_{vis}\Delta E_{vis} = c_{vis}\frac{27}{8}Z\frac{\nu^2\rho_0}{l}$ using $c_{vis} = 1$ for the calculation of the acceptance probability and $c_{vis} = 0$ for the calculation of c_i.

As explained in section 7.4, if the potential energy is positive, the freed energy is not uniquely distributed by a third to each velocity component. Instead, one velocity component could be preferred in getting energy.

$$\begin{aligned}\Delta E &= \sum_i \left(\Delta E_{kin,i} + \frac{1}{3}\sum c_{pot,i}\Delta E_{pot} + \frac{1}{3}\sum c_{mod}\Delta E_{mod} - \Delta E_{redist,i}\right)\\ &:= \sum_i \Delta\widetilde{E}_{kin,i} \qquad \text{(A.12)}\end{aligned}$$

$$c_{pot,i} = \begin{cases}(1;1;1) & \text{if potential energy is negative}\\ {}^3\!/_4\,(1;1;2) & \text{if potential energy is positive}\end{cases} \qquad \text{(A.13)}$$

These constants $c_{i,pot}$ are examples used within the smoke cloud calculation.

For better readability, the summation of potential and model energies is concluded.

$$\Delta\widetilde{E}_{pot} = \sum \left[c_{i,pot}\Delta E_{pot} + c_{mod}\Delta E_{mod}\right]$$

Now find solutions for c_i with $\Delta\widetilde{E}_{kin,i} = 0$, which results in $\Delta E = 0$.

$$c_i = \frac{27}{4l}\left(-u_{K,i} + \operatorname{sgn}(u_{K,i})\sqrt{u_{k,i}^2 + \alpha\sum_j T_{ij}u_{k,j}^2 - \frac{8}{27}\frac{1}{\rho_0 l}\frac{\Delta\widetilde{E}_{pot}}{3}}\right) \qquad \text{(A.14)}$$

The sign of the square root is chosen to be the opposite of $-u_{K,i}$ which is enforced by the sgn-function.

As introduced by Kerstein et. al. [48] the matrix T_{ij} has to obey the energy conservation ($\sum \Delta E_{redist,i} = 0$) and it has to be invariant under permutation of indices. Furthermore, for $\alpha = 1$ the main diagonal

of the matrix has to be one, resulting in a full distribution of the kinetic energy of one component to the other ones. Other typically used values for α are zero for no redistribution or $\alpha = {}^2\!/_3$ to emulate the tendency to isotropy.
As described by Ashurst and Kerstein [9] the kinetic energy of an eddy is proportional to its size l and turnover time τ. This eddy energy has to be provided by the kinetic energy of the flow and the freed potential energy. The maximum available energy that can be provided by the eddy is given by the sum of the minima of $\Delta\widetilde{E}(c_{i,\min})$.

$$\begin{aligned}
\frac{\partial \Delta\widetilde{E}_i}{\partial c_i} &= \frac{4}{27}\rho_0 l^3 c_i + \rho_0 l^2 u_{K,i} = 0 \\
c_{i,\min} &= -\frac{27}{4l} u_{K,i} && \text{(A.15)} \\
\Delta\widetilde{E}(c_{i,\min}) &= -\frac{27}{4}\rho_0 l u_{K,i}^2 + \frac{27}{8}\rho_0 l u_{K,i}^2 + \frac{1}{3}\Delta\widetilde{E}_{\text{pot}} \\
&\quad - \alpha\frac{27}{8}\rho_0 l \sum_j u_{K,j}^2 T_{ij} && \text{(A.16)} \\
\Delta E_{\min} &= \sum_i \Delta\widetilde{E}(c_{i,\min}) \\
&= -\frac{27}{8}\rho_0 l u_{K,i}^2 + \Delta\widetilde{E}_{\text{pot}} && \text{(A.17)}
\end{aligned}$$

Therefore, the eddy energy can be calculated as follows, where ${}^l\!/_\tau$ is an expression for the eddy velocity and $\rho_0 l \frac{l^2}{\tau^2}$ is the eddy energy per unit cross-sectional area of the eddy.

$$\begin{aligned}
\rho_0 l \frac{l^2}{\tau^2} &\sim -\Delta E_{\min} && \text{(A.18)} \\
\frac{l^2}{\tau^2} &\sim \sum_i u_{k,i}^2 - \frac{8}{27}\frac{1}{\rho_0 l}\Delta\widetilde{E}_{\text{pot}} \\
\frac{1}{\tau} &= \frac{C}{l}\sqrt{\sum_i u_{k,i}^2 - \frac{8}{27}\frac{1}{\rho_0 l}\Delta\widetilde{E}_{\text{pot}} - Z\frac{\nu^2}{l^2}} && \text{(A.19)}
\end{aligned}$$

Here, the viscous damping model energy ΔE_{vis} is excluded from the summed potential energies $\Delta\widetilde{E}_{\text{pot}}$ to highlight the consistency with other ODT publications. As explained in these publications, Z is a viscous penalty to avoid unphysical low-energy eddies that are prohibited by viscosity, and C is a proportionality constant.

A.2 VARIABLE DENSITY ODT

Within this section the main changes of the previous ODT derivation for a variable density formulation are summarized. A detailed description of the variable density formulation was published by Ashurst and Kerstein [9]. For simplicity only the potential energy due to buoyancy and the model energy for viscous damping are used within this derivation. It is further assumed that $c_{i,\text{pot}}$ is the same for positive and negative potential energy, wherefore it is skipped.

First a second kernel $J(z)$ has to be introduced to obey the momentum and the energy conservation at the same time.

$$\begin{aligned}
\Delta E_{\text{kin},i} &= \frac{1}{2}\int \rho(f(z))\left[u_i(f(z)) + c_iK(z) + b_iJ_{(}z)\right]^2\,dz \\
&\quad -\frac{1}{2}\int \rho(z)[u_i(z)]^2\,dz \\
&= \frac{1}{2}\Bigg[\underbrace{\int \rho(f(z))[u_i(f(z))]^2 - \rho(z)[u_i(z)]^2\,dz}_{=0} \\
&\quad + \frac{1}{2}c_i^2\underbrace{\int \rho(f(z))K(z)^2\,dz}_{\rho_{KK}} + \frac{1}{2}c_i\underbrace{\int \rho(f(z))u_i(f(z))K(z)\,dz}_{\rho_{K,i}} \\
&\quad + \frac{1}{2}b_i^2\underbrace{\int \rho(f(z))J(z)^2\,dz}_{\rho_{JJ}} + \frac{1}{2}b_i\underbrace{\int \rho(f(z))u_i(f(z))J(z)\,dz}_{\rho_{J,i}} \\
&\quad + \frac{1}{2}c_ib_i\underbrace{\int \rho(f(z))K(z)J(z)\,dz}_{\rho_{KJ}}\Bigg] \\
&= c_i\left(\rho_{K,i} + \frac{b_i}{c_i}\rho_{J,i}\right) + c_i^2\left(\frac{1}{2}\rho_{KK} + \frac{1}{2}\frac{b_i^2}{c_i^2}\rho_{JJ} + \frac{b_i}{c_i}\rho_{KJ}\right) \\
&= c_i\underbrace{(\rho_{K,i} - H\rho_{J,i})}_{P_i} + c_i^2\underbrace{\left(\frac{1}{2}\rho_{KK} + \frac{1}{2}H^2\rho_{JJ} - H\rho_{KJ}\right)}_{S}
\end{aligned} \tag{A.20}$$

Here H is $-\frac{b_i}{c_i}$. For $\rho(z) = \rho_0$ the constant b_i has to be zero. The additional kernel J is chosen to be $J(z) = |K(z)|$.

An analysis of momentum conservation gives:

$$\begin{aligned}
0 = \Delta J_i &= \int \rho(f(z))\left[u_i(f(z)) + c_iK(z) + b_iJ(z)\right]\,dz - \int \rho(z)u_i(z)\,dz \\
&= c_i\int \rho(f(z))K(z)\,dz + b_i\int \rho(f(z))J(z)\,dz \\
&= c_i\rho_K + b_i\rho_k \\
b_i &= -c_i\frac{\rho_K}{\rho_J}.
\end{aligned} \tag{A.21}$$

In principle, the fluid momentum can be changed if e. g. a two-way coupling to particles is simulated resulting in a different representation of momentum conservation.

To be consistent with the previous section ρ_K is defined as in equation (A.2) in contrast to the publication of Ashurst and Kerstein [9]. Therefore, ρ_J is also defined analogously to equation (A.2).

Due to the changes in the expression of the kinetic energy, the expressions of $\Delta E_{redist,i}$, $\Delta\widetilde{E}_{kin,i}$ and therefore c_i have changed.

$$\Delta E_{redist,i} = -\alpha\frac{1}{4S}\sum_j P_j^2 T_{ij} \tag{A.22}$$

$$\Delta\widetilde{E}_{kin,i} = c_i P_i + c_i^2 S - \alpha\frac{1}{4S}\sum_j P_j^2 T_{ij} + \frac{1}{3}\Delta E_{pot} \tag{A.23}$$

$$c_i = \frac{1}{2S}\left(-P_i + \operatorname{sgn}(P_i)\sqrt{P_i^2 + \alpha\sum_j P_j^2 T_{ij} - \frac{4}{3}S\Delta E_{pot}}\right) \tag{A.24}$$

Also, the calculation of the maximal extractable energy due to the eddy has changed.

$$c_{i,min} = -\frac{P_i}{2S} \tag{A.25}$$

$$\Delta E_{min} = -\sum_i \frac{P_i^2}{4S} + \Delta E_{pot} \tag{A.26}$$

In the variable density formulation the eddy energy is defined by $\frac{27}{4}\frac{\rho_{KK}}{l^2}\frac{l^2}{\tau^2}$, where $\frac{27}{4}\frac{\rho_{KK}}{l^2}$ is the equivalent to $\rho_0 l$ in the constant density formulation.
As explained in the erratum of the publication from Ashurst and Kerstein [9] the available energy needs a prefactor of $\frac{8}{27}$ to reduce to the corresponding constant density formulation. The viscous penalty term is formed by using quantities μ_{eff} and ρ_{eff}, which have to be harmonically averaged over the eddy region as presented by Echekki et al. [26], if they are not constant.

$$\frac{27}{4}\frac{\rho_{KK}}{l^2}\frac{l^2}{\tau^2} \sim \frac{8}{27}\left(\frac{P_i^2}{4S} - \Delta E_{pot}\right) - Z\frac{\mu_{eff}^2}{\rho_{eff} l} \tag{A.27}$$

A.3 VERIFICATION OF THE VARIABLE DENSITY FORMULATION

Within this section the equations from the last section are specialized to constant properties. For the buoyant potential energy the Boussinesq assumption is used.
Equation (A.21):

$$\begin{aligned} b_i &= -c_i\frac{\rho_K}{\rho_J} = -c_i\frac{\int \rho(f(z))K(z)\,dz}{\int \rho(f(z))J(z)\,dz} \\ &= -c_i\frac{\rho_0\int K(z)\,dz}{\rho_0\int J(z)\,dz} = 0 \end{aligned}$$

As described in section 2.2.2, the integral of the kernel K is zero while the integral of J is non-zero. Therefore, b_i is equal to zero for constant properties, resulting in (i) $H = -\frac{b_i}{c_i} = 0$ and (ii) the following expression for the change of the kinetic energy (A.20), P_i, and S:

$$\begin{aligned}
\Delta E_{\mathrm{kin},i} &= c_i P_i + c_i^2 S \\
&= c_i \left(\rho_{K,i} - H\rho_{J,i}\right) + c_i^2 \left(\frac{1}{2}\rho_{KK} + \frac{1}{2}H^2\rho_{JJ} - H\rho_{KJ}\right) \\
&= c_i \rho_{K,i} + c_i^2 \frac{1}{2}\rho_{KK} \\
P_i &= \rho_{K,i} - H\rho_{J,i} = \rho_{K,i} \\
S &= \frac{1}{2}\rho_{KK} + \frac{1}{2}H^2\rho_{JJ} - H\rho_{KJ} = \frac{1}{2}\rho_{KK}
\end{aligned}$$

Next, the integral expressions $\rho_{K,i}$ and ρ_{KK} are simplified:

$$\begin{aligned}
\rho_{K,i} &= \int \rho(f(z))u_i(f(z))K(z)\,dz \\
&= \rho_0 \int u_i(f(z))K(z)\,dz = \rho_0 l^2 u_{K,i} \\
\rho_{KK} &= \int \rho(f(z))K(z)^2\,dz \\
&= \rho_0 \int K(z)^2\,dz = \rho_0 l^3 KK = \frac{4}{27}\rho_0 l^3
\end{aligned}$$

Here the definition of $u_{K,i}$ and the result $KK = \frac{4}{27}$ introduced in equation (A.1) are used. Using these expressions, the kinetic energy change can be written as:

$$\begin{aligned}
\Delta E_{\mathrm{kin},i} &= c_i \rho_{K,i} + c_i^2 \frac{1}{2}\rho_{KK} \\
&= c_i \rho_0 l^2 u_{K,i} + \frac{2}{27} c_i^2 \rho_0 l^3,
\end{aligned}$$

which is the same as for constant properties (equation (A.1)).

Within the first equation of this section, it is derived that ρ_K is zero. This is needed to reduce the variable density formulation of the kinetic energy change to the constant density formulation. Using the same argumentation, also the potential energy would be zero. In contrast to the formulation of b_i, within the calculation of the potential energy, the integral ρ_K is multiplied by nonzero g, wherefore it has to be considered in the energy conservation.

Next the expression for c_i is simplified:

$$\begin{aligned}
c_i &= \frac{1}{2S}\left(-P_i + \operatorname{sgn}(P_i)\sqrt{P_i^2 + \alpha \sum_j P_j^2 T_{ij} - \frac{4}{3} S \Delta E_{\mathrm{pot}}}\right) \\
&= \frac{1}{\rho_{KK}}\left(-\rho_{K,i} + \operatorname{sgn}(\rho_{K,i})\sqrt{\rho_{K,i}^2 + \alpha \sum \rho_{K,i}^2 T_{ij} - \frac{2}{3}\rho_{KK}\Delta E_{\mathrm{pot}}}\right) \\
&= \frac{27}{4}\frac{1}{\rho_0 l^3}\left(-\rho_0 l^2 u_{K,i}\right. \\
&\qquad \left. + \operatorname{sgn}(u_{K,i})\sqrt{\rho_0^2 l^4 \left(u_{K,i}^2 + \alpha \sum u_{K,i}^2 T_{ij}\right) - \frac{8}{27}\rho_0 l^3 \frac{\Delta E_{\mathrm{pot}}}{3}}\right) \\
&= \frac{27}{4l}\left(-u_{K,i} + \operatorname{sgn}(u_{K,i})\sqrt{u_{K,i}^2 + \alpha \sum u_{K,i}^2 T_{ij} - \frac{8}{27}\frac{1}{\rho l}\frac{\Delta E_{\mathrm{pot}}}{3}}\right)
\end{aligned}$$

As last the expression for the eddy energy (A.27) has to be simplified:

$$
\begin{aligned}
\frac{27}{4}\,\frac{\rho_{KK}}{l^2}\,\frac{l^2}{\tau^2} &\sim \frac{8}{27}\left(\frac{P_i^2}{4S} - \Delta E_{\mathrm{pot}}\right) - Z\frac{\mu_{\mathrm{eff}}^2}{\rho_{\mathrm{eff}} l} \\
\frac{l^2}{\tau^2} &\sim 2\left(\frac{4}{27}\right)^2 \frac{l^2}{\rho_{KK}}\left(\frac{\rho_{K,i}^2}{2\rho_{KK}} - \Delta E_{\mathrm{pot}}\right) - Z\frac{\mu_{\mathrm{eff}}^2 l}{\rho_{\mathrm{eff}}\rho_{KK}}\,\frac{4}{27} \\
&\sim 2\left(\frac{4}{27}\right)^2 \frac{1}{\rho_0 l \frac{4}{27}}\left(\frac{\rho_0^2 l^4 u_{K,i}^2}{2\rho_0 l^3 \frac{4}{27}} - \Delta E_{\mathrm{pot}}\right) - Z\frac{\mu_0^2 l}{\rho_0\rho_0 l^3 \frac{4}{27}}\,\frac{4}{27} \\
&\sim u_{K,i}^2 - \frac{8}{27}\,\frac{1}{\rho_0 l}\Delta E_{\mathrm{pot}} - Z\frac{\mu_0^2}{\rho_0^2 l^2}
\end{aligned}
$$

This also verifies that the factor introduced by Ashurst and Kerstein [9] is needed as described in the erratum.

B

DERIVATION OF THE 1/4-RICHARDSON LAW FOR ODT

For the simulation of the smoke cloud it is essential to model the correct relationship between kinetic energy and potential energy caused by stratification. This relationship is expressed by the $Ri_{1/4}$ law where

$$Ri = \frac{\frac{g}{T_0}\frac{\partial T}{\partial z}}{\left(\frac{\partial u}{\partial z}\right)^2}. \tag{B.1}$$

The corresponding gradients can be seen as mean gradients over a specific region. Therefore, the gradients are constants and the functions T and u are linear functions like $g(z) = \alpha z + \beta$.
As discussed by J. S. Turner [93], if the Richardson number is smaller than $^1/_4$ the stratification is unstable and the velocity gradient provides enough energy to overcome the potential energy needed to move heavier parcels above lighter ones and to generate unstable stratified regions. In this view, the Richardson number can be expressed by

$$Ri = \frac{1}{\gamma} = \frac{\frac{g}{T_0}\frac{\partial T}{\partial z}}{\left(\frac{\partial u}{\partial z}\right)^2} \tag{B.2}$$

resulting in an unstable stratification if $\gamma \geqslant 4$. This provides a relationship between the functions of T and u as follows assuming that the velocity is given by a linear function as mentioned above.

$$\frac{\partial T}{\partial z} = \frac{1}{\gamma}\frac{T_0}{g}\left(\frac{\partial u}{\partial z}\right)^2 = \frac{1}{\gamma}\frac{T_0}{g}a^2 = \hat{a} \tag{B.3}$$

The gradient of ρ can be calculated using the Boussinesq approximation.

$$\begin{aligned}\rho &= \rho_0\left(1 - \frac{T - T_0}{T_0}\right)\\ &= \rho_0\left(1 - \frac{\hat{a}z + \hat{b} - T_0}{T_0}\right)\\ &= -\hat{a}\frac{\rho_0}{T_0}z + \rho_0\left(2 - \frac{\hat{b}}{T_0}\right) = -\widetilde{a}z + \widetilde{b}\end{aligned} \tag{B.4}$$

Within ODT the eddy rate expression (2.22) decides if an eddy can be accepted or not. An eddy can be accepted only if the radicand is positive which means that, neglecting the viscous damping term the kinetic energy has to be greater than the potential energy.

$$\begin{aligned}\sum_i E_{kin,i} &\geqslant E_{pot}\\ u_{K,x}^2 &\geqslant \frac{8}{27} l \frac{g}{\rho_0}\rho_K\end{aligned} \tag{B.5}$$

It is assumed that all kinetic energy is stored in the u_x velocity component.
For given linear functions for u and T the values u_K and T_K can be calculated analytically using the equations for $f(z)$ (2.12) and $K(z) = z - f(z)$.

$$
\begin{aligned}
g(z) &= \alpha z + \beta \\
g(f(z)) &= \begin{cases} \alpha(3z - 2z_0) + \beta & z_0 \leqslant z \leqslant z_0 + \frac{1}{3}l \\ \alpha(-3z + 4z_0 + 2l) + \beta & z_0 + \frac{1}{3} \leqslant z \leqslant z_0 + \frac{2}{3}l \\ \alpha(3z - 2z_0 - 2l) + \beta & z_0 + \frac{2}{3} \leqslant z \leqslant z_0 l \end{cases}
\end{aligned}
$$

$$
\begin{aligned}
K(z) &= z - f(z) \\
K(z) &= \begin{cases} -2z + 2z_0 & z_0 \leqslant z \leqslant z_0 + \frac{1}{3}l \\ 4z - 4z_0 - 2l & z_0 + \frac{1}{3} \leqslant z \leqslant z_0 + \frac{2}{3}l \\ -2z + 2z_0 & z_0 + \frac{2}{3} \leqslant z \leqslant z_0 l \end{cases}
\end{aligned}
$$

$$
\begin{aligned}
g_K &= \frac{1}{l^2} \int_{z_0}^{z_0+l} K(z) g(f(z))\, dz \\
&= \int_{z_0}^{z_0+\frac{1}{3}l} K(z) g(f(z))\, dz + \int_{z_0+\frac{1}{3}l}^{z_0+\frac{2}{3}l} K(z) g(f(z))\, dz \\
&\quad + \int_{z_0+\frac{2}{3}l}^{z_0+l} K(z) g(f(z))\, dz \\
&= -\frac{2}{27}\alpha l
\end{aligned}
\tag{B.6}
$$

Using equations (B.3)–(B.6) the ODT representation of the Richardson law can be derived.

$$
\begin{aligned}
u_{K,x}^2 &\geqslant \frac{8}{27} l \frac{g}{\rho_0} \rho_K \\
\left(-\frac{2}{27} a l\right)^2 &\geqslant \frac{8}{27} \frac{lg}{\rho_0} \left(-\frac{2}{27}(-\widetilde{a}) l\right) \\
1 &\geqslant \frac{4}{\gamma}
\end{aligned}
\tag{B.7}
$$

This shows that ODT is by construction obeying the Richardson law.

C

FURTHER IMPORTANT PARAMETERS OF AODT

Besides the three major parameters in ODT, C, Z and α, which are discussed in section 2.2, other parameters can influence computed results. Within this appendix first the effect of the numerical parameter influencing the mesh refinement $gdens$ is shown. Then the physical parameter l_{max} influencing the maximal eddy size $\max(l)$ is varied, followed by a discussion of the numerical parameter td. Finally, the effect of the target mean acceptance probability $\overline{p}_{\lambda\gamma}$ is shown. All simulations in this appendix are done for $Re_\tau = 590$ using $C = 10$, $Z = 600$ and $\alpha = {}^2/_3$. The minimum cell size is chosen to be $\Delta y_{\text{min}} = 0.00039$, which corresponds to a possible minimal cell size comparable to the cell size chosen for the uniform mesh of the channel flow test case within the BasicODT documentation [47].

Within the aODT code, mesh refinement is controlled by the value $gdens$, which is described in detail by Lignell et al. [56]. Its inverse is a reference arc length per cell for the profiles taken into account for the mesh adaption. For a constant profile, this results in a uniform cell size of $\frac{1}{gdens} L_{\text{dom}}$ corresponding to a number of cells equal to $gdens$, where L_{dom} is the domain length. For a linearly increasing profile the grid cells are smaller due to the fact that the arc length is increased compared to constant profile. Nevertheless, this algorithm could possibly result in cell sizes arbitrarily close to the domain length if the profile is constant except in a tiny part, where the profile has huge fluctuations resulting in an arc length which is dominated by the tiny part. Therefore, a second limitation of the cell sizes to a maximum of $\max(\Delta y) = \Delta y_{\text{max}} L_{\text{dom}}$, where Δy_{max} is an adjustable parameter and chosen to $\Delta y_{\text{max}} = \frac{1}{gdens}$ within this thesis. This ensures that the cell size varies in the range $\Delta y_{\text{min}} \leqslant \Delta y \leqslant \Delta y_{\text{max}}$.

Figure C.1 shows the results of varying $gdens$ and therefore also Δy_{max}. It can be seen that the grid density has only a negligible influence on the mean profile. In contrast for the RMS profile a convergence is seen for increasing grid density. The grid density should be chosen to converge all relevant statistical outputs.

Within this thesis, all simulations based on the channel flow presented in sections 5 and 6 are done with $gdens = 400$ or 1000. Even if this resolution is much finer than within the presented test, it is possible that for the highest friction Reynolds numbers the grid density has to be increased further. On the other hand it is also possible that the numerical transport caused by the adaption process rises for increasing grid density, which was not noticed within the presented test. Nevertheless, these values are used to make the presented Re_τ calculable and to ensure a fine grid with a negligible numerical transport.

Although, this test shows a convergence of results for increasing $gdens$, a full study of the influence of the parameters $gdens$ and Δy_{max}

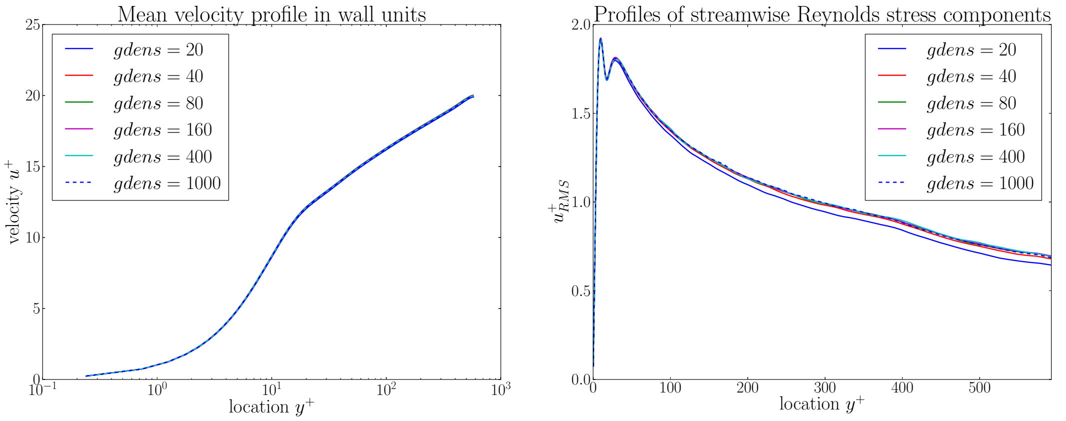

Figure C.1: Dependency of the law of the wall and the u_{RMS} velocity profile on the grid density parameter $gdens$ and therefore the largest possible cell size $\Delta y_{\max} = \frac{1}{gdens} L_{\mathrm{dom}}$.

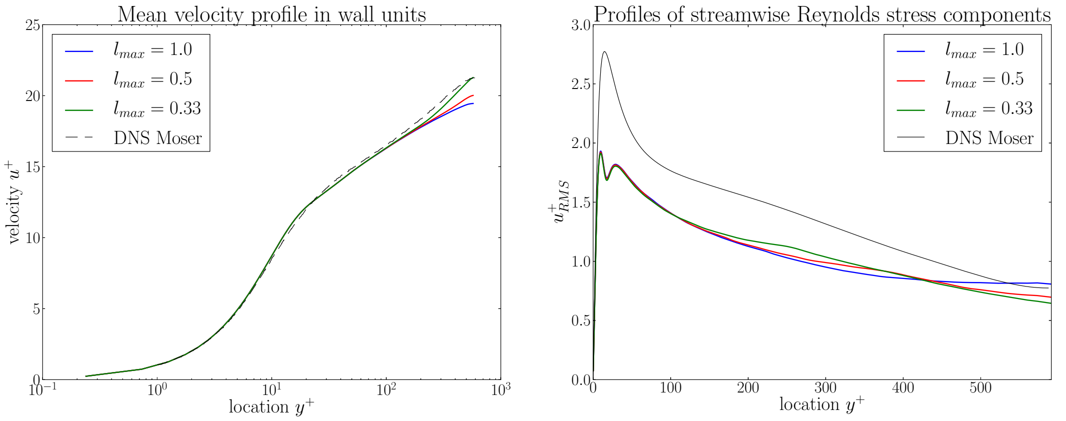

Figure C.2: Dependency of the law of the wall and the u_{RMS} velocity profile on the largest possible eddy size $l_{\max}$.

is needed. Furthermore, also a detailed discussion of the numerical transport caused by the mesh adaption process is needed and should be addressed by further investigations.

Likewise, the maximum eddy size was varied. A similar study was already done by Schmidt et. al [84] showing that for the fully developed channel flow, the maximum eddy size $l_{\max} = \frac{1}{2}$, resulting in $\max(l) = l_{\max} L_{\mathrm{dom}}$, gave good mean flow results.

Figure C.2 shows the results for varying the maximum eddy size. The simulations show that the center region of the channel varies. The mean flow increases with decreasing $l_{\max}$ due to reduced turbulent transport of mean momentum towards the wall. Within the u_{RMS} profiles the profile is reduced near the centerline and increased in the middle region between the center and the wall region. The reason for this behavior is currently unknown.

Although the choice of the maximum eddy size is arbitrary, within this thesis the maximum eddy size for channel flow simulations is set to $l_{\max} = \frac{1}{2}$ to be consistent with previous publications. Nevertheless, this study should be redone in more detail using a higher friction Reynolds number. With a higher friction Reynolds number, the meso

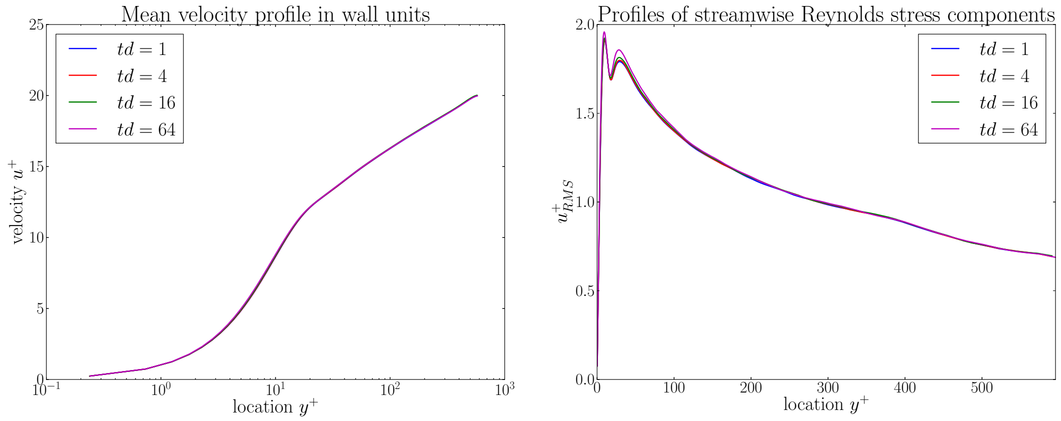

Figure C.3: Dependency of the law of the wall and the u_{RMS} velocity profile on the factor td influencing the time gap between two forced diffusion steps within ODT.

layer is fully developed wherefore the logarithmic layer is present as discussed in section 5.2.1.

At this point the influence of the minimum and average eddy size, l_{min} and l_{av}, influencing the estimated eddy size distribution should be briefly mentioned. While the minimum eddy size can be estimated by the Kolmogorow length scale η, the choice for the average eddy size is arbitrary. Even if the choice of l_{av} influences the estimated eddy size distribution, due to the oversampling process it has no effect on the results. On the other side, the choice of l_{av} can directly influence the calculation time, e. g. by increasing the likelihood of eddies of a size which are mostly rejected. Therefore, the calculation time can be optimized by setting l_{av} as close to the physical value as possible to match the estimated eddy size distribution to the physical one. Due to the fact that the physical distribution is *a priori* unknown, a good estimate used throughout this thesis is $l_{av} = 20 \cdot l_{min}$.

In figure C.3 the influence of the factor td is shown. As can be seen, the mean profile shows no dependency on the factor td. Also the RMS profile is mostly unaffected by the choice of td except the near wall region. To discuss this behavior it has be first explained how the factor td affects the simulation and how the data gathering within aODT is implemented. This effect is only seen by using an implicit solver. If an explicit solver is used, the time integration can be based on the information of each sub-time step Δt_{diff} instead of Δt.

As explained in section 4.1, within ODT two different times exist. The first one t_0 represents the physical time. The second one t is the time of ODT eddy sampling with $t_0 \leqslant t$. If an eddy is accepted at time t it is implemented at time t_0 and the diffusion process is time advanced from t_0 to t, so that t and t_0 are then equal.

Due to the stochastic character of ODT, it may occur that the time lag $\Delta t = t - t_0$ becomes so large that the diffusion, which would have been done since time t_0, would have changed the parameter profiles in such a way that a tested eddy would have been accepted instead of rejected. Therefore, the acceptable time lag should be bounded. Within ODT a diffusion step is forced if the time lag Δt exceeds $dt_{CU} =$

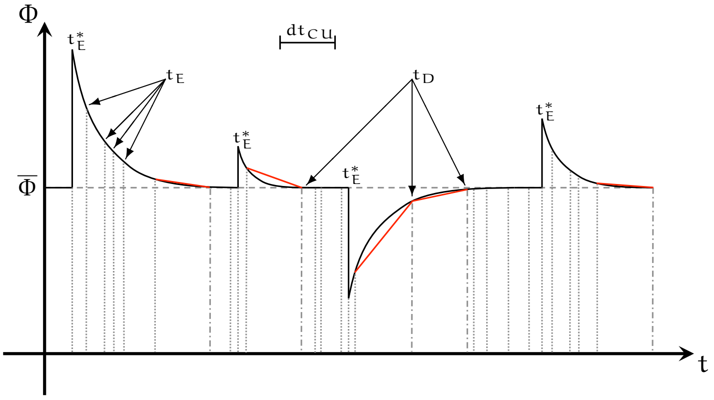

Figure C.4: Time development of Φ at a sample position on the ODT line, where $\overline{\Phi}$ is the mean value. The vertical dotted lines illustrate times of eddy events t_E. The times of eddy events, where the eddy influences the sample position are highlighted with t_E^*. The vertical dash-dotted lines illustrate times where the time lag Δt exceeds dt_{CU}, wherefore a forced diffusion step is calculated. The red lines illustrate the trapezoidal rule for integration.

$\mathrm{td} \cdot \Delta t_{\mathrm{diff}}$, where $\Delta t_{\mathrm{diff}} = {}^{(\Delta y_{\mathrm{min}})^2}/_{\omega}$ is the diffusion time step and ω is the largest relevant transport coefficient, which is the viscosity ν if there are no scalars.

The data gathering within ODT is currently implemented as time integration using the second order trapezoidal rule. Therefore, the integral is calculated as $\frac{1}{2}\Delta t\left(\Phi(y,t) + \Phi(y,t_0)\right)$, where the state at time t is (i) the one after eddy implementation or (ii) the state of the end time of the previous diffusion step. This results in the fact that the profile for integration is discontinuous. As long as the time step is short enough that the change of the profile Φ can be estimated as a linear change, the error of this procedure is small. This holds, if the eddy acceptance frequency is higher than the frequency of diffusion time steps needed.Again, due to the stochastic character of ODT this is not always valid, resulting in the possibility of greater numerical integration errors.

Within figure C.4 the time profile of a sample position on the ODT line is illustrated. The vertical dotted and dash-dotted lines illustrate the times of eddy events t_E or forced diffusen steps t_D, respectively. The eddy events influencing the sample position are termed t_E^*. The forced diffusion steps are done due to the fact that the time lag exceeds dt_{CU}. Therefore, the larger td the greater becomes the error due to the trapezoidal rule as illustrated by the red lines.

The illustrated that the increase in the RMS profiles for increasing td is a numerical error based on the time integration for data averaging. This effect is mainly seen in regions with high fluctuations, due to the fact that fluctuations would decrease exponentially instead of linearly as assumed by the trapezoidal rule.

As a last study the oversampling within ODT is varied. The results are shown in figure C.5. It can be seen that a variation of $\overline{p}_{\lambda\gamma}$ has no influence on the results for the channel flow. Even if this study shows no influence the mean acceptance rate should be much smaller than

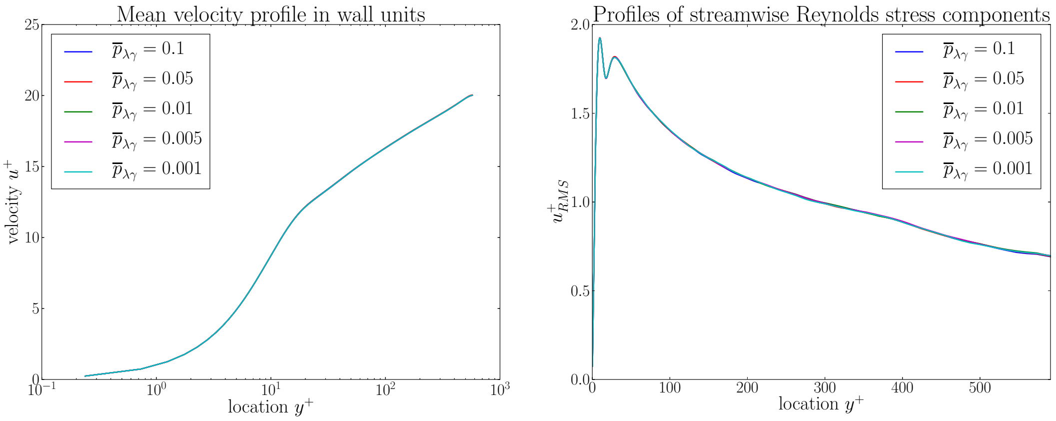

Figure C.5: Dependency of the law of the wall and the u_{RMS} velocity profile on the mean acceptance probability $\overline{p}_{\lambda\gamma}$ of eddies within ODT.

unity as described in section 2.2.3. Otherwise it could be that the distribution of accepted eddies varies from the physical distribution. Therefore, throughout this thesis $\overline{p}_{\lambda\gamma} = 0.002$ is chosen.

Although, the variation seems to have no influence on the results, it influences the calculation time. Table C.1 shows the reduction of calculation time compared to the reference case with $\overline{p}_{\lambda\gamma} = 0.001$. As

Table C.1: Relative time savings of calculation for varying $\overline{p}_{\lambda\gamma}$.

$\overline{p}_{\lambda\gamma}$	0.1	0.05	0.01	0.005	0.001
time savings	24%	41%	34%	17%	—

can be seen a reduction of the oversampling to $\overline{p}_{\lambda\gamma} = 0.05$ gives a reduction of the calculation time of about 41% for this test. The increase for a further reduction of $\overline{p}_{\lambda\gamma}$ possibly results from the additional calculation time needed due to adjustment of the mean sampling time δt.

PUBLICATIONS

Some ideas and figures have appeared previously in the publications [1, 4, 5]. The publications [2, 3] are in preparation. The author of this thesis is highlighted within the references.

[1] C. Glawe, **F. T. Schulz**, E. D. Gonzalez-Juez, H. Schmidt, and A. R. Kerstein. ODTLES simulation of turbulent flows through heated channels and ducts. *TSFP-8*, pages 1–6, 2013.

[2] **F. T. Meiselbach**, H. Schmidt, and A. R. Kerstein. ODT simulation of scalar transport in channel flows at high Reynolds and various Schmidt numbers. *in preparation*, 2015.

[3] **F. T. Meiselbach**, H. Schmidt, A. R. Kerstein, and A. de Lozar. Simulation of a smoke cloud top mixing layer using One Dimensional Turbulence. *in preparation*, 2015.

[4] A. Movaghar, M. Linne, M. Oevermann, **F. T. Meiselbach**, H. Schmidt, and A. R. Kerstein. Numerical study of liquid breakup at the surface of turbulent liquid jets using One-Dimensional Turbulence. *26th Annual Conference on Liquid Atomization and Spray Systems*, page 12, 2014.

[5] **F. T. Schulz**, C. Glawe, H. Schmidt, and A. R. Kerstein. Toward modeling of CO2 multi-phase flow patterns using a stochastic multi-scale approach. *Environmental Earth Sciences*, 70(8):3739–3748, 2013. doi: 10.1007/s12665-013-2461-5.

[6] C. Aalburg, K. A. Sallam, and G. M. Faeth. Properties of nonturbulent round liquid jets in uniform crossflows. *AIAA*, 42 (969), 2004.

[7] H. Alfredsson, A. V. Johansson, J. H. Haritonidis, and H. Eckelmann. The fluctuating wallshear stress and the velocity field in the viscous sublayer. *Physics of Fluids*, 31:1026–1033, 1988. doi: 10.1063/1.866783.

[8] P. H. Alfredsson, A. Segalini, and R. Örlü. A new scaling for the streamwise turbulence intensity in wall-bounded turbulent flows and what it tells us about the "outer" peak. *Physics of Fluids (041702)*, 23, 2011. doi: 10.1063/1.3581074.

[9] W. T. Ashurst and A. R. Kerstein. One-dimensional turbulence: Variable-density formulation and application to mixing layers. *Physics of Fluids*, 17(025107), 2005.

[10] G. I. Barenblatt, A. J. Chorin, and V. M. Prostokishin. Scaling laws for developed turbulent flow in pipes. *Applied Mechanics Reviews*, 50:413–429, 1997. doi: 10.1115/1.3101726.

[11] C. S. Bretherton, M. K. Macvean, P. Bechtold, A. Chlond, W. R. Cotton, J. Cuxart, H. Cuijpers, M. Khairoutdinov, B. Kosovic, D. Lewellen, C.-H. Moeng, P. Siebesma, B. Stevens, D. E. Stevens, I. Sykes, and M. C. Wyant. An intercomparison of radiatively driven entrainment and turbulence in a smoke cloud, as simulated by different numerical models. *Quarterly Journal of the Royal Meteorological Society*, 125(554):391–423, 1999.

[12] I. N. Bronstein, K. A. Semendyayev, G. Musiol, and H. Mühlig. *Handbook of mathematics*, volume 5. Springer, 2007. ISBN 978-3-662-21984-3.

[13] F Chillà and J Schumacher. New perspectives in turbulent Rayleigh-Bénard convection. *The European physical journal. E*, 35(7):25, 2012. doi: 10.1140/epje/i2012-12058-1.

[14] S. N. Chiu, D. Stoyan, W. S. Kendall, and J. Mecke. *Stochastic geometry and its applications*, volume 3. Wiley, 2013. ISBN 978-0-470-66481-0.

[15] F. H. Clauser. The turbulent boundary layer. *Advances in Applied Mechanics*, 4(1), 1956.

[16] R. E. Crochiere and L. R. Rabiner. *Multirate digital signal processing*, volume 2. Prentice Hall, 1983. ISBN 0-13-605162-6.

[17] Z. Dai, W.-H. Chou, and G. M. Faeth. Drop formation due to turbulent primary breakup at the free surface of plane liquid wall jets. *Physics of Fluids*, 10(5):1147–1157, 1998. doi: 10.1063/1.869639.

[18] A. de Lozar and J. P. Mellado. Direct numerical simulations of a smoke cloud-top mixing layer as a model for stratocumuli. *Journal of the Atmospheric Sciences*, 70(8):2356–2375, 2013. doi: 10.1175/JAS-D-12-0333.1.

[19] J. C. del Álamo and J. Jiménez. Direct numerical simulation of the very large anisotropic scales in a turbulent channel. *Center for Turbulence Research, Annual Research Briefs 2001*, 2001.

[20] J. C. del Álamo and J. Jiménez. Spectra of the very large anisotropic scales in turbulent channels. *Physics of Fluids*, 15 (6):L41, 2003. doi: 10.1063/1.1570830.

[21] J. C. del Álamo, J. Jiménez, P. Zandonade, and R. D. Moser. Scaling of the energy spectra of turbulent channels. *Journal of Fluid Mechanics*, 500:135–144, 2004. doi: 10.1017/S002211200300733X.

[22] E. Dietze, H. Schmidt, B. Stevens, and J. P. Mellado. Controlling entrainment in the smoke cloud using level set-based front tracking. *Meteorologische Zeitschrift*, 0(0):0, 2014. doi: 10.1127/metz/2014/0595.

[23] C. Dumouchel. On the experimental investigation on primary atomization of liquid streams. *Experiments in Fluids*, 45(3):371–422, 2008. doi: 10.1007/s00348-008-0526-0.

[24] S. G. Durbin, M. Yoda, and S. I. Abdel-Khalik. Impact of boundary-layer cutting and flow conditioning on free-surface behavior in turbulent liquid sheets. *Fusion Science and Technology*, 47(3):718–723, 2005.

[25] S. G. Durbin, M. Yoda, and S. I. Abdel-Khalik. Initial conditions and near-field dynamics in turbulent liquid sheets. *Flow, Turbulence and Combustion*, 79(3):307–320, 2007. doi: 10.1007/s10494-007-9092-4.

[26] Tarek Echekki, Alan R. Kerstein, Thomas D. Dreeben, and Jyh-yuan Chen. One-dimensional turbulence simulation of turbulent jet diffusion flames: Model formulation and illustrative applications. *Combustion and Flame*, 125:1083–1105, 2001. doi: 10.1016/S0010-2180(01)00228-0.

[27] J. H. Ferziger and M. Perić. *Computational Methods for Fluid Dynamics*, volume 3. Springer, 2002. ISBN 978-3-540-42074-3.

[28] M. Gad-el-Hak and P. Bandyopadhyay. Reynolds number effects in wall-bounded turbulent flows. *Applied Mechanics Reviews*, 47(307), 1994.

[29] W. K. Geoge and L. Castillo. The zero pressure-gradient turbulent boundary layer. *Applied Mechanics Reviews*, 50(12):689–729, 1997. doi: 10.1115/1.3101858.

[30] C. Glawe, H. Schmidt, A. R. Kerstein, and R. Klein. XLES Part II: From extended Large Eddy Simulation to ODTLES. *Journal of Computational Physics (in preparation*, 2015.

[31] E. D. Gonzalez-Juez, R. C. Schmidt, and A. R. Kerstein. ODTLES simulations of wall-bounded flows. *Physics of Fluids*, 23 (12):125102, 2011. doi: 10.1063/1.3664123.

[32] S. He and M. Seddighi. Turbulence in transient channel flow. *Journal of Fluid Mechanics*, 715:60–102, 2013. doi: 10.1017/jfm.2012.498.

[33] S. Hoyas and J. Jiménez. Scaling of the velocity fluctuations in turbulent channels up to $\mathrm{Re}_\tau = 2003$. *Physics of Fluids (011702)*, 18, 2006. doi: 10.1063/1.2162185.

[34] S. Hoyas and J. Jiménez. Reynolds number effects on the Reynolds-stress budgets in turbulent channels. *Physics of Fluids*, 20(10):101511, 2008. doi: 10.1063/1.3005862.

[35] A. K. M. F. Hussain and W. C. Reynolds. Measurements in fully developed turbulent channel flow. *Journal of Fluid Mechanics*, 97 (4), 568-580. doi: 10.1115/1.3448125.

[36] N. Hutchins, T. B. Nickels, I. Marusic, and M. S. Chong. Hot-wire spatial resolution issues in wall-bounded turbulence. *Journal of Fluid Mechanics*, 635:103, 2009. doi: 10.1017/S0022112009007721.

[37] B. Jähne. *Digitale Bildverarbeitung*, volume 7. Springer, 2012. ISBN 978-3-642-04951-4.

[38] J. Jiménez and S. Hoyas. Turbulent fluctuations above the buffer layer of wall-bounded flows. *Journal of Fluid Mechanics*, 611 (2008):215–236, 2008. doi: 10.1017/S0022112008002747.

[39] J. Jiménez and R. D. Moser. What are we learning from simulating wall turbulence? *Philosophical transactions. Series A, Mathematical, physical, and engineering sciences*, 365(1852):715–32, 2007. doi: 10.1098/rsta.2006.1943.

[40] M. Kaczorowski and C. Wagner. Analysis of the thermal plumes in turbulent Rayleigh-Bénard convection based on well-resolved numerical simulations. *Journal of Fluid Mechanics*, 618: 89–112, 2009. doi: 10.1017/S0022112008003947.

[41] Y. Kaneda, K. Morishita, and T. Ishihara. Small scale universality and spectral characteristics in turbulent flows. *International Symposium on Turbulence and Shear Flow Phenomena*, TSFP-8:1–6, 2013.

[42] H. Kawamura, H. Abe, and Y. Matsuo. DNS of turbulent heat transfer in channel flow with respect to Reynolds and Prandtl number effects. *International Journal of Heat and Fluid Flow*, 20: 196–207, 1999. doi: 10.1016/S0142-727X(99)00014-4.

[43] L. Keirsbulck, G. Fourrié, L. Labraga, and M. Gad-el-Hak. Scaling of statistics in wall-bounded turbulent flows. *Comptes Rendus Mécanique*, 340(6):420–433, 2012. doi: 10.1016/j.crme.2012.02.005.

[44] L. Keirsbulck, L. Labraga, and M. Gad-el-Hak. Statistical properties of wall shear stress fluctuations in turbulent channel flows. *International Journal of Heat and Fluid Flow*, 37, 2012. doi: 10.1016/j.ijheatfluidflow.2012.04.004.

[45] A. R Kerstein. Linear-eddy modelling of turbulent transport. Part 6. Microstructure of diffusive scalar mixing fields. *Journal of Fluid Mechanics*, 231:361–394, 1991. doi: 10.1017/S0022112091003439.

[46] A. R. Kerstein. One-dimensional turbulence: model formulation and application to homogeneous turbulence, shear flows, and buoyant stratified flows. *Journal of Fluid Mechanics*, 392:277–334, 1999. ISSN 00221120. doi: 10.1017/S0022112099005376.

[47] A. R. Kerstein. *Documentation of BasicODT, a simple ODT Code: Version 1*. 2007.

[48] A. R. Kerstein, Wm. T. Ashurst, S. Wunsch, and V. Nilsen. One-dimensional turbulence: Vector formulation and application to free shear flows. *Journal of Fluid Mechanics*, 447:85–109, 2001. doi: 10.1017/S0022112001005778.

[49] R. Klein. Semi-implicit extension of a Godunov-type scheme based on low mach number asymptotics I: One-dimensional flow. *Journal of Computational Physics*, 121:213–237, 1995.

[50] N. Krishnamoorthy. *Reaction models and reaction state parameterization for turbulent nonpremixed combustion*. PhD thesis, 2008.

[51] R. Lebas, T. Menard, P. A. Beau, A. Berlemont, and F. X. Demoulin. Numerical simulation of primary break-up and atomization: DNS and modelling study. *International Journal of Multiphase Flow*, 35(3):247–260, 2009. doi: 10.1016/j.ijmultiphaseflow.2008.11.005.

[52] J. Lee, B. Miller, and K. A. Sallam. Demonstration of digital holographic diagnostics for the breakup of liquid jets using a commercial-grade CCD sensor. *Atomization and Sprays*, 19(5): 445–456, 2009. doi: 10.1615/AtomizSpr.v19.i5.30.

[53] K. Lee, C. Aalburg, F. J. Diez, G. M. Faeth, and K. A. Sallam. Primary breakup of turbulent round liquid jets in uniform crossflows. *AIAA Journal*, 45(8):1907–1916, 2007. doi: 10.2514/1.19397.

[54] M. Lee, N. Malaya, and R. D. Moser. Direct numerical simulation for turbulent channel flow at high Reynolds number, 2012. 65th Annual Meeting of the APS Division of Fluid Dynamics.

[55] R. J. LeVeque. *Finite volume methods for hyperbolic problems*. Cambridge University Press, 2005. ISBN 0-521-00924-3.

[56] D. O. Lignell, A. R. Kerstein, G. Sun, and E. E. Monson. Mesh adaption for efficient multiscale implementation of One-Dimensional Turbulence. *Theoretical and Computational Fluid Dynamics*, 27(3-4):273–295, 2013. doi: 10.1007/s00162-012-0267-9.

[57] D. K. Lilly. Models of cloud-topped mixed layers under a strong inversion. *Quarterly Journal of the Royal Meteorological Society*, 94 (401):292–309, 1968. doi: 10.1002/qj.49709440106.

[58] R. R. Long and T.-C. Chen. Experimental evidence for the existence of the 'mesolayer' in turbulent systems. *Journal of Fluid Mechanics*, 105:19–59, 1981. doi: 10.1017/S0022112081003108.

[59] A. Lozano-Durán and J. Jiménez. Effect of the computational domain on direct simulations of turbulent channels up to $Re_\tau = 4200$. *Physics of Fluids*, 26(011702), 2014. doi: 10.1063/1.4862918.

[60] E. Lubarsky, J. R. Reichel, B. T. Zinn, and R. McAmis. Spray in crossflow: Dependence on Weber number. *Journal of Engineering for Gas Turbines and Power*, 132(2):021501, 2010. doi: 10.1115/1.2904892.

[61] A. Mansour and N. Chigier. Turbulence characteristics in cylindrical liquid jets. *Physics of Fluids*, 6(10):3380–3391, 1994. doi: 10.1063/1.868396.

[62] I. Marusic, B. J. McKeon, P. A. Monkewitz, H. M. Nagib, A. J. Smits, and K. R. Sreenivasan. Wall-bounded turbulent flows at high Reynolds numbers: Recent advances and key issues. *Physics of Fluids (065103)*, 22(6), 2010. doi: 10.1063/1.3453711.

[63] B. J. McKeon, J. Li, W. Jiang, J. F. Morrison, and A. J. Smits. Further observations on the mean velocity distribution in fully developed pipe flow. *Journal of Fluid Mechanics*, 501:135–147, 2004. doi: 10.1017/S0022112003007304.

[64] T. Ménard, S. Tanguy, and a. Berlemont. Coupling level set/VOF/ghost fluid methods: Validation and application to 3D simulation of the primary break-up of a liquid jet. *International Journal of Multiphase Flow*, 33(5):510–524, 2007. doi: 10.1016/j.ijmultiphaseflow.2006.11.001.

[65] M. M. Metzger and J. C. Klewicki. A comparative study of near-wall turbulence in high and low Reynolds number boundary layers. *Physics of Fluids*, 13(3):692, 2001. doi: 10.1063/1.1344894.

[66] C.-H. Moeng, W. R. Cotton, C. S. Bretherton, A. Chlond, M. Khairoutdinov, S. Krüger, W. S. Lewellen, M. K. Mac Vean, J. R. M. Pasquier, H. A. Rand, A. P. Siebesma, B. Stevens, and R. I. Sykes. Simulation of a stratocumulus-topped planetary boundary layer: Intercomparison among different numerical codes. *Bulletin of the American Meteorological Society*, 77(2):261–278, 1996. doi: 10.1175/1520-0477(1996)077<0261:SOASTP>2.0.CO;2.

[67] J. F. Morrison, B. J. McKeon, W. Jiang, and A. J. Smits. Scaling of the streamwise velocity component in turbulent pipe flow. *Journal of Fluid Mechanics*, 508:99–131, 2004. doi: 10.1017/S0022112004008985.

[68] R. D. Moser and J. Kim. Direct numerical simulation of turbulent channel flow up to $Re_\tau = 590$. *Physics of Fluids*, 11(4):943–945, 1999. doi: S1070-66319902204-7.

[69] I. Müller and W. H. Müller. *Fundamentals of Thermodynamics and Applications*. Springer, 2009. ISBN 978-3-540-74645-4.

[70] H. M. Nagib and K. A. Chauhan. Variations of von Kármán coefficient in canonical flows. *Physics of Fluids*, 20(10):101518, 2008. doi: 10.1063/1.3006423.

[71] R. Örlü and P. Schlatter. On the fluctuating wall-shear stress in zero pressure-gradient turbulent boundary layer flows. *Physics of Fluids (021704)*, 23:1–4, 2011. doi: 10.1063/1.3555191.

[72] P. O'Shea, A. Z. Sadik, and Z. M. Hussain. *Digital signal processing*. Springer, 2011. ISBN 978-3-642-15590-1.

[73] R. L Panton. Composite asymptotic expansions and scaling wall turbulence. *Philosophical transactions. Series A, Mathematical, physical, and engineering sciences*, 365(1852):733–54, 2007. doi: 10.1098/rsta.2006.1951.

[74] D. V. Papavassiliou and T. J. Hanratty. Transport of a passive scalar in a turbulent channel flow. *International Journal of Heat and Mass Transfer*, 40(6):1303–1311, 1997.

[75] L. Prandtl. Über Flüssigkeitsbewegung bei sehr kleiner Reibung, 1904. Verhandlungen des 3. Internationalen Mathematik Kongresses, Heidelberg.

[76] P. Sagaut. *Large Eddy Simulation for Incompressible Flows*. Springer, 2006. ISBN 978-3-540-26344-9.

[77] K. A. Sallam and G. M. Faeth. Surface properties during primary breakup of turbulent liquid jets in still air. *AIAA Journal*, 41(8):1514–1524, 2003. doi: 10.2514/2.2102.

[78] K. A. Sallam, Z Dai, and G. M. Faeth. Drop formation at the surface of plane turbulent liquid jets in still gases. *International Journal of Multiphase Flow*, 25(6-7):1161–1180, 1999. doi: 10.1016/S0301-9322(99)00042-7.

[79] K. A. Sallam, Z. Dai, and G. M. Faeth. Liquid breakup at the surface of turbulent round liquid jets in still gases. *International Journal of Multiphase Flow*, 28:427–449, 2002.

[80] K. a. Sallam, C. Aalburg, and G. M. Faeth. Breakup of round nonturbulent liquid jets in gaseous crossflow. *AIAA Journal*, 42 (12):2529–2540, 2004. doi: 10.2514/1.3749.

[81] B. J. Sayler and R. E. Breidenthal. Laboratory simulations of radiatively induced entrainment in stratiform clouds. *Journal of Geophysical Researchl*, 103(D8):8827–8837, 1998. doi: 10.1029/98JD00344.

[82] H. Schlichting and K. Gersten. *Grenzschicht-Theorie*. Springer, 2006. ISBN 978-3-540-23004-5.

[83] H. Schmidt, A. R. Kerstein, S. Wunsch, R. Nédélec, and B. J. Sayler. Analysis and numerical simulation of a laboratory analog of radiatively induced cloud-top entrainment. *Theoretical and Computational Fluid Dynamics*, 27(3-4):377–395, 2012. doi: 10.1007/s00162-012-0288-4.

[84] R. C. Schmidt, A. R. Kerstein, S. E. Wunsch, and V. Nilsen. Near-wall LES closure based on one-dimensional turbulence modeling. *Journal of Computational Physics*, 186:317–355, 2003. doi: 10.1016/S0021-9991(03)00071-8.

[85] R. C Schmidt, A. R Kerstein, and R. McDermott. ODTLES: A multi-scale model for 3D turbulent flow based on one-dimensional turbulence modeling. *Computer Methods in Applied Mechanics and Engineering*, 199(13-16):865–880, 2010. doi: 10.1016/j.cma.2008.05.028.

[86] M P Schultz and K A Flack. Reynolds-number scaling of turbulent channel flow. *Physics of Fluids*, 25(025104):13, 2013. doi: 10.1063/1.4791606.

[87] F. Schwertfirm and M. Manhart. DNS of passive scalar transport in turbulent channel flow at high Schmidt numbers. *International Journal of Heat and Fluid Flow*, 28(6):1204–1214, 2007. doi: 10.1016/j.ijheatfluidflow.2007.05.012.

[88] B. T. Shellabarger, S. G. Durbin, M. Yoda, S. I. Abdel-Khalik, and D. L. Sadowski. Primary breakup in turbulent liquid films on downward-facing surfaces. *Fusion Science and Technology*, 46 (4):571–576, 2004.

[89] J. Shinjo and A. Umemura. Simulation of liquid jet primary breakup: Dynamics of ligament and droplet formation. *International Journal of Multiphase Flow*, 36(7):513–532, 2010. doi: 10.1016/j.ijmultiphaseflow.2010.03.008.

[90] J. Shinjo and A. Umemura. Detailed simulation of primary atomization mechanisms in Diesel jet sprays (isolated identification of liquid jet tip effects). *Proceedings of the Combustion Institute*, 33(2):2089–2097, 2011. doi: 10.1016/j.proci.2010.07.006.

[91] C. Srinivasan and D. V. Papavassiliou. Direction of scalar transport in turbulent channel flow. *Physics of Fluids*, 23(115105):21, 2011. doi: 10.1063/1.3657825.

[92] J. Stoer and Bulrisch R. *Introduction to numerical analysis*. Springer, 2002. ISBN 978-1-4419-3006-4.

[93] J. S. Turner. *Buoyancy effects in fluids*. Cambridge University Press, 2012. ISBN 978-0-511-60882-7.

[94] D. C. Wilcox. *Turbulence modeling for CFD*. DCW Industries, 2006. ISBN 978-1-928-72908-2.

[95] D. H. Wolf, F. P. Incropera, and R. Viskanta. Measurement of the turbulent flow field in a free-surface jet of water. *Experiments in Fluids*, 18(6):397–408, 1995. doi: 10.1007/BF00208462.

[96] R. Wood. Stratocumulus Clouds. *Monthly Weather Review*, 140 (8):2373–2423, 2012. doi: 10.1175/MWR-D-11-00121.1.

[97] Martin Wosnik, Luciano Castillo, and William K. George. A theory for turbulent pipe and channel flows. *Journal of Fluid Mechanics*, 421:115–145, 2000. doi: 10.1017/S0022112000001385.

[98] P.-K. Wu and G. M. Faeth. Aerodynamic effects on primary breakup of turbulent liquids. *AIAA*, 31(93-0903), 1993.

[99] P.-K. Wu and G. M. Faeth. Onset and end of drop formation along the surface of turbulent liquid jets in still gases. *Physics of Fluids*, 7(11):2915–2917, 1995. doi: 1070-6631/95/7(11)/2915/3/\$6.00.

[100] P.-K. Wu, G. A. Ruff, and G. M. Faeth. Primary breakup in liquid / gas mixing layers. *AIAA*, 29(91-19219), 1991.

[101] P.-K. Wu, L.-K. Tseng, and G. M. Faeth. Primary breakup in gas/liquid mixing layers for turbulent liquids. *AIAA*, 30(92-0462), 1992.

[102] P.-K. Wu, R. F. Miranda, and G. M. Faeth. Effects of initial flow conditions on primary breakup of nonturbulent and turbulent liquid jets. *AIAA*, 32(94-0561), 1994.

[103] X. Wu and P. Moin. Transitional and turbulent boundary layer with heat transfer. *Physics of Fluids*, 22(085105), 2010. doi: 10.1063/1.3475816.

[104] S. Wunsch and A. R. Kerstein. A model for layer formation in stably stratified turbulence. *Physics of Fluids*, 13(3):702–712, 2001. doi: 10.1063/1.1344182.

[105] T. Yamaguchi and D. A. Randall. Cooling of Entrained Parcels in a Large-Eddy Simulation. *Journal of the Atmospheric Sciences*, 69(3):1118–1136, 2012. doi: 10.1175/JAS-D-11-080.1.

[106] D. You and P. Moin. A dynamic global-coefficient subgrid-scale model for large-eddy simulation of turbulent scalar transport in complex geometries. *Physics of Fluids*, 21 (045109), 2009. doi: 10.1063/1.3115068.

[107] M. V. Zagarola and A. J. Smits. Mean-flow scaling of turbulent pipe flow. *Journal of Fluid Mechanics*, 373:33–79, 1998. doi: 10.1017/S0022112098002419.

[108] E.-S. Zanoun, F. Durst, and H. Nagib. Evaluating the law of the wall in two-dimensional fully developed turbulent channel flows. *Physics of Fluids*, 15(10), 2003. doi: 10.1063/1.1608010.

[109] E.-S. Zanoun, H. Nagib, and F. Durst. Refined c_f relation for turbulent channels and consequences for high-*Re* experiments. *Fluids Dynamics Research*, 41(021405), 2009. doi: 10.

DECLARATION

I hereby certify that this thesis has been composed by me and is based on my own work, unless stated otherwise. No other person's work has been used without due acknowledgement in this thesis. All references and verbatim extracts have been quoted, and all sources of information, including graphs and data sets, have been specifically acknowledged.

Hiermit erkläre ich an Eides Statt, dass ich die vorliegende Arbeit selbstständig und nur unter Zuhilfenahme der ausgewiesenen Hilfsmittel angefertigt habe. Sämtliche Stellen der Arbeit, die im Wortlaut oder dem Sinn nach anderen gedruckten oder im Internet verfügbaren Werken entnommen sind, habe ich durch genaue Quellenangaben kenntlich gemacht.

Cottbus, March 2015

F. T. Meiselbach

COLOPHON

This document was typeset using the typographical look-and-feel `classicthesis` developed by André Miede. The style was inspired by Robert Bringhurst's seminal book on typography "*The Elements of Typographic Style*". `classicthesis` is available for both LaTeX and LyX:

`http://code.google.com/p/classicthesis/`

Happy users of `classicthesis` usually send a real postcard to the author, a collection of postcards received so far is featured here:

`http://postcards.miede.de/`